Fermilab Library
0 1260 0038016 4

KEK Report 92-16
December 1992
A/H/M

# JLC-I

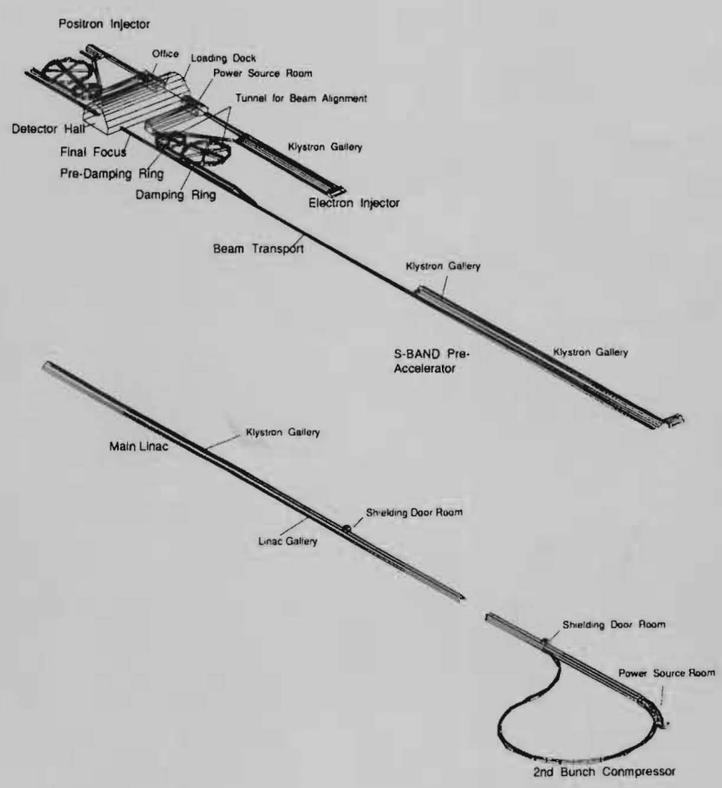


JLC Group

NATIONAL LABORATORY FOR
HIGH ENERGY PHYSICS

Report 92-16 JLC-I JLC Group

© **National Laboratory for High Energy Physics, 1992**

KEK Reports are available from:

Technical Information & Library
National Laboratory for High Energy Physics
1-1 Oho, Tsukuba-shi
Ibaraki-ken, 305
JAPAN

| | | |
|---|---|---|
| Phone: | 0298-64-1171 | |
| Telex: | 3652-534 | (Domestic) |
| | (0)3652-534 | (International) |
| Fax: | 0298-64-4604 | |
| Cable: | KEKOHO | |

# Contents


**1 Project Overview** **1**

1.1 Physics . . . . . 1

1.2 Starting the JLC-I Accelerator Construction . . . . . 2

**2 Physics** **5**

2.1 Physics Overview . . . . . 5

2.1.1 The Standard Model and its Missing Links . . . . . 5

2.1.2 Problems in the Standard Model . . . . . 7

2.1.3 Technicolor Scenario . . . . . 8

2.1.4 Supersymmetry . . . . . 9

2.1.5 Light Higgs: Messenger from the Grand Desert . . . . . 11

2.1.6 Roads to the Planck Scale . . . . . 11

2.2 The Light Higgs($h^0$) . . . . . 12

2.2.1 Introduction . . . . . 12

2.2.2 Discovery Strategy of Higgs Boson . . . . . 15

2.2.3 Detailed Study of Higgs Properties . . . . . 19

2.2.4 Br($h^0 \to \tau\bar{\tau}$) Measurement. . . . . 23

2.3 $H^0$, $A^0$, and $H^\pm$ . . . . . 24

2.3.1 Search Strategy . . . . . 24

2.3.2 $e^+e^- \to H^0Z^0$ . . . . . 24

2.3.3 $e^+e^- \to H^0A^0$ . . . . . 25

2.3.4 SUSY Scale from $m_{H^0}$ and $m_{A^0}$ Measurement . . . . . 27

2.4 SUSY Particles . . . . . 29

2.4.1 Model Assumptions . . . . . 29

2.4.2 Charginos . . . . . 30

2.4.3 Sleptons . . . . . 38

2.5 Tests of SUGRA-GUT Assumptions . . . . . 48

2.6 Top . . . . . 52

2.6.1 Measurements of Top Mass and $\alpha_s(M_Z)$ . . . . . 53

2.6.2 Measurement of Top Width . . . . . 55

2.6.3 Measurement of Top Yukawa Coupling . . . . . 55

2.6.4 Angular Analyses . . . . . 55

2.7 Precision Electroweak Physics . . . . . 58

2.7.1 Looking for New Physics in Loops . . . . . 58

2.7.2 Self-couplings of $W$, $Z$, and $\gamma$ . . . . . 63

2.8 CP Violation on the $Z$ Pole . . . . . 67

2.8.1 Compatibility with TeV Operation . . . . . 67

2.8.2 Forward-Backward Asymmetry . . . . . 68
2.8.3 Measurement of $B_d(\bar{B}_d) \to \Psi K_s$ . . . . . 69
2.8.4 Measurement of $B_s$-$\bar{B}_s$ Mixing . . . . . 69
2.9 Heavy Higgs or Strongly Interacting $W$'s . . . . . 71
2.9.1 W-fusion process . . . . . 72
2.9.2 Rescattering in $e^+e^- \to W^+W^-$ . . . . . 73

**3 DETECTOR** **81**
3.1 Detector Overview . . . . . 81
3.2 Vertex Detector . . . . . 83
3.2.1 Requirements for the Vertex Detector . . . . . 83
3.2.2 Configuration . . . . . 84
3.2.3 Operation of CCD Detectors . . . . . 85
3.2.4 Expected Performance . . . . . 86
3.2.5 Background Considerations . . . . . 88
3.3 Central Tracking Device . . . . . 88
3.3.1 Design Criteria . . . . . 89
3.3.2 Chamber Geometry and Cell Structure . . . . . 92
3.3.3 Readout Electronics . . . . . 93
3.4 Calorimeter . . . . . 94
3.4.1 Design Criteria . . . . . 94
3.4.2 Detector Configuration . . . . . 96
3.4.3 Mechanical Structure . . . . . 97
3.4.4 Electronics . . . . . 99
3.5 Muon Detector . . . . . 100
3.5.1 Design Criteria . . . . . 100
3.5.2 Detector Configuration . . . . . 100
3.5.3 Expected Performance . . . . . 100
3.6 Superconducting Solenoid Magnet . . . . . 101
3.6.1 General Characteristics . . . . . 101
3.6.2 Cooling System . . . . . 103
3.6.3 Superconductor . . . . . 104
3.6.4 Energy Extraction . . . . . 105
3.7 Background and Masking System . . . . . 105
3.7.1 Introduction . . . . . 105
3.7.2 Muons . . . . . 106
3.7.3 Synchrotron Radiations . . . . . 106
3.7.4 $e^+e^-$ pairs . . . . . 109
3.7.5 Masking System . . . . . 111
3.7.6 Background at the Vertex Detector . . . . . 114
3.8 The Underlying Hadronic Background . . . . . 114
3.8.1 The Model . . . . . 115
3.8.2 The Background Yield . . . . . 115
3.8.3 Effect on Physics Analyses . . . . . 117
3.9 Data Acquisition and Trigger . . . . . 118
3.9.1 Channel Count and Read-out Scheme . . . . . 118
3.9.2 Trigger Philosophy . . . . . 119

**4 Accelerator** **123**
4.1 Beam Parameters . . . 123
4.2 Electron and Positron Sources . . . 125
4.2.1 Electron source . . . 125
4.2.2 Polarized Electron Source . . . 133
4.2.3 Positron Source . . . 138
4.3 Damping Ring . . . 144
4.3.1 Introduction . . . 144
4.3.2 Lattice and Optics . . . 146
4.3.3 Dynamic Aperture and Alignment Tolerances . . . 149
4.3.4 Single Bunch Instability . . . 149
4.3.5 Multibunch Instabilities . . . 151
4.3.6 Injection and Extraction . . . 152
4.3.7 Magnet System . . . 152
4.3.8 RF System . . . 154
4.3.9 Instrumentation . . . 155
4.3.10 Vacuum system . . . 156
4.4 Bunch Compressor . . . 159
4.4.1 Introduction . . . 159
4.4.2 Basic parameters . . . 159
4.4.3 First Compressor . . . 160
4.4.4 Second Compressor . . . 162
4.4.5 Beam-Loading and Its Compensation . . . 163
4.5 0.3–0.5 TeV X-band Linac System . . . 166
4.5.1 Design of X-band linac . . . 167
4.5.2 X-band RF System . . . 173
4.6 0.3–0.5 TeV C-band Linac System . . . 184
4.6.1 Outline of C-band Linac . . . 185
4.6.2 C-band RF-Source . . . 186
4.6.3 C-Band Accelerating Structure . . . 192
4.7 0.3–0.5 TeV S-band Linac System . . . 195
4.7.1 S-band Linac . . . 195
4.7.2 S-band RF System . . . 200
4.8 Final Focus System . . . 201
4.8.1 Overview . . . 201
4.8.2 Design of Optics . . . 202
4.8.3 Optical Characteristics . . . 204
4.8.4 Tolerances . . . 206
4.8.5 The Nanometer Collision . . . 209
4.8.6 Collimator Section . . . 212
4.8.7 Final Focus Quadrupole Magnet . . . 214
4.9 Instrumentation and Control . . . 217
4.9.1 Instrumentation . . . 217
4.9.2 Control . . . 219
4.10 Civil Engineering . . . 220
4.10.1 Technical Site Criteria . . . 220
4.10.2 Construction Methods of Main Tunnel and Detector-Hall . . . 221

**5 Time Schedule and Cost Estimation** **231**
5.1 Time Schedule . . . . . 231
5.2 Cost Estimations . . . . . 231

**6 JLC as a spearhead of high technology** **233**
6.1 Application as a synchrotron light source . . . . . 233
6.1.1 Introduction . . . . . 233
6.1.2 Hard X-ray laser with JLC . . . . . 235
6.1.3 Application of X-ray laser . . . . . 235

**Acknowledgement** **237**

**JLC Group** **240**

# Chapter 1

# Project Overview

The JLC project is the post-TRISTAN high energy physics program recommended by the High Energy Committee in 1986. The project consists of the construction of a linear collider, and the experiments therewith, at an initial center of mass energy around 500 GeV which will eventually reach 1.5 TeV, along with successive machine upgrades[1, 2, 3]. The recommendation initiated a systematic R&D program, which has been producing many remarkable results. On the other hand, the recent precision measurements at LEP have greatly enhanced the importance of an $e^+e^-$ linear collider to explore the energy region just above LEP II[4].

We propose the construction of JLC-I, which is an $e^+e^-$ linear collider to cover the center of mass energy range of up to 500 GeV with a peak luminosity of $5 \times 10^{33}$ cm$^{-2}$sec$^{-1}$, as the phase-I machine of the JLC project.

## 1.1 Physics

The main purpose of JLC-I is to discover and study the Higgs boson and the top quark, which are the two missing constituents of the Standard Model.

The most exciting possibility is the discovery of a Higgs particle with a mass less than 200 GeV. This mass range is particularly interesting from the viewpoint of grand unified models with the grand desert hypothesis, which naturally explain charge quantization, anomaly cancellation, strengths of the gauge interactions, *etc.* Moreover, the Weinberg angle $\sin^2\theta_W$, which has been precisely measured at LEP, agrees well with the prediction of its simplest supersymmetric extension originally introduced to solve the naturalness problem. Grand unified models with weak-scale supersymmetry predict at least one light Higgs boson, which cannot be missed at JLC-I with $\sqrt{s} = 300$ GeV.

If the weak-scale supersymmetry is indeed the case, JLC-I has a good chance to find heavier Higgs bosons as well as supersymmetric particles. JLC-I, being an $e^+e^-$ collider, will provide a unique opportunity to carry out detailed studies of these particles and will possibly allow us to get insight into physics on the Planck scale.

On the other hand, if no Higgs boson exists within the reach of JLC-I, one is forced to abandon the weak-scale supersymmetry and simple grand unification scenario. The JLC-I project thus has the potential of guiding the future direction in particle physics.

The analysis results of precision electroweak measurements strongly indicate the existence of the top quark in the reach of JLC-I. The study of the top quark properties is a necessary step to establish and go beyond the Standard Model. The top quark has rich physics in itself distinct from the spectroscopy of other quarkonia. The strong coupling constant $\alpha_s$ can be measured

with little ambiguity, since perturbative QCD is applicable to the threshold region. It is also possible to detect the Yukawa interaction. Furthermore, the accurate determination of its mass, possible only at an $e^+e^-$ collider, will fix the radiative correction parameters. This enables us to look for new physics effects, when combined with the $W$- and $Z$-boson parameters to be precisely determined by JLC-I, making full use of its high luminosity and beam polarization.

The experiment at JLC-I will reveal the nature of the two missing constituents of the Standard Model. We believe that it will possibly probe the physics up to Planck scale and uncover the secrets of the creation and evolution of our Universe.

## 1.2 Starting the JLC-I Accelerator Construction

We consider here the technical feasibility of construction of the JLC-I accelerator. The key specification we impose upon the accelerator in its startup stage is to provide a 'bottom-line' luminosity of $5 \times 10^{32}$ cm$^{-2}$sec$^{-1}$ at $\sqrt{s} = 300$ GeV to achieve the initial physics goals.

The main linac was conceived to be of X-band, in which multi-bunched beams are accelerated at very high gradients. Therefore the key issues in the full scale R&D program started in 1987 have been to develop klystrons capable of emitting peak powers as high as about 100 MW and to experimentally verify high acceleration gradients as high as 100MV/m in linac structures, both of which were far beyond the state of the art of linac technology in 1987. Furthermore an accelerator test facility ATF was founded, where we first started to construct a test S-band linac, planning to later annex to it a test damping ring of extremely small beam emittances. All-around R&D studies have also been intensively carried for other topics such as electron/positron sources and final focus systems. In parallel with those studies, we have been making every effort to optimize parameters of the JLC for its various phases. Of particular concern is the RF frequency choice among S-, C-, or X-band for JLC-I, since the X-band technology is still in a developing stage. R&D work at overseas institutes such as SLAC, CERN, INP-Protovino/Novosibirsk and DESY has been more or less on similar lines and there have been frequent exchanges of informations between KEK and those institutes.

The results of the R&D work are very promising. We were able to achieve an output power of 41 MW for the X-band klystron, which is about the same level as achieved at SLAC and INP. Accelerating gradients well higher than 50 MV/m have been achieved successfully for S-band and X-band structures. A novel idea of the choke cavity was proposed which might play an important role to kill dangerous higher order modes in the mult-bunch operation. Those results suggest that we have caught up with the world-wide progress of key RF technologies. Hence it is fair to say that major technological difficulties have been basically resolved and we may be in a technically favorable position to propose the collider construction as far as JLC-I is concerned for which technological requirements are still not so stringent. There remain, of course, many difficult problems to be solved: attaining high reliability of various components, their mass production in the industry, system design of the whole accelerator complex, site problem, etc. The most important may, however, be that we can assert the JLC-I construction only on condition that we promote the international technical collaboration as before or more.

A very brief résumé about the present status of R&D work might be appropriate here in order to review the whole range of our activities.

**Electron/positron sources:** A large enough number of electrons is shown extractable from conventional thermionic gun. An RF gun with a laser triggered photocathode is successfully providing low emittance beams at a relativistic energy. World-record polarizations

have been obtained by use of special crystal structures of gallium-arsenic alloys. A thorough simulation study has been carried out for positron production.

**Damping ring with its injector:** Construction of a test damping ring at the ATF is in preparation to verify the possibility of achieving very low emittances required for linear colliders. An S-band injector linac is being constructed to provide 1.5 GeV electrons.

**X-band klystron:** High power tests of the JLC XB-72K klystron are being carried on and a peak power of 41 MW has already been obtained. The beam power was as high as 234 MW which is just as large as that achieved at SLAC.

**Accelerating structure:** An acceleration gradient of 80 MV/m was obtained for conventional structures at both S- and X-bands. Basic studies for precision machining of structure components are intensely pursued with convincing results at the KEK machine shop. Simulation studies for damped structures and detuned ones are also providing affirmative results. The choke cavity, a new idea for damping higher order modes, has been proposed.

**Final focus system:** A achromatic line with a fairly large momentum acceptance has been designed. A couple of final quads which must provide precise field distribution in a very small aperture were manufactured successfully and will be tested at the FFTB facility of SLAC. The compton beam profile monitor which was proposed at KEK is being manufactured and will be tested at the FFTB too to survey the possibility of measuring beam sizes of nanometers. Careful simulation studies are continued to clarify the background noise problem at the interaction region.

**Construction cost estimation:** A resonable estimation of boring the tunnel is obtained. Regarding the machine cost, the R&D work described above is still limited to proof-of-principle studies for each components. The cost reduction critically depends on mass-production effects, which we have to pursue seriously henceforth.

The proposed JLC-I project is, in a sense, a pilot project for the entire JLC program. The project aims at exploring a new frontier of $e^+e^-$ collider physics with a modest extension of technologies at hand. We believe that the construction of JLC-I is a necessary step for future TeV linear colliders.

Following the operation as an energy-frontier machine, JLC-I will remain active not only as a top factory but also, automatically, as a $Z$-factory( $b$-factory ) and a $W$-factory with polarized beams and with a two-orders-of-magnitude higher luminosity than those of existing facilities.

# Bibliography


[1] "TRISTAN and High Energy Accelerator Plans at KEK", K. Takata and Y. Kimura, Particle Accelerators, 1990, Vol. 26, p.87.

[2] "General Plan of JLC", Y. Kimura, KEK Proceedings 91-10, p.1.

[3] "JLC: The Japan $e^+e^-$ Linear Collider Project for Higher Energy Physics", S. Iwata, KEK Proceedings 91-10, p.397.

[4] "Proposal for JLC-300", presented by S. Orito at The Third Workshop on Japan Linear Collider( JLC ), held at KEK on Feburary 18-20, 1992, UT-ICEPP 92-01( in Japanese ); "The JLC Project", presented by S. Orito at the JPS Meeting, Yokohama, March 27-30, 1992, UT-ICEPP 92-03( in Japanese ).

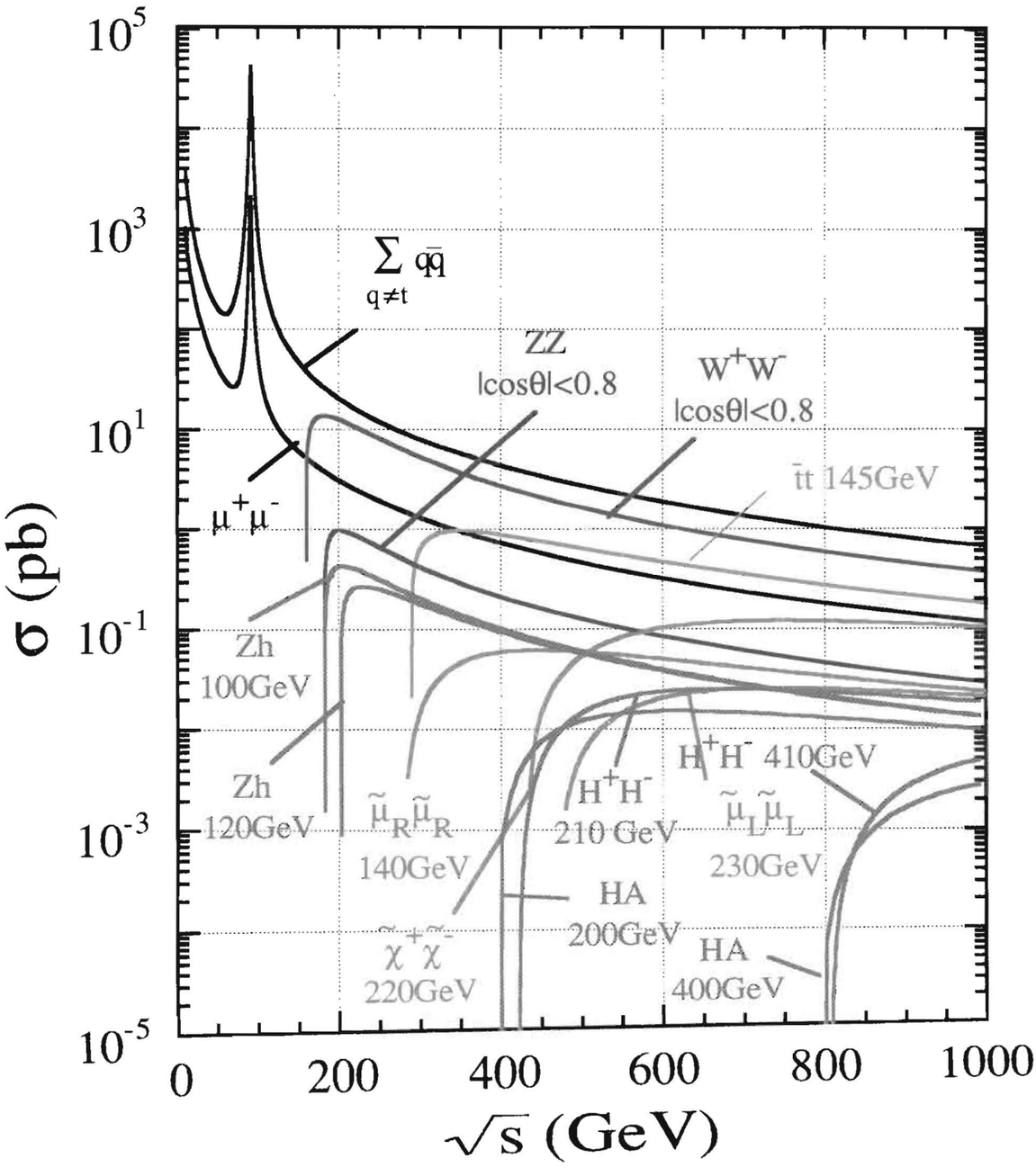
$10^5$
$10^3$
$10^1$
$10^{-1}$
$10^{-3}$
$10^{-5}$
σ (pb)
0
200
400
600
800
1000
$\sqrt{s}$ (GeV)
$\sum_{q\neq t} q\bar{q}$
ZZ
|cosθ|<0.8
$W^+W^-$
|cosθ|<0.8
$\bar{t}t$ 145GeV
$\mu^+\mu^-$
Zh
100GeV
Zh
120GeV
$\tilde{\mu}_R\tilde{\mu}_R$
140GeV
$\tilde{\chi}^+\tilde{\chi}^-$
220GeV
$H^+H^-$
210 GeV
HA
200GeV
$H^+H^-$ 410GeV
$\tilde{\mu}_L\tilde{\mu}_L$
230GeV
HA
400GeV

# Chapter 2

# Physics

## 2.1 Physics Overview

### 2.1.1 The Standard Model and its Missing Links

The goal of elementary particle physics is to identify the fundamental constituents of the physical world and the interactions among them, and find their simple description. Over these decades, it has become more and more certain that all but one of the four known interactions—electromagnetic, weak, and strong—can be described by the "Standard Model" [1], which is based on quantum field theory and gauge principle.

At the center of the Standard Model lies the concept of the spontaneous symmetry breaking [2], which generates the masses of the $W$- and $Z$-bosons. The discovery of these intermediate vector bosons at the predicted masses [3] is a great triumph of this concept. The masses of fermions are also generated by the spontaneous symmetry breaking, due to the Yukawa couplings of fermions to the Higgs boson.

The gauge principle has been tested with a very high precision. In particular, the quark-lepton universality, which motivated the introduction of gauge principle to the weak interaction physics [4], has been verified to 0.1% [5]

$$|V_{ud}|^2 + |V_{us}|^2 + |V_{ub}|^2 = 0.9991 \pm 0.0016, \tag{2.1}$$

where $V_{ij}$'s are the Kobayashi-Maskawa matrix elements [6]. The $SU(2)_L \times U(1)_Y$ quantum numbers of quarks and leptons have all been determined precisely at $e^+e^-$ colliders [7, 8]. The agreement in the measured values of the Weinberg angle obtained in a variety of ways (Fig. 2.1) demonstrates the validity of the gauge principle.

Although the Standard Model has been very successful, the observed particle spectrum is obviously incomplete. The axial vector coupling of the bottom quark to the $Z$-boson is measured to be one half [10]. The bottom quark thus belongs to an $SU(2)_L$ multiplet with a half-integral isospin, and must have (at least) one $SU(2)_L$ partner which has not been found yet. To establish the idea of the quantum field theory and the gauge principle, it is definitely necessary to discover this missing particle: the top quark.

Fortunately, we have an upper bound on the mass of the top quark, $m_t < 200$ GeV at more than 95% confidence level from analyses of the electroweak radiative corrections [11]. The measurements of particle masses, various cross sections and asymmetries we have accumulated at high-energy experiments are now so precise that we are already sensitive to the quantum effects of undiscovered particles. Thus discovery of the top quark within the predicted mass

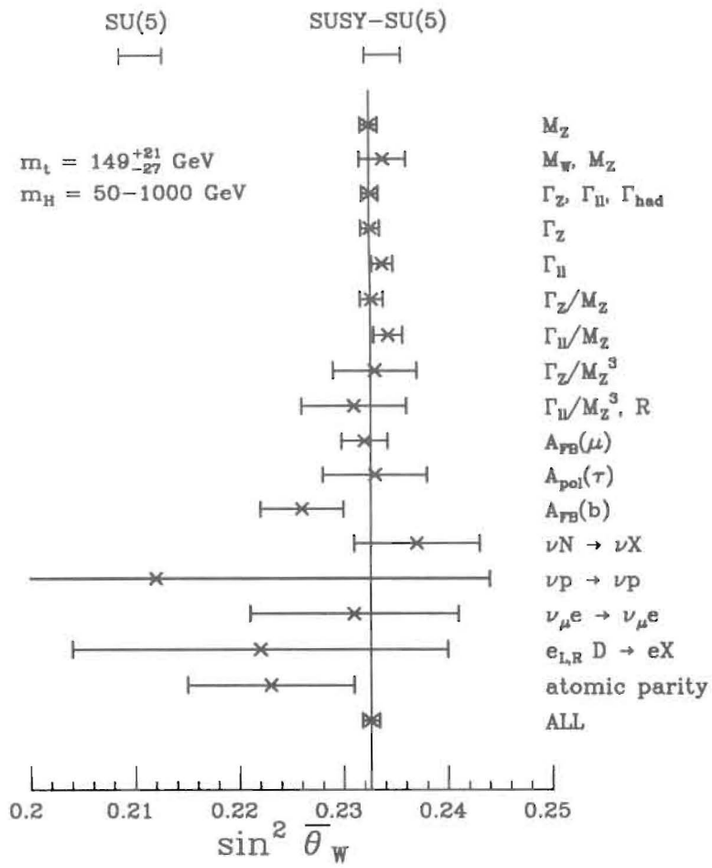


Figure 2.1: The $\overline{MS}$ Weinberg angle $\sin^2\bar{\theta}_W$ determined in a variety of ways, using the best-fit value $m_t = 149^{+21}_{-27}$ GeV and $m_H = 50$–1000 GeV. The data are taken from Ref. [9].

range, as well as the study of its properties, is an essential step to establish the Standard Model. An $e^+e^-$ collider at $\sqrt{s} = 500$ GeV cannot miss the top quark and provides an ideal place for this purpose.

The study of the top quark is an important subject by itself (Sect. 2.6). First of all, a precise measurement of its mass, $\Delta m_t < 500$ MeV, is possible at the $t\bar{t}$ threshold. The large width of the top quark acts as an infrared cutoff to the QCD interaction, allowing us to make definite theoretical predictions using perturbative QCD [12]. This remarkable feature provides a clean test of perturbative QCD as well as a precise measurement of the strong coupling constant $\alpha_s$. The width itself is also an important quantity, directly related to the unknown Kobayashi-Maskawa matrix element $V_{tb}$. If less than unity, it signals the existence of a fourth generation. On the other hand, the top quark may have a larger width than expected due to exotic decay modes like $t \to bH^+$ (charged Higgs boson) or $bP^+$ (pseudo-Goldstone boson). Furthermore, we may be able to probe the physics beyond the Standard Model from the analysis of the radiative corrections, once we know the mass of the top quark precisely; for example, the radiative corrections from the stop-sbottom sector in the Minimal Supersymmetric Standard Model may be extracted [13].

Another missing constituent of the Standard Model is the Higgs boson. Though this particle plays a key role in the Standard Model to give masses to both the gauge bosons and the

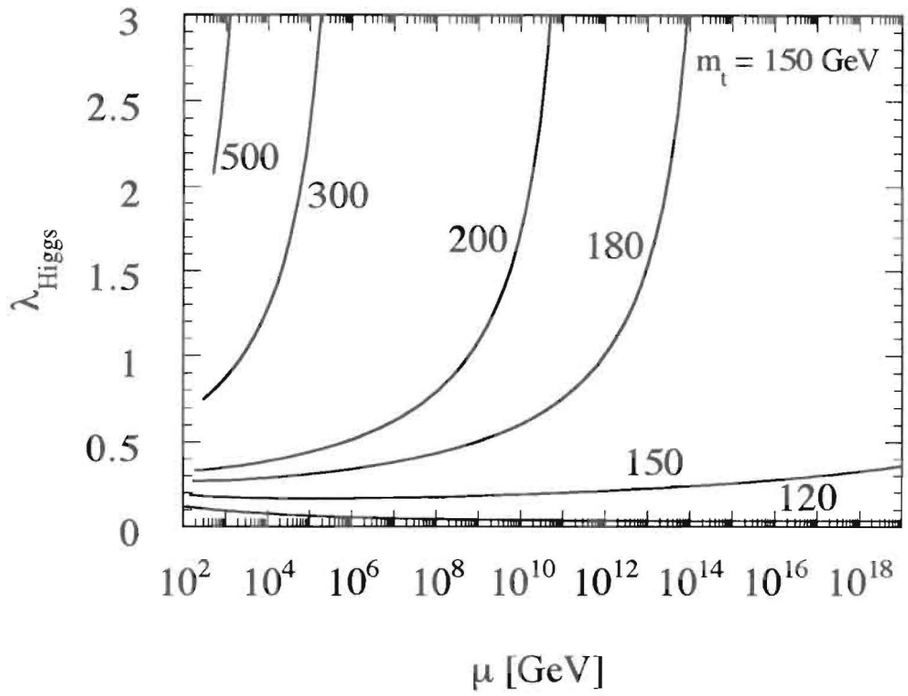


Figure 2.2: The renormalization group flow of the Higgs boson self-coupling constant $\lambda_{\rm Higgs}$ in the minimal Standard Model. The quoted values are the Higgs boson masses. The top quark mass is assumed to be $m_t = 150$ GeV.

quarks/leptons, little is known about its mass. Recall that the mass of the Higgs boson is related to its four-point self-coupling, which becomes stronger at higher energies. The running of the self-coupling constant is illustrated in Fig. 2.2. If the Higgs boson is relatively heavy, then the self-coupling blows up just above TeV scale. This singular behavior signals the breakdown of the Standard Model above that scale. On the contrary, the Higgs boson lighter than 180 GeV has a self-coupling which remains perturbative up to the Planck scale. Then the standard $SU(3)_C \times SU(2)_L \times U(1)_Y$ gauge theory may be valid up to a very high energy scale. Such a light Higgs boson lies well within the reach of JLC-I.

If the Higgs boson is lighter than $\sim 150$ GeV, we should be able to test the mechanism of the fermion mass generation. The top quark threshold region is sensitive to the Yukawa potential due to the Higgs boson exchange (Sect. 2.6). The study of the Higgs boson branching ratios can tell us if the Yukawa coupling constants are proportional to the fermion masses (Sect. 2.2). Such tests can be performed only at $e^+e^-$ colliders with a clean environment. In this way, JLC-I is able to thoroughly establish the Standard Model.

### 2.1.2 Problems in the Standard Model

Once the detailed studies of the top quark to be performed at JLC-I establish the $SU(3)_C \times SU(2)_L \times U(1)_Y$ gauge structure, we may start seriously asking many unresolved questions within the Standard Model. Why do the electric charges of electron and proton exactly balance? Why are the strengths of the gauge interactions so different? Why is the number of generations three? Why do the seemingly independent anomalies from the quark sector and lepton sector

cancel? Where do the fermion masses come from? Why is the CP invariance broken? And many others. Among them, the most important question is: Why is the electroweak symmetry broken, and why at the scale $\langle H \rangle = 246$ GeV?

The Standard Model cannot answer these questions. A general belief is that there lies a more fundamental physics at a higher energy scale which leads to the unanswered characteristics of the Standard Model. Then all the parameters and quantum numbers in the Standard Model can be *derived* from the more fundamental description of nature, leading to the Standard Model as an effective low-energy theory. In particular, the weak scale itself $\langle H \rangle = 246$ GeV should be a *prediction* of the deeper theory. The scale of the fundamental physics can be regarded as a cutoff to the Standard Model. Above this cutoff scale, the Standard Model ceases to be valid and the new physics takes over.

In the Standard Model, an elementary Higgs field is introduced to break the $SU(2)_L \times U(1)_Y$ symmetry. The mass term of the Higgs field is of the order of the weak scale. The natural scale one expects for the mass term is, however, the cutoff scale of the theory, since the quantum correction to the mass term is proportional to the cutoff scale squared because of the quadratic divergence. This problem, so-called the naturalness problem, is one of the main obstacles we encounter, when we wish to construct realistic models of the "fundamental physics" beyond the Standard Model. If the cutoff scale of the standard model is near the Planck scale, one needs to fine-tune the bare mass term of the Higgs potential to many orders of magnitude to keep the weak scale very tiny compared to the Planck scale. There are only two known possibilities to solve this problem. One is to assume that the cutoff scale of the Standard Model lies just above the weak scale, regarding the Higgs boson as a composite object. The technicolor scenario discussed in the next section belongs to this class. The other is the introduction of a new symmetry to eliminate the quadratic divergence: supersymmetry.

### 2.1.3 Technicolor Scenario

Technicolor scenario belongs to the first class discussed above, solving the naturalness problem by setting the cutoff just above the TeV scale. The elementary Higgs field is replaced by the Nambu-Goldstone bosons associated with a dynamical chiral symmetry breaking in the techni-fermion sector [14].

We can approach this scenario by precision experiments. Though these models preserve gauge invariance, there may be higher-dimensional operators induced by the strong dynamics at the TeV scale. Then, these operators appear as anomalous couplings among the gauge bosons, which can be measured with a precision better than 2–3% already at JLC-I, using the processes $e^+e^- \to W^+W^-$, $e^\pm \overset{(-)}{\nu_e} W^\mp$, and $\nu_e\bar{\nu}_e Z$ (Sect. 2.7). The high-luminosity $Z$-factory is also a good option for the precision measurements (Sect. 2.8), with high sensitivity to the symmetry breaking sector [15].

Although the idea of the dynamical symmetry breaking works beautifully in the gauge sector, it is not easy to generate fermion masses without conflicting the experimental constraints on flavor changing neutral currents. Walking technicolor [16] was proposed as a candidate mechanism to suppress the flavor-changing neutral currents while giving relatively large masses to the fermions. Then, the pseudo-Nambu-Goldstone bosons (techni-pions) are expected to appear below $O(100)$ GeV. Their properties are similar to those of the charged Higgs bosons in the multi-doublet models, whose detection is easy at JLC-I (Sect. 2.6).

Nevertheless, the large mass of the top quark [17] is very difficult to incorporate into this scenario. It is generally accepted that there is yet no well-defined model along this idea, and it is

extremely difficult to judge pros and cons experimentally in the absence of concrete prediction. On the contrary, the other scenario to solve the naturalness problem, supersymmetry, provides some definite predictions which can be clearly tested at JLC-I.

### 2.1.4 Supersymmetry

Supersymmetry (SUSY) [18] is a symmetry between bosons and fermions, and is the only known symmetry which eliminates the quadratic divergence of scalar mass parameters. Since the principal origin of the naturalness problem in the Standard Model is the quadratic divergence of the Higgs mass parameter, its absence in the supersymmetric models allows us to push the cutoff up to the Planck scale [19]. This possibility, that the cutoff scale may be very high, provides us an exciting scenario, that all the weak scale parameters are determined directly from those near the Planck scale, where the supersymmetry is naturally understood in the context of supergravity. Stated conversely, we can probe the physics near the Planck scale from the experiments at the weak scale. Wiping out the "TeV clouds," we may be able to see the physics near the Planck scale [20]. The large hierarchy between the Planck scale and the weak scale is stabilized thanks to the supersymmetry.

The idea that the weak scale parameters are directly determined from a very high energy scale naturally leads to the more interesting concept of the grand unified theory (GUT). GUT assumes that all the three gauge couplings in the standard model are derived from a single gauge coupling constant at a very high energy [21]. The most important prediction of the GUT is that of the Weinberg angle. Historically, the renormalization group analysis [22] showed that the Weinberg angle should be close to 0.2 in the simplest GUT model, in rough agreement with the measured value. Note that the qualitative success of this concept is that the strong coupling is always the strongest, the weak coupling the next, and the electromagnetic one the weakest, due to the simple inequality $3 > 2 > 1$. The successful prediction of the Weinberg angle $\sin^2\theta_W \sim 0.2$ is a concrete manifestation of this qualitative success. Furthermore, the baroque structure of the fermion quantum numbers in the Standard Model was naturally embedded into the $SU(5)$ gauge group, leading to the exact quantization of the electric charge and the precise cancellation of the anomalies. It was also pointed out that the simple GUT models predict equal bottom quark and tau lepton masses at the GUT scale, leading to the correct mass ratio after renormalization down to the GeV scale [23].

Since there are many GUT models, with or without supersymmetry, based on various gauge groups, it is important to be able to distinguish among them by comparing their predictions on the Weinberg angle with its experimental value. The Weinberg angle measured precisely at LEP experiments [11] agrees remarkably well with the prediction of the simplest supersymmetric GUT model [24]. The history of the measurement of $\sin^2\theta_W$ is illustrated in Fig. 2.3. Also shown is the unification of the coupling constants in supersymmetric GUT in Fig. 2.4. Here the supersymmetry successfully combined with the the concept of GUT, in a consistent manner with the assumption of a large cutoff scale.

It is worth mentioning that a heavy top quark has been suggested within the supersymmetric models, before the PEP/PETRA/TRISTAN experiments set a surprisingly high lower bound on its mass. The so-called radiative breaking scenario assumes that the electroweak symmetry breaking is triggered by the top quark Yukawa coupling, whose quantum effect drives the Higgs boson mass squared to negative at lower energies. Indeed, the preferred top quark mass is between 100 and 200 GeV within the scenario [27]. This range is just the one predicted from the precision measurements of the Standard Model.

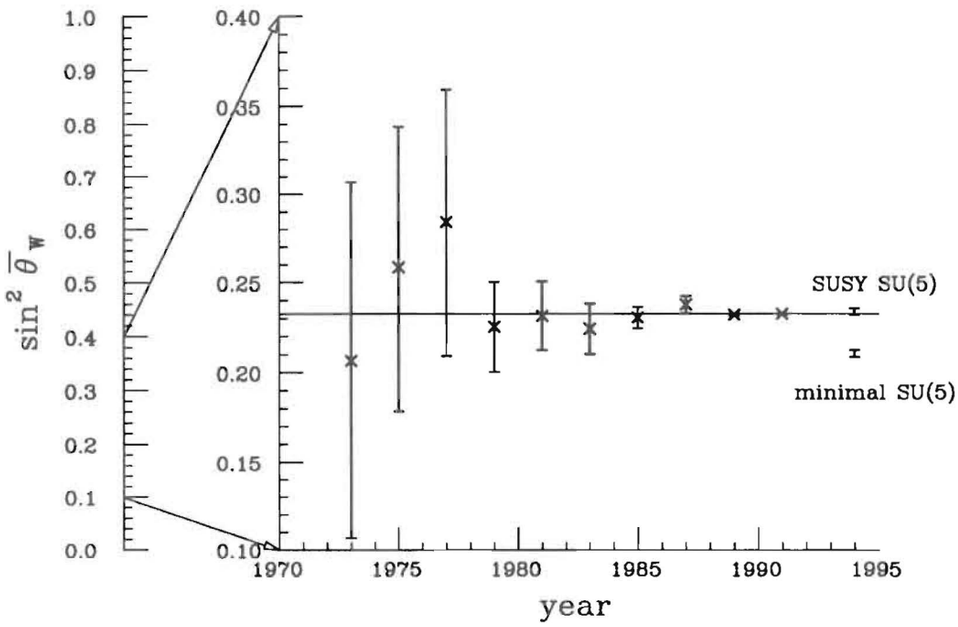


Figure 2.3: The history of the measurements of the Weinberg angle. Also shown are the predictions of the minimal (non-SUSY) $SU(5)$-GUT and minimal SUSY $SU(5)$-GUT.

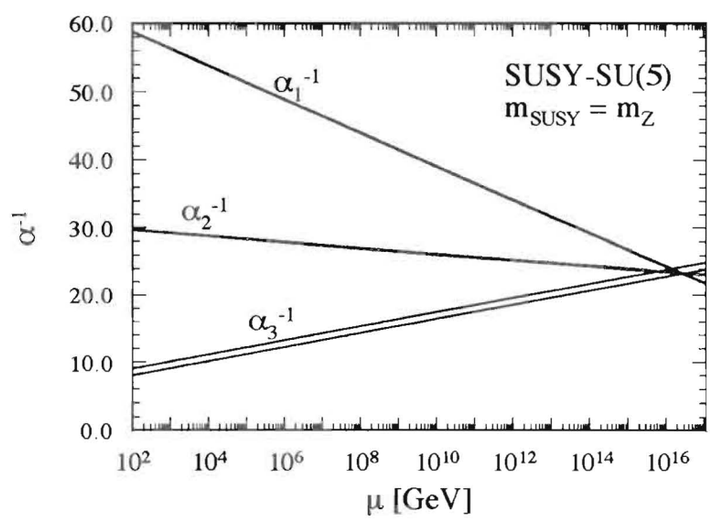


Figure 2.4: The renormalization group flow of the gauge coupling constants in the minimal SUSY Standard Model. The SUSY-breaking scale is set at $m_Z$.

### 2.1.5 Light Higgs: Messenger from the Grand Desert

An immediate consequence of SUSY is the existence of a light Higgs boson. It has been known that the lightest Higgs should be lighter than $m_Z$ at the tree-level [28], and it was regarded as one of the main targets at LEP-II. Recently, it was shown that the upper bound on the lightest Higgs boson is raised by the radiative correction due to the top quark Yukawa coupling [25], and the parameter space cannot be exhausted at LEP-II. However, one still has a stringent upper bound on the lightest Higgs boson mass, which is 170 GeV within the minimal SUSY Standard Model. Even the addition of singlets and extra families can push the upper bound only up to 200 GeV [26]. Thus JLC-I is an ideal place to discover SUSY Higgs or otherwise to exclude SUSY completely. On the other hand, it is hard to detect such a light Higgs boson at hadron supercolliders, leaving possibilities to miss it even if supersymmetry does exist.

Once a light Higgs boson is discovered, then we will be able to perform a detailed study on its properties, such as its mass, production cross sections, and decay branching ratios (Sect. 2.2). Such a detailed study is only possible at an $e^+e^-$ collider. Then we may be able to distinguish between the minimal Higgs boson in the Standard Model and non-minimal Higgs bosons like those in its supersymmetric extension. It is also possible that the other components of the Higgs multiplets will be discovered as well. Then careful studies may show whether their properties are those of the general two-doublet models, or those of the supersymmetric model which is more restrictive.

The existence of such a light Higgs is required even without supersymmetry, as long as there exists a "Grand Desert" between the weak scale and a high-energy scale like the Planck-scale, the GUT-scale, or an intermediate scale ( $\gtrsim 10^{10}$ GeV) [29]. Since the Higgs self-coupling constant should remain perturbative up to the new physics scale, its mass should be smaller than $\lesssim 200$ GeV in any models (See Fig. 2.2).

Thus, an $e^+e^-$ collider with $\sqrt{s} \lesssim 300$ GeV allows us to perform a definitive test on the "Grand Desert" hypothesis. If a light Higgs boson is discovered at JLC-I, it strongly supports the idea of grand unification. If *not*, there *must* be a low-lying new physics scale, and all the conventional GUT models will have to be abandoned.

### 2.1.6 Roads to the Planck Scale

If a light Higgs boson is indeed found, then we should go to the next step, to search for superparticles directly. For SUSY being relevant to solve the naturalness problem, the masses of superparticles should be lighter than $O(1)$ TeV. Among them, the color-singlet superparticles like sleptons, charginos, and neutralinos are expected to be lighter than the colored superparticles. We have a good chance to discover one of the color-singlet superparticles in the energy range $\sqrt{s} = 300$ to 500 GeV. On the other hand, colored superparticles like gluino and squarks, main targets at hadron supercolliders, are in general relatively heavy and require much higher energies to discover. The discovery potential of proposed hadron supercolliders is comparable with that of JLC-I.

Since the supersymmetry allows us to push the cutoff scale up to the Planck scale, the study of its low-energy consequences will enable us to probe the physics at the Planck scale. It is generally believed that the origin of the SUSY breaking should be attributed to the supergravity interactions. In other words, the superparticle masses are the reminiscent of the dynamics at the Planck scale. To measure the SUSY breaking parameters at the weak-scale is the most important task to explore physics at the Planck scale. Then we may obtain clues to the truly unified theory including gravity, like superstring theory. For example, the discovery of the

sleptons alone will give us a good opportunity to measure the SUSY-breaking parameters at the Planck scale. We can predict the masses of squarks and gluinos from the study of the sleptons, within the minimal supergravity model. The large beam polarization at JLC-I will allow clear separation of left-handed and right-handed sleptons and the study of energy distributions of the decay products will provide the mass of the lightest supersymmetric particle. The study of interference between $s$-channel and $t$-channel amplitudes will resolve the neutralino mass spectrum. If lucky, we can measure all but one parameters within the minimal supergravity model. This amusing possibility is discussed in detail in Sect. 2.4.

The clean environment, high luminosity, and the large beam polarization at JLC-I may lead us to make an entirely new step towards the deeper understanding of nature.

## 2.2 The Light Higgs($h^0$)

### 2.2.1 Introduction

One of the most important physics targets of JLC-I is the Higgs particle. Since the mass of the Higgs particle is a parameter of the Standard Model, its prediction is only possible when we go beyond the Standard Model. As described in the previous section, the low mass Higgs particle ( $\lesssim$ 200 GeV) is a general conclusion of models based on the GUT and Grand Desert scenario, while composite Higgs models such as technicolor models allow a high mass Higgs particle. In the case of the former scenario, many SUSY particles may exist below 1 TeV according to the natualness argument. While in the latter case, the exploration of multi-TeV energy region will be required to fully understand the underlying dynamics. Therefore, the search for the low mass Higgs particle will be the branch point to decide the future direction of collider physics.

The current lower limit on the mass of the Standard Model Higgs particle is 58 GeV at the 95 % confidence level [31]. The LEP II will cover the mass region up to 80 $\sim$ 90 GeV [32]. Future hadron colliders (LHC and SSC) will be sensitive to the Standard Model Higgs particle of a mass from 80 GeV to about 1 TeV[66]. At hadron colliders, the search for the Standard Model Higgs particles with a mass larger than $2 \times m_Z$ is relatively easy by using the $H^0 \to Z^0 Z^0 \to 4l$ mode. However, the search for an intermediate mass Higgs ($m_Z < m_H < 2 \times m_Z$) is not easy at hadron colliders. Especially if $m_H \lesssim 130$ GeV, one can use only one decay mode $H_{SM} \to \gamma\gamma$, with a small branching ratio of about $10^{-3}$, therefore one needs high luminosity and ultimate detector performance. The situation becomes much worse in the case of the SUSY Higgs, as the branching ratio for $h^0 \to \gamma\gamma$ is suppressed to be $\sim 10^{-4}$ or much smaller in a large domain of the parameter space, due to the increase of the dominant decay width $\Gamma(h^0 \to b\bar{b})$. It was reported that hadron colliders can not discover any of the MSSM Higgs particles, if model parameters are in some unlucky region[33].

As described in the previous section, the recent precision measurements strongly favours the scenario with GUT, Grand Desert and low energy SUSY particles, while non-GUT scenarios, such as Technicolor Model now facing a tough experimental challenge. Therefore the search for low mass Higgs particles becomes more important than ever. As will be discussed in the following subsections, at $e^+e^-$ colliders, the Higgs particle can be searched for, using the main decay mode. Therefore, the search at JLC-I will never miss the Higgs in the intermediate mass region. In this sense, the search at JLC-I is complementary to that at Hadron colliders.

In the minimal supersymmetric standard model (MSSM), the Higgs sector consists of two doublets, resulting in five physical Higgs particles: two CP-even scalars, i.e. a light one ($h^0$) and a heavy one ($H^0$), one CP-odd scalar ($A^0$), and a pair of charged Higgs ($H^\pm$). There are

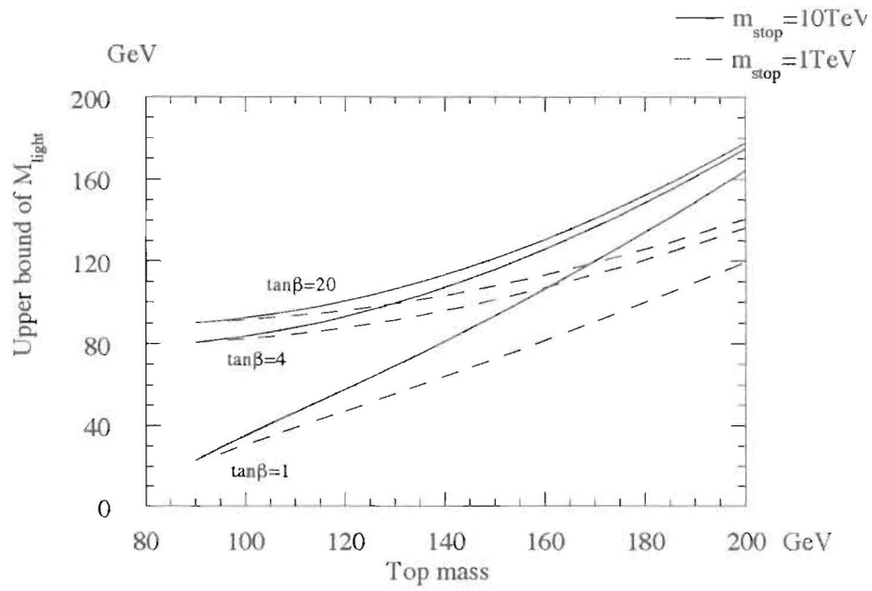


Figure 2.5: The Higgs mass as a function of the top quark mass for various $\tan\beta$ values and two extreme SUSY scale cases. Solid line correspond to $m_{\tilde{t}} = 10$ TeV and trilinear soft breaking parameter (A term) equal to $\sqrt{6}$, dashed line $m_{\tilde{t}} = 1$ TeV and A=0. These masses are calculated with a formula improved by renormalization group equations[67].

relations among the masses of these particles. $m_{h^0}$, $m_{H^0}$, and $m_{H^\pm}$ can be given in terms of $m_{A^0}$ and $\tan\beta$, where $\tan\beta$ is the ratio of the two vacuum expectation values of two Higgs doublets. Especially, the lightest Higgs boson mass is less than the mass of $Z^0$ at the tree level. But, when the radiative correction is taken into account, the upper bound can exceed $m_{Z^0}$ due to the top and stop loops. The correction to the upper bound of the lightest Higgs mass squared is proportional to $m_t^4 \ln \frac{m_{\tilde{t}}}{m_t}$, where $m_{\tilde{t}}$ is the scalar top mass. The upper bound on $m_{h^0}$ for various $\tan\beta$ values and two extreme SUSY scales is shown in Fig. 2.5 as a function of the top quark mass. Experimentally, the top quark mass is bounded between 89 GeV and 200 GeV[30, 11]. If the low energy supersymmetry is the solution to the naturalness problem, the SUSY scale should not exceed O(10) TeV. Taking these bounds into account, $m_h$ should be less than 180 GeV.

Even if one extends the MSSM by introducing a gauge singlet Higgs or adding extra matter super multiplets, one can still obtain a tight upper bound on the lightest Higgs boson mass as long as one assumes GUT. In these models, the lightest Higgs boson mass does not exceed 200 GeV, if the SUSY breaking scale is 1 TeV.

The tree level total cross sections of the processes $e^+e^- \to H^0_{SM}Z^0$ (for various $m_H$ values), $e^+e^- \to Z^0Z^0$, and $e^+e^- \to W^+W^-$ are shown in Fig. 2.6, as functions of the center of mass energy. At $\sqrt{s} = 300$ GeV, the total cross section of $e^+e^- \to H^0_{SM}Z^0$ with $|\cos\theta_H| < 0.7$ is ~30fb. Therefore, an integrated luminosity of 5 fb$^{-1}$ will be sufficient for the discovery of the Standard Model Higgs particle with a mass up to 200 GeV.

In the case of the SUSY Higgs (MSSM), the cross sections are related to that of the Standard Model Higgs particle as follows:

$$\sigma(e^+e^- \to h^0Z^0) = \sin^2(\beta - \alpha)\sigma(e^+e^- \to H_{SM}Z^0)$$

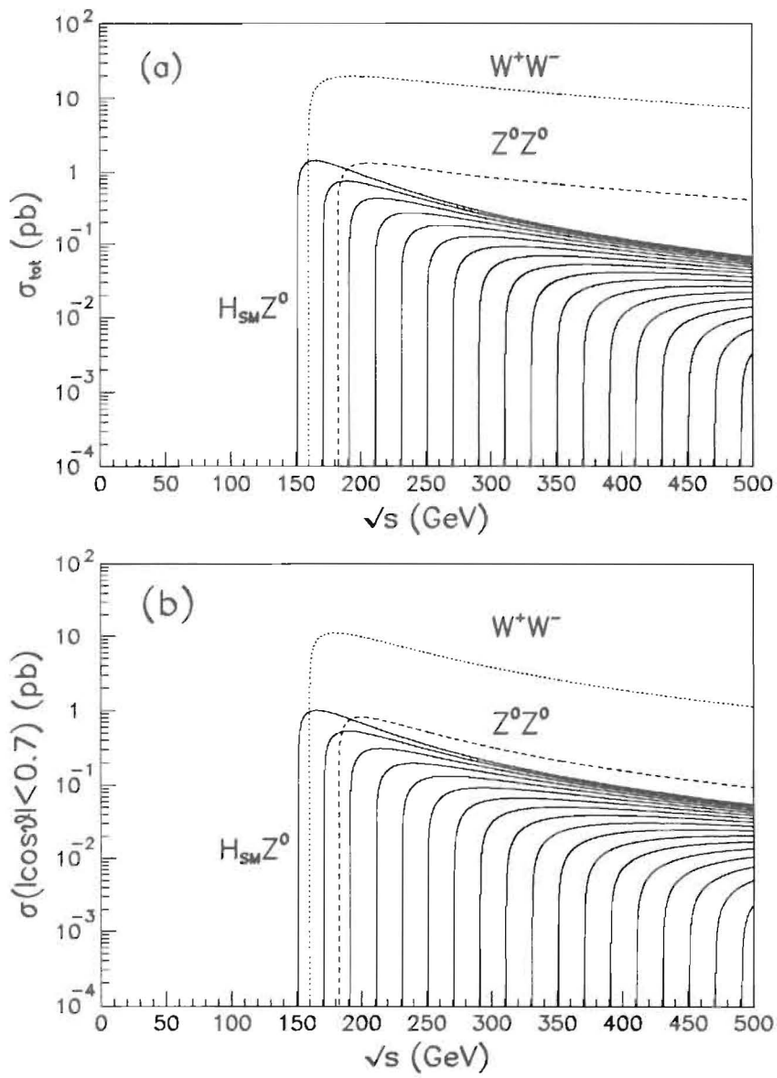


Figure 2.6: (a) The total cross sections for the reactions $e^+e^- \to W^+W^-$ (dotted curve), $e^+e^- \to Z^0Z^0$ (dashed curve) and $e^+e^- \to H^0_{SM}Z^0$ (solid curves:$m_{H_{SM}}$ from 60 GeV to 400 GeV in 20 GeV steps) as functions of the center of mass energy. (b) A similar figure with an angular cut: $|\cos\theta| < 0.7$.

$$\sigma(e^+e^- \to H^0Z^0) = \cos^2(\beta - \alpha)\sigma(e^+e^- \to H_{SM}Z^0)$$

where $\alpha$ is the mixing angle of the CP-even Higgs particles. The value $\sin^2(\beta - \alpha)$ is a function of $(\tan\beta, m_A)$ in the MSSM, and is close to 1 if $m_A$ is large ($m_A \gtrsim 150$ GeV) while it is close to 0 if $m_A$ is small. When $m_A$ is large, the masses of $H^0$ and $H^\pm$ are close to $m_A$ and the mass of $h^0$ is close to the maximum depending on $m_t$, $m_{\tilde{t}}$, and $\tan\beta$. When $m_A$ is small ($m_A \lesssim 150$ GeV), the masses of $H^0$ and $H^\pm$ are also small, therefore, all Higgs particles are kinematically accessible at JLC-I.

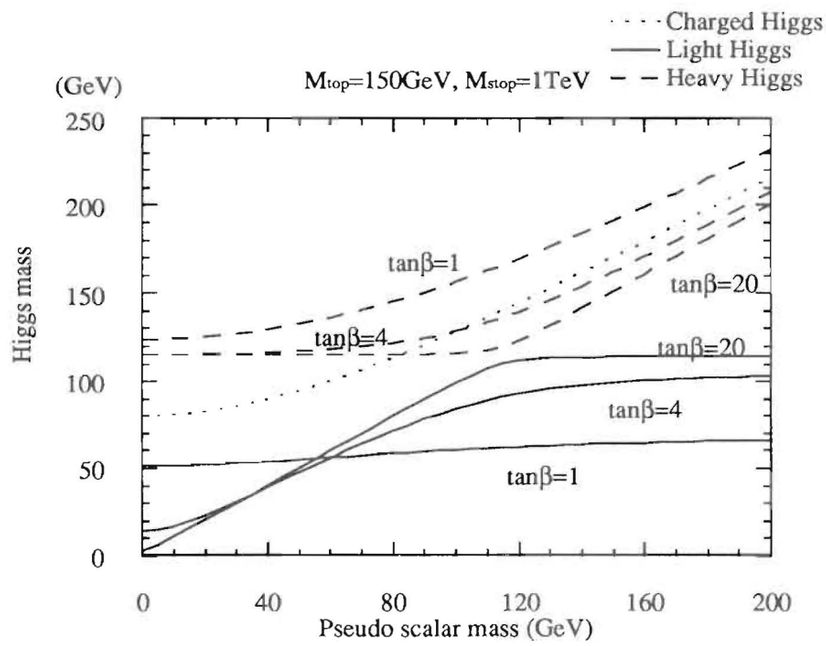


Figure 2.7: The mass of $h^0$, $H^0$, and $H^\pm$ in MSSM as a function of the mass of $A^0$ for various $\tan\beta$ values.

Thus the MSSM Higgs phenomenology at JLC-I can be summarized as either the production of only the light Higgs particle with a cross section similar to that of the Standard Model Higgs particle or the simultaneous productions of $h^0$, $H^0$, $A^0$, and $H^\pm$. In any case, the sum of the cross section $e^+e^- \to h^0Z^0$ and $e^+e^- \to H^0Z^0$ is more than 60fb at $\sqrt{s} = 300$ GeV, even if the top quark mass and the SUSY scale are close to their maximum values. This feature guarantees the discovery of at least one Higgs particle at JLC-I if nature is really SUSY-GUT.

In the following subsections, we will describe the search strategy for the Standard Model Higgs particle and a possible strategy for the study of the Higgs particle after the discovery. The analysis will also applicable to the search of $h^0$ in the MSSM when $m_A$ is large. The searches for $A^0$, $H^0$, and $H^\pm$ will be described in the next section.

### 2.2.2 Discovery Strategy of Higgs Boson

At JLC-I, the detection of the Standard Model Higgs particle in the intermediate mass region is easy[37, 36], using the process $e^+e^- \to H^0_{SM}Z$. Depending on the decay modes of $Z^0$, event topologies of the process $e^+e^- \to H^0_{SM}Z^0$ are classified into (1) $\nu\bar{\nu}b\bar{b}$, (2) $l\bar{l}b\bar{b}$, and (3) $q\bar{q}b\bar{b}$. A

typical event of each topology is shown in Fig. 2.8. The Higgs will be observed as a peak in the invariant mass distribution of two-jet system, requiring the rest of the system (two jets, two leptons, or nothing, depending on the topologies) to be consistent with $Z^0$.

The main background comes from the processes $e^+e^- \to Z^0Z^0$ and $e^+e^- \to W^+W^-$, whose differential cross sections peak in the forward direction. Therefore, the key points in the Higgs reconstruction are (1) to select events produced in the central region (for example, require reconstructed Higgs and $Z$ directions to satisfy an angular cut such as $|\cos\theta| < 0.7$), (2) to tag the $b$-jets efficiently, and (3) to achieve a high resolution for the invariant mass of the Higgs. For the second point, we will use a CCD-type vertex detector as described in the following chapter. It will enable us to tag $b\bar{b}$ jets from the Higgs decays with an efficiency higher than 61 % ( double tag ). The third point is crucial for Higgs studies, especially when its mass is close to that of $W$ or $Z$. The required resolution can be realized by high resolution calorimetry and tracking systems, which can identify electrons and muons in jets and can link each track to its corresponding calorimeter cluster. A possible detector design will be described in the following chapter.

By the first $e^+e^-$ collision at JLC-I, the mass of the top quark will be fixed by the collider experiments at Fermi Laboratory if the mass is low enough for discovery, or the precision measurement at LEP-II will constrain the top quark mass with a good precision ($\Delta m_t = 5 \sim 10$ GeV). The initial beam energy of JLC-I will be set at $2 \times m_{top}$ so as to guarantee the physics output from the study of the top quark. This run will also serve as the "Discovery Run" of the Higgs particle, because the threshold of the Higgs particle production by the process $e^+e^- \to h^0Z^0$ is lower than $2 \times m_{top}$ as long as $m_{top} > 90$ GeV (see Fig. 2.5).

Let's assume that the top quark mass is 150 GeV. We start the "Discovery Run" at $\sqrt{s} =$ 300 GeV with a relatively wide beam energy spread of 2% full width. Under this condition, JLC-I will provide a luminosity of $3 \times 10^{33}\mathrm{cm}^{-2}\mathrm{s}^{-1}$ corresponding to an integrated luminosity of $\int Ldt = 30\mathrm{fb}^{-1}$ a year ($\sim$ 100 running days). Fig. 2.9 shows the reconstructed $m_h$ distributions at the stage of $\int Ldt$=4fb$^{-1}$, for the signal process: $e^+e^- \to H^0_{SM}Z^0$ with $m_{H^0_{SM}}$= 80, 100, 120, 140, 160, and 180 GeV, and the background process: $e^+e^- \to Z^0Z^0$. For the $Z^0 \to l^+l^-$ channel, we apply a kinematical fit to suppress the effect of the beam energy spread and initial state radiation. A clean peak, well separated from that of the $e^+e^- \to Z^0Z^0$ background, can be observed in the $\nu\bar{\nu}b\bar{b}$ and $q\bar{q}b\bar{b}$ modes already at 4fb$^{-1}$, if $m_{H^0_{SM}}$ is less than 160 GeV. If $m_{H^0_{SM}}$ is greater than 160 GeV, the other decay mode such as $H^0_{SM} \to W^+W^-$ will be useful for the Higgs discovery at the stages of low integrated luminosity. When we accumulate 30 fb$^{-1}$, a clean Higgs signal well separated from the $Z^0$ peak can be observed in each of the three decay channels as seen in Fig. 2.10, if the difference between $m_{H^0_{SM}}$ and $m_Z$ is greater than $\sim$10 GeV. The measurements in the three decay channels are independent of one another. Even if $m_{H^0_{SM}}$ is close to $m_Z$ and the signal peaks are overlapped with the background $e^+e^- \to Z^0Z^0$ peaks, the total numbers of events in the overlapped peaks will hint the existence of $h^0$[38]. In addition, the difference between the decay angular distribution of $Z^0$ and $H^0_{SM}$ will help us project out the Higgs signal[39].

In the Discovery Run, the distribution of the recoil mass $m_H^{rec}$ in the decay channel $H^0_{SM} \to b\bar{b}$ and $Z^0 \to \ell^+\ell^-$ is strongly affected by the relatively large beam energy spread as shown in Fig. 2.11a. An idea to reduce this effect is to collide the higher energy positrons with the lower energy electrons and vice versa such that the center of mass energy is kept constant. With this technique we can control the center of mass energy to $\Delta\sqrt{s}/\sqrt{s} = 0.2\%$ full width, although the system may be boosted along the beam axis. Fig. 2.11b shows the $m_H^{rec}$ distribution fairly improved by this technique.

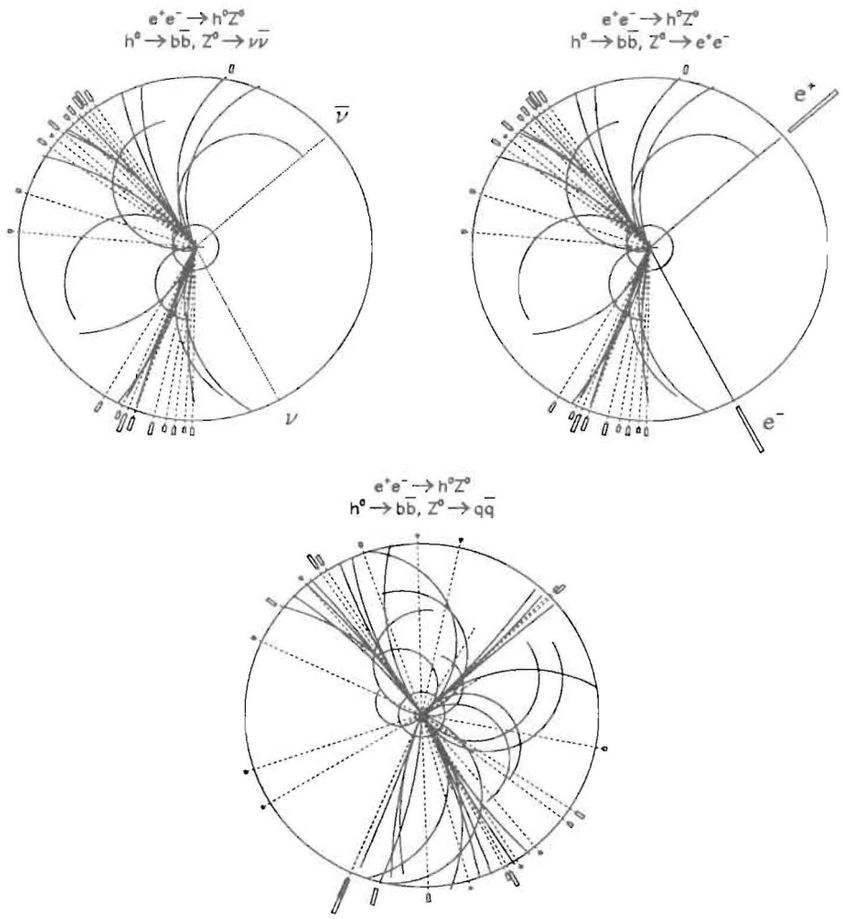


Figure 2.8: Typical $e^+e^- \to H^0_{SM}Z^0$ events with $m_{H_{SM}} = 120$ GeV at $\sqrt{s} = 300$ GeV: (a) $H^0_{SM} \to b\bar{b}$ and $Z^0 \to \nu\bar{\nu}$, (b) $H^0_{SM} \to b\bar{b}$ and $Z^0 \to e^+e^-$, (c) $H^0_{SM} \to b\bar{b}$ and $Z^0 \to q\bar{q}$. In pictures (a) to (c), the solid curves represent tracks of the charged particles in the central tracking chamber with a magnetic field of 2.0 Tesla and active radius of 0.3 to 2.3 m, while the dotted lines show photon emissions. The surrounding boxes are electromagnetic clusters, and the lengths of the boxes correspond to their energies.

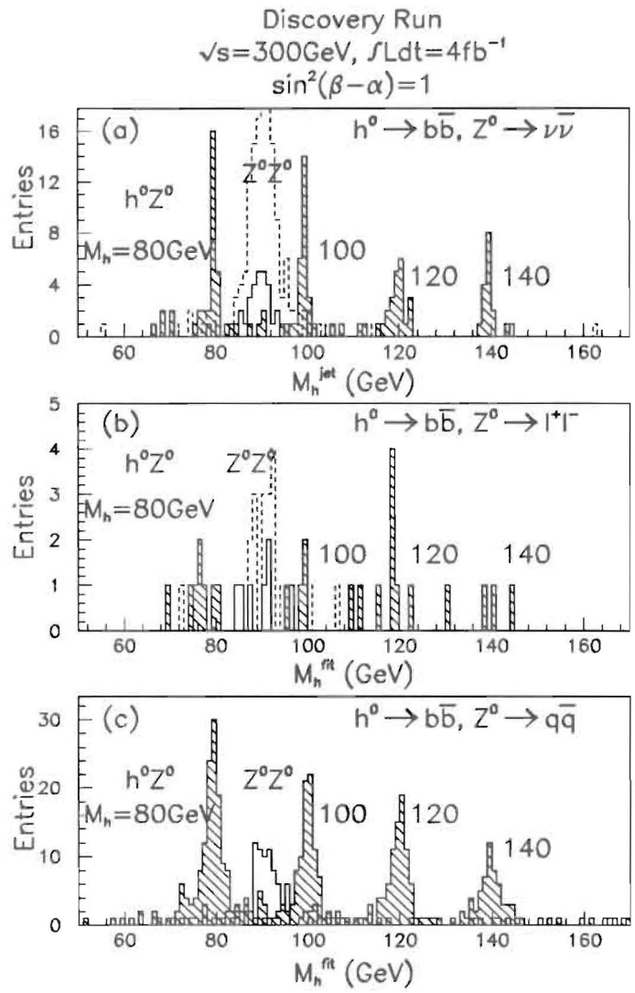


Figure 2.9: The reconstructed mass distributions for the three decay channels after the Discovery Run of $\int Ldt = 4\text{fb}^{-1}$. (a) The $m_h^{jet}$ distribution for the decay channel $H^0_{SM} \to b\bar{b}$ and $Z^0 \to \nu\bar{\nu}$. (b) The $m_h^{fit}$ distribution for the decay channel $H^0_{SM} \to b\bar{b}$ and $Z^0 \to \ell^+\ell^-$. (c) the $m_h^{fit}$ distribution of the decay channel $M^0_{SM} \to b\bar{b}$ and $Z^0 \to q\bar{q}$. In the figures, the hatched histograms are for the signal process $e^+e^- \to H^0_{SM}Z^0$ with $m_{H^0_{SM}}$=80, 100, 120, 140, 160, and 180 GeV. The blank histograms are for the background process $e^+e^- \to Z^0Z^0$. The dashed histograms in figures (a) and (b) are for the background process $e^+e^- \to Z^0Z^0$ without $b$-tagging.

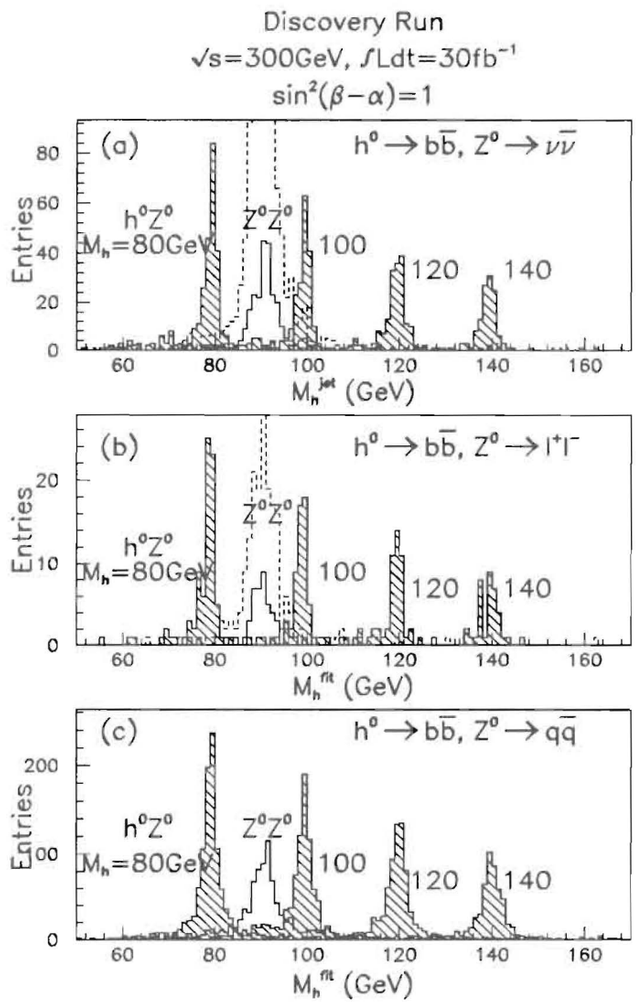


Figure 2.10: Same as Fig. 2.9, but with an integrated luminosity of $30\text{fb}^{-1}$

If the Discovery Run tells us that $m_{H^0}$ is close to $m_Z$, we move to the "Precision Mode" with a small beam energy spread of 0.4% full width and $\sqrt{s} = 200$ GeV. We assume that the luminosity is $1 \times 10^{33}\text{cm}^{-2}\text{s}^{-1}$ under this condition. We utilize here the recoil mass $m_h^{rec}$ in the decay channel of $h^0 \to b\bar{b}$ and $Z^0 \to \ell^+\ell^-$. Fig. 2.12 shows the recoil mass distribution for an integrated luminosity of 10 $\text{fb}^{-1}$ (~100 days). Because of the small beam energy spread (and the good momentum resolution), the mass resolution is much better than the total decay width of $Z^0$. We can thus find a clean signal peak even if it is right on the top of the background peak from $e^+e^- \to Z^0Z^0$.

### 2.2.3 Detailed Study of Higgs Properties

Once a Higgs particle is discovered, a detailed study should come next. We will set the beam energy at the maximum of the Higgs production cross section and JLC-I is turned into a Higgs factory. The question to be answered here is whether the Higgs sector is minimal or

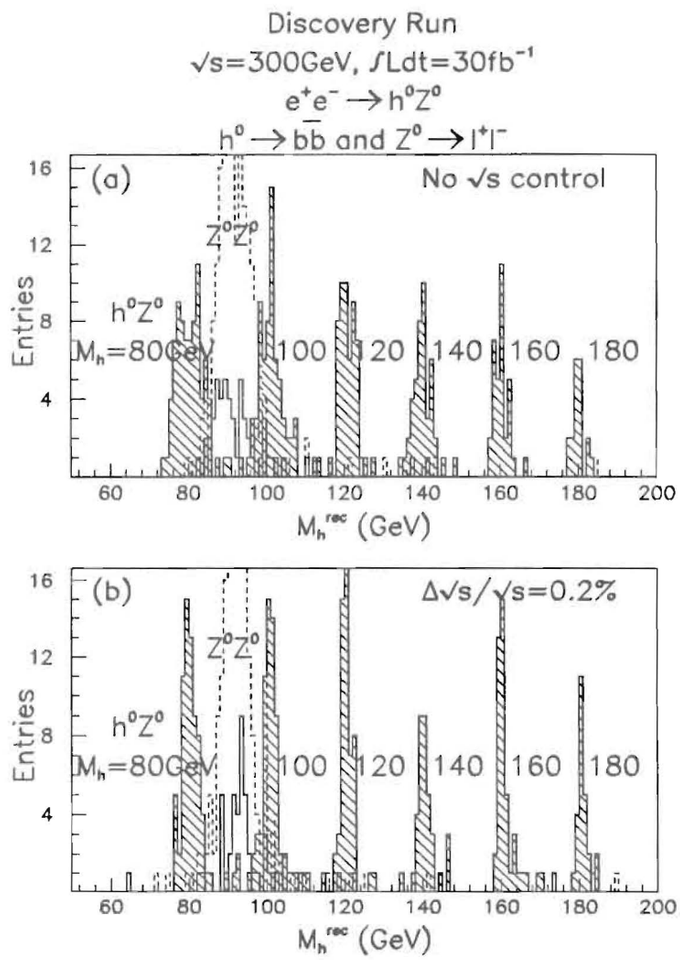


Figure 2.11: Comparison of the recoil mass distributions for the decay channel of $H^0_{SM} \to b\bar{b}$ and $Z^0 \to \ell^+\ell^-$, with the Discovery Run of $\int Ldt = 30\text{fb}^{-1}$: (a) without and (b) with the control of $\sqrt{s}$ (see text). The hatched histograms are for the signal process $e^+e^- \to H^0_{SM}Z^0$ with $m_{H_{SM}}$=80, 100, 120, and 140 GeV. The blank and dotted histograms are for the background process $e^+e^- \to Z^0Z^0$, with and without $b$-tagging, respectively.

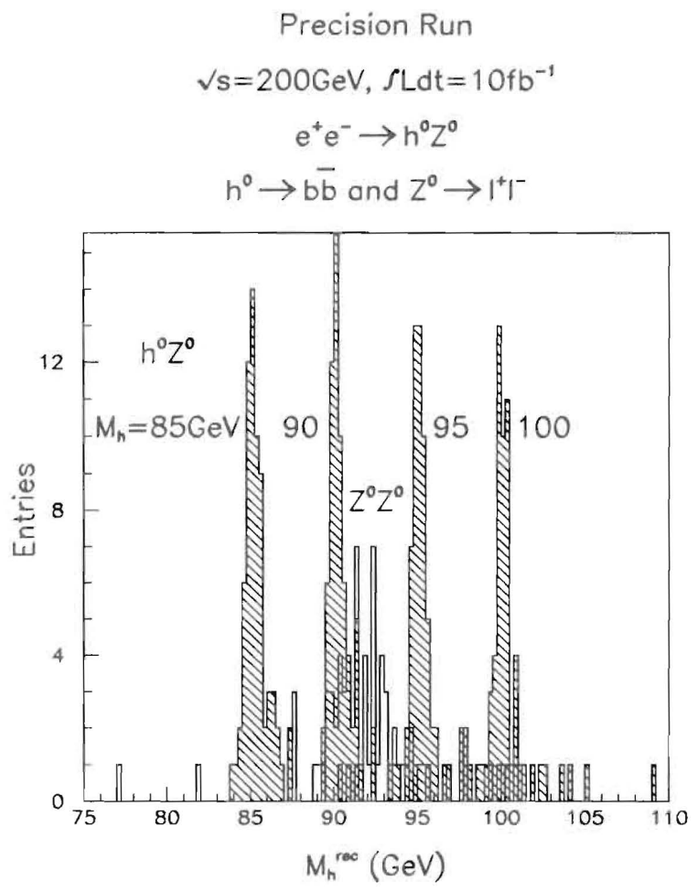


Figure 2.12: The recoil mass distributions of the decay channel of $H^0_{SM} \to b\bar{b}$ and $Z^0 \to \ell^+\ell^-$, with the Precision Run of $\int Ldt = 10\text{fb}^{-1}$. The hatched histograms are for the signal process $e^+e^- \to H^0_{SM}Z^0$ with $m_{H_{SM}}$=85, 90, 95, and 100 GeV. The blank histogram is for the background process $e^+e^- \to Z^0Z^0$, with $b$-tagging.

non-minimal. Precise measurements of the production cross section and the decay width will answer this question.

Fig. 2.13 shows the contours of the total width of the MSSM Higgs in the $m_A$ and $\tan\beta$ plane. When $m_A$ is small and $\tan\beta$ is large, the total width of the MSSM Higgs becomes very large due to the large coupling to $b\bar{b}$, compared to the total width of the standard model Higgs in this mass range which is about 5 MeV. Since we can measure the total width down to 200 MeV, we can establish the non-minimality of the Higgs boson, when $m_A$ is smaller than 120 GeV and $\tan\beta$ is greater than 8.

Another way to establish the non-minimality of the Higgs boson is to measure the total cross section of $e^+e^- \to h^0Z^0(\sigma_{Zh})$ multiplied by Br($h \to b\bar{b}$) and to compare it with the standard model prediction. The number of events observed in $\nu\bar{\nu}h$ and $q\bar{q}h$ mode with b-tagging is proportional to $\sigma_{Zh} \times Br(h \to b\bar{b})$. A detailed Monte Carlo simulation showed that, if $m_h$ = 110 GeV, we can accumulate 2000 $\nu\bar{\nu}h$ and $q\bar{q}h$ events total, when we accumulate about 80 fb$^{-1}$ of data. Therefore we can measure $\sigma_{Zh} \times Br(h \to b\bar{b})$ with an error of 2%

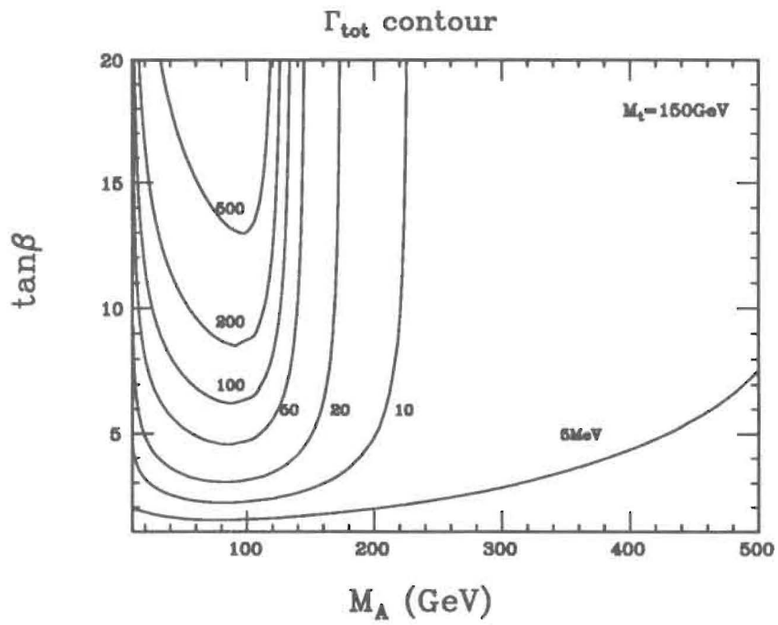


Figure 2.13: The contour of the total width of $h^0$. In this calculation, $m_t = 150$ GeV, $m_{SUSY} = 1$ TeV, therefore, $m_h < 120$ GeV. The total width of the Standard Model Higgs ($m_H$) for this mass region is a few MeV at maximum.

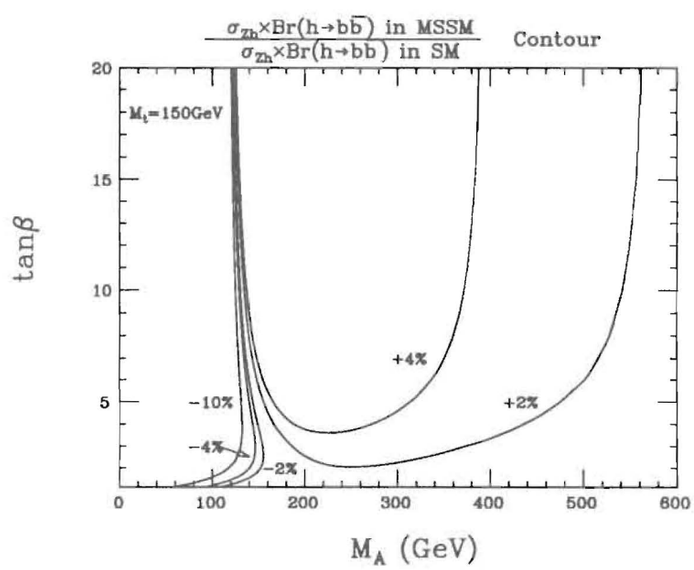


Figure 2.14: $\sigma \times Br(h^0 \to b\bar{b})$ in the MSSM compared with that of the Standard Model.

($1\sigma$). The difference of the $\sigma_{Zh} \times Br(h \to b\bar{b})$ in the MSSM from the standard model($\Delta\sigma_{Zh}$) is shown in Fig. 2.14 as contours in the $m_A$ and $\tan\beta$ plane. In the small $m_A$ region, $\Delta\sigma_{Zh}$ is negative because $\sigma_{Zh}$ is smaller than the standard model value due to the $\sin(\beta - \alpha)$ factor in the $ZZh$ vertex. Although $\sigma_{Zh}$ is quite close to the standard model value in the large $m_A$ region, $Br(h \to b\bar{b})$ is still significantly larger than the standard model value, thereby extending the sensitivity to the large $m_A$ region.

The decay branching ratios of $h^0$ also provide important information about the Higgs properties. The most interesting decay channel is $h^0 \to \gamma\gamma$. The branching ratio is $\sim 10^{-3}$ for the Standard Model Higgs, but can be $\sim 10^{-4}$ or much smaller for large $\tan\beta$ and relatively small $m_A$ in the MSSM. Since the signature of this mode is very clean, the measurement of this mode will provide an important constraint to the Higgs sector, when we accumulate enough statistics to study such a rare decay mode ( $\gtrsim$ 100 fb$^{-1}$ ). The Br($h \to c\bar{c}$) is equivalently important. It is several percent in the standard model, but can be much smaller in the MSSM. Though the identification of charm quarks in a large $b$-jet background is experimentally challenging, the non-observation of $c\bar{c}$ mode in the Higgs decay will confirm the non-minimality.

The above measurements will set strong constraints on the parameter space ($\tan\beta$,$m_A$) and will possibly distinguish the MSSM Higgs from the Standard Model Higgs. The estimation of $m_A$ will be invaluable in setting the energy range of JLC-II.

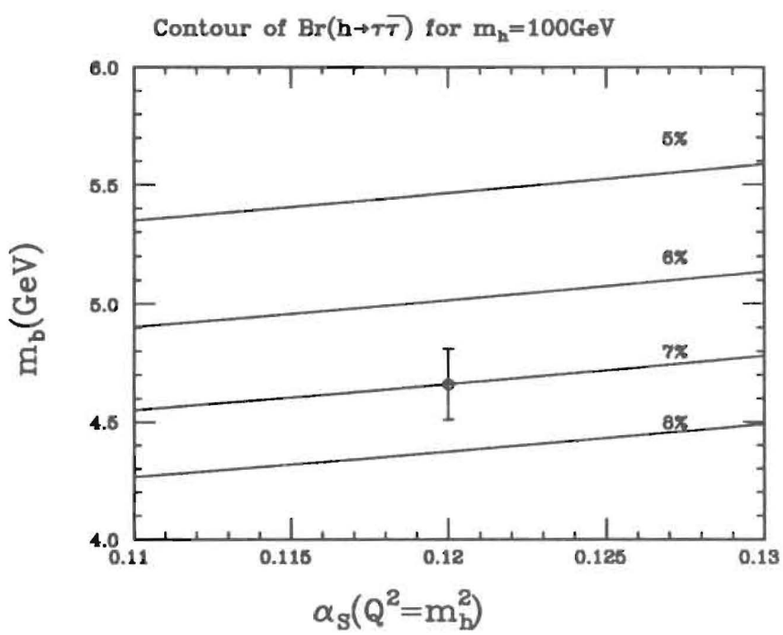


Figure 2.15: The contour of $Br(h^0 \to \tau\bar{\tau})$ in the $\alpha_s$ and $m_b$ plane. The parameters of the Higgs boson are adjusted to obtain $m_h$=100 GeV.

### 2.2.4 Br($h^0 \to \tau\bar{\tau}$) Measurement.

The Higgs studies also provide us with a possibility to probe higher-energy-scale physics through the mass ratio of the bottom quark to the tau lepton, which has been successfully predicted by the SUSY-GUT. At present, large theoretical error on $m_b$ from the $b\bar{b}$ potential prevents

us from making a precise test of GUT predictions. However, if the mass of the Higgs boson is in the region where the main decay mode is $b\bar{b}$, we can make a precise measurement of the $b$-quark mass by measuring the branching ratio for $h^0 \to \tau\bar{\tau}$. In any models which generate the $b$-quark and $\tau$ lepton masses from the same Higgs doublet, the ratio of the branching fraction for $h^0 \to b\bar{b}$ and $h^0 \to \tau\bar{\tau}$ is completely fixed up to the ambiguities in $m_b$ and $\alpha_s$. Fig. 2.15 shows contours of the branching ratio for $h^0 \to \tau\bar{\tau}$ in the plane of $\alpha_s$ and $m_b$. For 100 fb$^{-1}$ of data, we will have about 200 events of $e^+e^- \to Zh$ with $Z \to l\bar{l}$ or $q\bar{q}$ and $h \to \tau\bar{\tau}$, if we assume $\sigma \sim 360$ fb (the cross section at $\sqrt{s} = 220$ GeV for $m_h$=110 GeV) , $\eta \sim 0.1$, and $\mathrm{Br}(h^0 \to \tau\bar{\tau}) \sim 7\%$. Therefore we can measure $\mathrm{Br}(h^0 \to \tau\bar{\tau})$ with a precision of 0.5%, which corresponds to an error of about 150 MeV ($1\sigma$) in the $b$-quark mass, which is largely free from theoretical ambiguities from the $b\bar{b}$ potential and the evaluation of the renormalization group equation in the low $Q^2$ region.

## 2.3 $H^0$, $A^0$, and $H^\pm$

### 2.3.1 Search Strategy

The direct evidence of the non-minimality of the Higgs sector expected in the SUSY models is the detection of one or more extra-Higgs bosons : $H^0$, $A^0$, and $H^\pm$. Their masses are functions of $m_A$ and $\tan\beta$ as shown in Fig. 2.16. In the large $m_A$ region, $m_h$ approaches a constant value depending on $\tan\beta$, and the masses of $H^0$, $A^0$, and $H^\pm$ become degenerate. In the small $m_A$ region, the masses of $H^0$ and $H^\pm$ are close to their minimums (in the tree level calculation, $m_{H^0} \to m_Z$ and $m_{H^\pm} \to m_W$) with little dependence on $m_A$.

These particles are produced in the processes: (1) $e^+e^- \to H^0Z^0$, (2) $e^+e^- \to H^0A^0$, (3) $e^+e^- \to h^0A^0$, and (4) $e^+e^- \to H^+H^-$. The cross sections of processes (1) and (3) are proportional to $\cos^2(\alpha-\beta)$ and that of (2) is proportional to $\sin^2(\alpha-\beta)$, where $\cos^2(\alpha-\beta)$ is large in the small $m_A$ region while it is small in the large $m_A$ region. The total cross section of process (4) does not depend on $m_A$ nor $\tan\beta$ except for the phase space factor. Therefore, the non-minimal Higgs particles can be searched for using processes (1), (3), and (4) in the small $m_A$ region and (2) and (4) in the large $m_A$ region. The feasibility of searching for a charged Higgs with a relatively low mass ($m_{H^\pm} < 200$ GeV) is studied in ref.[40] and [41]. In the following subsections, studies of processes (1) and (2) are described.

### 2.3.2 $e^+e^- \to H^0Z^0$

The cross section of this process is large when $m_A$ is small. In this parameter region, the decay mode of $H^0$ is mainly $b\bar{b}$ unless $H^0 \to h^0h^0$ is kinematically allowed in the small $\tan\beta$ region [34]. Therefore the search method discussed for the $h^0$ detection in the previous section can be applied.

It should be noted that in some parameter region with an intermediate $\sin^2(\alpha-\beta)$ value, we have a chance to discover simultaneously $h^0$ and $H^0$ at $\sqrt{s} = 300$ GeV. Such an example is shown in Fig.2.17 for $m_h$=100 GeV, $m_H = 120$ GeV, and $\sin^2(\beta-\alpha) = 0.33$.

At $\sqrt{s} = 300$ GeV we can thus discover "either $h^0$ or $H^0$" or "both $h^0$ and $H^0$", depending on the SUSY parameters.

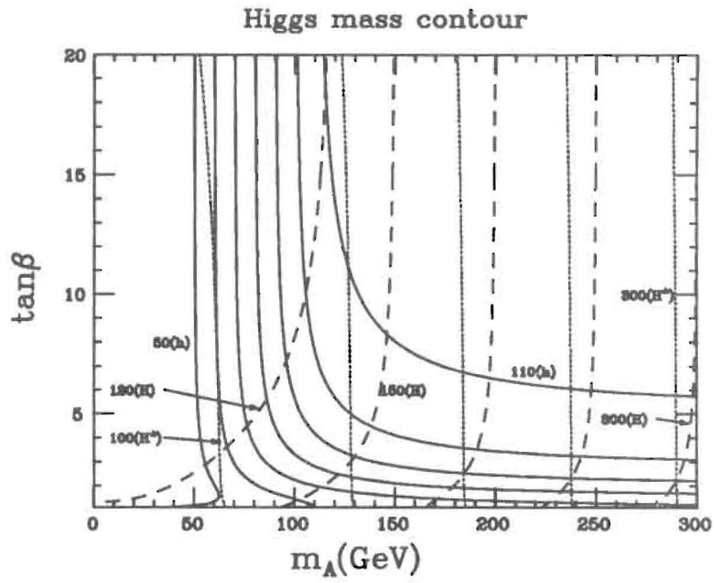


Figure 2.16: Higgs mass contours of $h^0$(solid), $H^0$(dashed), and $H^{\pm}$(dotted) in the $m_A$ and $\tan\beta$ plane. The masses are 50, 60, 70, 80, 90, 100, and 110 GeV for $h^0$, 120, 150, 200, 250, and 300 GeV for $H^0$, and 100, 150, 200, 250, and 300 GeV for $H^{\pm}$. The used parameters are $m_t = 150$ GeV, $m_{\tilde{q}} = 1$ TeV, and $A_t = A_b = \mu = 0$. For this parameter set, the maximum of $m_h$ is 114.4 GeV and the maximums of $m_H$ and $m_{H^{\pm}}$ are 144.5 and 83.7 GeV, respectively.

### 2.3.3 $e^+e^- \to H^0A^0$

In the large $m_A$ region, the usable search modes for the non-minimal Higgs particles are $e^+e^- \to H^0A^0$ and $e^+e^- \to H^+H^-$ and the search region is limited by the collider energy. The total cross sections of $e^+e^- \to H^0A^0$ and $e^+e^- \to H^+H^-$ are shown in Fig. 2.18, for $m_A = 100, 150$, and 200 GeV, where $m_H$, $m_{H^{\pm}}$, and $\sin^2(\beta-\alpha)$ are calculated assuming $\tan\beta = 10$, $m_t = 150$ GeV, and $m_{\tilde{t}} = 1$ TeV. The cross sections are typically O(10) fb in the energy range $\sqrt{s} = 300 \sim 500$ GeV.

Here we present the result of a simulation performed for the $H^0A^0$ process at $\sqrt{s} = 500$ GeV with $\int Ldt = 100$ fb$^{-1}$, assuming $m_t = 150$ GeV, $\tan\beta = 10$, and $m_A = 200$ GeV. These parameters lead to $m_H = 201$ GeV and the coupling $\sin^2(\beta-\alpha) \sim 1$.

The dominant decay modes of $H^0$ and $A^0$ for this parameter set are $b\bar{b}$. We used the values $Br(H^0, A^0 \to b\bar{b}) = 0.92$ and $Br(H^0, A^0 \to \tau^+\tau^-) = 0.08$ in the simulation. With these decay branching ratios, the process $e^+e^- \to H^0A^0$ leads to the following three types of final states: (1) $e^+e^- \to$ 4jets ($\sim 84.6$ %), (2) $e^+e^- \to \tau^+\tau^-$jet jet ($\sim 14.7$ %), and (3) $e^+e^- \to \tau^+\tau^-\tau^+\tau^-$ ($\sim 0.6$ %).

Here we concentrate on the first type. Although this is the dominant one, its signal must be extracted from the large background of $e^+e^- \to t\bar{t}$ due to the heavy top mass. The background from other processes is negligible. The second type, which is more distinctive against the background, may be used if the production rate is sufficient for discovery. A simulation study of the search for the second type of final state can be found elsewhere [42]. The third type is the cleanest, but the production rate is too small.

To select 4-jet events, cuts are first made on visible energy ($> 75$ % of $\sqrt{s}$), momentum

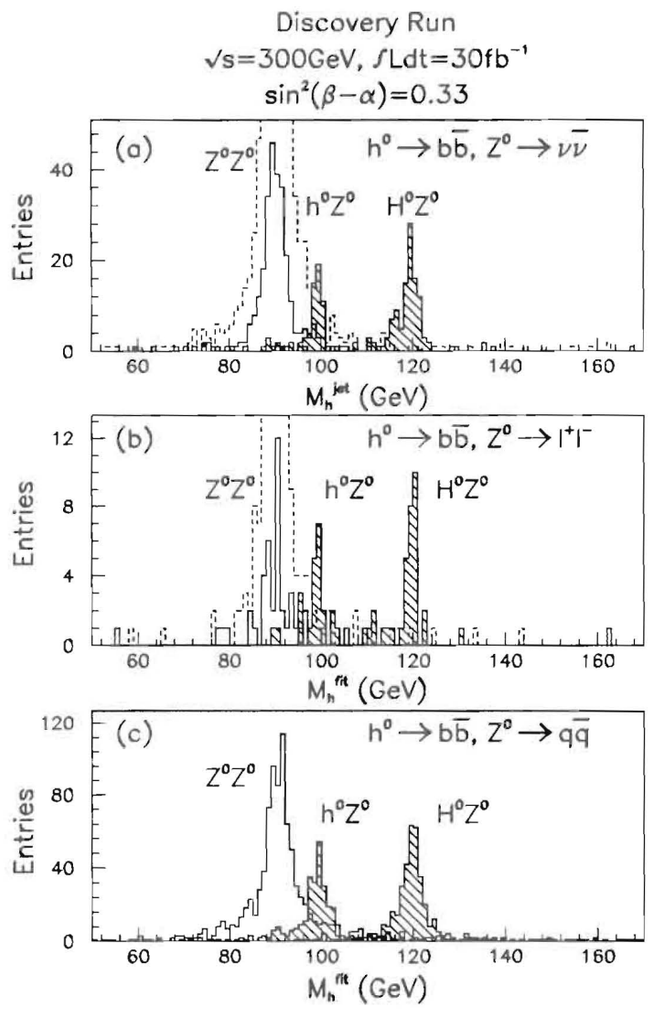


Figure 2.17: The reconstructed mass distributions for the three decay modes after the Discovery Run of $\int Ldt$=30 fb$^{-1}$. (a) The $m_h^{jet}$ distribution for $h^0/H^0 \to b\bar{b}$ and $Z^0 \to \nu\bar{\nu}$. (b) The $m_h^{fit}$ distribution for $h^0/H^0 \to b\bar{b}$ and $Z^0 \to \ell^+\ell^-$. (c) The $m_h^{fit}$ distribution for $h^0/H^0 \to b\bar{b}$ and $Z^0 \to q\bar{q}$. In the figures, the hatched histograms are for the signal processes $e^+e^- \to h^0Z^0$ and $e^+e^- \to H^0Z^0$ with $m_h = 100$ GeV, $m_H = 120$ GeV, and $\sin^2(\beta - \alpha) = 0.33$. The blank histograms are for the background process $e^+e^- \to Z^0Z^0$. The dashed histograms in figures (a) and (b) are for the background process $e^+e^- \to Z^0Z^0$ without $b$-tagging.

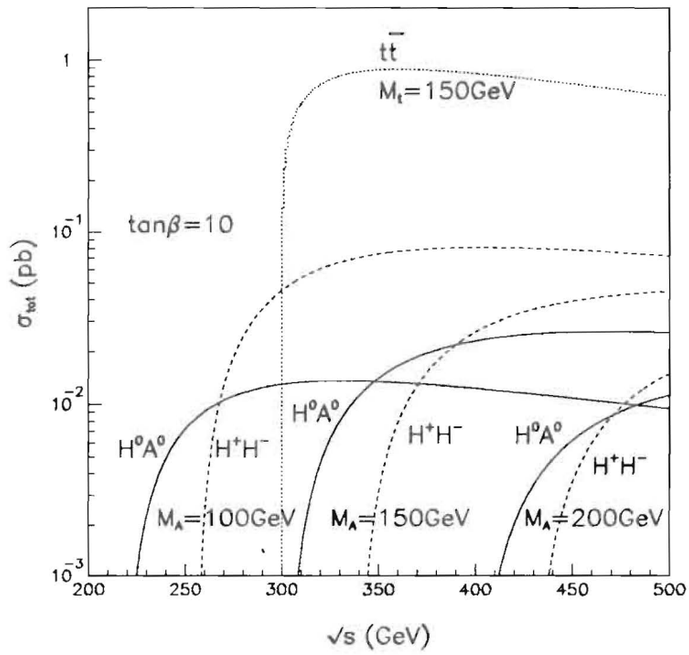


Figure 2.18: The total cross sections for the reactions $e^+e^- \to H^0A^0$ (solid curves) and $e^+e^- \to H^+H^-$ (dashed curves) for $m_A$ = 100, 150, and 200 GeV, assuming $\tan\beta$ = 10, $m_t$ = 150 GeV, and $m_{\tilde{t}}$ = 1 TeV. The dotted curve shows the cross section of the background process $e^+e^- \to t\bar{t}$.

balance (< 20%), thrust axis ($|\cos\theta_{thrust}| < 0.7$), and thrust value (< 0.75). A jet finding algorithm optimized for 200 GeV Higgs is then applied and further cuts are made on the number of jets (=4), charged multiplicity in each jet (> 3) and the lepton energy in each jet (< 20 % of the jet energy). The remaining events are fed to a kinematical fit assuming a four-body final state with a photon radiated from the initial state. The final cut is made on the goodness of the fit. Among the combinations of jets of the selected events, the one which minimizes $|M_{ij} - M_{kl}|$ (the difference of the invariant masses of two jet-pairs) is taken, as the mass difference of $H^0$ and $A^0$ is small.

The lego plots of the two invariant masses are shown in Fig. 2.19, both for the signal ($H^0A^0$) and the background ($t\bar{t}$). The plot peaks at (200 GeV, 200 GeV) for the signal, while the background does not peak anywhere. We can thus discover $H^0$ and $A^0$ with masses up to ~200 GeV at JLC-I of $\sqrt{s}$ = 500 GeV, although it is difficult to distinguish $H^0$ from $A^0$.

### 2.3.4 SUSY Scale from $m_{H^0}$ and $m_{A^0}$ Measurement

Due to the radiative correction, the masses of Higgs particles are related to the SUSY scale. Fig. 2.20 shows contours of $m_{h^0}$ in the plane of scalar quark mass and $\tan\beta$, for $m_t$=150 GeV, and $m_A$=160 GeV, when the Higgsino mass term and trilinear couplings are set to zero. As seen in the figure, $m_{\tilde{q}}$ is determined by $m_{h^0}$ if $\tan\beta$ is large ( $\gtrsim$ 7).

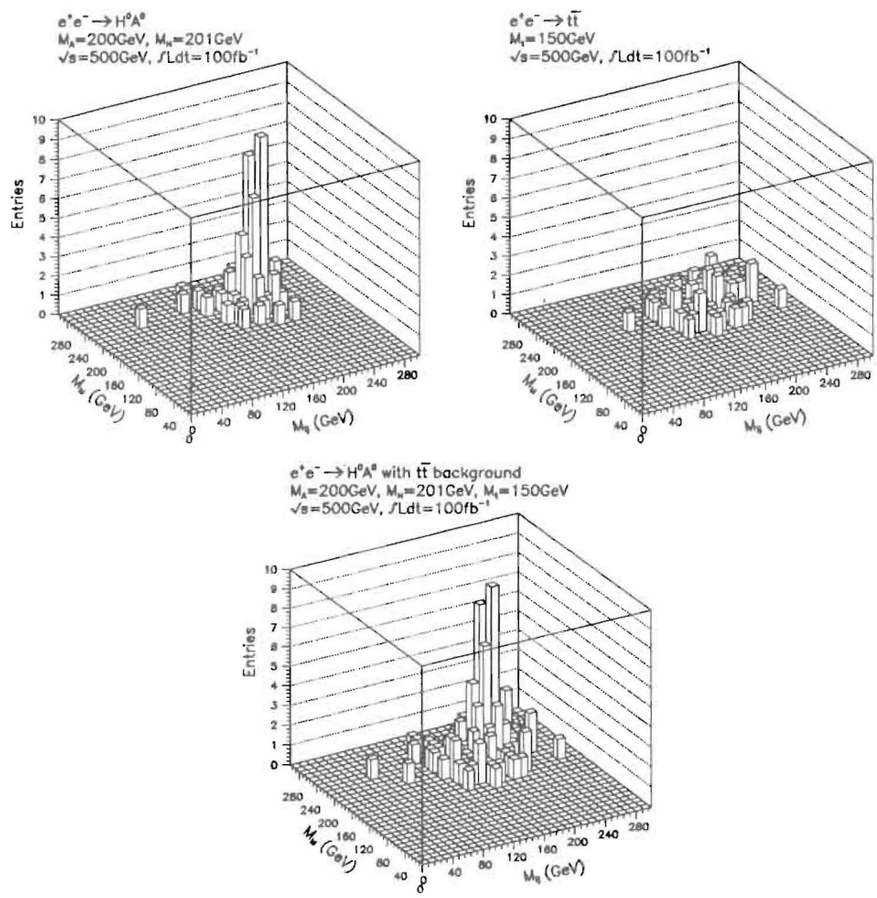


Figure 2.19: The lego plots of the reconstructed masses of the two jet pairs, at $\sqrt{s} = 500$ GeV with $\int Ldt$ 100 fb$^{-1}$. (a) The lego plot for the signal process $e^+e^- \rightarrow H^0A^0$ with $m_A = 200$ GeV and $m_H = 201$ GeV. (b) The lego plot for the background process $e^+e^- \rightarrow t\bar{t}$ with $m_t = 150$ GeV. (c) The sum of (a) and (b).

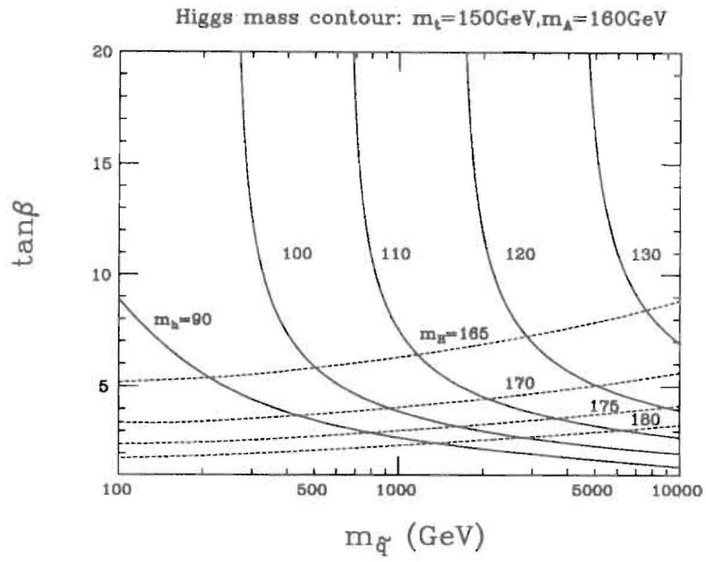


Figure 2.20: The contours of the masses of $h^0$(Solid) and $H^0$(dashed) in the plane of $m_{\tilde{q}}$ and $\tan\beta$.

## 2.4 SUSY Particles

Supersymmetry predicts the existence of a light neutral Higgs boson whose discovery at JLC is easy, as described in the previous sections. However the discovery of the lightest neutral Higgs boson alone is not enough to prove the supersymmetry. It is definitely necessary to discover *at least* one supersymmetric particle. We have emphasized that there are a lot of chances to discover at least one SUSY particle at JLC-I[43]. Although which is the first to be discovered is model-dependent, the SUSY search methods to be invoked at JLC-I is largely model-independent and, once we find one SUSY particle, it will tell us where to look for the next. Moreover, the mass determinations of the SUSY particles can be carried out model-independently, thereby allowing us to test model assumptions. It should be also noted that the polarized electron beam will play an essential role, in the course of the SUSY searches and studies.

### 2.4.1 Model Assumptions

We will work within the framework of supergravity (SUGRA) models with the "GUT-condition"s. These models involve, in general, the following parameters: ($m_0$, $M_2$, $\mu$, $\tan\beta$), which determine the mass spectra and the interactions of supersymmetric particles[44]. $\mu$ is the higgsino mixing mass parameter and $\tan\beta$ is the ratio of the two vacuum expectation values of two Higgs doublets. $m_0$ is the scalar mass parameter, which is common to all the scalar particles in the case of supergravity models (the hidden sector SUSY breaking). $M_2$ is the $SU(2)$ gaugino mass parameter, which is related to the $SU(3)$ and $U(1)$ gaugino mass parameters:

$$\frac{M_1}{\frac{5}{3}\alpha/\cos^2\theta_W} = \frac{M_2}{\alpha/\sin^2\theta_W} = \frac{M_3}{\alpha_s}$$

under the GUT conditions. As demonstrated later, these SUGRA-GUT assumptions can be tested to a high precision.

In order to avoid unnecessary complications, we will make the following simplifying assumptions: a) the $R$-parity is exactly conserved which implies that SUSY particles can only be pair-produced and the lightest SUSY particle (LSP) is absolutely stable and b) the LSP is the lightest neutralino to be consistent with cosmology. In addition, we further assume that c) the supersymmetric particle in question is the lightest charged SUSY particle, unless otherwise stated.

As we will see below, assumption (c) ensures a reasonable branching fraction for direct decays into the LSP[45]. Therefore, the signal for SUSY particle productions is a missing transverse momentum or a large acoplanarity. Since colored SUSY particles are heavier than uncolored ones in general (see Figs. 2.21-a) and -b) which show the lighter chargino mass contours in the $\mu$-$M_2$ plane and sfermion mass contours in the $m_0$-$M_2$ plane, respectively), we will focus our attention on chargino and slepton pair productions. In any case, it is usually straightforward to discover these SUSY particles at JLC-I, once their thresholds are crossed. Moreover, we will be able to study their properties in detail. It should be emphasized that detailed studies of the first SUSY particle alone can teach us a lot about the model parameters and will guide us to the discovery of the next.

### 2.4.2 Charginos

Generality of the Lighter Chargino Properties

First, we discuss the case where the chargino is the first SUSY particle to be discovered at JLC-I. The charginos $\chi_1^\pm$, $\chi_2^\pm$ are the mixtures of charged wino $\tilde{W}^\pm$ and charged higgsino $\tilde{H}^\pm$ obtained from the diagonalization of the mass matrix

$$\mathcal{L}_{\rm mass} = (\tilde{W}^+ \quad \tilde{H}^+) \begin{pmatrix} M_2 & \sqrt{2}m_W \cos\beta \\ \sqrt{2}m_W \sin\beta & \mu \end{pmatrix} \begin{pmatrix} \tilde{W}^- \\ \tilde{H}^- \end{pmatrix}.$$

Notice that this mass matrix is given in terms of the three SUSY parameters: ($M_2$, $\mu$, $\tan\beta$) of which $M_2$ and $\mu$ mainly control the mixing between weak eigenstates. When the splitting between $M_2$ and $\mu$ is large, the mixing is small and pure states, charged wino and higgsino, essentially become mass eigenstates. Our target chargino, the lighter of the two, is either the charged wino or the charged higgsino, depending on whether $M_2 \ll \mu$ or $M_2 \gg \mu$. If $M_2$ and $\mu$ are comparable, there is a substantial mixing between these two states and the properties of the lighter chargino share those of the charged wino and the charged higgsino. It is thus a good idea to start our discussion with the pure states, since, by doing so, we can gain intuitions into a more general case with substantial mixing.

i) Wino

When the lighter chargino state $\chi_1^\pm$ is almost a pure wino state, then the LSP is also almost a pure bino state. The charged wino, being the super partner of the $W$ boson, does not directly couples to binos, while it couples to a left-handed fermion-sfermion pair. By our assumption, $\tilde{W}$ is lighter than all the sfermions, therefore, the decay of a wino $\tilde{W}$ into a bino $\tilde{B}$ proceeds only through a virtual sfermion exchange:

$$\tilde{W}^+ \to f_u \bar{\tilde{f}}_{d_L}^* \to f_u \tilde{B} \bar{f}_d,$$

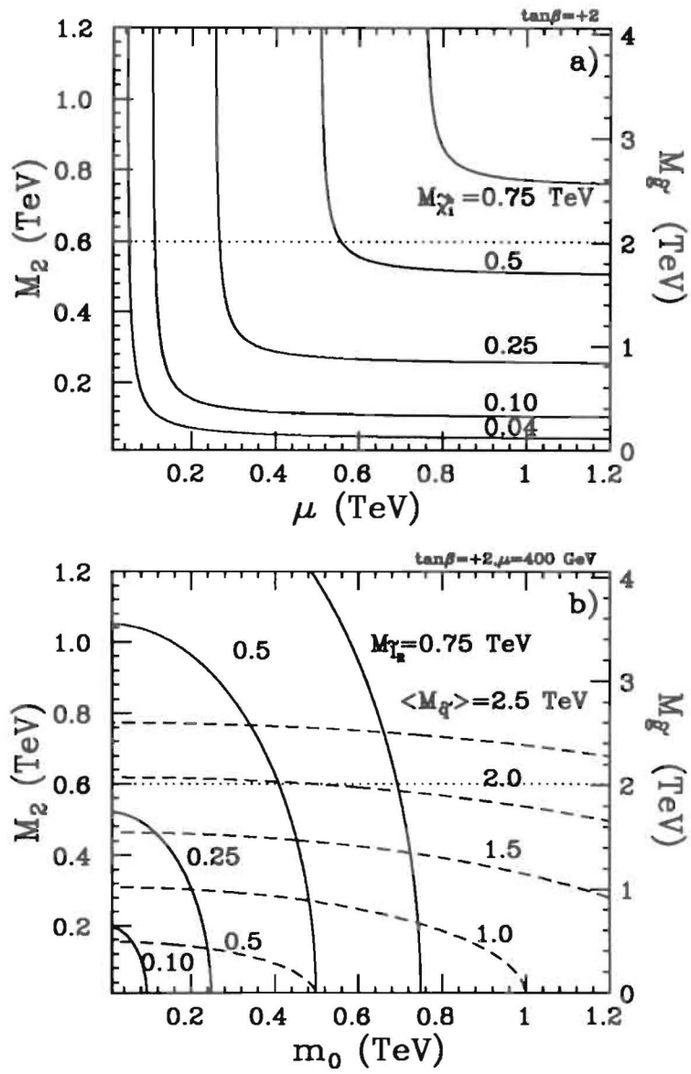


Figure 2.21: (a) Lighter chargino mass contours in the plane of the $SU(2)$ gaugino mass $M_2$ and the higgsino mixing mass $\mu$ for $\tan\beta \equiv v_2/v_1 = +2$. The right vertical axis is the corresponding gluino mass. Dotted line is the expected sensitivity limit for SSC and LHC. (b) Scalar fermion mass contours in the plane of $M_2$ and the common scalar mass $m_0$ for $\tan\beta = +2$ and $\mu = 400$ GeV. Solid lines are for scalar leptons and dashed lines for scalar quarks. Again the dotted line represents the expected sensitivity limit for SSC and LHC.

or

$$\tilde{W}^+ \to \tilde{f}^*_{u_L} \bar{f}_d \to f_u \tilde{B} \bar{f}_d,$$

where $f_u$ and $f_d$ denote up-type and down-type fermions, respectively.

ii) Higgsino or Mixtures

When the lighter chargino state is dominated by the higgsino component, so is the LSP. The lighter chargino and the LSP are then almost mass-degenerate. This time, there exits a $\tilde{h}^+\tilde{h}^0 W$ vertex which allows a direct decay to the LSP:

$$\tilde{h}^+ \to \tilde{h}^0 W^{(*)+} \to \tilde{h}^0 f_u \bar{f}_d.$$

The decay into a fermion and a virtual sfermion is suppressed in general, since the corresponding vertex originates from Yukawa interactions. By the same token, the t-channel sneutrino exchange diagram, active in the wino case, is negligible in this case.

The only exception is the decay into a $b$-quark and a virtual stop which subsequently decays into a top and the LSP. Of course, this requires a sufficiently large mass difference between the LSP and the lighter chargino. The large mass splitting, in turn, implies a substantial mixing which requires a light gaugino, since the mass splitting can be only of the order of $O(m_Z^2/(m_{\tilde{B}} - m_{\tilde{h}}))$.

In order to quantify the qualitative discussions presented above, we will examine below the production and decay of the lighter chargino($\tilde{\chi}_1^\pm$) more closely.

Chargino Production

Fig. 2.22 shows the contours of the lighter chargino pair production cross section at $\sqrt{s} =$ 500 GeV in the $\mu$-$M_2$ plane. The comparison of this figure with Fig. 2.21-a) tells us that

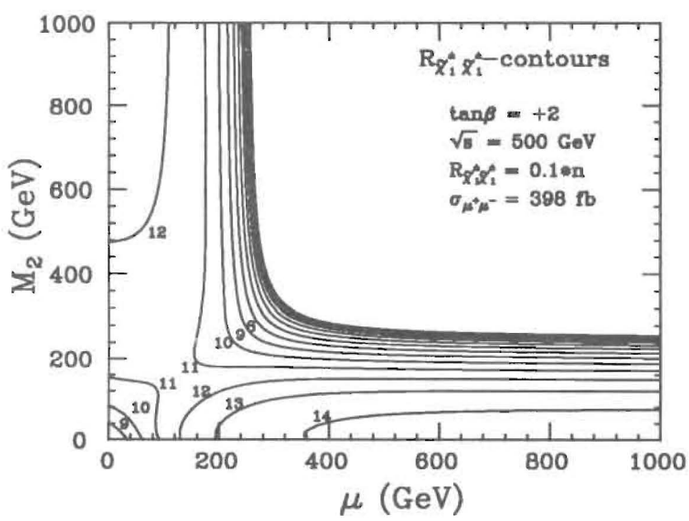


Figure 2.22: Cross section contours in the $\mu$-$M_2$ plane for the lighter chargino pair productions. The cross sections are expressed in terms of the $R$-ratio and are calculated with $m_{\tilde{\nu}} = 500$ GeV and $\tan\beta = +2$.

the cross section is large enough everywhere above the threshold, even though the parameter dependence is rather large. Fig. 2.23-a) compares the $\sqrt{s}$ dependence of the production cross

section for the following three typical cases: pure winos, equal mixtures of wino and higgsino, and pure higgsinos when the sneutrino mass is kept constant at $m_{\tilde{\nu}} = 1000$ GeV. Notice that the $s$-channel diagram alone cannot provide any information on $m_0$, since the chargino mass and the chargino-gauge-boson vertices are completely specified by $\mu$, $M_2$, and $\tan\beta$. The magnitude of the production cross section, thus, determines the mixing angle between the charged wino and the charged higgsino in this case. Fig. 2.23-b) is the same figure for $m_{\tilde{\nu}} = 250$ GeV, where we can see that the $t$-channel sneutrino exchange diagram modifies the threshold shape as well as its magnitude. In this way, for a relatively light $m_0$, the $t$-channel sneutrino exchange diagram provides a possibility to determine $m_0$ through cross section measurements.

Chargino Decay

Under our assumption that the lighter chargino is the lightest charged SUSY particle, $\tilde{\chi}_1^{\pm}$ becomes the next to the lightest SUSY particle. Here we note that, when $\Delta m \equiv M_{\tilde{\chi}_1^{\pm}} - M_{\tilde{\chi}_1^0} > M_W$, the direct decay to $\tilde{\chi}_1^0 W$ dominates, unless the higgsino component is negligible. Fig. 2.24 shows this mass difference in the $\mu$-$M_2$ plane. If this two-body decay mode is kinematically forbidden, the general discussions presented above apply.

We first deal with the lighter chargino which is almost a pure wino state. The supergravity models predict that the lightest sfermions are either sleptons or stop. On the other hand, the discovery of wino at JLC-I implies $\tilde{W} < 250$ GeV. Therefore, if sleptons are the lightest sfermions, we expect that the lightest sleptons are right-handed ones $\tilde{e}_R$, $\tilde{\mu}_R$, $\tilde{\tau}_R$, which are essentially mass-degenerate. Left-handed charged sleptons $\tilde{e}_L$, $\tilde{\mu}_L$, $\tilde{\tau}_L$, and left-handed neutral ones $\tilde{\nu}_e$, $\tilde{\nu}_\mu$, $\tilde{\nu}_\tau$, are nearly mass-degenerate, though they are heavier than the right-handed ones by the contribution of the gaugino mass to the renormalization group equations for the slepton masses. Since the wino component couples only to left-handed states, the decay of the wino-rich chargino thus proceeds as

$$\tilde{\chi}_1^+ \to \nu_l \tilde{l}_L^{+*} \to \nu_l \tilde{\chi}_1^0 l^+,$$

or

$$\tilde{\chi}_1^+ \to \tilde{\nu}_{l_L}^* l^+ \to \nu_l \tilde{\chi}_1^0 l^+,$$

where $l$ can be any of $e$, $\mu$, and $\tau$. The pair-produced charginos $\tilde{\chi}_1^+ \tilde{\chi}_1^-$ appear as acoplanar lepton-pair events, with remarkable universality between electron, muon, and tau events. Notice that, in this case, the decay into $q\bar{q}\tilde{\chi}_1^0$ is suppressed by the heavy squark mass appearing in the squark propagator and the smallness of the weak hypercharge relevant to the coupling to the LSP which is essentially a bino state.

If stop is the lightest sfermion, then wino-rich chargino decays in the chain

$$\tilde{\chi}_1^+ \to \bar{b}_l \tilde{t}_L^* \to \bar{b}_l \tilde{\chi}_1^0 t.$$

This decay leads to an eight-jet final state with a large missing transverse momentum, which should be easy to detect.

When the lighter chargino has a sizable higgsino component, its decay is dominated by a "beta-decay", since the above mentioned $f\tilde{f}^*$ modes are strongly suppressed by the sfermion propagator, in the case where the sfermions are heavier than the lighter chargino and thus are much heavier than the $W$ boson. This time, the decay into $q\bar{q}\tilde{\chi}_1^0$ becomes the major decay mode (67 %), while keeping a reasonable branching fraction for the leptonic mode, thereby allowing us to distinguish between the two cases.

When the $t\bar{b}\tilde{\chi}_1^0$ final state is open, the branching fraction to this mode may be large. The signature is the same as that of the light stop case for the wino-rich chargino.

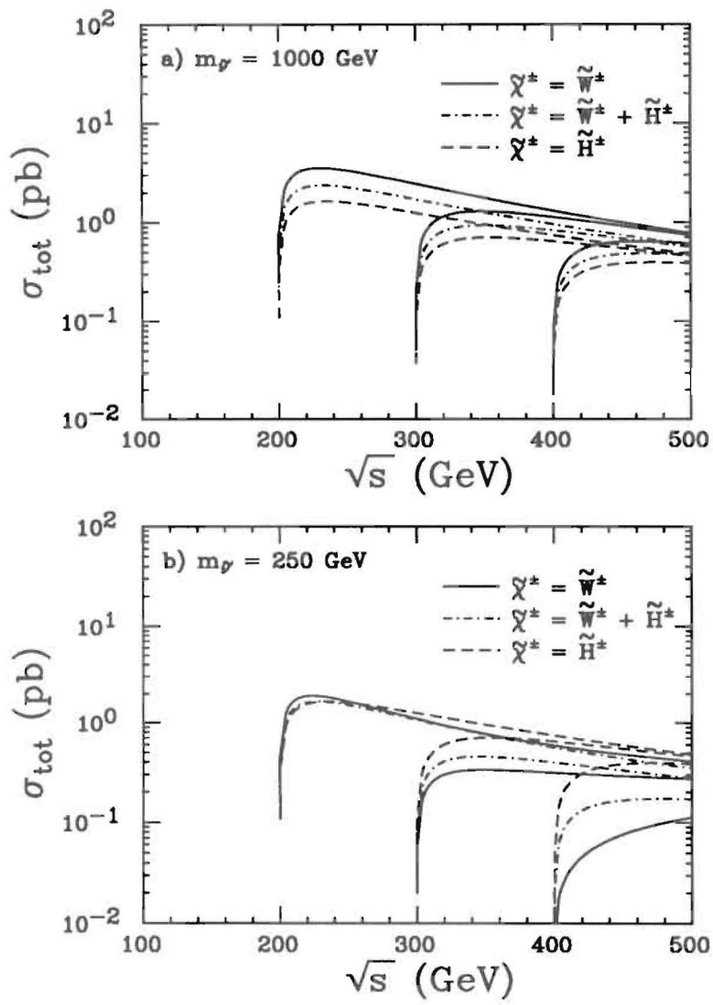


Figure 2.23: The total cross section for the pair production of the lighter charginos of $M_{\tilde{\chi}^{\pm}} =$, 100, 150, and 200 GeV as a function of $\sqrt{s}$ when (a) $m_{\tilde{\nu}} = 1000$ GeV and (b) $m_{\tilde{\nu}} = 250$ GeV. The solid, the dot-dashed, and the dashed curves correspond to pure winos, equal mixtures of wino and higgsino, and pure higgsinos, respectively.

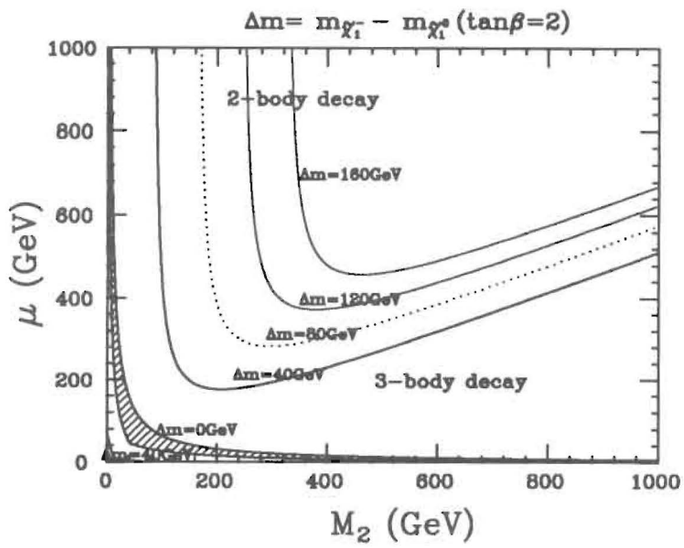


Figure 2.24: Mass difference contours in the $\mu$-$M_2$ plane for the lighter chargino in the case of $\tan\beta = +2$. The shaded region is excluded by our assumption that the LSP is the lightest neutralino.

Chargino Search

Notice that in the parameter space of our interest: $m_0 \gtrsim 200$ GeV, $\mu \lesssim 1$ TeV, and $M_2 \lesssim 200$ GeV, the branching ratio for the hadronic mode always exceeds $\sim 50$ %, even if the lighter chargino is wino-rich. On the other hand, the branching ratio for the leptonic mode is at least 33 % which increases with the fraction of the wino component.

When the decay into a real $W(\tilde{\chi}_1^- \to \tilde{\chi}_1^0 W^-)$ is kinematically allowed, the best signal is an acoplanar pair of $W$'s reconstructed from a four-jet final state, since the potentially most serious background from $e^+e^- \to W^+W^-$ is absent and the remaining background from $e^+e^- \to W^+W^-Z$ has only a small cross section. In this case, the detection of the chargino is straightforward.

In the following, therefore, we will focus our attention on the case where the two-body decay is kinematically forbidden. Considering the background from $W$-pair productions and two-photon processes, the best channel, in this case, is again the four-jet mode. However, we will try to use the final state where one of the chargino decays hadronically: $\tilde{\chi}_1^- \to q\bar{q}\tilde{\chi}_1^0$, while the other decays leptonically: $\tilde{\chi}_1^- \to l^-\bar{\nu}\tilde{\chi}_1^0$, since the combinatorial ambiguity is absent in this mode and, therefore, the determinations of the chargino and the LSP masses are easy.

Notice that the background from $W$-pair productions can be effectively removed by requiring that the invariant mass of the two-jet system and that of the lepton and the reconstructed neutrino are inconsistent with the $W$-pair hypothesis, while the two-photon processes can be eliminated by requiring an energetic isolated lepton. The remaining $W$-pair contamination can be further reduced by cuts on the polar angles of the isolated lepton and the two-jet system and a cut on the acoplanarity.

The signature to look for is then two jets and a single energetic isolated lepton with a large missing transverse momentum or a large acoplanarity, for which the $W$-pair hypothesis is disfavored, provided that the mass difference $\Delta m \equiv M_{\tilde{\chi}_1^\pm} - M_{\tilde{\chi}_1^0}$ is sufficiently large to produce the energetic isolated lepton. As already shown in Fig. 2.24, this mass difference is large enough

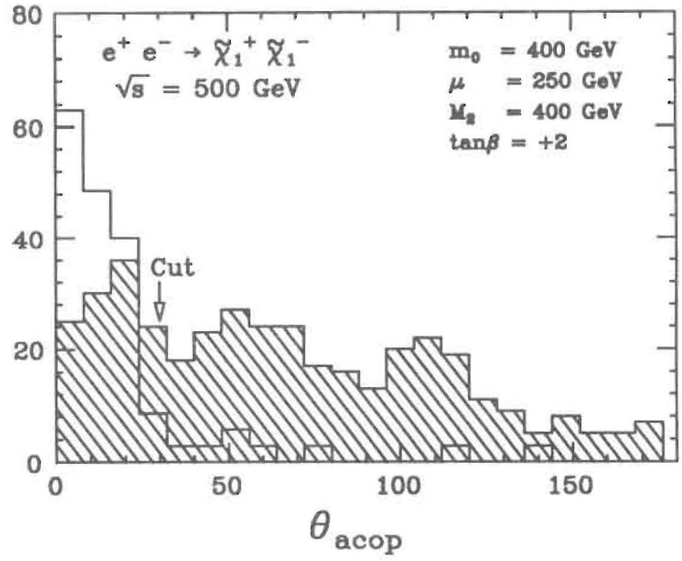


Figure 2.25: An example of the acoplanarity distribution for the two-jet+lepton final states from the lighter chargino pair productions in the case of $m_0 = 400$ GeV, $M_2 = 400$ GeV, $\mu = 250$ GeV, and $\tan\beta = +2$. The Monte Carlo data correspond to an integrated luminosity of 10 fb$^{-1}$ at $\sqrt{s} = 500$ GeV. The hatched histogram is the signal events, while the open histogram is the background from $W$-pair productions.

for detection in most of the parameter space. The remaining question is whether this is large enough for the separation from the potential background processes such as two-photon processes or $W$-pair productions.

Fig. 2.25 is an example of the acoplanarity distribution of the two-jet+lepton final states from the chargino decays for an integrated luminosity of 10 fb$^{-1}$ (20 days) at $\sqrt{s} = 500$ GeV. Also shown is the $W$-pair background (open histogram). Both the signal and the background are with all the cuts except for the one on the acoplanarity. The cut at $\theta_{acop} = 30°$ provides a virtually background-free sample of the chargino pairs with a reasonable efficiency $\epsilon \gtrsim 13$ %, including the branching fraction of 30 %.

Chargino Study

When the chargino signal is detected, the next task is the determination of the chargino and the LSP masses. For this, we look at the energy distribution of the two-jet systems from the chargino decays which is shown in Fig. 2.26. Notice that the distribution depends on the structure of the decay vertex. Nevertheless, the end points of the distribution are determined by the chargino and the LSP masses. Therefore the shape of the distribution may provide us with additional information on the SUSY parameters.

The expected statistical errors on $M_{\tilde{\chi}_1^\pm}$ and $M_{\tilde{\chi}_1^0}$ are 3.2 GeV and 2.0 GeV, respectively, when we fit the distribution to a polynomial.

The LSP mass together with the lighter chargino mass fixes two out of the three parameters ($M_2$, $\mu$, and $\tan\beta$) in the chargino-neutralino mass matrices, leaving only one parameter undetermined. If the LSP is lighter than the observed chargino by a factor of $\alpha_W/(3/5)\alpha_Y$, then it strongly suggests that they are almost pure wino and bino states. The interactions of the particles are then completely fixed by the supersymmetry, which enables us to estimate

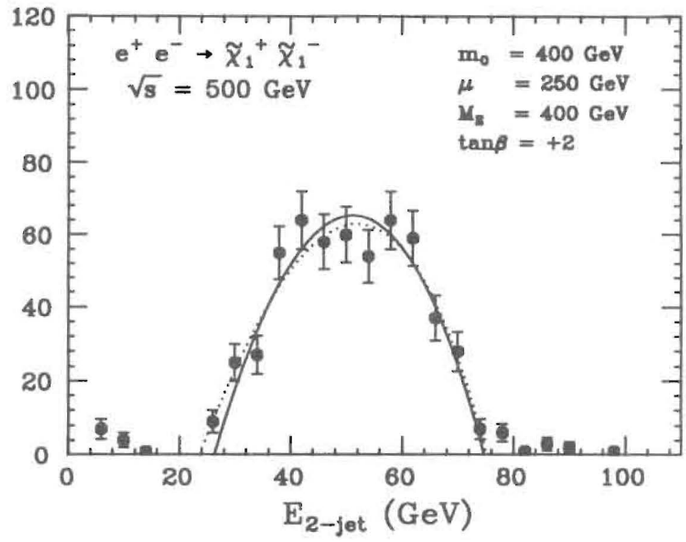


Figure 2.26: The energy distribution of the two-jet systems from the lighter chargino decays for Monte Carlo data corresponding to an integrated luminosity of 21 $fb^{-1}$, where the SUSY parameters are the same as with Fig. 2.25. The solid line corresponds to the input masses, while the dotted line is the best fit curve from a polynomial fit.

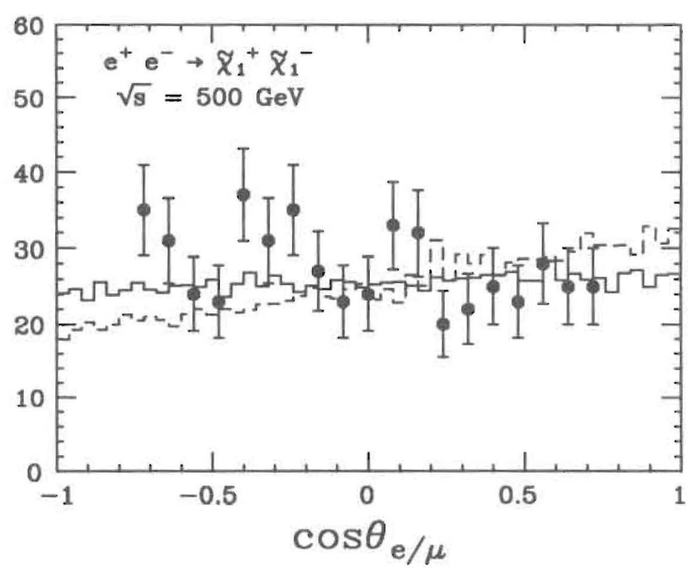


Figure 2.27: An example of the polar angle distribution for $l^-$'s from the lighter chargino decays compared with the theoretical predictions for different sets of the SUSY parameters: the solid histogram for $m_0 = 400$ GeV, $M_2 = 400$ GeV, $\mu = 250$ GeV, and $\tan\beta = +2$ and the dashed histogram for $m_0 = 400$ GeV, $M_2 = 250$ GeV, $\mu = 250$ GeV, and $\tan\beta = +2$. Notice that the vertical scale for the dashed histogram is arbitrarily adjusted to show the difference in the angular dependence. The Monte Carlo data corresponds to an integrated luminosity of 21 $fb^{-1}$ and were generated with the same SUSY parameters as with the solid histogram.

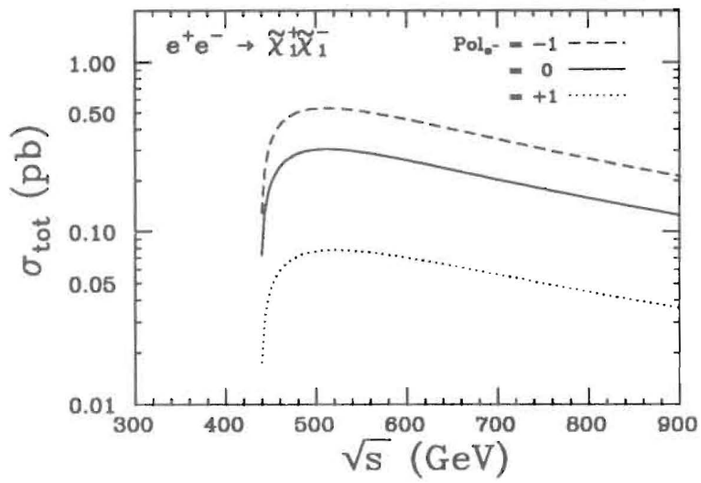


Figure 2.28: The polarization dependence of the chargino pair-production cross section for $m_0 = 400$ GeV, $M_2 = 400$ GeV, $\mu = 250$ GeV, and $\tan\beta = +2$, shown as a function of $\sqrt{s}$.

the cosmic abundance of the LSP. By requiring that their contribution to the cosmic density does not exceed the critical one, we will obtain an *upperbound* on the sfermion masses. For example, $m_{\tilde{B}} = 100$ GeV implies that $m_{\tilde{f}} < 350$ GeV for degenerate sleptons and squarks, and a stronger bound $m_{\tilde{l}} < 300$ GeV for $m_{\tilde{l}} \ll m_{\tilde{t}}$. On the other hand, if the mass ratio of the LSP and the chargino is different from $\alpha_W/(3/5)\alpha_Y$, it signals a substantial mixing with higgsino states, indicating a light higgsino. For instance, a 10% shift requires the higgsinos to be lighter than $\sim 10 m_{\tilde{\chi}^0}$.

The differential cross section gives us yet another handle to determine the SUSY parameters. Fig. 2.27 shows the corresponding polar angle distribution of the $l^-$'s from the $\tilde{\chi}_1^-$ decays which is compared with the theoretical predictions for different sets of the SUSY parameters. The polarized electron beam is also a powerful tool to study the nature of the chargino, since, for instance, we can switch off the $t$-channel sneutrino diagram by choosing a right-handed electron beam. The right-handed electron beam, at the same time, kills most of the contribution from the wino component, since the $\tilde{W}^+\tilde{W}^-Z$ and $\tilde{W}^+\tilde{W}^-\gamma$ vertices come from the $\tilde{W}^+\tilde{W}^-W^3$ vertex which vanishes for the right-handed beam in the massless $Z$ limit. Therefore, the right-handed beam allows us to study the higgsino component separately. Fig. 2.28 shows the polarization dependence of the chargino pair-production cross section for $m_0 = 400$ GeV, $M_2 = 400$ GeV, $\mu = 250$ GeV, and $\tan\beta = +2$. The threshold shape is essentially controlled by the $S$-wave phase space factor $\beta^1$, indicating that the chargino in this case is higgsino-rich and the $t$-channel sneutrino exchange contribution is small.

Combining this information together with that from the SUSY Higgs studies, we can learn a lot about the SUSY parameters from a single charged SUSY particle by virtue of the cleanness of JLC experiments.

### 2.4.3 Sleptons

General Discussions on Sfermion Mass Spectrum

The discovery of sleptons at JLC-I allows us to thoroughly explore the supersymmetric

mass spectrum. Studies on $\tilde{e}$, $\tilde{\mu}$, and $\tilde{\tau}$ can be carried out simultaneously, giving much useful information on gaugino and scalar masses, and even on $\mu$ and $\tan\beta$. This unique opportunity is provided by the following mass formulae:

$$\begin{aligned}
m^2_{\tilde{l}_L} &= m_0^2 - \left(\frac{3}{2}(\alpha_2^2 - \alpha_0^2) + \frac{1}{22}(\alpha_1^2 - \alpha_0^2)\right)\frac{M_2^2}{\alpha_2^2} - \frac{1}{2}m_Z^2\cos 2\beta(1 - 2\sin^2\theta_W), \\
m^2_{\tilde{\nu}_L} &= m_0^2 - \left(\frac{3}{2}(\alpha_2^2 - \alpha_0^2) + \frac{1}{22}(\alpha_1^2 - \alpha_0^2)\right)\frac{M_2^2}{\alpha_2^2} - \frac{1}{2}m_Z^2\cos 2\beta, \\
m^2_{\tilde{l}_R} &= m_0^2 - \frac{2}{11}(\alpha_1^2 - \alpha_0^2)\frac{M_2^2}{\alpha_2^2} - m_Z^2\cos 2\beta\sin^2\theta_W. \qquad (2.2)
\end{aligned}$$

By virtue of an accidental cancellation, the mass splitting between $\tilde{l}_L$ and $\tilde{l}_R$ uniquely determines the wino mass parameter $M_2$ and puts a tight constraint on the universal scalar mass $m_0$ and $\tan\beta$. These mass formulae also ensure that masses of all the sleptons are close to each other, with slight differences among the four groups: (1) ($\tilde{e}_L$, $\tilde{\mu}_L$), (2) ($\tilde{e}_R$, $\tilde{\mu}_R$), (3) $\tilde{\tau}_1$, (4) $\tilde{\tau}_2$. The right-handed ones (2) are always lighter than the left-handed ones (1), whose splitting "measures" the gaugino mass. Anyway, if one of these sleptons is found, the chance to discover the others is greatly enhanced.

Slepton Production

Smu- and stau-pair productions take place through $e^+e^-$ annihilations into a virtual photon or $Z$ and their differential cross sections behave as $\sin^2\theta$. Their total cross sections are completely specified by their quantum numbers. The contours of the cross sections for smu and stau pairs at $\sqrt{s} = 500$ GeV are plotted in Fig. 2.29 in the $m_0$-$M_2$ plane. Notice that the contours resemble those in Fig. 2.21-b), indicating that sensitivity limit extends up close to the production threshold.

Selectron pair production is more complicated since there exist $t$-channel neutralino exchange diagrams which depend strongly on the masses and couplings of the neutralinos. Fig. 2.30 is similar to Fig. 2.29 for selectron pair productions. The existence of the $t$-channel diagrams also modifies the angular distribution. Fig. 2.31 is an example of the differential cross sections for selectron pair productions.

Slepton Decay

Since the production cross sections for slepton pairs are of reasonable size, if they are produced at all, their detection should be easy when the direct decays into the LSP dominate and the mass difference between the target slepton and the LSP is large. This condition is satisfied when the LSP has a sizable component of the bino state. Figs. 2.32-a) and -b) show the branching fractions for the direct decays for super partners of left-handed and right-handed muons, respectively, in the $m_0$-$M_2$ plane. The figures indicate that the direct mode indeed dominates the $\tilde{\mu}_R$ decays. Figs. 2.33-a) and -b) are the corresponding contours for the mass differences. Almost everywhere in the parameter space, the mass differences are large enough for detection. In this case, the signal of slepton pair productions is again an acoplanar lepton-pair, similar to the wino-pair events. However, the two-body decay of sleptons gives a flat energy distribution for the final state leptons, which can be easily separated from the three-body decay of a charged wino. At the threshold of sleptons, the final state leptons are almost monochromatic. Furthermore, due to the difference in the threshold behavior of the total cross sections, $\beta^3$ for sleptons and $\beta$ for winos, we are able to distinguish the former from the latter. If the LSP is higgsino-like, then the sleptons may decay in a completely different manner:

$$\tilde{l} \to l\tilde{w}^{0*} \to l\tilde{h}^0 h^0.$$

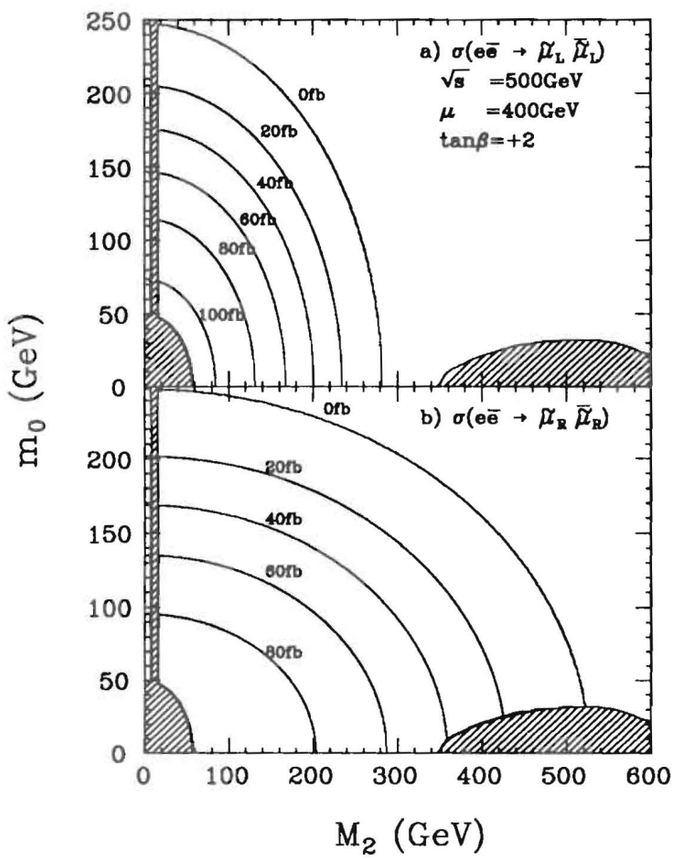


Figure 2.29: Cross section contours for slepton ($\tilde{l} \neq \tilde{e}$) pair productions in the $m_0$-$M_2$ plane, in the case of $\mu = 400$ GeV and $\tan\beta = +2$ and $\sqrt{s} = 500$ GeV: (a) $e^+e^- \rightarrow \tilde{\mu}_L^+\tilde{\mu}_L^-$ and (b) $e^+e^- \rightarrow \tilde{\mu}_R^+\tilde{\mu}_R^-$. The shaded regions are forbidden by our assumption that the LSP is the lightest neutralino.

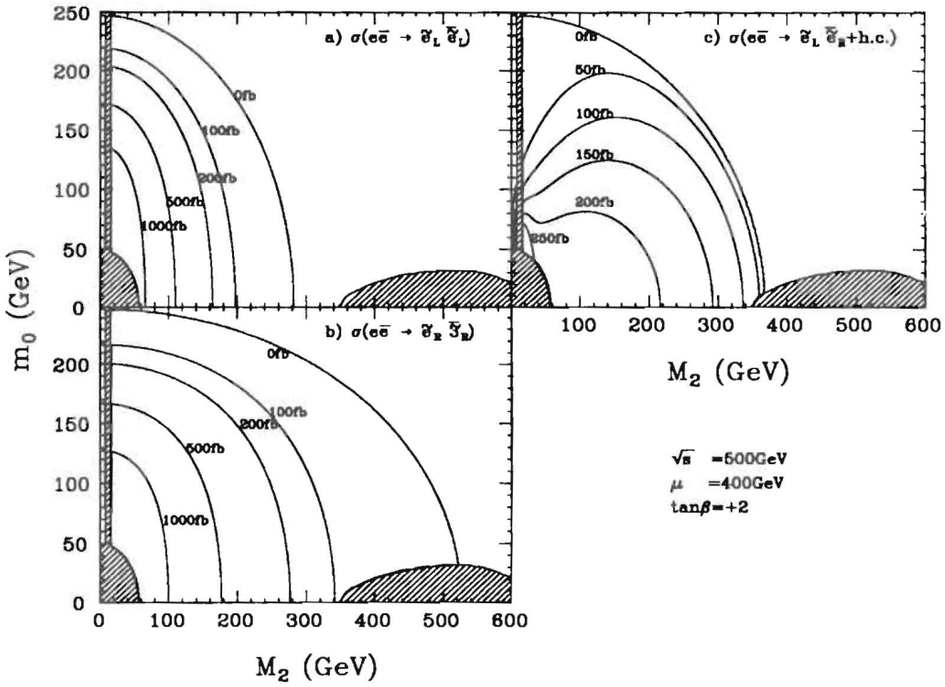


Figure 2.30: A similar plot to Fig. 2.29 for selectron pair productions: (a) $e^+e^- \to \tilde{e}_L^+\tilde{e}_L^-$, (b) $e^+e^- \to \tilde{e}_R^+\tilde{e}_R^-$, and (c) $e^+e^- \to \tilde{e}_L^+\tilde{e}_R^- + \tilde{e}_R^+\tilde{e}_L^-$.

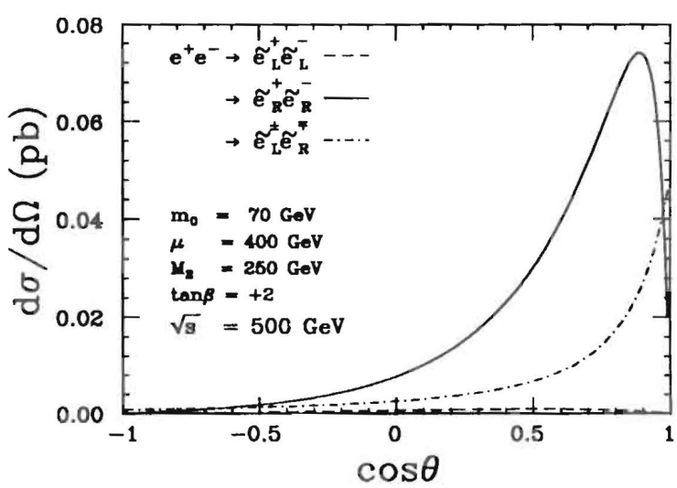


Figure 2.31: The differential cross sections for selectron pair productions in the case of $m_0 = 70$ GeV, $M_2 = 250$ GeV, $\mu = 400$ GeV, and $\tan\beta = +2$. The three curves correspond to $e^+e^- \to \tilde{e}_L^+\tilde{e}_L^-$(dash), $e^+e^- \to \tilde{e}_R^+\tilde{e}_R^-$(solid), and $e^+e^- \to \tilde{e}_L^\pm\tilde{e}_R^\mp$(dot-dashed), respectively.

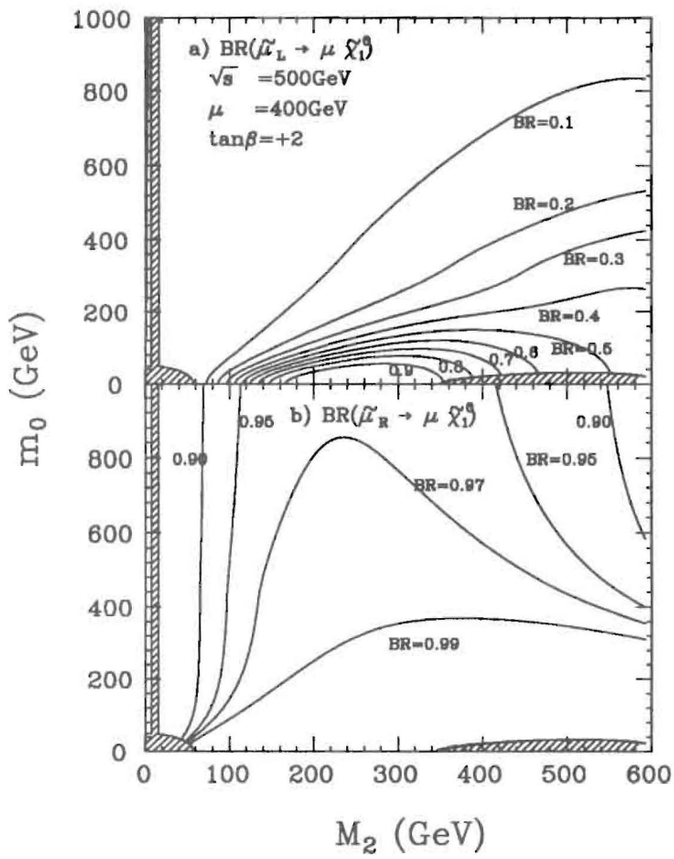


Figure 2.32: Branching fraction contours in the $m_0$-$M_2$ plane for (a) $\tilde{\mu}_L$ and (b) $\tilde{\mu}_R$ in the case of $\mu = 400$ GeV and $\tan\beta = +2$. The shaded regions are excluded by our assumption that the LSP is the lightest neutralino.

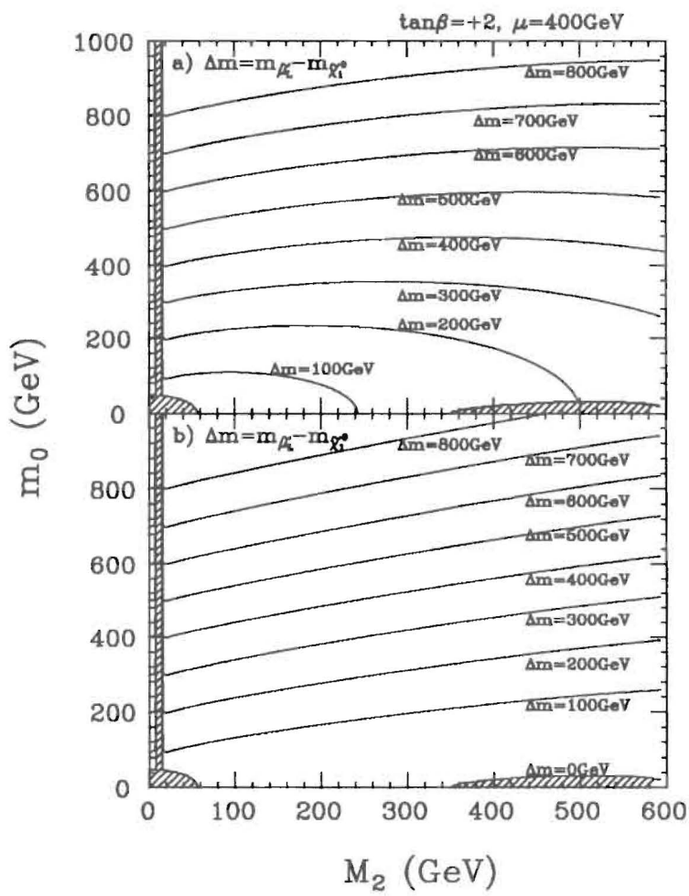


Figure 2.33: Mass difference contours in the $m_0$-$M_2$ plane for (a) $\tilde{\mu}_L$ and (b) $\tilde{\mu}_R$ in the case of $\mu = 400$ GeV and $\tan\beta = +2$.

This decay results in a spectacular event consisting of a lepton-pair and four jets with an invariant mass peak at $m(jj) \sim m_h$. In this case, the absence of the $t$-channel higgsino exchange amplitude provides a good proof that the LSP is indeed higgsino-like. Since the detection of this decay mode is straightforward, we will concentrate on the case of a bino-like LSP below.

Slepton Search

Figs. 2.34-a) and -b) are examples of acoplanarity distributions for selectron and smuon pair productions, respectively, after the accumulation of 10 fb$^{-1}$ (20 days) at $\sqrt{s} = 350$ GeV. Notice that the SUSY parameters used here were so chosen that both $\tilde{l}_L^{\pm}$ and $\tilde{l}_R^{\pm}$ can be produced at $\sqrt{s} = 500$ GeV, while $m_{\tilde{l}_R^{\pm}} < M_{\tilde{\chi}_1^{\pm}}$ to be consistent with our assumption. We can see that the signals can be effectively enhanced over the background mainly consisting of $W$ pairs, by applying a cut on the acoplanarity angle. A detection efficiency of $\epsilon \gtrsim 50$ % is easily achieved with a signal to background ratio of $S/B \gtrsim 1.6$ even for smuons. The signal to background ratio can be further improved by using a right-handed electron beam, since the production cross section for smuon pairs almost doubles, while the $W$-pair cross section essentially vanishes, as shown in fig. 2.34-c).

Slepton Study

Once a slepton is discovered, we can determine the masses of the slepton

and the LSP from the energy spectrum of the final state leptons more reliably than in the chargino case, since we know the shape of the spectrum. Fig. 2.35-a) is the energy distribution of muons from smuon decays for an integrated luminosity of 18 fb$^{-1}$ with a right-handed electron beam. Though the distribution is a little bit different from the expected rectangular shape due, primarily, to selection cuts, the lower and the higher edges are sharp enough. These end points of the energy spectrum determine $m_{\tilde{\mu}}$ and $M_{\tilde{\chi}_1^0}$. Fig. 2.35-b) shows the contours obtained from the fit to the Monte Carlo data. We can determine the smuon and the LSP masses with statistical errors of 1.4 GeV and 1.0 GeV, respectively.

If the LSP is bino-like, then its $t$-channel exchange also contributes to the selectron pair production. JLC's polarized electron beam will, again, play a crucial role here since the $t$-channel diagrams exist only for the selectron with the same chirality as the beam electron. Fig. 2.36 plots the production cross section of selectron pairs as a function of $\sqrt{s}$ for $\mathrm{Pol}_{e^-} = -1, 0$, and $+1$. Notice that the $t$-channel exchange contribution comes only from the bino-component in the cases of $\tilde{e}_R^+\tilde{e}_R^-$ and $\tilde{e}_L^{\pm}\tilde{e}_R^{\mp}$ productions. The $\tilde{e}_L^{\pm}\tilde{e}_R^{\mp}$ production is of particular interest, since there is no $s$-channel contribution, which allows an unambiguous test of the $t$-channel contribution. Thus detailed studies of the interference effects combined with the beam polarization measure the mass of the LSP exchanged in the $t$-channel *and* its coupling to the electron. We can check whether the LSP is indeed bino-like in this way. If we vary the energy and cross the threshold of $\tilde{e}_L^+\tilde{e}_L^-$ production, we may also be able to see the $t$-channel exchange of the second lightest neutralino, presumably the neutral component of wino.

Figs. 2.37-a) to -c) plot the differential cross sections for four different chirality combinations of the final state selectrons. We can see that the final state chirality combinations can be effectively selected by choosing an appropriate helicity of the electron beam. The magnitudes and the shape of the differential cross sections will tell us about the nature of the active neutralinos in the $t$ channel.

We can play a similar game for smuon-pair productions. Fig. 2.38 is a similar plot to Fig. 2.36 for smuon pair productions. Since the cross section is completely specified by quantum numbers, the polarization dependence will confirm that the produced particles are actually smuons. When the mass splitting of $\tilde{\mu}_L$ and $\tilde{\mu}_R$ is small, however, the importance of the beam polarization increases, since it greatly helps us separate one from the other.

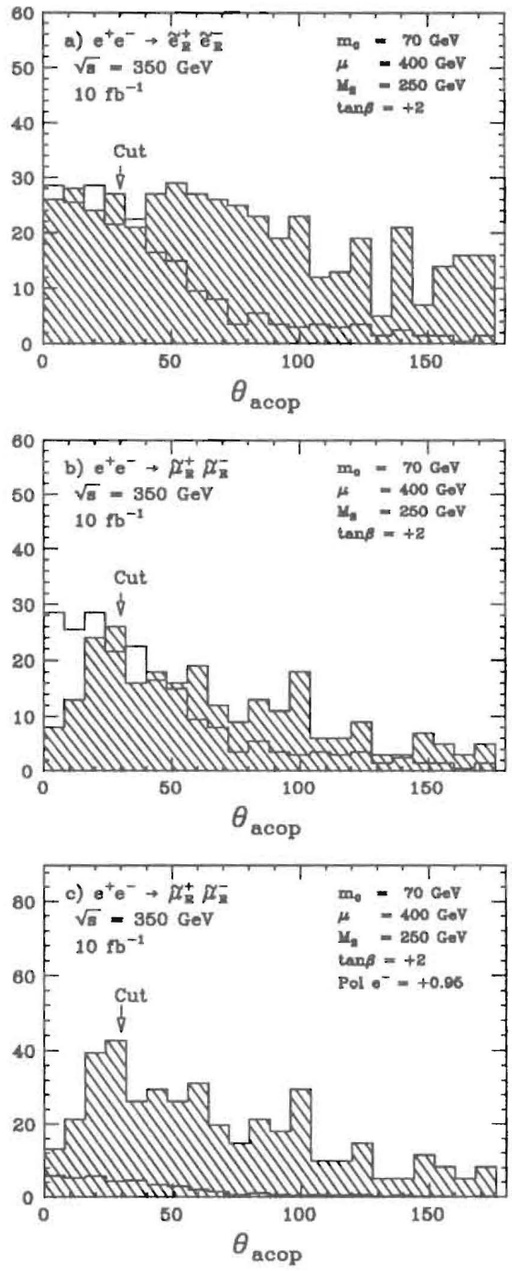


Figure 2.34: Examples of acoplanarity distributions for (a) selectron pair and (b) smuon pair productions. The Monte Carlo data correspond to an integrated luminosity of 10 $\text{fb}^{-1}$ at $\sqrt{s} = 350$ GeV with an unpolarized electron beam. The hatched histograms are for the signal events, while the open histograms are the background from $W^+W^-$ productions. The effect of the right-handed electron beam is demonstrated in (c).

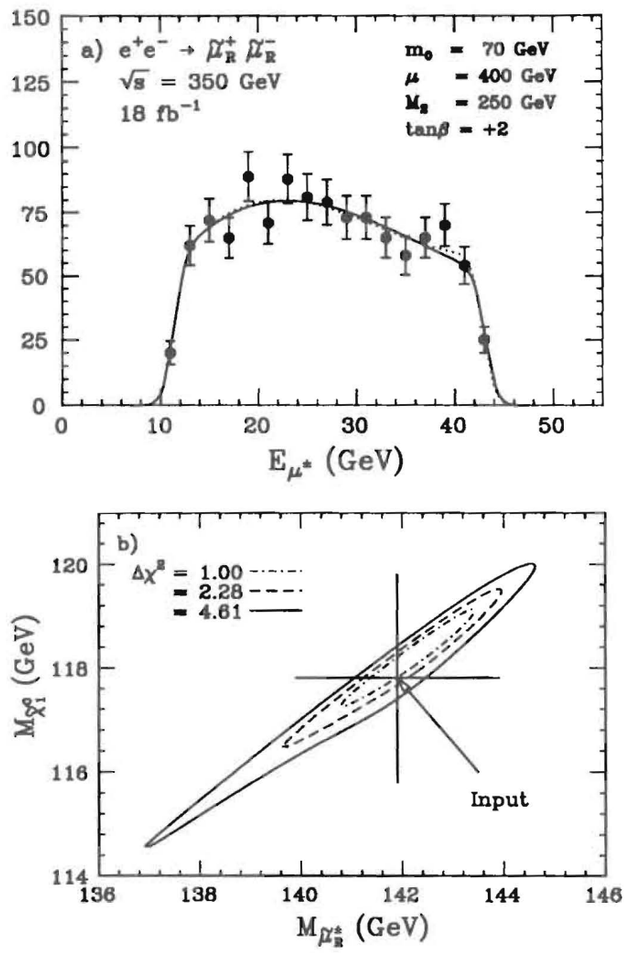


Figure 2.35: (a) The energy distribution of muons from smuon decays for the same Monte Carlo parameters as with Fig.2.34 but with a right-handed electron beam and with a doubled statistics. The solid line is the result of a fit to the Monte Carlo data with $m_{\tilde{\mu}}$ and $M_{\tilde{\chi}_1^0}$ fixed at their input values, while the doted line corresponds to the best fit curve, letting these two masses move freely. (b) The contours in the $m_{\tilde{\mu}}$-$M_{\tilde{\chi}_1^0}$ plane obtained from the fit to the energy distribution.

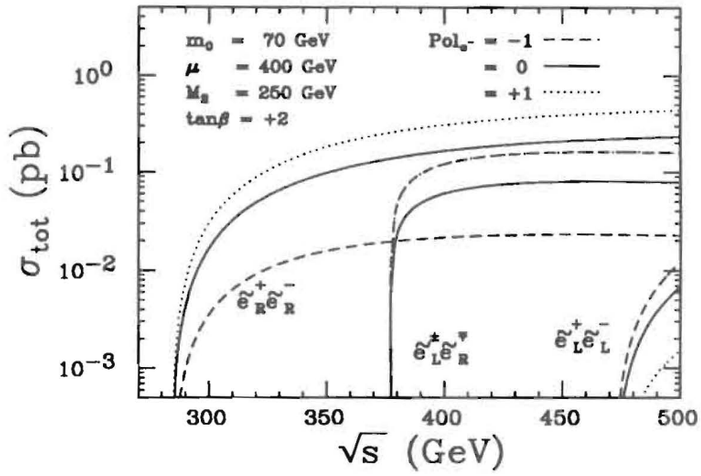


Figure 2.36: The electron polarization dependence of the selectron pair production cross section in the case of $m_0 = 70$ GeV, $M_2 = 250$ GeV, $\mu = 400$ GeV, and $\tan\beta = +2$. The solid lines are for no polarization, while the dashed and the dotted curves are for left-handed and right-handed electron beams, respectively. Notice that $\tilde{e}_L^{\pm}\tilde{e}_R^{\mp}$ production is forbidden when wrong polarization is selected.

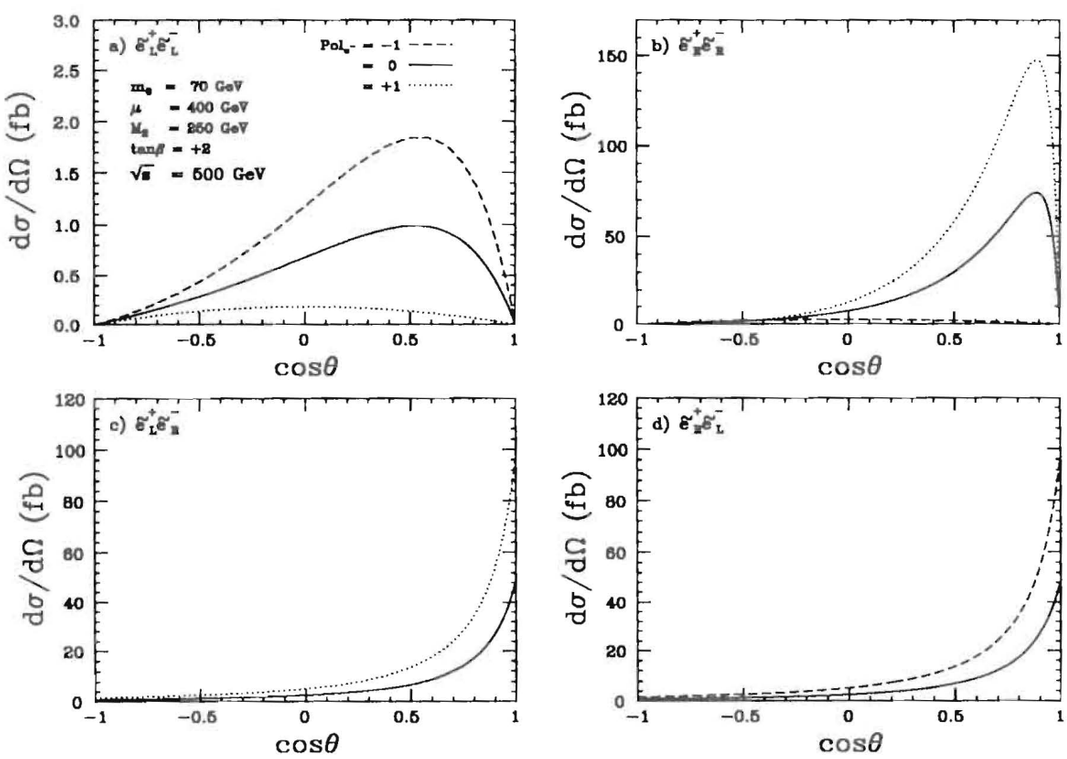


Figure 2.37: The differential cross sections for different chirality combinations for selectron pairs: (a) $\tilde{e}_L^+\tilde{e}_L^-$, (b) $\tilde{e}_R^+\tilde{e}_R^-$, (c) $\tilde{e}_L^+\tilde{e}_R^-$, and (d) $\tilde{e}_R^+\tilde{e}_L^-$.

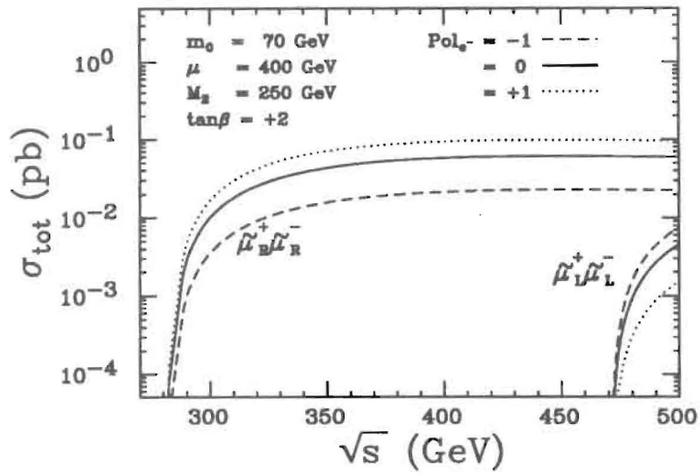


Figure 2.38: A similar plot to Fig. 2.36 for smuon pair productions.

Once the gaugino and the slepton masses are fixed in this way, then we can predict the gluino and squark masses and decide the next energy to go.

## 2.5 Tests of SUGRA-GUT Assumptions

As shown in the previous subsections, JLC-I can discover SUSY particles roughly to their kinematical limits, with a capability of detailed studies on their masses and decay distributions. We demonstrate in this subsection that this very capability enables us to test the SUSY-GUT and supergravity scenario. Once the lightest charged SUSY particle is found, it will serve us a great deal of information about the SUSY-particle spectrum, and we can set the c.m. energy for the next SUSY hunting. Then we will be able to find series of SUSY particles. The SUSY mass spectrum will put strong constraints on the supergravity parameters, especially on $M_2$ (universal gaugino mass) and $m_0$ (universal scalar mass). In a lucky situation, we will have opportunity to determine all the SUSY-breaking parameters in the minimal supergravity, ($M_2$, $m_0$, $\mu$, $\tan\beta$, $A$, $B$). It is further possible to check whether the SUSY mass spectrum is indeed determined by this small number of parameters. In this way, we will explore physics at the Planck scale, since the nature of the SUSY-breaking mechanism is believed to come from the supergravity interactions.

We will demonstrate below an example of the SUSY-study strategy, for the case where the charged slepton is the first SUSY particle to be discovered. The supergravity models predict either right-handed charged slepton or chargino will be found first. The right-handed charged slepton masses are expected to be degenerate among generations.

The right-handed selectron $\tilde{e}_R$ has larger production cross section than smu $\tilde{\mu}_R$ or stau $\tilde{\tau}_R$ due to the $t$-channel bino $\tilde{B}$-exchange diagram. After first observations of highly acoplanar electron pair events, we will use the right-handed electron beam to suppress the background from $W$-pair production. Then the detection of all three right-handed charged sleptons ($\tilde{e}_R$, $\tilde{\mu}_R$, and $\tilde{\tau}_R$) is relatively easy as shown in the previous subsections. Using the energy distributions of final-state charged leptons, we can measure masses of sleptons and the LSP at the percent level. Already at this point, we can check one of the most important assumptions in the minimal

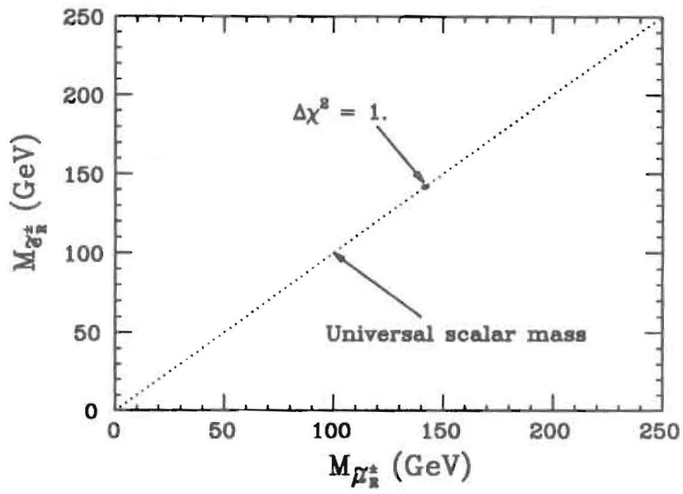


Figure 2.39: The expected $\Delta\chi^2 = 1$ contour in the $m_{\tilde{\mu}_R}$-$m_{\tilde{e}_R}$ plane. The hidden sector SUSY breaking implies the generation-independence of the right-handed slepton masses.

supergravity, that the scalar masses are degenerate among generations. The universality of the masses of $\tilde{e}_R$, $\tilde{\mu}_R$, and $\tilde{\tau}_R$ will strongly support the hidden-sector scenario of SUSY-breaking (see Fig. 2.39).

The selectron production is enhanced by the $t$-channel $\tilde{B}$-exchange diagram compared to the smu and stau productions which have only $s$-channel $\gamma$- and $Z$-exchange contributions. Thus the selectron production cross section essentially measures the bino mass $M_1$. Since the LSP mass $m_{\rm LSP}$ is already fixed, one can test whether the LSP is bino-like or higgsino-like. If the cross section is consistent with the $t$-channel exchange of the LSP, then it is almost a pure bino. If the cross section is almost the same with that of smus or staus, then the LSP is almost a pure higgsino. In the mixed case, the mass of the LSP and the cross section put two constraints on the neutralino-chargino mass parameters ($M_2$, $\mu$, $\tan\beta$). In any case, it is remarkable that we can set an upperbound on the mass of the lighter chargino from $m_{\rm LSP}$ alone. Fig. 2.40 shows the upper limit on the lighter chargino mass as a function of the LSP mass. For the LSP mass greater than 30 GeV, the lighter chargino mass never exceeds twice the LSP mass. For a higgsino-like LSP, the lighter chargino (almost a pure charged higgsino) lies just above the LSP. For a bino-like LSP, the lighter chargino (almost a pure charged wino) is roughly twice as heavy as the LSP.

From the upperbound on the lighter chargino mass obtained from $m_{\rm LSP}$, we will fix the c.m. energy for the chargino search. We have shown that the lighter chargino mainly decays into LSP+$W$, whose detection is easy. Even in a small region of the parameter space where it decays into three-body final states, we can discover the chargino as far as it is heavier than the LSP by $\Delta m \gtrsim O(5)$ GeV. We can measure its mass $m_{\tilde{\chi}^\pm}$, and its production cross sections both for right-handed electron beam $\sigma_R(\tilde{\chi}^\pm)$ and left-handed beam $\sigma_L(\tilde{\chi}^\pm)$. Combining $m_{\rm LSP}$, $m_{\tilde{\chi}^\pm}$, and $\sigma_R(\tilde{\chi}^\pm)$, it is possible to fix all the three parameters of the neutralino-chargino sector ($M_2$, $\mu$, $\tan\beta$), assuming the GUT-condition $M_1/M_2 = \alpha_1/\alpha_2$, if the gaugino-higgsino mixing is large (*i.e.*, $M_2 \simeq \mu$). In this case, the mass of the heavier chargino can be predicted, and should lie near above the lighter one. Its discovery at the predicted mass will confirm the GUT-condition here assumed. In our example case of $M_2 < \mu$, the lighter chargino is almost a

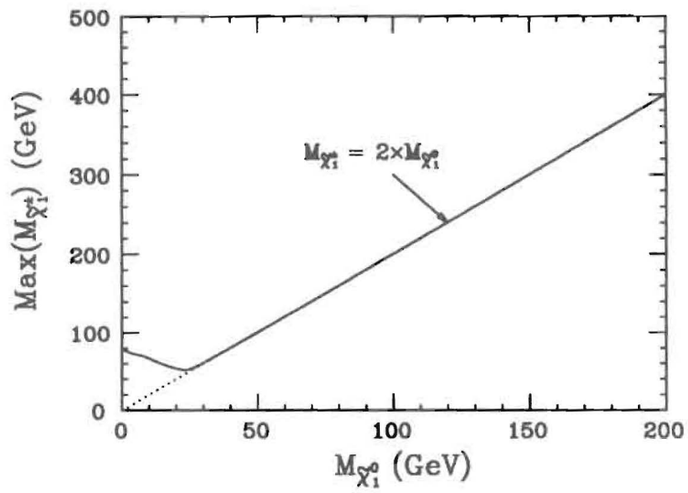


Figure 2.40: The upper limit on the lighter chargino mass as a function of the LSP mass.

pure charged wino. Then it is not easy to fix $\mu$ and $\tan\beta$. However even in this case, we can test the GUT-condition. The bino mass $M_1$ is roughly $m_{\rm LSP}$, and the wino mass $M_2$ is roughly the chargino mass $m_{\tilde{\chi}^\pm}$. Fig. 2.41 shows the $\Delta\chi^2 = 1$ contour in the ($M_1$, $M_2$) plane, which clearly demonstrates the possibility of a precision test of the SUSY-GUT assumption.

There is another information we can obtain from the study of the lighter chargino. The cross section from the left-handed electron beam $\sigma_L(\tilde{\chi}^\pm)$ carries the contribution from the $t$-channel sneutrino ($\tilde{\nu}_L$) exchange. The dependence of $\sigma_L$ on $m_{\tilde{\nu}_L}$ is shown in Fig. 2.42.

Note that $m_{\tilde{\nu}_L}$ is related to the mass of the left-handed charged slepton $m_{\tilde{l}_L}$ in a model-independent way,

$$m^2_{\tilde{\nu}_L} \leq m^2_{\tilde{l}_L} = m^2_{\tilde{\nu}_L} + (1-\sin^2\theta_W)m_Z^2|\cos(2\beta)| \leq m^2_{\tilde{\nu}_L} + (1-\sin^2\theta_W)m_Z^2, \qquad (2.3)$$

for $\tan\beta \geq 1$. This observation will fix the next c.m. energy to go.

The left-handed charged slepton will be searched first in the process $e^-_R e^+ \to \tilde{e}^-_R \tilde{e}^+_L$, from the $t$-channel bino-exchange. The discovery of the left-handed selectron at the predicted mass confirms the SUSY-nature of the sleptons. If lucky, it is even possible to determine $\tan\beta$ from the above formula. The important implication of the measured $m_{\tilde{l}_L}$ is that we can check the universal scalar mass hypothesis in the hidden-sector scenario of the SUSY-breaking. The SUSY-GUT alone predicts

$$m^2_{\tilde{l}_L} = m_5^2 - \left(\frac{3}{2}(\alpha_2^2-\alpha_0^2) + \frac{1}{22}(\alpha_1^2-\alpha_0^2)\right)\frac{M_2^2}{\alpha_2^2} - \frac{1}{2}m_Z^2\cos 2\beta(1-2\sin^2\theta_W), \qquad (2.4)$$

$$m^2_{\tilde{\nu}_L} = m_5^2 - \left(\frac{3}{2}(\alpha_2^2-\alpha_0^2) + \frac{1}{22}(\alpha_1^2-\alpha_0^2)\right)\frac{M_2^2}{\alpha_2^2} - \frac{1}{2}m_Z^2\cos 2\beta, \qquad (2.5)$$

$$m^2_{\tilde{l}_R} = m_{10}^2 - \frac{2}{11}(\alpha_1^2-\alpha_0^2)\frac{M_2^2}{\alpha_2^2} - m_Z^2\cos 2\beta\sin^2\theta_W, \qquad (2.6)$$

where $m_5$ and $m_{10}$ are masses common for the **5**- and **10**-dimensional representations. The universal scalar hypothesis suggests $m_5 \simeq m_{10}$. Then the difference between left-handed and

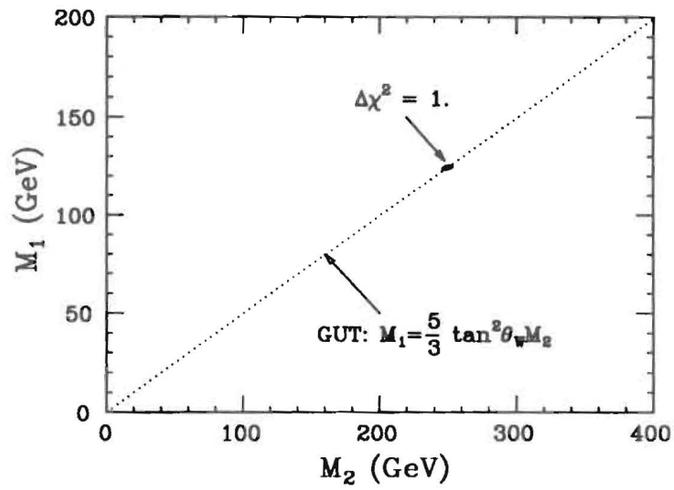


Figure 2.41: The expected $\Delta\chi^2 = 1$ contour in the $M_2$-$M_1$ plane. The dotted line shows the expectation from the SUSY-GUT condition.

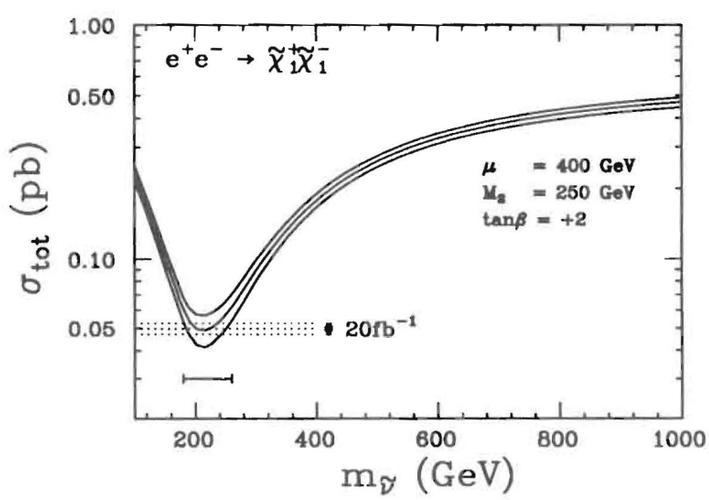


Figure 2.42: The lighter chargino pair production cross section as a function of the sneutrino mass. The three curves represent the ambiguity (1-$\sigma$) from the chargino mass determination.

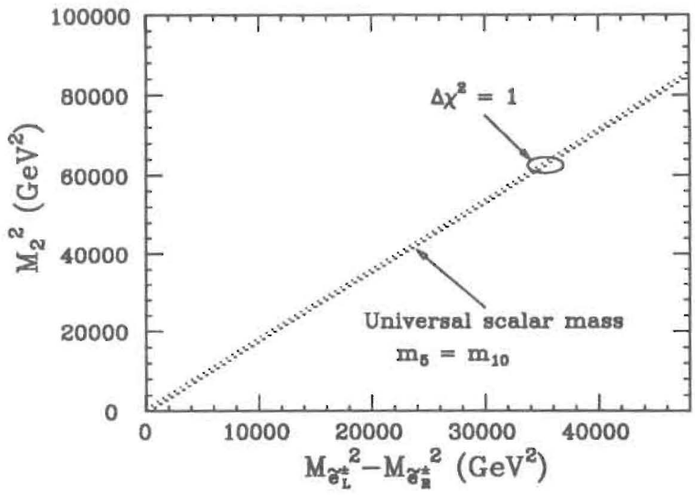


Figure 2.43: The expected $\Delta\chi^2 = 1$ contour in the plane of the squared mass difference of the left-handed and right-handed selectrons versus $M_2^2$. The doted lines represent the universal scalar mass hypothesis for $\tan\beta = 0, +2, +30$.

right-handed charged slepton masses is determined solely by the gaugino mass

$$m_{\tilde{l}_L}^2 - m_{\tilde{l}_R}^2 \simeq \left(\frac{3}{2}(\alpha_0^2 - \alpha_2^2) - \frac{5}{22}(\alpha_0^2 - \alpha_1^2)\right)\frac{M_2^2}{\alpha_2^2}. \tag{2.7}$$

The expected $\Delta\chi^2 = 1$ contour in the plane $m_{\tilde{l}_L}^2 - m_{\tilde{l}_R}^2$ versus $M_2^2$ is shown in Fig. 2.43, with the prediction of the universal scalar mass hypothesis. Thus the measurement of $m_{\tilde{l}_L}$ will put a strong constraint on the supergravity model building.

Finally, the discovery of other left-handed charged sleptons $\tilde{\mu}_L$ and $\tilde{\tau}_L$ will again put constraints on the hidden-sector scenario of SUSY-breaking which predicts the mass degeneracy among generations. Furthermore, the $t$-channel neutral wino ($\tilde{W}^0$) exchange diagram exists for the $\tilde{e}_L$-pair production from the left-handed electron beam, which serves as a cross-check of the measured SUSY parameters.

Though we have concentrated on the case where the right-handed charged slepton is the first to be discovered at JLC-I, the strategy is similar to the case where the lighter chargino is the first. The study of the chargino will determine the three parameters of the neutrino-chargino sector, and also the sneutrino mass can be measured from $\sigma_L(\tilde{\chi}^\pm)$. Then we obtain upperbound on $m_{\tilde{l}_L}$, and the same analysis as above can be carried out.

## 2.6 Top

Since we all know that top must exist and is no heavier than 200 GeV, top physics is guaranteed for JLC-I[46]. The top quark we are going to deal with has many unique features, compared to quarks of other flavors. This is primarily due to its large mass and width. We will examine below some of the new features, which will manifest themselves in the course of detailed top studies.

### 2.6.1 Measurements of Top Mass and $\alpha_s(M_Z)$

Here, we will start with the measurement of the top mass. There are two ways to determine the top mass: the first by threshold scan and the other by the invariant mass measurement of the 3-jet system from top decays.

Threshold Scan

For the threshold scan, there is one very important difference from the charm and bottom cases: a heavy top quark has a large width dominated by $t \to bW^+$ decays. The large width allows a $t\bar{t}$ system to form only a limited number of onium states. At first glance, this seems rather disappointing but, to the contrary, turns out to be advantageous in many ways. First remember that the continuation of multiple resonances to the continuum region has always been a troublesome process in the traditional onium spectroscopy, since the intermediate region suffers from nonperturbative and, therefore, uncontrollable theoretical ambiguities. These ambiguities are absent from the $t\bar{t}$ system because the large width acts like an infrared cutoff and prevents the non-perturbative part of the potential from affecting the threshold calculation. This implies that the cross section in the whole threshold region can be calculated from first principles( QCD ). Experimentally, this new feature benefits us significantly in determinations of parameters that enter the threshold cross section:

$$\sigma(\sqrt{s}; m_t, \Gamma_t, \alpha_s(M_Z), M_H, \beta_H).$$

The identification of $t\bar{t}$ events is straightforward and we can easily get an overall detection efficiency in excess of 25 % with a signal to background ratio greater than 10. Fig. 2.44-a) is an example of a threshold scan, selecting $t\bar{t}$ events in the 6-jet final states, where we have assumed 11 points with 1 fb$^{-1}$ each. The Monte Carlo data were generated with $\alpha_s(M_Z) = 0.12$ and $m_t = 150$ GeV without the contribution from Higgs exchange. When we fit these data points to the cross section formula, letting $\alpha_s(M_Z)$ and $m_t$ move freely, we obtain the contours shown in Fig. 2.44-b). Even if $\alpha_s(M_Z)$ is totally unconstrained, we can determine $m_t$ with a precision $\Delta m_t \simeq 0.2$ GeV.

3-Jet Invariant Mass

On the other hand, we can also determine $m_t$ directly from the 3-jet invariant mass. Fig. 2.45[47] plots the invariant mass for a 3-jet system which consists of a jet pair corresponding to a $W$ boson candidate and a $b$-jet candidate chosen from the remaining two jets. We can see a clear top quark peak over a broad background coming from wrong combinations. The width of the peak is dominated by detector resolutions. An integrated luminosity of 10 fb$^{-1}$ at $\sqrt{s} = 500$ GeV enables us to achieve a statistical error $\Delta m_t \simeq 0.1$ GeV. When the measurement reaches this precision, we must take a proper account of various systematic errors. It should be noted that the theoretical ambiguities due to nonperturbative QCD effects might be minimal again because of the large top width acting as an infrared cutoff. Assuming that this is actually the case and that the systematic errors in calorimetry can be well controlled, we can input this $m_t$ information to the threshold scan. This may allow us to make a reliable measurement of $\alpha_s(M_Z)$ which is largely free from theoretical ambiguities due to nonperturbative QCD, unlike those from jet shape variables.

The importance of this $\alpha_s(M_Z)$ measurement is enhanced in the SUSY scenario, since, there, the $\alpha_s(M_Z)$ is the key link between the weak scale and the GUT scale. In this case, the significance of the precision $m_t$ measurements cannot be underestimated, since the top mass, which determines the top Yukawa coupling, is an indispensable input parameter for the calculations of masses and widths of Higgses and SUSY particles.

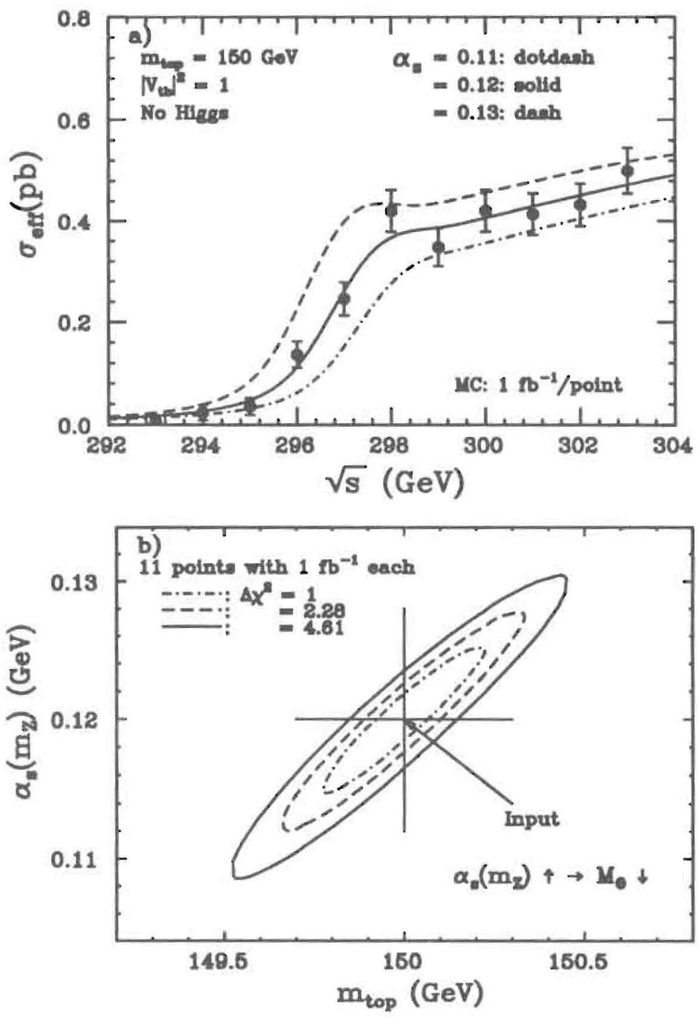


Figure 2.44: (a) An example of energy scan to determine $m_t$ and $\alpha_s(M_Z)$ where each point corresponds to 1 fb$^{-1}$. (b) The contour resulting from the fit to the data points.

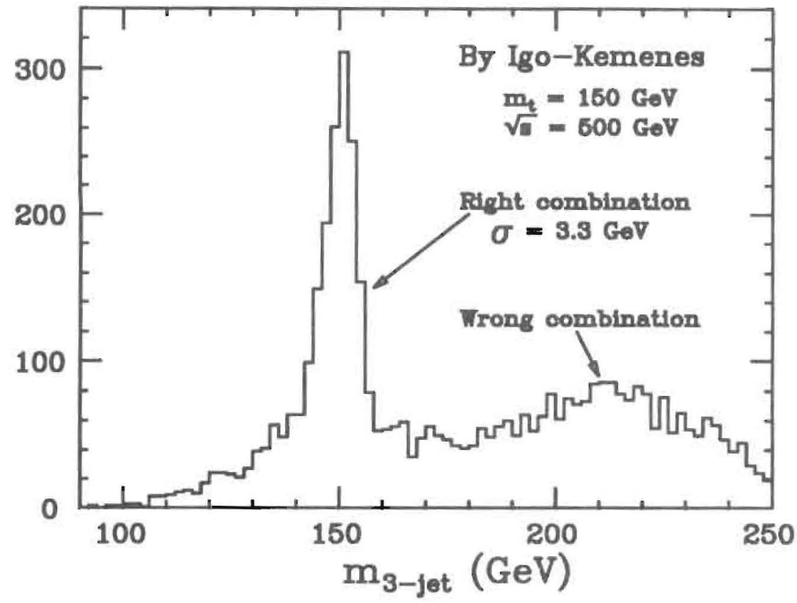


Figure 2.45: Invariant mass distribution for the 3-jet system resulting from $t \to bW$ decays.

### 2.6.2 Measurement of Top Width

The threshold scan also allows us to measure the top width. Fig. 2.46-a) compares the same Monte Carlo data as used for Fig. 2.44-a) with theoretical expectations for various onium widths. Fig. 2.46-b) shows the contours obtained from the fit to the Monte Carlo data, letting the top width and the top mass move freely. The expected statistical error is $\Delta|V_{tb}|^2 = 0.15 \sim 0.20$. We can improve this by optimizing the energy points and, of course, by increasing statistics. $|V_{tb}|^2 < 1$ suggests a fourth generation, while $|V_{tb}|^2 > 1$ signals some exotic decay mode such as $t \to bH^+$ or $t \to \tilde{t}\tilde{\chi}_1^0$.

### 2.6.3 Measurement of Top Yukawa Coupling

The heaviness of the top quark, on the other hand, allows us to directly measure the top Yukawa coupling. One way to do this is to examine closely the threshold shape. Notice that, if it were not for the large top width, the reliable estimation of the QCD contribution would become impossible and would make hopeless the extraction of the effect of Higgs exchange. Figs. 2.47-a) and -b) compare the same Monte Carlo data shown in Fig. 2.44-a) with theoretical expectations for various $M_H$ and $\beta_H$( the normalized top Yukawa coupling ). A 2-parameter fit to the data yields the contours shown in Fig. 2.47-c). The expected precision for a standard model Higgs of $M_H = 100$ GeV is about $\Delta\beta_H = 0.2$ for $m_t = 150$ GeV. We can also measure the Yukawa coupling using the process $e^+e^- \to t\bar{t}H$. The precision expected in this case is comparable to that from the threshold scan.

### 2.6.4 Angular Analyses

There is yet another new and remarkable property of a heavy top quark: the heavy top will decay before forming a top-hadron. This will, for the first time, enable us to measure the helicities

of parent quarks via angular analyses of their decay daughters. The helicity measurement will provide us with a powerful tool to systematically investigate the top quark's production and decay vertices, in particular, when the vertices involve new particles expected in the SUSY scenario.

As a warmup exercise, let us first try to determine the polarization of $W$'s from top decays. Heavy top quarks predominantly decay into longitudinal $W$ bosons which are a good probe to investigate the symmetry breaking sector. Therefore, if the symmetry breaking sector is different from that of the standard model, the branching fraction

$$R = \frac{\Gamma(t \to bW_L)}{\Gamma(t \to bW_T) + \Gamma(t \to bW_L)}$$

might also differ from the standard model prediction. Fig. 2.48-a) is an example of the helicity angle distribution for jets from $W$ decays. The Monte Carlo events, which were generated with the standard model coupling, agree well with the standard model prediction. A fit to the helicity angle distribution results in the 1-$\sigma$ bounds shown in Fig. 2.48-b) as a function of $m_t$. Given a data sample of 1k top events, it is easy to determine the branching fraction $R$ with a statistical error of less than 2 %.

To see the capability of the top helicity determination, we consider here an imaginary case, in which the $tbW$ vertex is right-handed, and compare the resultant angular distribution with that of the left-handed( the standard model ) case in Fig. 2.49[48]. The Monte Carlo data correspond to 10 fb$^{-1}$ with an electron beam polarization of 80 %. The difference is clear.

## 2.7 Precision Electroweak Physics

So far, we have been assuming the existence of a light Higgs boson. In this section, we will turn our attention to the case in which no light Higgs bosons have been found. As we stressed earlier, the absence of light Higgs bosons itself will make a very strong impact on high energy physics, since it implies the death of low energy supersymmetry and GUT.

In the absence of the light Higgs boson, we have to learn as much as possible from what we have at hand, $W$, $Z$, and top. The important lesson at LEP is that precision measurements can provide valuable information to guide us in deciding our next step. This virtue of $e^+e^-$ colliders will persist as we will see below.

### 2.7.1 Looking for New Physics in Loops

In the standard model, the Higgs mass, the $W$ mass, and the top mass are interrelated through radiative corrections as shown in Fig. 2.50[49]. Therefore, we can estimate the Higgs mass by measuring the masses of $W$ and top. For a precise determination of the $W$ mass, we go down to the $Z$-pole and measure the polarization asymmetry for lepton pair productions, taking advantage of a highly polarized electron beam ( $P_e > 90$ % ) which is available only at linear colliders. The polarization asymmetry is directly related to $\sin^2\theta_W$ which, in turn, determines $M_W$. Given the design luminosity of JLC-I, the error on $\sin^2\theta_W$ will be dominated by the error on the beam polarization( see Fig. 2.51). If we can control this error down to the one percent level, the error on $\sin^2\theta_W$ will be about 0.1 %. Including theoretical ambiguities due to light quark loop corrections, we expect $\Delta M_W = 21$ MeV. The measurements of $M_W$ and $m_t$ determine the allowed range of the Higgs mass through the relation shown in Fig. 2.50. Plotted

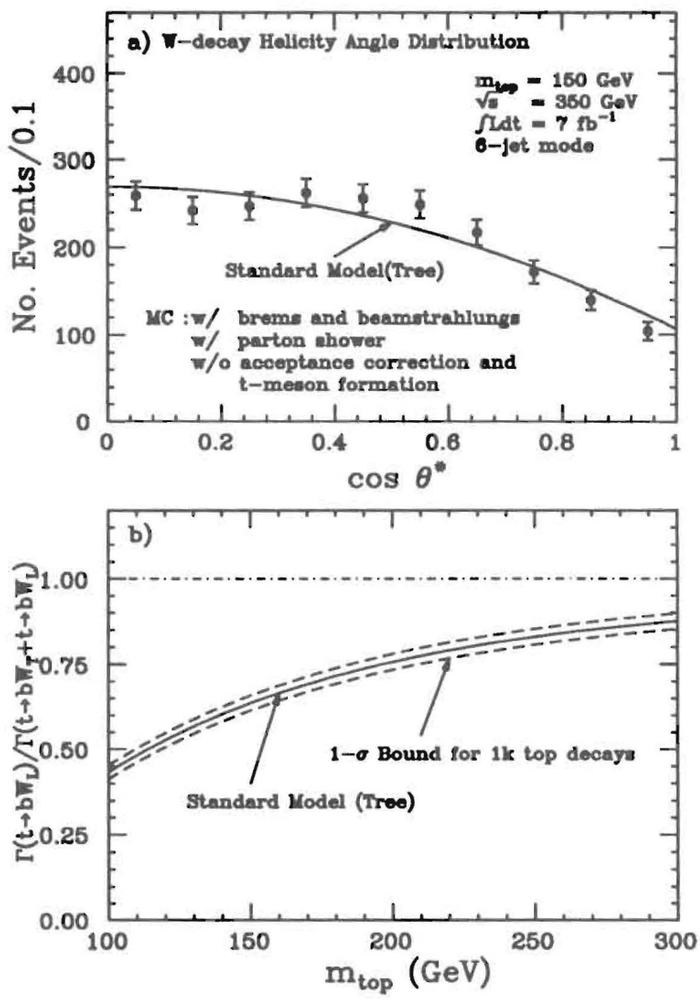


Figure 2.48: (a) Helicity angle of $q$ or $\bar{q}$ from $W$ decay. (b) Branching fraction of the $t \to bW_L$ decay as a function of $m_t$. The dashed curves indicate 1-$\sigma$ boundaries expected for 1k top decays.

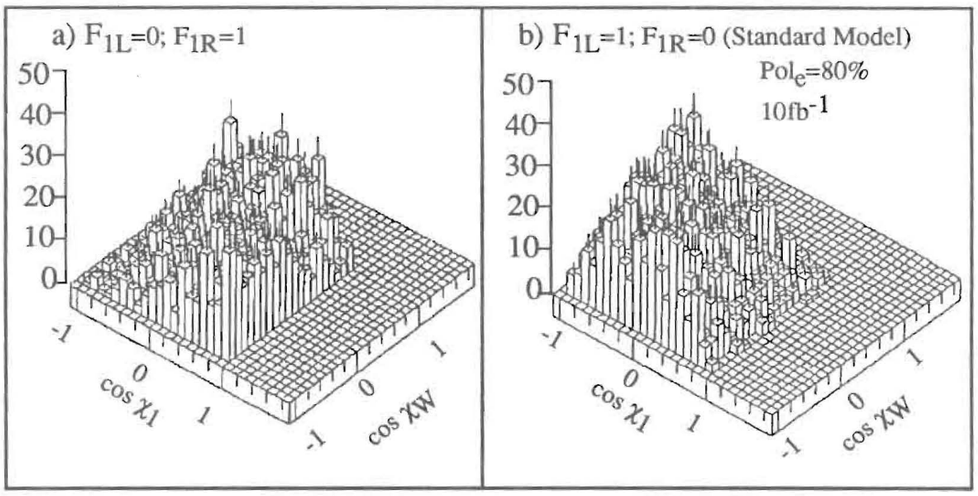


Figure 2.49: The top decay angle distributions for (a) $F_{1L} = 0$ and $F_{1R} = 1$ and (b) $F_{1L} = 1$ and $F_{1R} = 0$( Standard Model ). $\chi_W$ is the helicity angle of $W$ in the $t$ rest frame and $\chi_l$ is the helicity angle of the lepton in the $W$ rest frame.

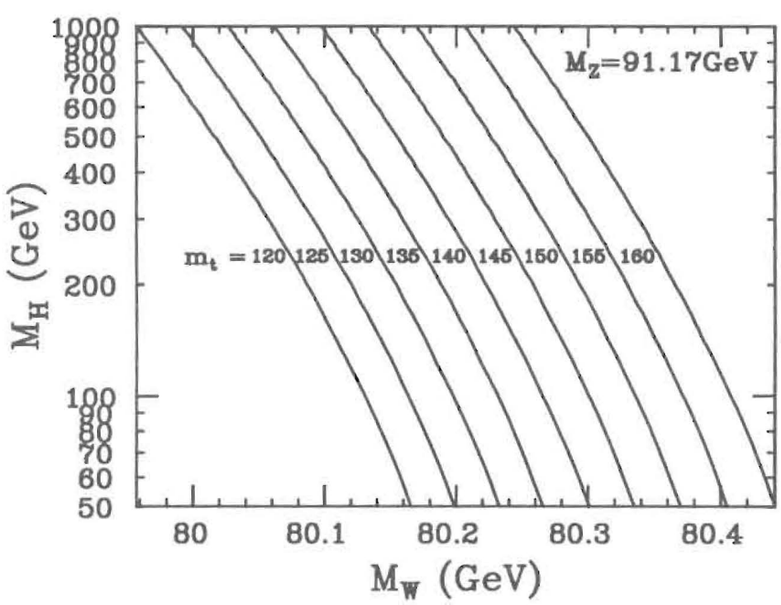


Figure 2.50: The mass of the standard model Higgs as a function of the $W$ mass for various top masses.

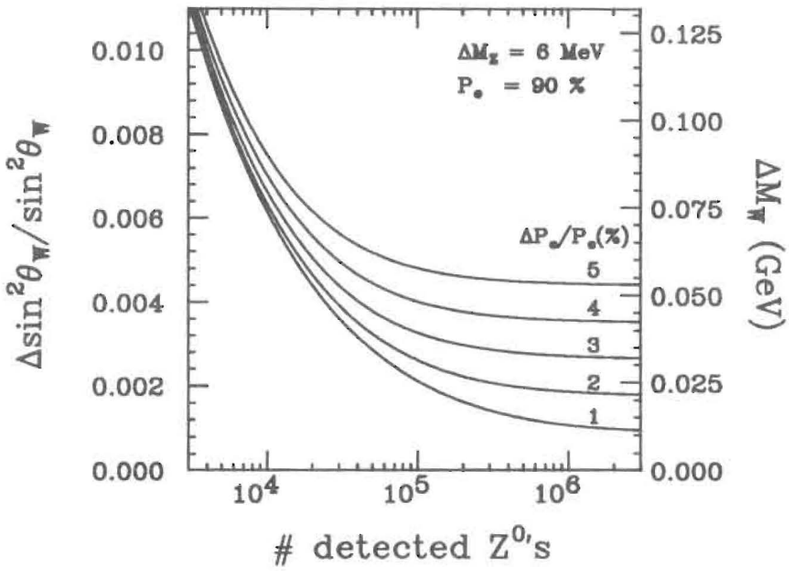


Figure 2.51: The expected error on $\sin^2\theta_W$ from the measurement of the electron beam polarization asymmetry as a function of the number of detected lepton pairs. Different curves correspond to different errors on the beam polarization.

in Fig. 2.52 are 1-$\sigma$ contours in the $m_t$-$M_H$ plane corresponding to different measurement errors on $m_t$: $\Delta m_t = 0.5$, 5.0, and 10.0 GeV, for $M_H = 500$ GeV and $m_t = 150$ GeV. This figure clearly demonstrates the importance of a precise determination of the top mass. As demonstrated in the last section, we can determine the top mass with a precision better than 0.5 GeV, which means the Higgs mass bound will be essentially controlled by the error on the $W$ mass. Fig. 2.53 indicates the 1-$\sigma$ bound for the Higgs mass as a function of the input Higgs mass. We can see that the JLC experiments will be able to significantly improve the present bound on the Higgs mass and will show us the next step to take.

The analysis presented above is based on the standard model framework. We can generalize the analysis with the help of the $S$ and $T$ parameters, which have been introduced by Peskin and Takeuchi[51] to parametrize loop contributions from new high-mass-scale physics. $S$ and $T$ represent, respectively, the effects of isospin-conserving and isospin-breaking loop contributions to weak boson self-energies. The power of the precision measurements at JLC-I can be best demonstrated in the $S$-$T$ plane as shown in Fig. 2.54. The dotted line is the current limit[51] obtained from the precision electroweak data at LEP and other low energy data including those from deep-inelastic scattering and atomic parity violation experiments. The limit will be improved to the dot-dashed line, when the $M_W$ measurement at LEP-II with $\Delta M_W = 100$ MeV becomes available. The three solid lines correspond to the JLC-I limits when $\Delta M_W = 21, 50$, and 100 MeV, respectively. Notice that the JLC-I limits are estimated by assuming center values at $S = T = 0$ and a 0.1 % measurement of $\sin^2\theta_W$ and a 0.14 % measurement of $R_Z$ which is the ratio of the hadronic and the leptonic widths of the $Z$ boson. It should be emphasized that the JLC-I limits are *free* from hadronic and atomic uncertainties inherent in the present-day low energy data. When compared with the predictions of technicolor models indicated by arrows in the figure, one can see that the JLC-I limits severly constrain the possible scenarios.

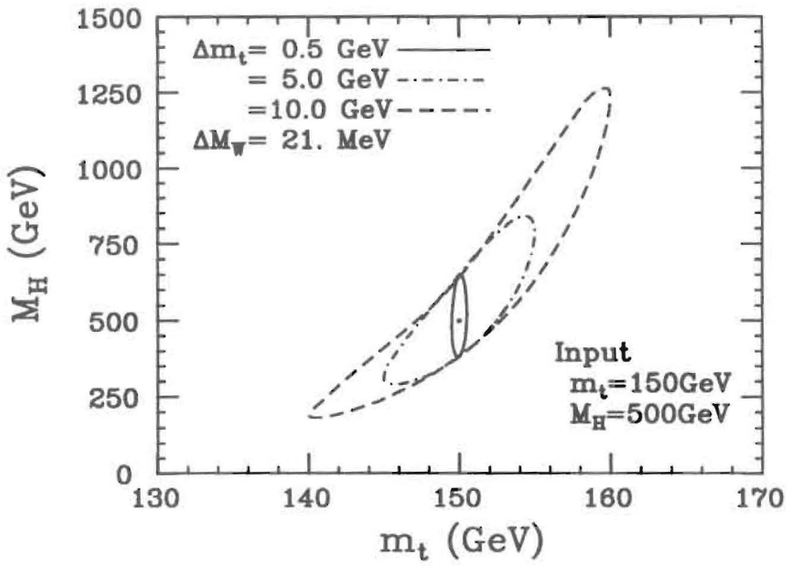


Figure 2.52: The 1-$\sigma$ contours in the $m_t$-$M_H$ plane showing how the Higgs mass bound improves with the error on $m_t$. The input values are $m_t = 150$ GeV and $M_H = 500$ GeV.

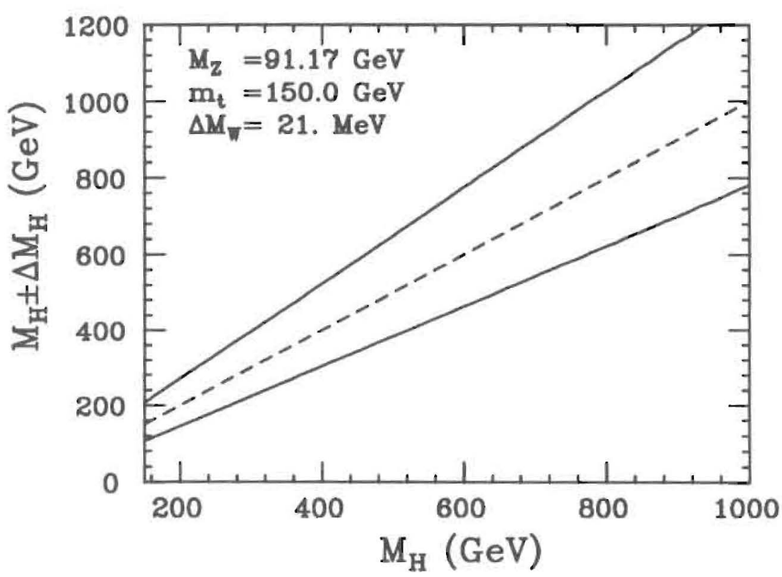


Figure 2.53: The 1-$\sigma$ bounds on the Higgs mass as a function of the input Higgs mass.

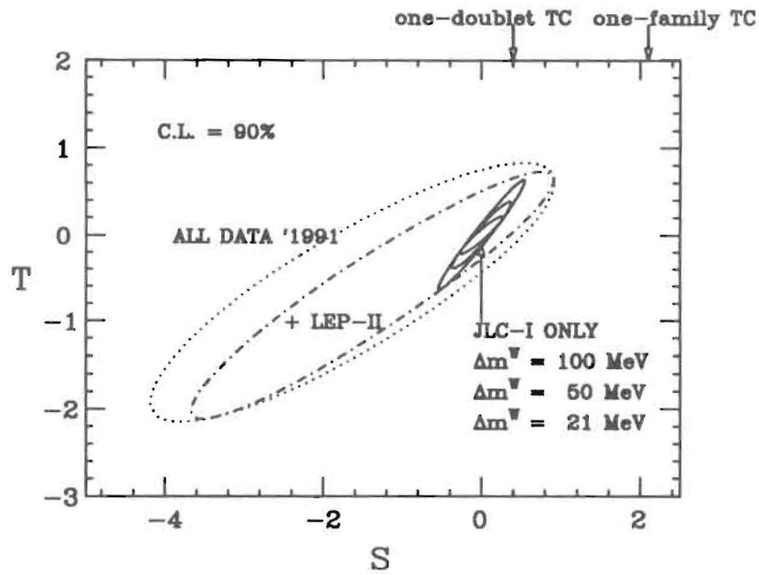


Figure 2.54: The 90 % confidence level limits on the $S$ and $T$ parameters. The dotted line is the present limit obtained from all the available data as of 1991[51]. The dot-dashed line is the expected limit after the precision $M_W$ measurement at LEP-II: $\Delta M_W = 100$ MeV. The three solid lines are the limits expected for JLC-I data alone with $\Delta M_W = 21, 50$, and 100 MeV, respectively.

### 2.7.2 Self-couplings of $W$, $Z$, and $\gamma$

If the expected mass of the Higgs boson enters the heavy Higgs regime, the most likely scenarios will then become those based on a strongly interacting Higgs sector. In this case, one of the most important questions to address is whether only the longitudinal components of $W$ and $Z$ are composite or both of their transverse and longitudinal components are composite. In order to answer this question, we need to scrutinize the self-interactions of the vector bosons: $W$, $Z$, and $\gamma$. Though the possible forms of the self-interactions are rescricted, to some extent, by the data available at present[52, 53], the study of the direct productions of the weak bosons is inevitable to reveal the possible non-gauge nature of the weak bosons.

The total cross sections of the processes involving the weak bosons in the JLC energy region are shown in Fig. 2.55, together with the other standard model processes. In the JLC energy region, the weak boson production processes occupy the major part of the $e^+e^-$ annihilation cross section. This is in contrast with the lower energy region such as of TRISTAN and LEP-I, where the dominant annihilation processes are fermion-pair productions. The processes, $e^+e^- \to W^+W^-$, $e^\pm\nu W^\mp$, and $\nu\bar{\nu}Z$ include the three-vector-boson coupling, while the processes such as $e^+e^- \to W^+W^-Z$ and $\nu\bar{\nu}W^+W^-$ include both the three- and the four-vector-boson couplings. Therefore the study of these processes allows us to test various aspects of the self-interactions among the vector bosons[54]. Such a study is discussed below, taking the anomalous three-vector-boson coupling as an example.

If there were anomalous pieces in three-vector-boson couplings, CP-conserving terms for

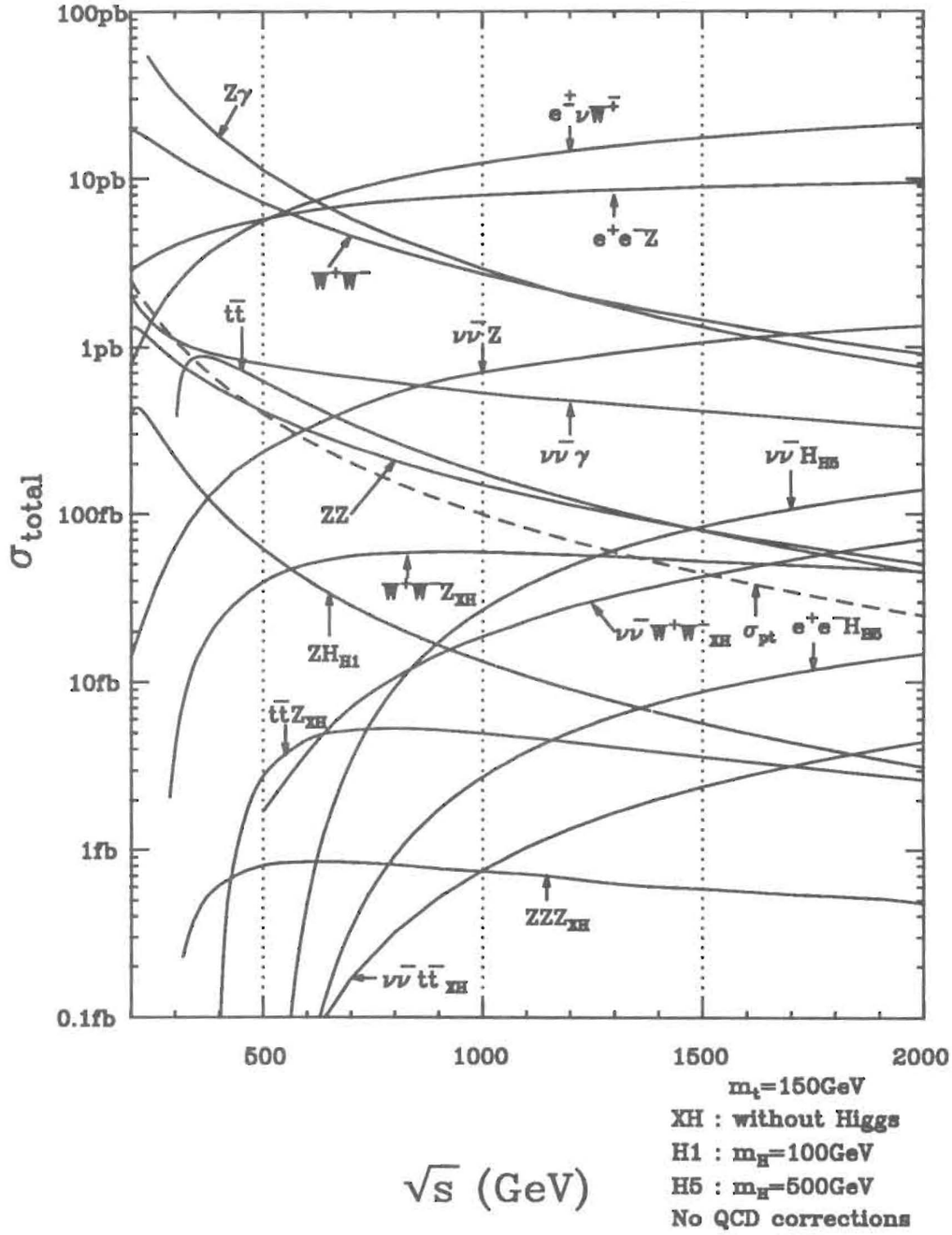


Figure 2.55: The total cross sections of the standard model processes in the JLC energy region. We require $E_\gamma > 0.1 \times E_{beam}$ and $|\cos\theta_\gamma| < 0.85$ for the $\nu\bar{\nu}\gamma$ process.

them can be parametrized as

$$\Delta L_{WWV} \sim \Delta\kappa_V W_\mu^\dagger W_\nu V^{\mu\nu} + \frac{\lambda_V}{M_W^2} W_{\rho\mu}^\dagger W_\nu^\mu V^{\nu\rho}$$

where

$$F^{\mu\nu} \equiv \partial^\mu F^\nu - \partial^\nu F^\mu \quad (F = W/V)$$

and $V$ stands for either $\gamma$ or $Z$. At JLC-I, we can study the $WW\gamma$ couplings, using the following three processes: $e^+e^- \to W^+W^-$, $e^\pm\nu W^\mp$, and $\nu\bar{\nu}\gamma$. The $e^\pm\nu W^\mp$ and $\nu\bar{\nu}\gamma$ processes are sensitive only to the $WW\gamma$ couplings; the $e^\pm\nu W^\mp$ process contains the $WWZ$ couplings, however, its contribution to the total cross section is negligible. On the other hand, the $W^+W^-$ process is sensitive to both the $WW\gamma$ and the $WWZ$ couplings.

Fig. 2.56 compares the expected limits on the anomalous $WW\gamma$ couplings obtained from these processes for an integrated luminosity of 30 fb$^{-1}$ and a beam polarization of 80 %, when the self-couplings are those of the standard model. As seen in the figure, the most sensitive is

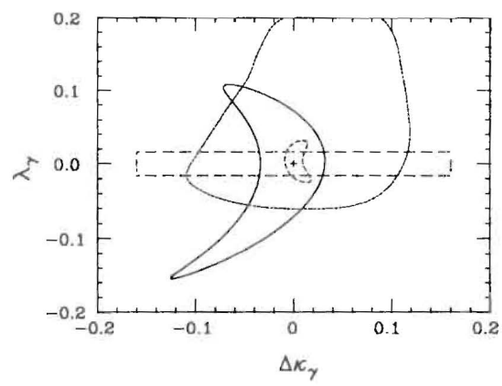


Figure 2.56: The expected 90% confidence level contours representing the sensitivities to the anomalous couplings in the plane of $\Delta\kappa_\gamma$ and $\lambda_\gamma$, when an integrated luminosity of 30 fb$^{-1}$ is accumulated at $\sqrt{s} = 500$ GeV with a beam polarization of 80 %. The solid, dashed, and dotted curves are the limits obtained from the processes, $e^+e^- \to e^\pm\nu W^\mp$, $W^+W^-$, and $\nu\bar{\nu}\gamma$, respectively. The dot-dashed curve is that expected at SSC[55]. The vertical cross symbol indicates the input values corresponding to the standard model.

the process $e^+e^- \to W^+W^-$, because of the severe gauge cancellation among the diagrams.

Though this process contains both the $WW\gamma$ and the $WWZ$ vertices, the measurements of the full differential cross section including the $W$-decay angular distributions, as well as the beam polarization dependence, help us disentangle possible anomalous self-couplings. Figs. 2.57-a) to -d) show the expected limits on various combinations of anomalous couplings for an integrated luminosity of 30 fb$^{-1}$ at $\sqrt{s} = 500$ GeV[50], when we fit the differential cross section of the $e^+e^- \to W^+W^-$ process for the Monte Carlo data generated with the standard model couplings ($\Delta\kappa = \lambda = 0$). In the figures, the solid and the dashed lines are those obtained with and without the beam polarization asymmetry, respectively, and the dot-dashed lines are the limits expected from SSC. Notice that the polarized electron beam plays a crucial role here. It should also be emphasized that JLC experiments are indispensable to constrain $\Delta\kappa$, though SSC can set similarly stringent limits on the $\lambda$ couplings.

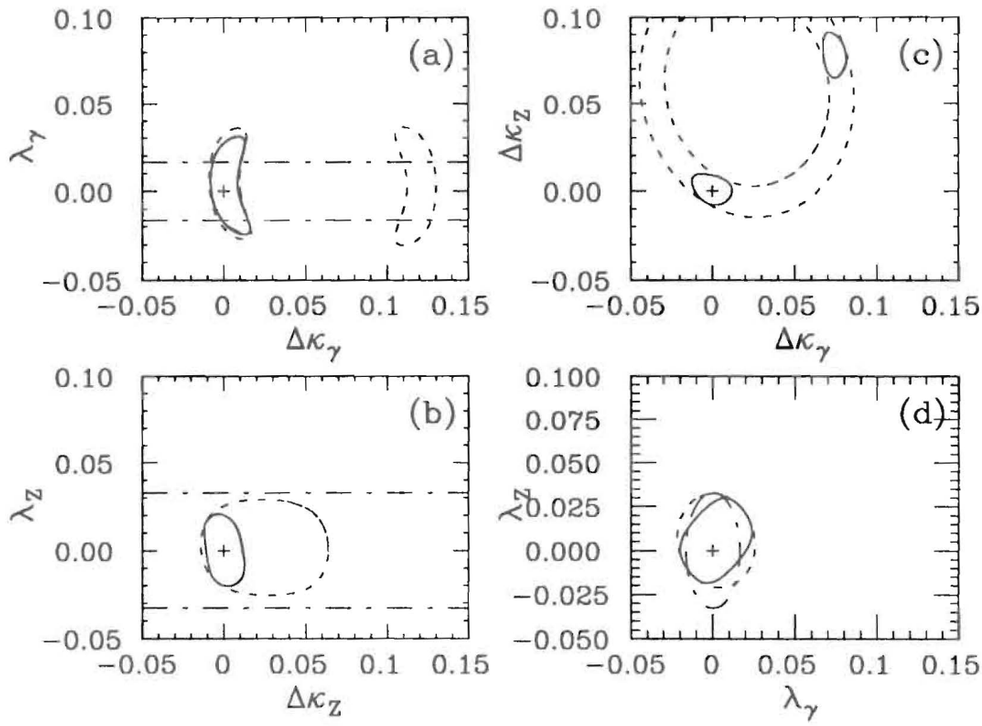


Figure 2.57: The expected 90 % confidence level limits on pairs of anomalous self-couplings for an integrated luminosity of 30 fb$^{-1}$ at $\sqrt{s} = 500$ GeV. (a) $\Delta\kappa_\gamma$ and $\lambda_\gamma$. (b) $\Delta\kappa_Z$ and $\lambda_Z$. (c) $\Delta\kappa_\gamma$ and $\Delta\kappa_Z$. (d) $\lambda_\gamma$ and $\lambda_Z$. The vertical cross symbols indicate the standard model positions used as inputs. Solid and dashed lines are with and without using 80 %-polarized electron beam. Dot-dashed lines correspond to expected SSC limits.

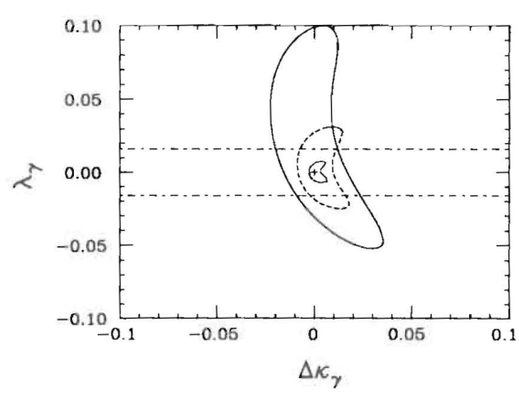


Figure 2.58: Same as Fig. 2.56-a) but at three different energies, $\sqrt{s} = 300$ GeV (solid), 500 GeV (dashed), and 1000 GeV (dotted). Also shown is that expected for SSC (dot-dashed).

The higher the energy, the severer the gauge cancellation becomes. Therefore, we expect that the sensitivity to the anomalous couplings is enhanced at higher energies. Fig. 2.58 shows, for three different energies, the expected sensitivity of the $e^+e^- \rightarrow W^+W^-$ process to the anomalous $WW\gamma$ couplings. The advantage of the higher energy is clear. Since this energy dependence and the higher luminosity more than compensate the cross section drop, the expected JLC limits exceed the precision obtainable at LEP-II by more than one order of magnitude and reach the expected size of loop-corrections. The existence of a light Higgs boson will not, therefore, diminish the importance of the precision measurement of this process, since, then, it will open up the possibility to get insights into physics at higher energy scales through radiative corrections.

## 2.8 CP Violation on the $Z$ Pole

In the standard model, CP violation and flavor mixing have the same origin, the Yukawa sector governing the Yukawa interactions of fermions with the Higgs boson. When the Higgs field acquires a vacuum expectation value (the electroweak symmetry breaking), the Yukawa interactions give rise to the flavor-mixing represented by the Kobayashi-Masukawa matrix. Since this mixing matrix has a physical phase, meaning that at least one of its components is complex, CP violation naturally results. The underlying principle to determine the Yukawa couplings is, however, completely unknown. The relevant physics is presumably at very high energies, of the GUT scale or even of the Planck scale. Moreover, there are many ways to violate CP, for instance, a model with two Higgs doublets implies, in general, CP violation in its Higgs sector. The studies of CP violation and mixing are, therefore, not only essential to test the standard model, but also very important to probe the underlying physics at very high energies. In order to sort out many possible mechanisms for CP violation, however, we definitely need information on the physics beyond the standard model. We believe that, when SUSY particles are found and studied in detail at JLC-I, the range of the possibilities will be narrowed and the importance of the studies on CP violation and flavor mixing will be greately enhanced.

In this section, two topics of $B$-physics, CP-violation of $B_d$ meson in $B_d \rightarrow \Psi K_s$ decay and $B_s$-$\bar{B}_s$ mixing, are discussed. There are four advantages to investigating $B$-physics on the $Z$-pole with JLC-I: (1) high luminosity, $L > 1.0 \times 10^{33}\ \mathrm{cm}^{-2}s^{-1}$, which is 50 times larger than that of LEP-I, (2) a highly polarized electron beam, which enables the tagging of $b$ and $\bar{b}$ quarks in a geometrical way, (3) a large production cross section of $B$ mesons, which is 5 times larger than that on $\Upsilon(4S)$, and (4) the narrow beam, which allows us to install a vertex detector very close to the interaction point to detect the $B$-decay vertices. The background due to beamstrahlung will be manageable on the $Z$-pole.

### 2.8.1 Compatibility with TeV Operation

The possibility to investigate $B$ physics on the $Z$-pole with a linear collider was discussed at Snowmass '88[56] in comparison with other accelerators. It should be emphasized, however, that the design concept of the linear collider discussed there was quite different from that of JLC-I. At that time, there was a general belief that high repetition rate ($\geq$ kHz) would be necessary on the $Z$-pole to get high luminosity with a linear collider, so that it would be incompatible with a TeV linear collider design assuming a rather low repetition rate (about 200 Hz). A

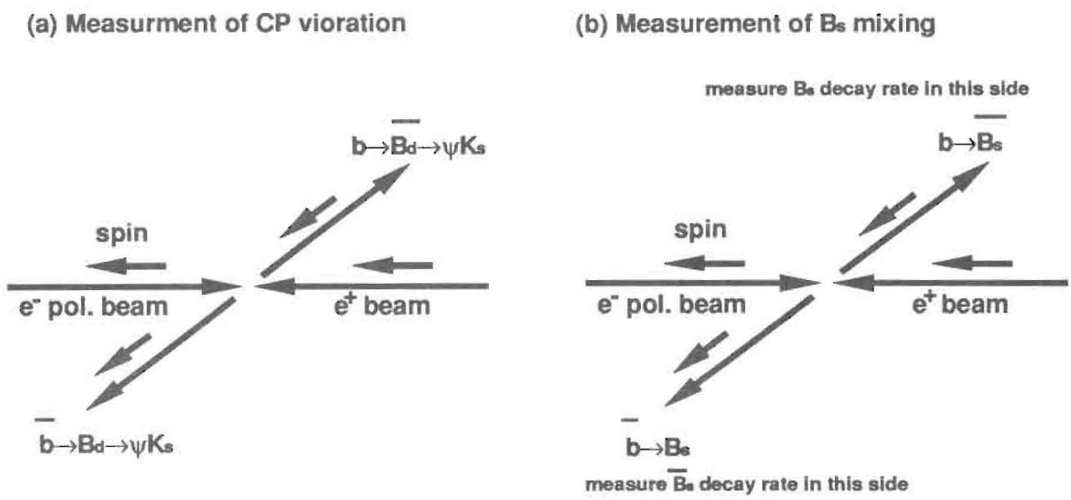


Figure 2.59: Schematical figures of relation between electron spin and b-quark spin in favoring condition. (a) is for CP violation measurement and (b) is for $B_s$ mixing.

recent study at KEK[57], however, shows that a linear collider optimized for TeV operation can also serve a high-enough luminosity on the $Z$-pole, $L = 2.0 \times 10^{33}$ cm$^{-2}s^{-1}$, without crab-crossing, provided that its final focus system is properly modified. JLC-I is, therefore, capable of producing fruitful results not only in the TeV region but also on the $Z$-pole.

### 2.8.2 Forward-Backward Asymmetry

A large forward-backward asymmetry caused by the polarization of an electron beam plays an essential role (geometrical tagging) in the measurements of both CP violation and $B_s$-$\bar{B}_s$ mixing[58]. When the electron beam is polarized left handed, a $b$-quark ($\bar{B}$ meson) prefers to go in the forward direction (direction of the electron beam) as shown schematically in Figs.2.59-a) and -b). When we use a 95%-polarized beam[59] and detect the events in the polar angle region of $0.22 < |\cos\theta| < 0.94$, the forward-backward (F-B) asymmetry is 76% and the wrong-tag fraction is 12%. This wrong-tag fraction should be compared with 43.5% expected for an unpolarized beam for which the F-B asymmetry is 13%. CP violation can be measured by comparing the decay rates for $B_d(\bar{B}_d) \to \Psi K_s$, in the forward and the backward hemispheres. In order to enhance the sensitivity, we measure the decay rate as a function of the decay proper time,

$$\Gamma(B_d(\bar{B}_d) \to \Psi K_s) \propto e^{-\Gamma t}\{1 \pm \sin 2\phi_1 \sin X_d \Gamma t\},$$

where $X_d$ is a mixing parameter (=0.7), $\Gamma$ is the total decay width, and $\sin 2\phi_1$ is the CP violation parameter. The most probable value of $\sin 2\phi_1$ is estimated to be[60]

$$\sin 2\phi_1 = 0.37 \begin{array}{l} +0.54 \\ -0.21 \end{array}.$$

To observe the $B_s$-$\bar{B}_s$ mixing, we measure the decay rate of $B_s(\bar{B}_s)$ in the forward (backward) hemisphere. Then we fit the oscillation of the decay rate as a function of the decay proper time.

### 2.8.3 Measurement of $B_d(\bar{B}_d) \to \Psi K_s$

To study the detection sensitivity, we made an event-generator which includes the forward-backward asymmetry with a polarized electron beam. In our generator, $B_d$ mesons decay into $\Psi K_s$ (the signal), or into $\Psi K_s \pi^0$ which is the most serious background. The $\Psi$'s decay into leptonic channels with a 100% branching ratio ($e^+e^-$ and $\mu^+\mu^-$), instead of the real branching ratio of 14%. The $K_s$ mesons decay into $\pi^+\pi^-$ and $\pi^0\pi^0$ with branching ratios of 69% and 31%, respectively. Parameters used for the generation are $X_d = 0.7, \Gamma = 1/(13.1 \times 10^{-13}$ sec), and $|\cos\theta_b| < 0.94$.

The $\Psi K_s$ events are selected as follows. We first look for a pair of opposite sign tracks which has an invariant mass within $\pm 35$ MeV around the $\Psi$ mass and require that at least one track is identified as an electron or a muon: a track which has a momentum larger than 1.5 GeV and $E/P$ larger than 0.5 is identified as an electron, while 95% of muons whose momentum are larger than 3.5 GeV are randomly selected as identified muons. For an unidentified track, no momentum cut is applied. $K_s$'s are then reconstructed by looking for a pair of oppositely charged tracks, each of which has the closest distance to the z-axis larger than 0.04 cm and is identified neither as an electron nor as a muon. We require the pair to have an invariant mass consistent with that of $K_s$. Finally, if the pair of the $K_s$ and the $\Psi$ has an invariant mass within $\pm 50$ MeV around the $B_d$ mass, it is identified as $B_d$.

Fig.2.60 shows the invariant mass distributions of $\Psi K_s$ pairs for $B_d(\bar{B}_d) \to \Psi K_s$ (solid line) and $B_d(\bar{B}_d) \to \Psi K_s \pi^0$ (dotted line), respectively. One can see a clear peak of $B_d$ in the solid histogram. On the other hand, the dotted histogram has a broad distribution of invariant masses ranging from 3.92 to 5.16 GeV, because of escaping $\pi^0$s. The detection efficiency for $B_d(\bar{B}_d) \to \Psi K_s$ is 37.1%, when we take the average in the $|\cos\theta|$ range between 0.22 and 0.94. Since the peak is clearly separated from the broad distribution, we neglect the background coming from $B_d(\bar{B}_d) \to \Psi K_s \pi^0$ which has an opposite CP to that of $B_d(\bar{B}_d) \to \Psi K_s$. To compromise the wrong-tag fraction and statistics, the $B_d(\bar{B}_d)$ mesons are required to be detected at $|\cos\theta|$ between 0.22 and 0.94.

We use a maximum likelihood method to get the CP violation parameter $\sin 2\phi_1$ from the distributions of decay proper time and $\cos\theta$. When the branching ratio for $B_d(\bar{B}_d) \to \Psi K_s$ is taken to be 0.03%, the expected $\sin 2\phi$ range of 0.16 to 0.91 requires an integrated luminosity of $(2.7 \sim 0.083) \times 10^{40}$ cm$^{-2}$, in order to confirm the CP violation in the $B$-meson decay at the level of three standard deviations. The required integrated luminosity corresponds to $1.4 \sim 0.043$ years (we assume 100 days operation per year) of JLC-I operation on the Z pole (Fig.2.61). If we assume the most probable value (0.37) of $\sin 2\phi_1$, quarter a year is enough to measure it. If we do not apply the maximum likelihood method and just use the integrated event ratio of $B_d(\bar{B}_d) \to \Psi K_s$ in the forward and backward regions, we need 2.6 times more statistics.

### 2.8.4 Measurement of $B_s$-$\bar{B}_s$ Mixing

We use $B_s \to l\nu D_s$ as the signal of $B_s$ decay, where $l$ is an electron or a muon to be identified as described above, while the $D_s$ has to be detected through its decay into three charged hadrons and neutral particles, if any. There are altogether four charged tracks expected to have finite impact parameters. These four tracks are, therefore, required to be more than $2\sigma$-away from the z-axis, where $\sigma$ is the impact parameter resolution of the vertex detector. The three charged hadrons have to have an invariant mass less than 2 GeV to be consistent with the $D_s$ decay. In

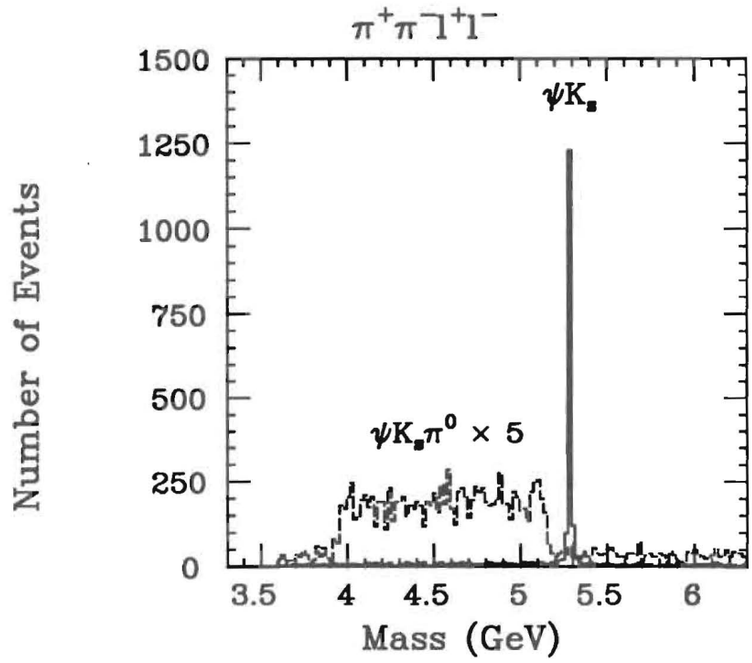


Figure 2.60: Invariant mass distributions of $\pi^+\pi^-l^+l^-$. The solid histogram shows $\psi K_s$ decay and the dotted one shows $\psi K_s\pi^0$ decay.

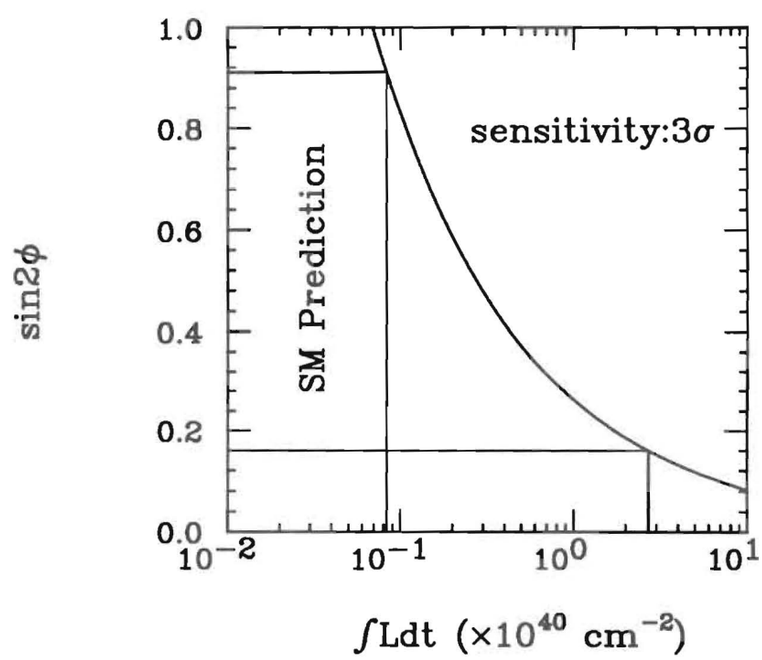


Figure 2.61: The required luminosity to measure $sin2\phi_1$ with three standard deviation.

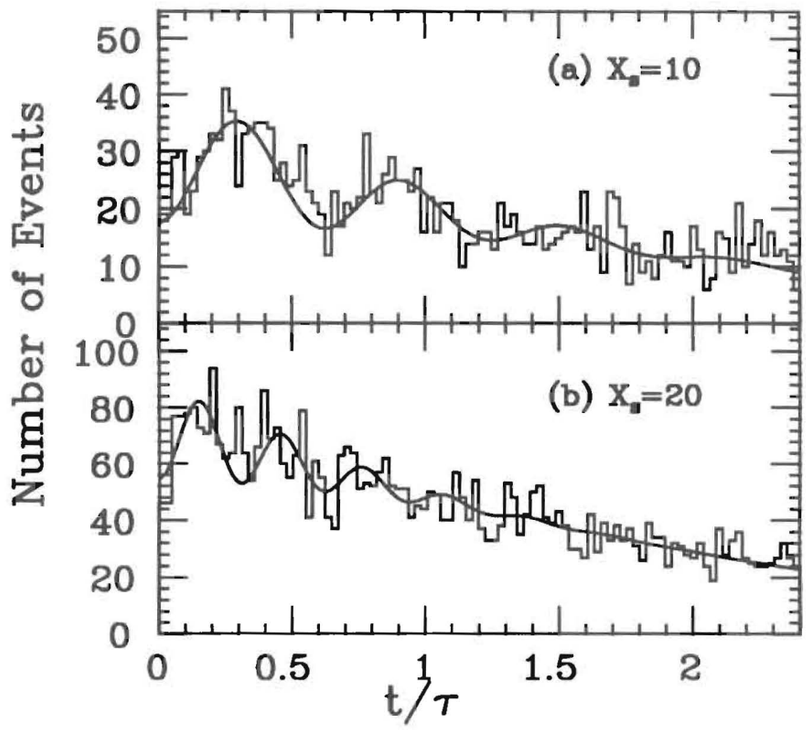


Figure 2.62: The decay proper time distribution for (a) $X_s = 10$ and (b) $X_s = 20$.

addition, we require that the decay point of $D_s$ (the vertex formed by the three hadron tracks) is farther away from the interaction point, when compared with the decay point of $B_s$ (the vertex formed by the lepton track and the combined momentum vector of the three hadron tracks). These cuts are very effective to eliminate the background from non-$b\bar{b}$ jets.

To calculate the decay proper time from the decay point, it is necessary to know the $B_s$ momentum. Its event-by-event determination is, however, impossible because of the missing neutrino from the $B_s$ decay and the unidentified neutral particles from the $D_s$ decay. We, therefore, use the average momentum of $B_s$'s estimated by the Monte Carlo simulation. This approximation is justified, as long as we use a tight sphericity cut. We thus require the event to have a sphericity smaller than 0.05. After this final cut, the efficiency for detecting $b\bar{b}$-jets is 4%, while that for $c\bar{c}$-jets (the most serious background) is only 0.2%. The backgound from light quarks is negligible. The resultant $b\bar{b}$-jet sample contains 20% of $B_s$ mesons.

The vertex resolution for $B_s$ decay is 90 $\mu m$ mainly limited by the effect of missing neutral particles. Figs.2.62-a) and -b) show that the oscillation of the $B_s$ decay can be clearly observed for both of $X_s = 10$ and 20, respectively. The amount of data used for the fitting in Figs.2.62-a) and -b) are $2.0 \times 10^6$ $Z^0$ and $4.0 \times 10^6 Z^0$, respectively, which correspond to less than half a day and one day of data acquisition with JLC-I on the $Z$-pole.

## 2.9 Heavy Higgs or Strongly Interacting $W$'s

Even if JLC-I does not find any light Higgs bosons at center-of-mass energies up to 500 GeV, it can predict the Higgs mass through the precision electroweak measurements as described in

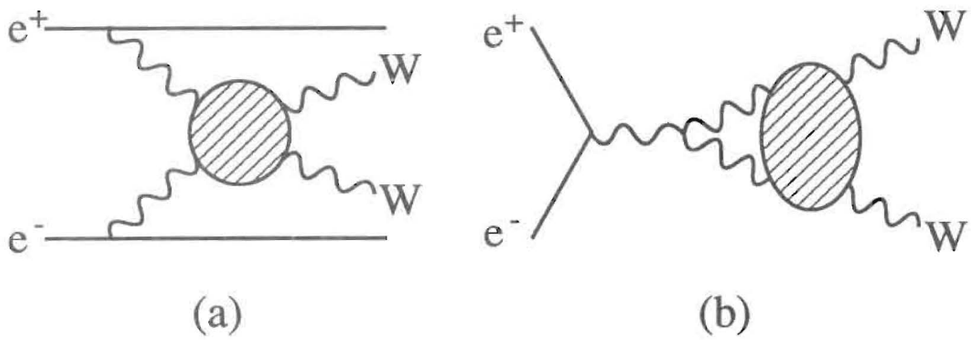


Figure 2.63: a) W-fusion process. b) Rescattering in W-pair creation.

the previous section. If this is the case, we have to upgrade the machine and increase the beam energy accordingly, to detect the Higgs boson. Such a heavy Higgs boson can be searched for in the $W$-fusion process shown in Fig.2.63-a).

If the predicted Higgs mass exceeds O(1 TeV), however, it does not necessarily mean the existence of an elementary Higgs boson of this mass. The Higgs mass should be regarded as the energy scale of a new strong interaction which is resposnsible for the mass-generation of the weak bosons. In this case, we need to understand the underlying dynamics governing the new strong interaction. The best probe to investigate it is the longitudinal components of the weak bosons, since they are closely related to the mass-generation[61]. At JLC, we can study the interaction of the longitudinal weak bosons via the $WW$-rescattering process shown in Fig.2.63-b).

In this section, we describe the heavy Higgs search via the $W$-fusion process and the search for a new strong interaction between $W$ bosons via the $WW$-rescattering at JLC with $\sqrt{s} \gtrsim 1$ TeV.

### 2.9.1 W-fusion process

First we discuss the JLC's capability of heavy Higgs search at $\sqrt{s} = 1$ TeV and 1.5 TeV via the $W$-fusion process: $e^+e^- \to \nu_e\bar{\nu}_e W^+W^-$. The background to this process consists of

$$\begin{aligned} e^+e^- \quad &\to e^+e^-W^+W^-, \\ &\to \nu_e\bar{\nu}_e Z^0Z^0, \\ &\to e^-\bar{\nu}_e W^+Z^0, \ (e^+\nu_e W^-Z^0), \\ &\to e^+e^-Z^0Z^0, \\ &\to W^+W^-. \end{aligned}$$

The exact cross-section calculations of these processes are quite complicated, since there are many diagrams leading to the same final states. We have carried out the calculations, using the helicity amplitude technique with the help of GRACE/CHANEL[62].

It should be emphasized that, if the Higgs boson mass is greater than 800 GeV, the $S$-wave amplitude for the scattering of longitudinally polarized gauge bosons violates unitarity at the tree level[63]. To avoid this unitarity violation, we enlarged the width of the Higgs boson by a minimal amount in our cross section calculations.

Given these cross sections, we can study the feasibility of heavy Higgs search at JLC. The analysis proceeds as follows: we first select four-jet events from which $W$-pair events are selected

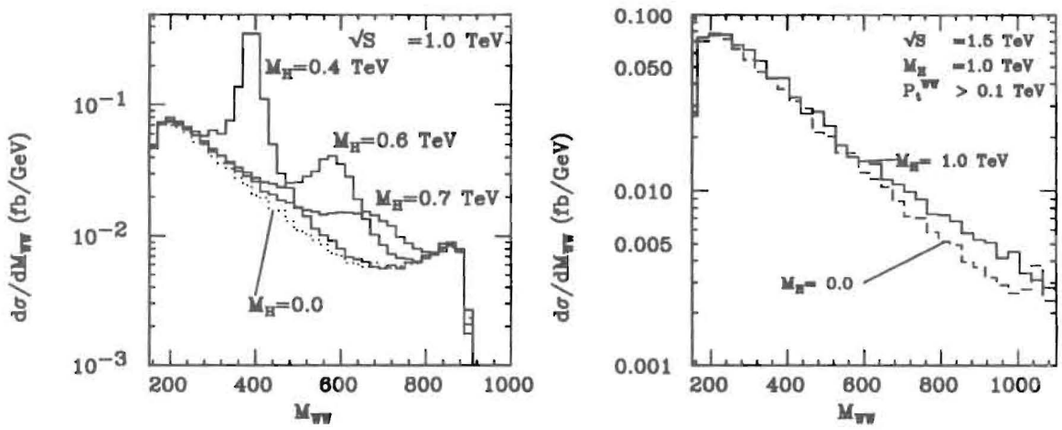


Figure 2.64: Differential cross sections as a function of $WW$ invariant mass at (a) $\sqrt{s} = 1$ TeV and for Higgs masses of 0, 400 GeV, 600 GeV, and 700 GeV, and at (b) $\sqrt{s} = 1.5$ TeV and for Higgs masses of 0 and 1.0 TeV.

by reconstructing jet-jet invariant masses. We then look for a resonance or an excess of events in the invariant mass distribution of the so reconstructed $W$-pairs, by comparing the distribution with that expected for $m_{H_{SM}} = 0$ (the massless Higgs case). Figs.2.64-a) and -b) show the differential cross sections at $\sqrt{s} = 1.0$ and 1.5 TeV, respectively, as a function of the $W$-pair mass.

When the Higgs mass is greater than 700 GeV, the signal of the Higgs boson becomes less significant compared with the massless Higgs case. The largest background, before making any cuts, comes from $e^+e^-W^+W^-$ and $e^+e^-Z^0Z^0$ (two-photon processes). To reduce the background events from these two processes, we vetoed the events which had high energy electrons in the visible area. When the electrons go through the beam pipe, the $W$-pair cannot have a large transverse momentum with respect to the beam axis. If it is required that the transverse momentum of the $W$-pair should be greater than 70 GeV at $\sqrt{s} = 1$ TeV (100 GeV for 1.5 TeV), and that the events with an electron which has an energy greater than 50 GeV and a polar angle greater than 150 mrad are vetoed, about 95% of the two-photon events are rejected. The $W$-pair production process ($e^+e^- \to W^+W^-$) can also be a background source, when the electron or positron emits high energy photon(s) due to beamstrahlung or initial state radiation. This background is also reduced by the cut on missing transverse momentum. For further reduction of the $W$-pair background, we use the decay angle distribution of quarks in the $W$-boson rest frame. The details of the analysis are described elsewhere[64].

After all of these cuts, the $WW$ invariant mass distributions shown in Figs.2.65-a) and -b) are expected for an integrated luminosity of 200 fb$^{-1}$. We can detect the excess due to the heavy Higgs boson signal over the background coming from the processes listed above, at the level of three standard-deviations.

### 2.9.2 Rescattering in $e^+e^- \to W^+W^-$

As demonstrated above, the Higgs search at JLC will never fail, if there is an elementary Higgs boson at all. Therefore, its non-observation at JLC will force us to consider that at least the longitudinal components of the weak bosons are some composite objects governed by a new strong interaction. If their transverse components are also composite, there must exist

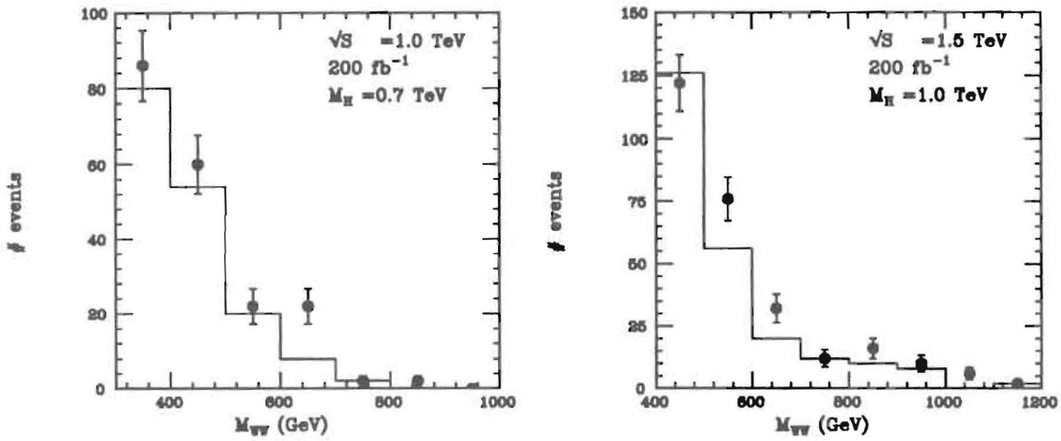


Figure 2.65: The expected distribution of $W$-pair invariant masses for an integrated luminosity of 200 fb$^{-1}$ at $\sqrt{s}$=1.0 TeV (1.5 TeV). The data points were calculated with a Higgs mass of 0.7 TeV (1.0 TeV) and the histograms with the massless Higgs.

some anomalous self-coupling among the weak bosons, which can be observed as discussed in subsection 2.7.2. When no such anomalous coupling is observed and the transverse components are verified to be gauge-like, the remaining possibility is that the weak bosons are gauge bosons which acquire their masses from the spontaneous symmetry breaking induced by a new strong interaction. In this subsection, we consider such a case and discuss how to observe the new strong interaction through studies of the $e^+e^- \to W^+W^-$ process.

There are nine $WW$ helicity combinations for the $e^+e^- \to W^+W^-$ process, of which only the following three survive at high energies ($s \gg m_W^2$): $W_+^+W_-^-$, $W_-^+W_+^-$, and $W_0^+W_0^-$, where suffixes indicate the $W$ helicities. The new strong interaction among the longitudinal weak bosons induces a rescattering of the final-state $W_0^+W_0^-$. The rescattering gives rise to a $P$-wave phase shift $\delta_{11}(s)$, since the lowest order amplitude is predominantly in $J = 1$, and a possible form-factor effect $|F(s)|$, in the $W_0^+W_0^-$ amplitude:

$$\mathcal{T}(e^+e^- \to W_0^+W_0^-) \approx \mathcal{T}^{(lowest)}|F(s)|e^{i\delta_{11}(s)}.$$

The amplitudes for the other two helicity combinations, $W_\pm^+W_\mp^-$, remain the same and are almost real. Here, we assume, conservatively, no techni-$\rho$-like resonance ($|F(s)| = 1$) and the phase shift given by the low energy theorem: $\delta_{11} = 0.055(0.12)$ rad. at $\sqrt{s} = 1$ TeV (1.5 TeV). We can observe this phase shift through the interference of the $W_\pm^+W_\mp^-$ and $W_0^+W_0^-$ amplitudes, which is possible after the weak bosons decay into fermion pairs[61].

The phase shift appears as a change in the correlation of the azimuthal angles of the final-state fermions. Let $\phi(\bar{\phi})$ be the azimuthal angle of the final-state fermion from $W^+(W^-)$, with respect to the axis formed by the two $W$ momenta, measured from the production plane (the plane spanned by the beam direction and the $W$ momenta), then the variable sensitive to the strong $WW$ final-state interaction is the sine of the sum of the two azimuthal angles, $\sin(\phi + \bar{\phi})$.

The sensitivity to the phase shift is maximum in the kinematical region where the magnitude of the $W_0^+W_0^-$ amplitude and those of the $W_\pm^+W_\mp^-$ amplitude are of the same order. Therefore, we require the production angle ($\Theta$) of the $W^-$ to satisfy $-1 < \cos\Theta < 0.5$, since the production amplitude for $W_\pm^+W_\mp^-$ peaks at $\cos\Theta = 1$ due to the $t$-channel neutrino exchange diagram. We also impose cuts on the decay polar angles ($\theta$ and $\bar{\theta}$) of the final-state fermions: $|\cos\theta| < 0.9$

and $|\cos\bar{\theta}| < 0.9$, since the decay amplitude of a longitudinal $W$ boson behaves like $\sin\theta(\bar{\theta})$, while that of a transvers $W$ boson like $1 \pm \cos\theta(\bar{\theta})$.

After all of these cuts, we obtain the angular distributions, with and without the rescattering at $\sqrt{s} = 1.5$ TeV, plotted in Fig.2.66-a). The effective cross section after the cuts is 52 fb. In the figure, the $\cos(2(\phi+\bar{\phi}))$ structure, corresponding to the four peaks, is due to the interference between the transverse $W$ bosons, which has nothing to do with the rescattering. Our signal is the $\sin(\phi + \bar{\phi})$ structure, which results in an asymmetry in the peak heights.

In order to carry out this analysis, we need to measure all the angles defined above. This requires the full reconstruction of the final state. For this purpose, we select events in which one of the $W$ bosons decays leptonically, and the other hadronically. We can then solve the kinematics, even if there is a beamstrahlung or bremsstrahlung photon. In addition, since we know the charge of the leptonic side, the charm tagging for $W^+(W^-) \to c\bar{s}(\bar{c}s)$ enables us to uniquely assign the charges to the final-state fermions.

The sensitivity to the phase shift $\delta_{11}$ of this measurement is shown in Fig.2.66-b). For example, for the low-energy-theorem phase shift at $\sqrt{s} = 1.5$ TeV, about 800 fully reconstructed $WW$ events are necessary to confirm the strong rescattering at the 90% confidence level. This corresponds to an integrated luminosity of about 300 fb$^{-1}$, if the charm tagging efficiency is 100%. If a techni-$\rho$-like resonance exists in the $J = 1$ channel, the prospect of seeing the effect becomes brighter[65].

The complete understanding of the new strong interaction becomes possible only after extensive spectroscopic studies of the $WW$ system and probably after weak-boson-jet studies to investigate the perturbative regime of the underlying dynamics. We believe that, if there is a new strong interaction among the weak bosons, its evidence obtained through the studies described above will place a solid foundation to promote construction of a new multi-TeV linear collider.

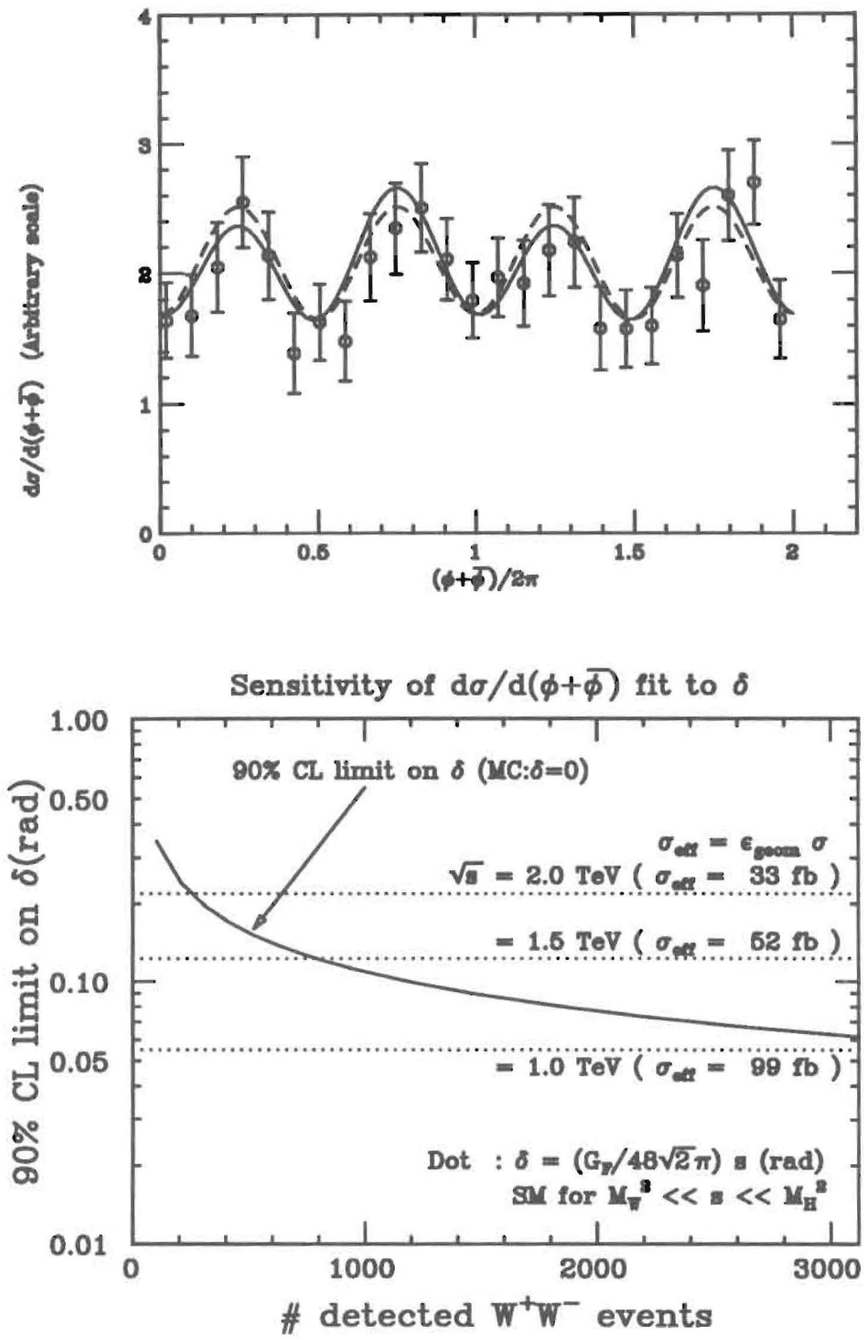


Figure 2.66: (a) The azimuthal angle correlation for $e^+e^- \rightarrow W^+W^-$ at $\sqrt{s}$=1.5 TeV. The solid line corresponds to a rescattering phase $\delta_{11}$=0.1 and the dashed line to no rescattring. The data points are for 1000 fully reconstructed Monte Carlo events. (b) Sensitivity to the phase.

# Bibliography


[1] S. Weinberg, *Phys. Rev. Lett.* **19** (1967) 1264;
A. Salam, Proc. 8th Nobel Sympos., Stockholm, ed. by N. Svartholm (Almqvist and Wiksell, Stockholm, 1968) p. 367.

[2] Y. Nambu and G. Jona-Lasinio, *Phys. Rev.* **122** (1961) 345;
P.W. Higgs, *Phys. Lett.* **12** (1964) 132, *Phys. Rev.* **145** (1966) 1156.

[3] UA1 Collaboration, *Phys. Lett.* **122B** (1983) 103, **126B** (1983) 398;
UA2 Collaboration, *Phys. Lett.* **122B** (1983) 476; **129B** (1983) 130.

[4] S.L. Glashow, *Nucl. Phys.* **22** (1961) 579.

[5] W.J. Marciano, BNL-45999 (April, 1991).

[6] M. Kobayashi and T. Maskawa, *Prog. Theor. Phys.* **49** (1973) 652.

[7] TOPAZ collaboration, *Phys. Lett.* **B255** (1991) 613, *KEK Preprint 92-49*; VENUS collaboration, *Phys. Lett.* **B278** (1992) 499, *Phys. Lett.* **B278** (1992) 393; AMY collaboration, *Phys. Lett.* **B218** (1989) 112, *Phys. Rev. Lett.* **64** (1990) 983.

[8] DELPHI collaboration, *Phys. Lett.* **B260** (1991) 240; L3 collaboration, *Z. Phys.* **C51** (1991) 179; OPAL collaboration, *Phys. Lett.* **B264** (1991) 269.

[9] P. Langacker, Pennsylvania preprint, UPR-0492T, (Jan 1992).

[10] TOPAZ collaboration, *Phys. Lett.* **B268** (1991) 457; ALEPH collaboration, *Phys. Lett.* **B263** (1991) 325; OPAL collaboration, *Phys. Lett.* **B263** (1991) 311.

[11] LEP Collaborations, *Phys. Lett.* **B276** (1992) 247.

[12] V.S. Fadin and V.A. Khoze, *JETP Lett.* **46** (1987) 525;
M.J. Strassler and M.E. Peskin, *Phys. Rev.* **D43** (1991) 1500;
Y. Sumino, K. Fujii, K. Hagiwara, H. Murayama and C.K. Ng, KEK preprint, KEK-TH-284, (Mar 1992);
H. Murayama and Y. Sumino, Tohoku University preprint, TU-401, (May 1992).

[13] L. Alvarez-Gaumé, J. Polchinski and M.B. Wise, *Nucl. Phys.* **B221** (1983) 495;
R. Barbieri and L. Maiani, *Nucl. Phys.* **B224** (1983) 32;
C.S. Lim, T. Inami and N. Sakai, *Phys. Rev.* **D29** (1984) 1488;
M. Drees and K. Hagiwara, *Phys. Rev.* **D42** (1990) 1709;
M. Drees, K. Hagiwara and A. Yamada, *Phys. Rev.* **D45** (1992) 1725.

[14] See E. Farhi and L. Susskind, *Phys. Rep.* **74** (1981) 277, and references therein.

[15] B. Holdom and J. Terning, *Phys. Lett.* **B247** (1990) 88;
M. Golden and L. Randall, *Nucl. Phys.* **B361** (1991) 3;
M. Peskin and T. Takeuchi, *Phys. Rev. Lett.* **65** (1990) 964;
W.J. Marciano and J.L. Rosner, *Phys. Rev. Lett.* **65** (1990) 2963;
G. Altarelli and R. Barbieri, *Phys. Lett.* **B253** (1991) 161.

[16] B. Holdom, *Phys. Lett.* **B150** (1985) 301;
T. Akiba and T. Yanagida, *Phys. Lett.* **B169** (1986) 432;
T. Appelquist, D. Karabali and L.C.R. Wijewardhana, *Phys. Rev. Lett.* **57** (1986) 957; *Phys. Rev.* **D35** (1987) 2605;
K. Yamawaki, M. Bando and K. Matsumoto, *Phys. Rev. Lett.* **56** (1986) 1335; *Phys. Lett.* **B178** (1986) 308.

[17] CDF Collaboration, *Phys. Rev.* **D45** (1992) 3921.

[18] D.V. Volkov and V.P. Akulov, *Phys. Lett.* **46B** (1973) 109;
J. Wess and B. Zumino, *Nucl. Phys.* **B70** (1974) 39.

[19] M. Veltman, *Acta Phys. Pol.* **B12** (1981) 437;
L. Maiani, *Proc. Summer School of Gil-sur-Yvette* (Paris, 1980) p. 3.

[20] H. Sugawara, talk presented at *the Symposium on the Electroweak Symmetry Breaking and Accelerator Projects*, in 47th Annual Meeting of the Physical Society of Japan, March, 1992.

[21] H. Georgi and S. Glashow, *Phys. Rev. Lett.* **32** (1974) 438.

[22] H. Georgi, H.R. Quinn and S. Weinberg, *Phys. Rev. Lett.* **33** (1974) 451.

[23] A.J. Buras, J. Ellis, M.K. Gaillard and D.V. Nanopoulos, *Nucl. Phys.* **B135** (1978) 66.

[24] S. Dimopoulos, S. Raby and F. Wilczek, *Phys. Rev.* **D24** (1981) 1681;
S. Dimopoulos and H. Georgi, *Nucl. Phys.* **B193** (1981) 150;
N. Sakai, *Z. Phys.* **C11** (1981) 153.

[25] Y. Okada, M. Yamaguchi and T. Yanagida, *Prog. Theor. Phys.* **85** (1991) 1, *Phys. Lett.* **B262** (1991) 54;
J. Ellis, G. Ridolfi and F. Zwirner, *Phys. Lett.* **B257** (1991) 83;
H.E. Haber and R. Hempfling, *Phys. Rev. Lett.* **66** (1991) 1815.

[26] T. Moroi and Y. Okada, Tohoku preprint, TU-405 (June 1992).

[27] K. Inoue, A. Kakuto, H. Komatsu and S. Takeshita, *Prog. Theor. Phys.* **68** (1982) 927;
L.E. Ibanez and G.G. Ross, *Phys. Lett.* **110B** (1982) 215;
K. Inoue, A. Kakuto and S. Takeshita, *Prog. Theor. Phys.* **71** (1984) 348;
L. Alvarez-Gaumé, J. Polchinski and M.B. Wise, *Nucl. Phys.* **B221** (1983) 495;
J. Ellis, J.S. Hagelin, D.V. Nanopoulos and K. Tamvakis, *Phys. Lett.* **125B** (1983) 275.

[28] K. Inoue, A. Kakuto, H. Komatsu and S. Takeshita, *Prog. Theor. Phys.* **67** (1982) 1889.

[29] N. Cabbibo, L. Maiani, G. Parisi and P. Petronzio, *Nucl. Phys.* **B158** (1979) 295.

[30] F. Abe et al., CDF collaboration, *Phys. Rev. Lett.* **64** (1990) 142.

[31] F. Merrit, talk presented at *ASPEN Winter Conference*, Aspen, 12th-19th January 1992.

[32] T. Kawamoto, talk presented at the JPS Meeting, 27th-30th March 1992.

[33] J. F. Gunion and Lynne. H. Orr, *UCD-91-15*, November, 1991.

[34] A. Yamada, *Mod. Phys. Lett.* **A7** (1992) 2877.

[35] A. Yamada, *Proceedings of the Third Workshop on Japan Linear Collider*, KEK, 1992, ed. by A. Miyamoto, *KEK Proceedings 92-13*, December, 1992.

[36] J. Alexander, *et al.*, *SLAC-PUB-4775*, January, 1989.

[37] K. Kawagoe, *Proceedings of the Third Workshop on Japan Linear Collider*, KEK, 1992, ed. by A. Miyamoto, *KEK Proceedings 92-13*, December, 1992.

[38] J. Kanzaki,*Proceedings of the Second Workshop on Japan Linear Collider*, KEK, 1990, ed. by S. Kawabata, *KEK Proceedings 91-10*, November, 1991.

[39] J. Kanzaki, talk presented at *the Workshop on Physics and Experiments with Linear Colliders*, Saariselkä, Finland, 1991; see also K. Fujii, *KEK Preprint 92-31*, May, 1992.

[40] S. Komamiya, *Phys. Rev.* **D38** (1988) 2158.

[41] P. Eerola and J. Sirkka, *CERN-PPE/92-76*, May, 1992.

[42] P. Janot, *LAL 91-61*, November, 1991.

[43] R. Barbieri and G. Giudice, *Nucl. Phys.* **B296** (1988) 75;
T. Kon and M. Jimbo, *Proceedings of the First Workshop on Japan Linear Collider*, KEK, 1989, ed. by S. Kawabata, *KEK Report* 90-2, April, 1990, p.280;
K. Inoue, M. Kawasaki, M. Yamaguchi, and T. Yanagida, *Phys. Rev.* **D45** (1992) 328.

[44] K. Hikasa, "JLC Supersymmetry Manual", in preparation.

[45] T. Tsukamoto, *KEK Preprint 92-34*, May, 1992.

[46] K. Fujii, *KEK Preprint 92-6*, April, 1992;
Y. Sumino, *UT 612*, May, 1992;
K. Fujii, *KEK Preprint 92-159*.

[47] P. Igo-Kemenes, private communication.

[48] M. Petradza, a talk presented at *Workshop on Physics and Experiments with Linear Colliders*, Saariselkä, Finland, Sep. 9-14, 1991.

[49] The calculations are based on the program provided by Z. Hioki.

[50] A. Miyamoto, talk presented at *the Workshop on Physics and Experiments with Linear Colliders*, Saariselkä, Finland, 1991.

[51] M. Peskin and T. Takeuchi, *Phys. Rev.* **D46** (1992) 381.

[52] K. Hagiwara, *KEK TH-320*, February, 1992

[53] A. De Rújula, M. B. Gavela, P. Hernandez and E. Massó, *CERN-TH-6272-91*, October, 1991.

[54] See for example; E. Yehudai, *SLAC-383*, August, 1991; S. Y. Choi and F. Schrempp, *DESY 91-155*, December, 1991; E. N. Argyres, *et al.*, *Phys. Lett.* **B259** (1991) 195.

[55] G. L. Kane, J. Vidal, and C.- P. Yuan, *Phys. Rev.* **D39** (1989) 2617.

[56] R.H.Siemann, *et al.*, *Proceedings of Summer Study:Snowmass '88, High Energy Physics in the 1990's*, Snowmass, Colorad, June 27-July 15, 1988.

[57] See section 4.1

[58] W.B.Atwood, *et al.*, *Phys. Lett.* **B216** (1989) 227;
T.Omori, *et al.*, *Proccedings of the Second Workshop on Japan Linear Collider*, KEK, Tsukuba, November 6-8, 1990;
Y.Kurihara, *et al.*, *Proccedings of Summer Study on High Energy Physics:SNOWMASS 1990*, Snowmass, July, 1990.

[59] Electron source of 95% polarization is not yet available.
However R/D efforts for high polarization show significant progress. We assume 95%-polarized source will be ready in near future.
Y.Kuriharam, *et al.*, *Nucl. Instr. and Meth.* **A313** (1992) 393;
H.Aoyagi, *et al.*, *Phys. Lett.* **A167** (1992) 415;
T.Maruyama, *et al.*, *PLAC-PUB-5731*, February, 1992.

[60] K.Abe, *et al.*, *KEK Report 90-23*, (1991)

[61] K. Hikasa, *KEK preprint 91-214*, *KEK-TH-319*, 1992.

[62] H. Tanaka, *Comp. Phys. Comm.* **58** (1990) 153;
H. Tanaka, T. Kaneko, Y. Shimizu, *Comp. Phys. Comm.* **64** (1991) 149.

[63] S. Willenbrok and G. Valencia, *Phys. Lett.* **B245** (1990) 341;
D. A. Dicus and W. W. Repko, *Phys. Rev.* **D42** (1990) 3660.

[64] Y. Kurihara, R. Najima, *KEK preprint 92-79*, August, 1992.

[65] T. Barklow, a talk presented at *Workshop on Physics and Experiments with Linear Colliders*, Saariselkä, Finland, Sep. 9-14, 1991.

[66] SDC Collaboration, "Technical Design Report", *SSCL-SR-1215*, April, 1992.

[67] J. Okada, M. Yamaguchi and T. Yanagida, *Phys. Lett.* bf B262 (1991) 54.

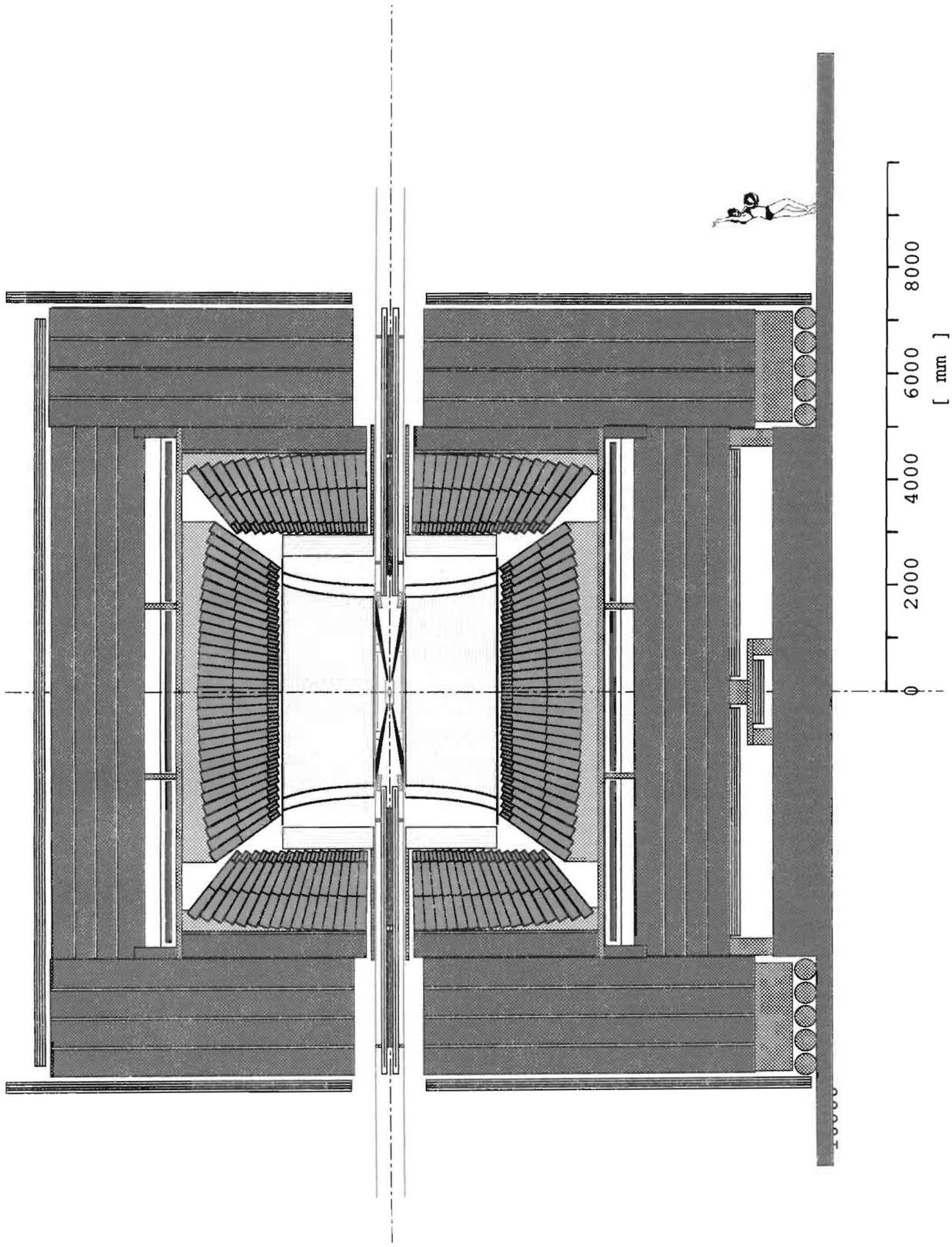
0
2000
4000
6000
8000
[ mm ]

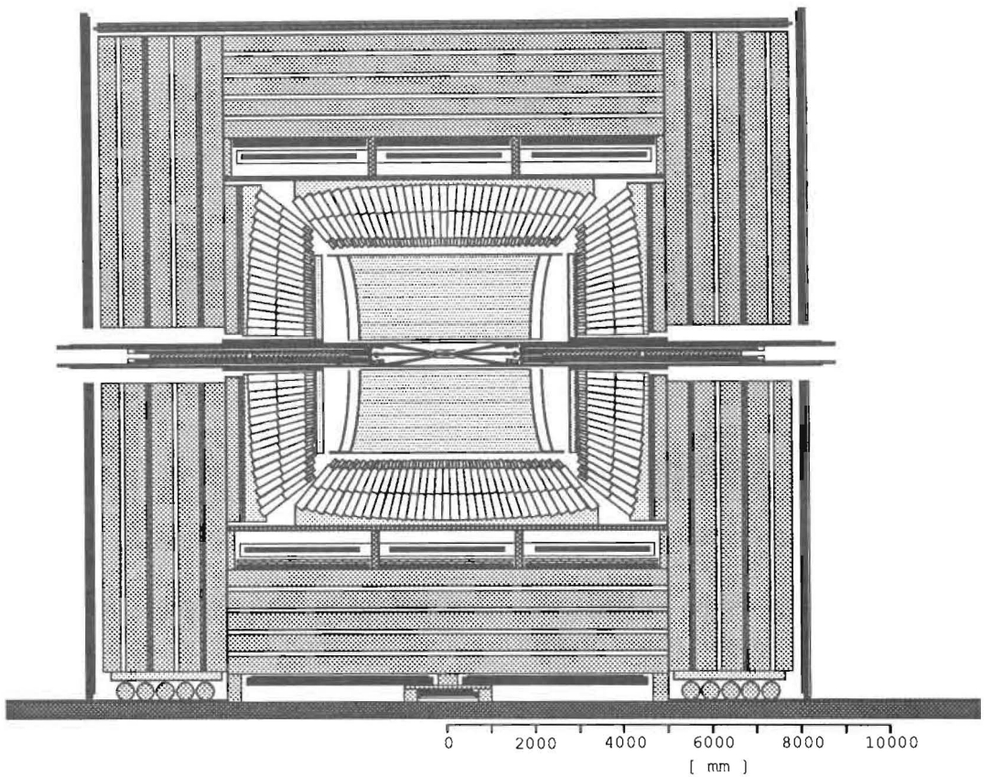


Figure 3.1: Schematical drawing of the JLC detector

| DETECTOR | TYPE | CONFIGURATION | PERFORMANCE |
|---|---|---|---|
| VTX ( Vertex Detector ) | Silicon CCD | Pixel Size ; 25 μm<br>Number of Layers ; 2 layers<br>Layer Position ; r=2.5cm & 7.5cm<br>Thickness ; 500 μm / layer<br>$\lvert\cos\theta\rvert < 0.95$ | Position Resolution ; $\sigma = 7.2$ μm<br>Impact Parameter Resolution $\delta$ [μm];<br>$\delta^2 = 11.4^2 + (28.8/p)^2 / \sin^3\theta$ |
| CDC ( Central Drift Chamber ) | Small-cell Jet Chamber | Radius ; r = 0.3 - 2.3 m<br>Length ; l = 4.6 m<br>Number of Sampling = 100<br>$\lvert\cos\theta\rvert < 0.70$ ( full sampling )<br>$\lvert\cos\theta\rvert < 0.95$ ( 20 samplings ) | Position Resolution ;<br>$\sigma_x = 100$ μm ( / axial wire )<br>$\sigma_z = 2$ mm ( / stereo wire )<br>Momentum Resolution ;<br>$\sigma_{Pt} / Pt = 1.1\times10^{-4} Pt \oplus 0.1\%$<br>$\sigma_{Pt} / Pt = 5\times10^{-5} Pt \oplus 0.1\%$<br>( with vertex constraint ) |
| CAL | Lead + Plastic Scintillator Sandwitch<br>( Compensated ) | EM part ; thickness = 29 Xo<br>cell size = 10cm x 10cm<br>HAD part ; thickness = 5.6 λo<br>cell size = 20cm x 20cm<br>Si Pad ; pad size = 1cm x 1cm<br>$\lvert\cos\theta\rvert < 0.99$ | Energy Resolution ;<br>$\sigma_E / \sqrt{E} = 15\% / \sqrt{E} \oplus 1\%$ ( e & γ )<br>$\sigma_E / \sqrt{E} = 40\% / \sqrt{E} \oplus 2\%$ (hadron)<br>Si Pad Position Resolution ; $\sigma = 3$ mm<br>Si Pad e/π Rejection = 1/50 |
| MUON | Single Cell Drift Chamber | Number of Superlayers ; 6<br>$\lvert\cos\theta\rvert < 0.99$ | Position Resolution ; $\sigma = 500$ μm<br>Pt > 3.5 GeV ( barrel ) |

* All momentum and energy are expressed in [ GeV ].

Table 3.1: Parameters and performances of the JLC detector

of each detector component. All the tracking devices and the calorimeter are placed inside the 2-Tesla superconducting solenoid to achieve a good hermeticity.

**Vertex detector (VTX)** : The vertex detector consists of 2 layers of Si-CCD arrays that can accomodate background tracks and $\gamma$'s due to $e^+e^-$ pairs created by beamstrahlung photons. The first and the second layers are placed at $r$=2.5cm and $r$=7.5cm, respectively, and the expected impact parameter resolution is 30 $\mu$m ( 90°, $p$=1GeV/c).

**Central drift chamber (CDC)** : The central tracking detector is a small-cell jet chamber. The inner and outer radii are 30cm and 230cm, respectively, and 100 points are sampled with a spatial resolution of 100$\mu$m. To use maximally the charged track information, we require two-track separation capability of 1mm. The resolution in the $z$-coordinate is designed to be less than 2mm at the front face of the calorimeter to achieve a good track-cluster matching.

**Calorimeter (CAL)** : The calorimeter is of a lead-scintillator sandwich type that has an equal response to electromagnetic and hadron showers. The calorimeter is longitudinally segmented into three sections: the fine sampling electromagnetic shower section of 29 $X_0$ thickness (ECAL), Si-pads to detect electromagnetic pre-showers located after the first 4.3 $X_0$ of ECAL, and a hadron section of 5.6 interaction lengths (HCAL). The barrel and the endcap calorimeters consist of 2500 and 1250 tower modules, each pointing to the interaction region.

**Muon detector (Muon)** : The muon detector consists of six super-layers of single cell drift chambers. Since it only provides muon identification, a modest spatial resolution of 500 $\mu$m is required. The threshold momentum for muon identification is 3.5 GeV/c due to the large energy loss in the calorimeter.

The interaction region is quite different from those we have experienced at the storage ring experiments. To get a stable collision of nanometer-size beams, we have to control the final quadrupole magnets with comparable accuracy. In this detector design, the Q-magnets of both electron and positron sides are fixed in the same cylinder made of CFRP to cancel common mode vibrations. Inside the cylinder, the magnet positions are monitored by laser interferometers whose signals are fed back to piezo transducers for precision active alignment.

Background arising from beam-beam interactions has been systematically studied for both QED and QCD processes. The beam mask configuration shown in Fig. 3.2 is designed to effectively shield the most troublesome soft photons from $e^+e^-$ pairs created by beam-beam interactions.

## 3.2 Vertex Detector

### 3.2.1 Requirements for the Vertex Detector

The vertex detector (VTX) measures the track positions of charged particles very precisely near the interaction point. The major role of the VTX is to reconstruct the secondary and tertiary decay vertices from $B$ and $D$ meson decays, to tag $b$- or $c$-quark jets. The $b$-quark jet tagging is of essential importance, particularly in the search for the intermediate mass Higgs ($m_H \sim 100$ GeV), as discussed in section 2.2. The VTX should have a spatial (or impact parameter) resolution good enough to get a high rejection ratio for light quark jets, while keeping a good efficiency for $b$-quark jets.

The VTX also plays an important role in the momentum measurements of charged particles. Since the VTX has much better spatial resolution than the central drift chamber (CDC), it puts a strong constraint on the track fitting and improves the momentum resolution by a factor of two. The effect of the VTX constraint will be discussed in detail in section 3.3.

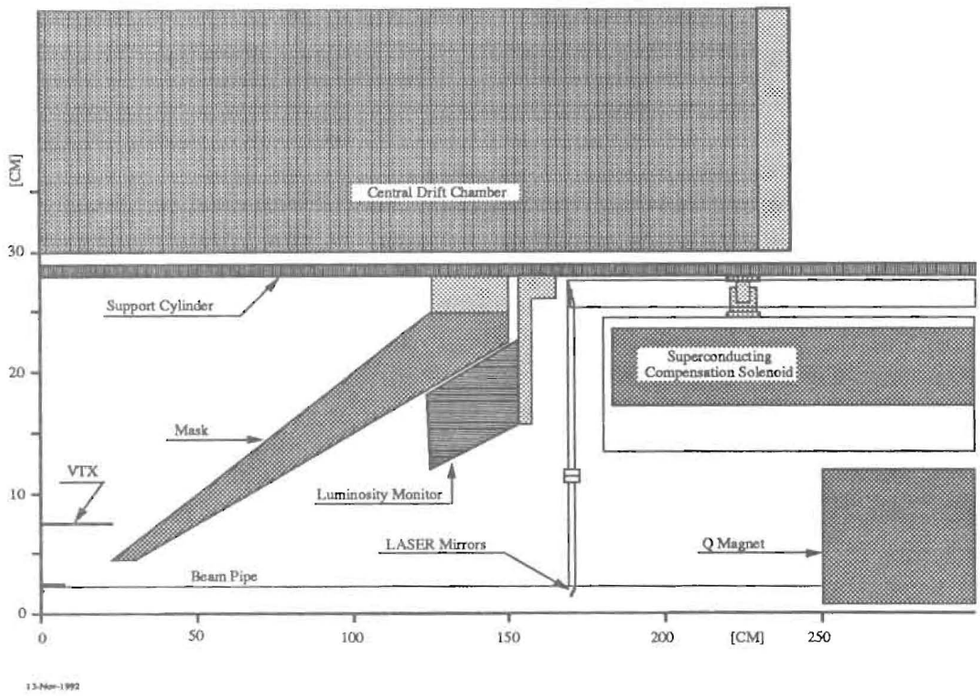


Figure 3.2: Layout of the interaction region

As the energy increases, particles in the jets become more and more collimated. Since the VTX is located close to the interaction point, the track density in the VTX is quite high. For unambiguous track reconstruction, the detector should be able to measure two-dimensional points rather than their projections. Therefore, pixel detectors should be used for the VTX.

### 3.2.2 Configuration

The VTX consists of two concentric layers of silicon pixel detectors made of charge coupled devices (CCDs). The impact parameter resolution can be written as

$$\delta^2 = \sigma^2\{(\frac{r_{out}}{r_{out} - r_{in}})^2 + (\frac{r_{in}}{r_{out} - r_{in}})^2\} + (\frac{0.014 r_{in}}{p\beta})^2 \frac{X_r}{\sin^3\theta},$$

where $p$ is the momentum of the charged particle in GeV/c, $r_{in}$ and $r_{out}$ are the radii of the inner and outer layers, $X_r$ is the thickness of the inner layer (including the beam pipe) in radiation lengths, and $\sigma$ is the resolution of the vertex detector. The first term comes from measurement error and the second term from multiple scattering. This equation tells us that we should put the inner layer as close to interaction point as possible and outer layer as far as possible. However there are several constraints on the radii. First of all, the radius of the inner layer should be large enough to avoid the background from low-energy $e^+e^-$ pairs created by beam-beam interactions (see section 3.7). As for the radius of the outher layer, we should take into account the cost of the VTX which increases $\propto r_{out}^2$, while the gain in resolution is little. In addition, the precise supporting and alignment of the VTX becomes more difficult for a larger size, and the resolution might get worse, if $r_{out}$ is too large. Therefore the present design adopts

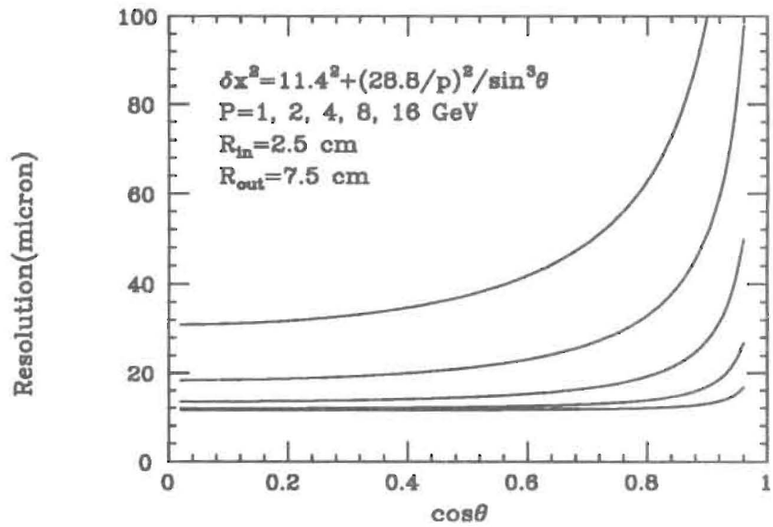


Figure 3.3: Impact parameter resolution as functions of momentum $p$ and $\cos\theta$.

the following parameters. The inner and the outer layers are at $r_{in} = 2.5$ cm and $r_{out} = 7.5$ cm. It covers the angular region of $|\cos\theta| < 0.95$. The total lengths in the $z$-direction are $\pm 7.6$ cm for the inner layer and $\pm 22.8$ cm for the outer layer. The pixel size is 25 $\mu$m $\times$ 25 $\mu$m, which corresponds to a spatial resolution of 7.2 $\mu$m. If the center-of-gravity method works, we can get still better resolution. The total area of the CCDs is $\sim 2400$ cm$^2$, and the total number of pixels is $\sim 4 \times 10^8$. For these parameters, the impact parameter resolution becomes

$$\delta^2 = 11.4^2 + (28.8/p\beta)^2/\sin^3\theta \ (\mu\mathrm{m}^2).$$

The impact parameter resolution $\delta$ is plotted as functions of $\cos\theta$ for several momenta in fig. 3.3.

### 3.2.3 Operation of CCD Detectors

The CCDs will be operated close to room temperature (*i.e.* $> 0°$C). In general, operating CCDs at room temperature causes large dark currents (dark current increases exponentially as temperature goes up) and hence a large shot noise which is a serious problem in the detection of minimum ionizing particles (m.i.p.). Furthermore, the non-uniformity of dark currents causes a non-flatness of the output baseline. These problems, however, can be avoided by the following methods:

1. Since the shot noise is a statistical fluctuation of the integrated charge coming from dark currents ($\propto \sqrt{i_d t}$), this can be reduced by a quick readout.

2. If the signal charge is large enough, an increase in the noise does not matter so much. This can be achieved by making the depletion region thicker than the present CCDs used for video cameras.

At JLC-I, beam bunch trains make crossings at intervals of 6.7 ms (150 Hz). Each CCD is read out during this period almost continuously. By reading out continuously, each pixel in the same

vertical line accumulates the same amount of charge due to dark currents, and the pattern of the baseline non-flatness is the same for every horizontal line. Therefore, the non-flatness can be corrected easily by subtracting the pattern of non-flatness which is stored in a analog shift register. If a dark current of 5 nA/cm$^2$ is assumed, the average shot noise becomes about 40 electrons. This number is comparable to other noise sources.

The thickness of the depletion region can be extended to $\sim 30\mu$m using high resistivity ($\sim$ 1 k$\Omega$cm) silicon wafers without a serious increase in dark currents due to defects in the crystal. In this case, more than 2000 electrons can be obtained for a m.i.p. track. If defect free silicon wafers with higher resistivity become available in the future, we can get CCDs with a still thicker depletion region.

The area of each CCD has to be small enough to be read out in 6.7 ms. If the same rate as for the present CCDs for video cameras is assumed, $\sim$ 0.4 cm$^2$ can be read out in this period. Since the total area of the VTX is $\sim$ 2400 cm$^2$, the number of readout channels is $6 \times 10^3$.

Collected charge from each pixel is shifted to the output node and read out through on-chip FETs. The output signal is processed through a correlated double sampling (CDS) circuit to eliminate reset noise, corrected for the non-flatness of the baseline, and digitized by a flash ADC. The ADC data and pixel address are stored in the memory, if the ADC counts exceed a certain threshold.

### 3.2.4 Expected Performance

There are two approaches of selecting $b$-quark jets using the VTX. One method is to select $b$ jets exclusively by identifying the successive decay vertices of $B$ and $D$ mesons. The other way is to select heavy flavor jets by requiring that a certain number of tracks have a finite impact parameter (heavy flavor tagging). The latter method is, compared with the former one, easier and more efficient, though it is impossible to separate $c$- and $b$-quark jets clearly.

We have made a simulation of the heavy flavor tagging by impact parameter method, assuming the VTX described above. Two-jet events $e^+e^-(\sqrt{s} = 90$ GeV$) \rightarrow u\bar{u}$, $s\bar{s}$, $c\bar{c}$, $b\bar{b}$ are generated and charged particle tracks are smeared according to the resolution of the vertex detector. In order to tag the heavy flavor jet, we search for tracks which do not originate from the interaction point (I.P.). If a jet has more than two (or three) charged tracks with an impact parameter in the three-dimensional space $b$ which satisfies $b/\sigma > \sigma_{cut}$, where $\sigma$ is the impact parameter resolution expected from the momentum and angle, the jet is regarded as a heavy flavor jet. If the invariant mass of the two tracks is consistent with the mass of the $K_S$, those tracks are rejected. Fig. 3.4 shows distributions of the normalized impact parameter for the charged particles from the primary vertex (I.P.) and for the secondary and tertiary vertices ($B$ or $D$ decay). Tagging efficiency is plotted in fig. 3.5 for $s$-, $c$-, and $b$-quark jets as functions of $\sigma_{cut}$. The tagging efficiency for $b$-quark jets is 78% (63% ) if at least two (three) tracks are required to have impact parameters $b/\sigma > 2.5$. For a light quark jet, if we require at least two (three) tracks with $b/\sigma > 2.5$, the tagging efficiency is $\sim$ 0.5% (0.25% ), which means the light quark jets can be suppressed by a factor of 200 (400). It should be noted that the efficiency for the $c$-quark jet is much lower than the $b$-quark jet due to its shorter decay length and we can expect a suppression of the $c$-quark jets to some extent. If one tries to discriminate $b$-quark jets from $c$-quark jets more distinctively, more cuts, which could reduce the efficiency, are necessary. For a suppression of the $W$-pair background in $H \rightarrow b\bar{b}$, however, heavy flavor tagging works well enough because the decay mode $W \rightarrow c\bar{b}$, which can not be suppressed enough by the heavy flavor tagging, has a very small branching ratio ($|V_{cb}| \sim 0.05$). If we take the product

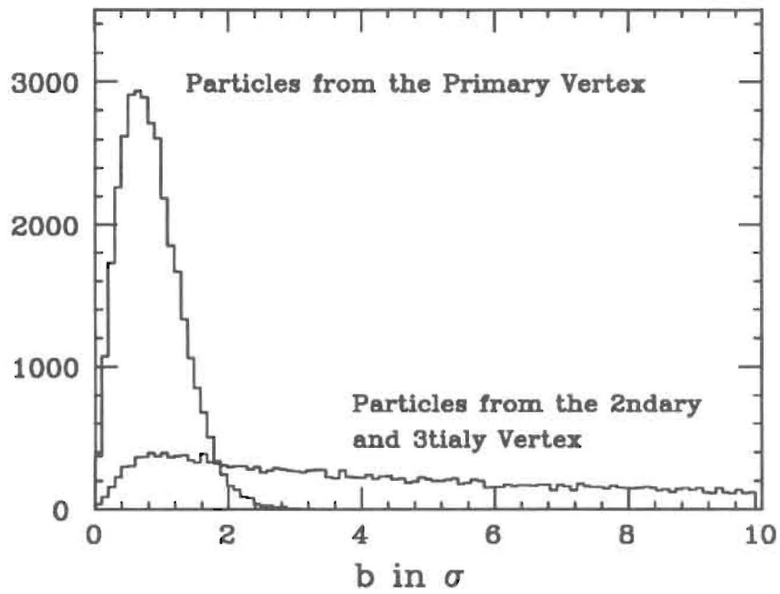


Figure 3.4: Distributions of normalized impact parameter in the three-dimensional space for the charged particles from the primary vertex and for those from the secondary and tertiary vertices.

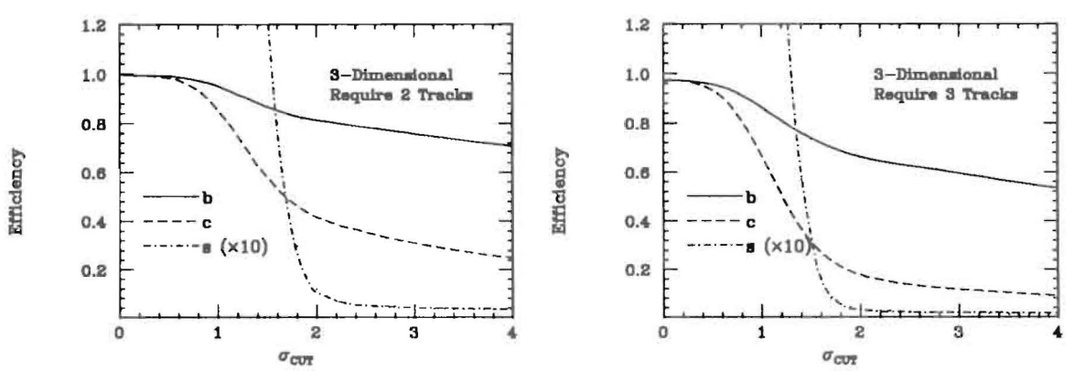


Figure 3.5: Tagging efficiency for $s$-, $c$-, and $b$-quark jets as functions of $\sigma_{cut}$. The curve for $u$ jets which is not plotted here is almost same as that for $s$ jets.

of efficiencies for two jets and the branching ratio, the suppression ratio for the background process $W \to q\bar{q}'$ becomes $\sim 1.2\ (0.27) \times 10^{-3}$ for the case of $\geq 2\ (3)$ tracks double tag, while the efficiency for the signal process ($H \to b\bar{b}$) is $\sim 62\ (39)\%$ . In the case of the intermediate mass Higgs search through the process $e^+e^- \to HZ$, with $H \to b\bar{b}$ and $Z \to l^+l^-$ or $\nu\bar{\nu}$, the main background comes from $e^+e^- \to ZZ \to l^+l^-(\nu\bar{\nu})q\bar{q}$. This background cannot be suppressed as much as in the case of $W$ pair background because the process including $Z \to b\bar{b}$, which has a sizable branching ratio, has the same topology as the signal process. However, we don't need such stringent light quark suppression as in the case of $W$ pair background because the cross section is not as large as the $W$ pair production. If we require at least one jet to be identified as a $b$-quark jet with $\geq 2\ (3)$ tracks having large impact parameter, the background is suppressed to 31% (24% ), with a tagging efficiency of 95% (86% ).

### 3.2.5 Background Considerations

As discussed in section 3.7.6, the beam background in linear collider experiments is quite different from that of storage ring experiments. The main background to detectors consists of photons emitted from the front surface of the final quadrupole magnet, which is bombarded by electron-positron pairs created by beam-beam interactions. These electrons/positrons themselves could be the background near the beam line as described in section 3.7.6. The spectrum of the background photons shows a broad peak around 200 keV and a sharp annihilation peak at 0.5 MeV.

A large number of the background photons flow out from the aperture of the tungsten mask. The inner layer of the VTX is exposed to direct hits from the photons and the outer layer is hit by photons scattered by inner materials including the beam pipe. If we assume that both the inner and outer layers are exposed to the photons directly as a worst case, the number of pixels hit by the background photons is

$$N_{bg} = N_p V_p \lambda I,$$

where $N_p$ is the number of pixels ($4 \times 10^8$), $V_p$ is sensitive volume of a pixel ($= 25 \times 25 \times 50\ \mu\text{m}^3$ if the effective thickness is 50 $\mu$m), $\lambda$ is the linear attenuation coefficient for photons in silicon (0.3/cm at 200 keV), and $I$ is the intensity of the photon flux per unit area. The number of electrons/positrons hitting the final quadrupole magnet is estimated to be $\sim 5 \times 10^6$, and the number of back-scattered photons per electron/positron is $\sim 1$. Since the VTX is about 2 m away from the photon source (the front surface of the final quadrupole magnet), the intensity of photons at the VTX is $I = 5 \times 10^6 \times (2\pi \times 200^2)^{-1} \sim 20$. Putting those numbers into the equation, we get $N_{bg} = 75$, which is negligibly small compared with the background due to the direct hits by the electron/positron tracks.

## 3.3 Central Tracking Device

The central tracking device plays a crucial role, in particular, in Higgs studies, where we have assumed an ultimate momentum resolution and one-to-one matching of a calorimeter hit to a charged track in the central tracker. In addition, the central tracker has to survive the expected backgrounds from beam-beam interactions. We will demonstrate below that a small jet-cell type cylindrical drift chamber (CDC) can realize the required performance within the presently available detector technology. Brief discussions on electronics followed by cost estimation will be also given in this section.

### 3.3.1 Design Criteria

#### Momentum Resolution

The most stringent constraint on momentum resolution comes from the required missing mass resolution for lepton pairs from decays of $Z^0$ bosons produced in the process $e^+e^- \rightarrow Z^0h$. In order that the measurement error might be negligible compared with the beam energy spread, the momentum resolution should be better than 0.4 % for a 50 GeV track. This requirement on the momentum resolution sets the design goal for the resolution of the reciprocal transverse momentum $\kappa = 1/p_T$. If this goal is achieved, the momentum resolution is good enough for the charge separation of even 5 TeV leptons.

The $\kappa$ resolution is given by $\sigma_\kappa^2 = (\sigma_\kappa^{meas})^2 + \left(\sigma_\kappa^{MS}\right)^2$, where the first term in the right-hand side is from coordinate measurement errors while the second term from multiple scattering in the chamber gas:

$$\begin{aligned} \sigma_\kappa^{meas} &\simeq \left(\frac{\alpha\sigma_x}{BL^2}\right)\sqrt{\frac{720}{n+4}} \\ \sigma_\kappa^{MS} &\simeq \left(\frac{\alpha C}{BL}\right)\sqrt{\frac{10}{7}\left(\frac{X}{X_0}\right)} \cdot \kappa \end{aligned}$$

with $\alpha = 333.56$ ( cm $\cdot$ T $\cdot$ GeV$^{-1}$ ), $C = 0.0141$ ( GeV ), $L$ = lever arm length (cm), $B$ = magnetic field (T), $\left(\frac{X}{X_0}\right)$ = thickness in radiation length, and $n$ = the number of sampling points. We have, for instance,

$$\left(\frac{\sigma_{p_T}}{p_T}\right)^2 = (1.1 \times 10^{-4} \cdot p_T[GeV])^2 \; + \; (1.5 \times 10^{-3})^2$$

for $L$ = 200 cm, $B$ = 2 T, $\sigma_x$ = 100 $\mu$m, $n$ = 100, and $(X/X_0)$ = 1.1 % when $CO_2$-isobutane(90/10) is used as the chamber gas. The effect of the constant term (multiple scattering) is less than 15 % on $\sigma_\kappa$ for $p_T \geq 20$ GeV in this case. This example is already very close to our design goal.

In order to see how the interaction point (IP) constraint or the extra-coordinate information improves the momentum resolution, we have to take proper accounts of the multiple scattering. We will focus our attention on the detector configuration shown in Fig.3.6. The radiation lengths of the relevant materials are listed in Table 3.2. The IP constraint improves the momentum resolution by approximately a factor of two even in the presence of multiple scattering. If we include the Si vertex detector into track fitting, coordinate information from the Si vertex detector is equivalent to the use of the IP constraint.

Taking these into account, we fix the detector parameters as follows:$B$ = 2 T, $r_{in}$ = 30 cm, $r_{out}$ = 230 cm, $n$ = 100, and $\sigma_x$ = 100 $\mu$m. Figs.3.7-a) and -b) show the polar angle dependence of the momentum resolution without and with the IP constraint, respectively. With the IP constraint, the momentum resolution obtainable with this set of detector parameters satisfies the design requirement from Higgs studies.

#### Cluster Track Matching

In order to get an ultimate resolution for jet invariant mass, the essential point is one-to-one matching of a calorimeter cluster and a charged track in the CDC. Since the calorimeter will exploit a Si pad detector of 1 $\times$ 1 cm$^2$, our goal is to keep the track extrapolation error reasonably below this size. The position resolution in the azimuthal direction automatically satisfies this requirement when we demand the momentum resolution required from Higgs

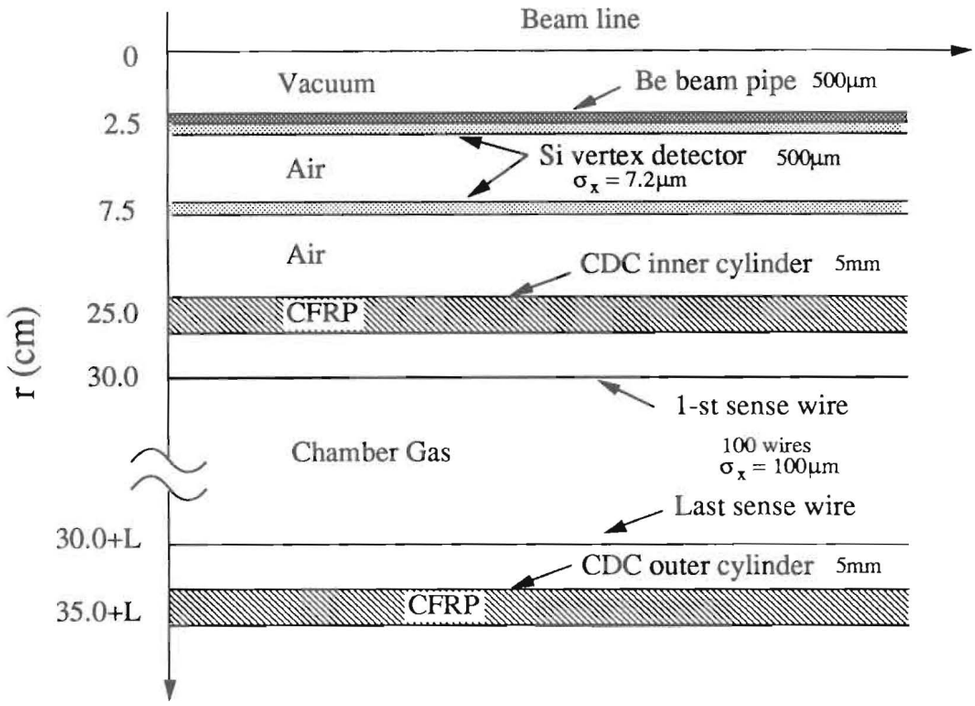


Figure 3.6: The configuration of tracking devices.

studies. Therefore, our main concern is the $z$-resolution at the front face of the electromagnetic section of the calorimeter. The calorimeter front face is at $r = 250$ cm and there is no massive material but the CDC's outer cylinder made of CFRP(0.5 cm) between the CDC and the barrel calorimeter.

An error matrix calculation showed that the effect of multiple scattering quickly disappears when the momentum exceeds 5 GeV and that a $z$-resolution of 1 mm or better can be achieved at the calorimeter front face, if seven stereo layers with $\sigma_z = 1$ mm are available.

| Material | $X_0^{-1}$(%/cm) |
|---|---|
| Be | 2.8 |
| Si | 10.7 |
| CFRP | 3.0 |
| Air(1atm) | 0.0035 |
| $CO_2/C_4H_{10}$(90/10) | 0.0055 |

Table 3.2: A list of materials and their radiation thickness per unit length.

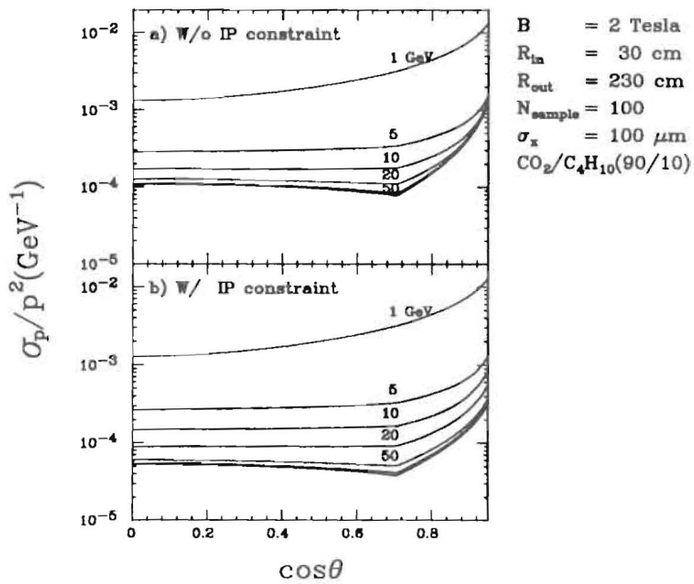


Figure 3.7: $\sigma_p/p^2$ as a function of the cosine of the polar angle: (a) without and (b) with the IP constraint. The different curves correspond to different momenta: $p = 1$, 5, 10, 20, 50, 100, and 250 GeV.

### 2-Track Separation

A limited capability of two-track separation (two-hit separation) is one of the most important effects to deteriorate the measured track quality. The fraction of missing hits for decay daughters from a single $W$ boson whose momentum is 250 GeV was investigated. The cell size is assumed to be 10 cm (the maximum drift length is 5 cm). The effect of Left/Right ambiguity is also taken into account. If the two hits separated by 1 mm each other can be distinguished, only five percent of the hits are missed at the innermost layer and one percent at the outermost layer. A two-hit separation capability of 1 mm can be achieved by our CDC design. After 100 nsec (equivalent to a 1 mm drift) from the arrival of the first electron, the pulse height become about one half of the peak so it is easy to separate two hits whose distance is greater than 1 mm.

### Self $T_0$ determination

Since the JLC beam has a multi-bunch structure, each hit has its own $T_0$ depending on which bunch makes the hit. The CDC should have self-$T_0$ determination capability. The $T_0$ determination can be done as follows: the drift distances are given as a function of one hundred discrete values of $T_0$'s. After track finding, the $T_0$ is determined to give a minimum $\chi^2$ in circle-fit of the track. To meet the requirement of a spatial resolution of 100 $\mu$m with a drift velocity of 10 $\mu$m/nsec, the timing resolution should be 10 ns for each hit. Thus one can expect a 1.0 ns timing resolution for one track which has 100 hit points. Adjacent beam bunches locate 2.8 standard-deviation away from the bunch which has an event. The track-based $T_0$ determination can be done easily.

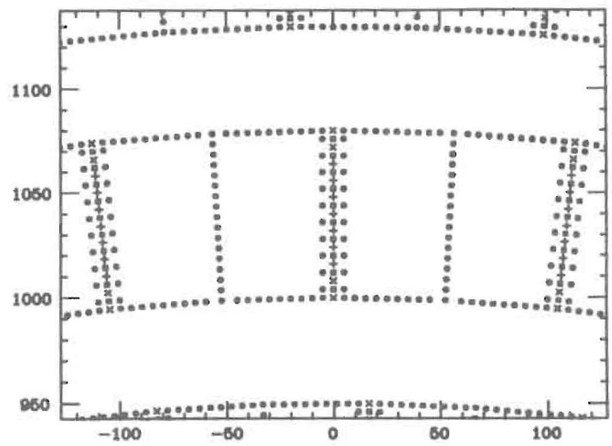


Figure 3.8: The basic cell structure.

**Backgrounds**

i) Soft photon background

The primary background electrons and positrons are produced through coherent and incoherent QED processes. They hit the wall of the mask and produce a lot of photons as the secondary background[1]. The energy spectrum of these photons has a broad peak near 100 keV and a narrow steep peak at 500keV from annhilation. The total number of the primary electrons produced at a beam crossing and hitting on the outer surface of the mask is at most $10^4$ at center-of-mass energy of 500 $/rmGeV$. Since the conversion ratio of the primary electron to the secondary photon is about one, $10^4$ photons come into the CDC volume. 2.5 photons are scattered off in each 1cm sampling thickness by the chamber gas and 1.3 photons from wires in one superlayer. The expected background hit per sense wire is 0.06 at the innermost layer and less than 0.01 at the outermost layer. The tracking can be done under these photon backgrounds.

ii) Mini-jet background

It is pointed out that two-photon induced hadronic events, so called "mini-jets", can be a background at the JLC[2]. At a center-of-mass energy of 500 GeV, the mean value of total energy of mini-jet within the CDC acceptance is expected to be 2.5 GeV and charged multiplicity is about five[3]. The number of mini-jets whose transverse momentum is greater than 1 GeV is estimated to be $1 \sim 20$ jets at one beam crossing for c-band case. Since the CDC can distinguish the tracks from different bunches, the mini-jet cannot be a problem. Even if the mini-jet ratio is, as the worst case, ten jets a beam crossing, the probability that at least one mini-jet overlapping the real event in the same bunch is 9.6%.

### 3.3.2 Chamber Geometry and Cell Structure

As shown in the previous subsection, a small cell type cylindrical jet chamber can realize the required performance. Details of the CDC structure are given in this subsection.

The super layer structure allows to find a track segment as a vector hit in each super layer. The number of super layers is calculated from the thickness of one super layer (8 cm), the

thickness of gap between adjacent super layers (5 cm), and the lever arm length (200 cm). The gap between super layers is determined by the stereo angle. We can get 15 super layers in the CDC: 8 axial layers and 7 stereo layers. Stereo angle is set to be 100 mrad to give $\sigma_z = 1$ mm per superlayer.

The basic cell structure is shown in Fig.3.8. One jet-cell has 7 sense wires of $30\mu m\phi$ tungsten. Maximum drift length is 5cm. They are strung with 8mm spacing and are applied +2.5kV. The outermost two wires and innermost two wires are dummy sense wires and their voltage is 1.8kV. Between sense wires,a potential wire is strung and is grounded. The grid wires are placed at 5mm away from the sense wire plane. Their voltage is set to be -0.5kV. The grid wires allow us to make good equi-drift time shape and to minimize a sence wire displacement due to electric force from adjacent layers. All wires except for the active sense wires are $150\mu m\phi$ alminum wires to reduce total wire tension. Sense wire planes are staggered not to align any two sense wire planes on the same radial line.

Using an electric field calculation program, we studied the basic charactaristics of this wire configuration with chamber gas of $CO_2$-isobutane(90:10). The Lorentz angle of this gas is about 15 degrees. Fig.3.9 shows the equi-drift time map. The calculation shows that about ten electrons arrive at the sense wire within a first time bin whose width is 5 nsec. This suggests that if the threshold is set at a few electrons, the required timing resolution (100ns) can be achieved.

Since the CDC is 4.6 m long in z-direction, gravitational sagging is not negligible. To minimize total sagging from gravitational and electro-static forces, we set the tension of sense wires at 145 gw and that of other wires at 500 gw to equalize the gravitational sagging of all the wires (250 $\mu$m). The displacement of sense wires from their nominal positions due to electro-static force is calculated to be from 25 to 54 $\mu$m assuming massless wires in the multi-cell configuration. The accuracy in machining of the chamber endplate is 10 $\mu$m.

The total number of jet-cells is 1200 and the total number of wires is 115000. The total wire tension is 50 tons, which is tolerable for the following mechanical structure. To support the total wire tension, the outer cylinder is made of CFRP of 5 mm thickness and end-plates are made of aluminum of 25 mm thickness. When the end-plates are supported by the outer cylinder only, the displacement at the inner edge of the end-plate is estimated to be 8 mm.

### 3.3.3 Readout Electronics

The central tracking device should have good spatial resolution and two-track separation capability in a multi-hit environment. Also fairly good resolution on the charges of the ionization pulses is required to have rough z-coordinate information by the charge division method.

To meet these requirements, slow repetetion rate of the JLC ($\sim$ 200 Hz) allows the use of waveform sampler (Flash ADC), which logs the whole time developement of the drift chamber signal. The chamber signal will be readout from the both ends of sense wires.

Output from amplifiers will be fed to Flash ADC's with 12 bits for energy bin and 1024 time bins clocked at the rate of 200 MHz, i.e. total time window of 5 $\mu$s with a time slice of 5 ns. The conceptual block diagram is shown in fig.3.10.

Making use of the full information on the waveform, accurate determination of the arrival time is possible by the double threshold leading edge method[4]. The time resolution will be a fraction of the time slice of the sampling, hence the contribution on the spatial resolution of $\sim 20\mu m$ from the electronics systyem is expected in our case. By sampling the whole waveform, we can also get the drift time and the charge of the the multiple hits, even if we have the later

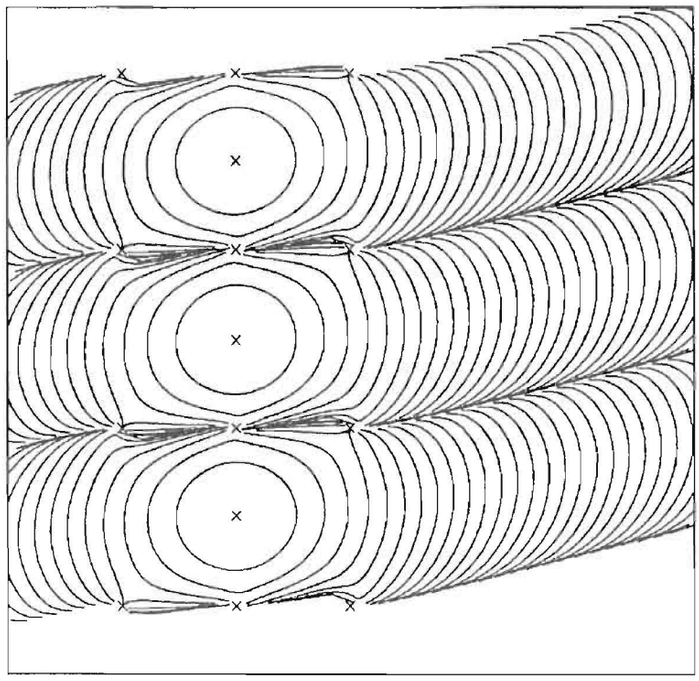

Figure 3.9: Equi-drift time map.

one overlapped with the tail of the first pulse. This is essential to the efficient tracking in the multi-hit environment.

## 3.4 Calorimeter

### 3.4.1 Design Criteria

Our primary purpose at the first stage of the JLC experiment is to detect the intermediate mass Higgs boson if it exists. Such a Higgs boson should be produced by $Z^0$ associated processes at JLC energies, and can be most clearly detected when the $Z^0$ boson is identified through its leptonic decay into electrons or muons. Although the branching fractions of these decay modes sum up to only 7%, the good momentum resolution of charged leptons measured by the CDC is of great help in identifying the Higgs boson as a recoiling system of these lepton pairs. Other decay modes of the $Z^0$ boson have larger branching fractions: quark pair decays have about 70 % branching fraction and neutrino modes have about 20 %. If we can make use of these decay modes, the intermediate mass Higgs boson can be discovered evev if the luminosity of the JLC is not as large as expected.

In the absence of charged lepton pairs in the final state of the $Z^0H^0$ process, the mass of the Higgs boson should be solely reconstructed from the invariant mass of the dijet with $b$-quark flavors. With the help of $b$-flavor tagging by the vertex detector, background events from $W^+W^-$ pair production process can be greatly suppressed and practically can be ignored. The most significant background for the hadronic detection of the intermediate mass Higgs boson come from the $Z^0Z^0$ pair production process, resulting in four hadronic jet or two hadronic

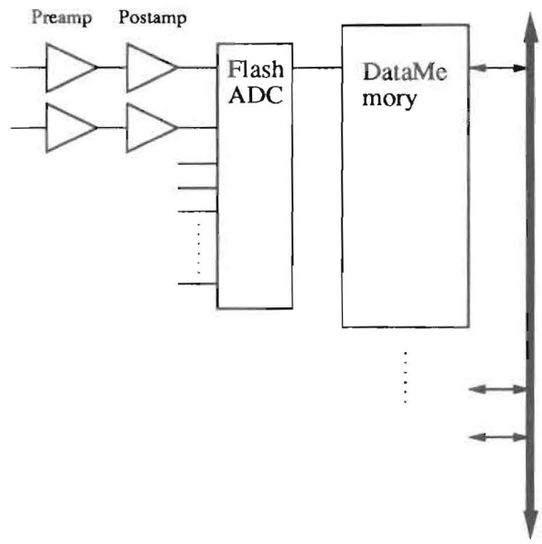


Figure 3.10: Schematic diagram of waveform sampling.

jet final states. Especially good jet-invariant mass resolution is required in order to separate reconstructed Higgs bosons from background $Z^0$ bosons in this mass region of the Higgs.

Detector induced effects on the dijet invariant mass resolution include:

- calorimeter segmentation,
- calorimeter energy resolution and
- nonlinearity of the hadron calorimeter.

The calorimeter segmentation is closely related to the position resolution of reconstructed hadronic and electromagnetic clusters and to the separation of two detected clusters. If we can measure the position of the hadronic clusters precisely, and separate two nearby hadronic clusters inside hadronic jets, then charged particles detected in the central tracking chamber can be correctly connected to these clusters. Precisely measured momenta of these particles by the CDC will greatly improve the invariant mass resolution of the dijet.

We have studied the dijet invariant mass resolution of our detector. We assumed a calorimeter based on interspersed scintillator plates and Pb absorber plates. Its inner surface is located at 2.5 m in radiusand is about 6 m long. The first 40 layers form the electromagnetic calorimeter (ECAL) and the remaining layers form the hadronic calorimeter (HCAL). In order to measure shower position precisely, Si pads of $1 \times 1\text{cm}^2$ are put into ECAL at a depth of 4.3 radiation length, which provide a position measurement of about 3 mm resolution. Each calorimeter wedge contains four ECAL towers of about $10 \times 10\text{cm}^2$ at the inner surface of the barrel part and one HCAL tower of about $20 \times 20\text{cm}^2$ at its innermost surface. The energy resolutions of these modules are assumed to be:

$$\begin{aligned} \sigma_E/E &= 15\%/\sqrt{E} \oplus 1\% \text{ for ECAL and} \\ \sigma_E/E &= 40\%/\sqrt{E} \oplus 2\% \text{ for HCAL.} \end{aligned}$$

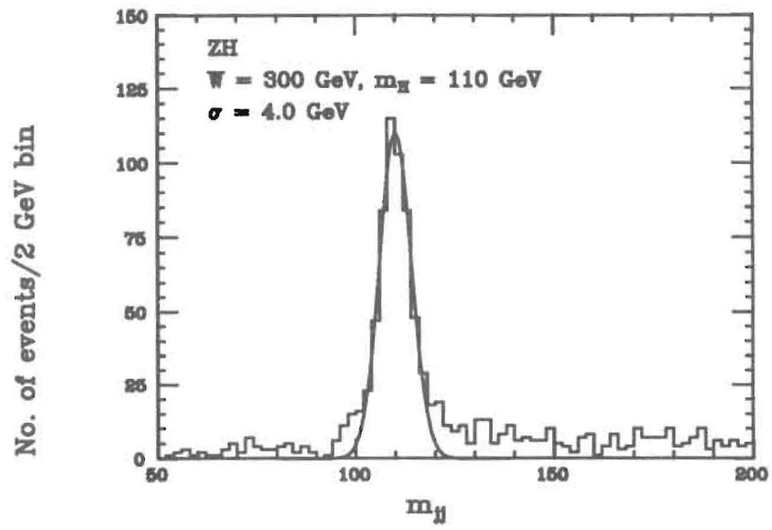


Figure 3.11: Jet mass resolution for Higgs

In Fig. 3.11, we present the result of a calculation of the dijet mass resolution for our model calorimeter. We can get reasonably good jet mass resolution with the assumed detector. A design of the calorimeter which can achieve the assumed performance is described in the following subsections.

### 3.4.2 Detector Configuration

In order to achieve good hadron energy resolution, a compensated lead/plastic scintillator(PMMA) sandwich calorimeter scheme is adopted. It consists of a fine-sampling ECAL of 29 radiation lengths, a coarse-sampling HCAL of 5.6 interaction lengths, and a silicon pad detector located behind the first $4.3X_0$ of the ECAL. The schematic view of the calorimeter assembly is shown in Fig. 3.1. The whole calorimeter is placed inside the solenoid to achieve good energy resolution and hermeticity. It has a tower structure and each tower nearly points to the interaction point.

The ECAL consists of 40 layers of 4mm thick lead plates and 40 layers of 1mm thick PMMA plates. Its thickness is chosen to contain 250 GeV electron shower. According to simulations[5], this configuration is expected to give a stochastic term for the energy resolution of

$$\sigma_E/E = 15\%/\sqrt{E} \oplus 1\% \tag{3.1}$$

for EM showers, where a constant term of 1% is assumed. Beam test results by ZEUS[6] and SPACAL[7] also support this estimation for the stochastic term, while the constant term of 1% is a bit of a challenge. The segment size is 10cm × 10cm, which is too big to calculate the shower center position from the energy deposit distribution over different segments. Instead, a silicon pad detector is installed. This is described later. The particle densities of reactions are thin enough to avoid multiple neutral particles coming into one segment.

The HCAL consists of 8mm thick lead plates and 2mm thick PMMA plates. The total thickness is 120cm (5.6 interaction length) which is limited by the available space and by mechanical strength. The ECAL and HCAL give 6.5 interaction lengths in total, which is thick

enough to contain 98% of a 20GeV pion's energy and 95% of a 200GeV pion's energy. This configuration is expected to achieve an energy resolution of

$$\sigma_E/E = 40\%/\sqrt{E} \oplus 2\% \tag{3.2}$$

for hadrons, extrapolated from the results of SPACAL[7]. The segment size is 20cm × 20cm and one segment contains 75% of the energy of a 10GeV pion shower when it is injected at the center of the segment[6].

Photons from the scintillator are collected by wave length shifter plates (WLS) located on both sides of the scintillator plates of the HCAL, and at one side of those of ECAL. Position dependence of the light output is corrected using the silicon pad information. The WLS's extend to the bottom of the tower, and photo-diodes are attached at the ends to read out the photons. About 2000 photo-electrons are expected to be obtained as an output of the photo-diode for a 1GeV shower. The noise level of the preamp is about 700 electrons (FWHM) equivalent if typical photo-diodes are used, which corresponds to about 300MeV. This noise level is a little too high, and APD's or forth-coming devices like VLPC or image intensifier+CCD may be needed[9]. In order to avoid the WLS walls pointing to the interaction point, the tower projection has a little offset in both the $\theta$ and $\phi$ directions.

A silicon pad detector (Si-pad) is located after the first $4.3X_0$ of the ECAL. A pad size of 1cm × 1cm is presently assumed, and this achieves a position resolution of about 3mm. This good position resolution is necessary for track-cluster matching. Excellent two-cluster recognition can also be achieved, and these help to identify particles and to assign the correct energy to photons when photons overlap charged particles. The pads give a signal of 16000 electrons for minimum ionizing particles, and can separate e, $\mu$ and $\pi$ in combination with ECAL and HCAL energy information. The system is expected to achieve a pion rejection factor of about 1/50 for an electron efficiency of 90%[8].

### 3.4.3 Mechanical Structure

Calorimeter towers are assembled to the whole detector as shown in Fig. 3.1. The barrel part has an inner radius of 2.5m, the outer radius of 4.0m, and the length of 6m, and it consists of 2500 towers. Each tower weighs about 600kg, and the total weight of the barrel part is about 1500 tons. This weight is supported by a half-cylinder with negligible deformation as shown in Fig. 3.12. The towers are first attached to a ring, and the rings are then placed on the support cylinder. During the tower construction, it stands vertically while lead and scintillator plates are stacked. In order to attach the towers to a ring, the towers must have a self-supporting structure so that we can lay them horizontally to attach them to the ring structure. This can be achieved by mounting each component in a box made of 2mm thick stainless steel as shown in Fig. 3.13. This simple structure can hold the weight of 600kg with a maximum displacement of 1mm at the front face of the tower even when the tower is held horizontally and fixed at the bottom end only. After attaching them to the ring, each ring is put on the supporting cylinder, slidden inward, and fixed at the design location. The half-cylinder is made of 10cm thick stainless steel and is supported by the iron structure. The solenoid is divided into three pieces as shown in Fig. 3.1 to support the cylinder not only at both ends but also at two additional points between the ends. This four-point support has a maximum deformation of only 10$\mu$m at the center of the cylinder, while a several millimeter deformation is introduced if the cylinder is supported only at both ends.

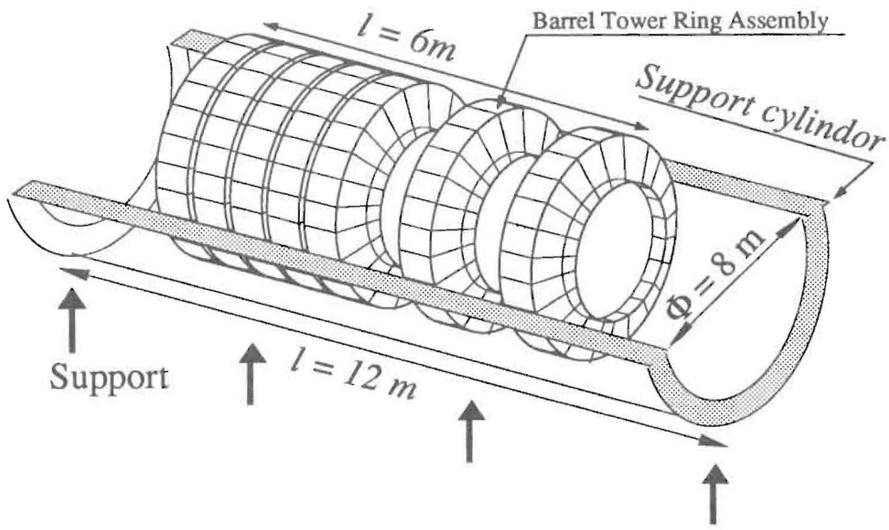


Figure 3.12: Schematical view of the calorimeter assembly

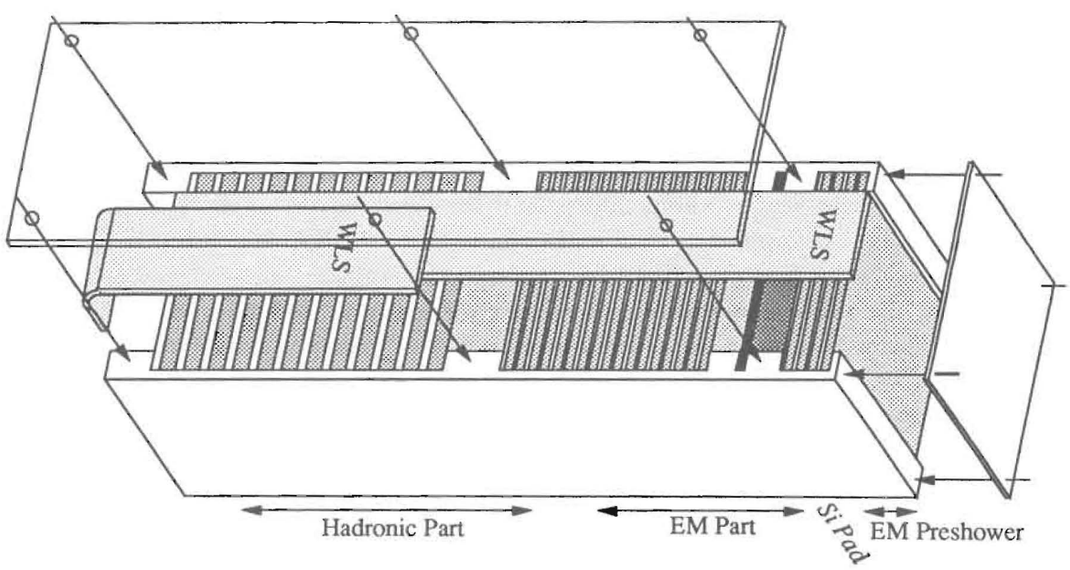


Figure 3.13: Schematical view of the calorimeter tower

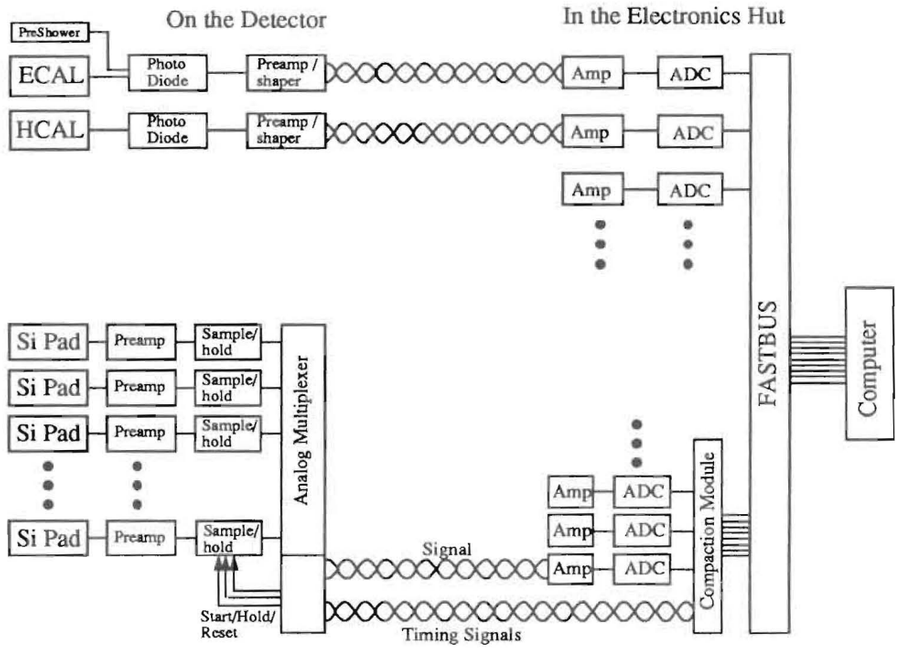


Figure 3.14: Layout of DAQ system

Each endcap calorimeter assembly has an outer radius of 4m, an inner radius of 0.35m, and a thickness of 1.5m. It has a tower structure similar to the barrel part. Each endcap calorimeter consists of about 1250 towers and weighs about 640 tons.

### 3.4.4 Electronics

Photons from the scintillators are collected by WLS's and are read out by photo-diodes because the whole calorimeter is placed in the magnetic field. Low noise preamps are located in each tower. The capacitances of both the photo-diodes and the Si-pads are about 80pF, which gives a noise level of $\sim$ 700 electrons (FWHM). The dynamic range of the signal is from $\sim$ 100 MeV ( well below the MIP signal on ECAL ) to $\sim$ 250GeV ( Bhabha electron energy at $\sqrt{S}$ = 0.5TeV), which can be measured with a standard bi-linear 12bit ADC. The number of channels for ECAL and HCAL is only 20k and 5k, respectively. Thus the calorimeter signals are easily delivered to the electronics hut, amplified, and read out with a conventional FASTBUS ADC system as shown in Fig. 3.14.

The Si-pad detector has $2 \times 10^6$ channels in total, and to read out these signals is not trivial. To lay down two million cables from the detector to the electronics hut is not a practical solution. Thus we will install an analog multiplexer in each tower and transmit 400 channels of data serially to the electronics hut. These data are pedestal-suppressed by compaction modules and read out through FASTBUS.

## 3.5 Muon Detector

### 3.5.1 Design Criteria

The requirements for the muon detector are rather simple because it need not measure the momentum of muons, it simply needs to tag muons.

Since the CDC has very good momentum resolution, the muon momentum is known very precisely once a matching between a CDC track and muon detector hits is successfully made. For this purpose, many position measurements along the muon track are essential, while the resolution of each position measurement is not so important. Timing measurements are also needed to reject cosmic ray muons. Modest timing resolution can reject cosmic ray muons effectively since the duty factor of the data taking is very low.

Muons are usually the cleanest signal in a search for new particles, and we must minimize the region which is not sensitive to muons.

### 3.5.2 Detector Configuration

The muon detector consists of six super-layers of single-cell drift chambers and one layer of plastic scintillation counters as shown in Fig 3.15.

In the case of the barrel part, the innermost and outermost super-layers are located inside and outside of the flux return yoke, respectively, and have four layers with xx'yy' wire configuration to measure both $\phi$ and z coordinates. The remaining four super-layers are interleaved between the yokes and have two layers with an xx' configuration to measure the $\phi$ location only. Each layer consists of a single-cell drift chamber with a cell size of 10cm $\times$ 5cm and a wire length of 10m. A wire support is located at the middle of the wire to reduce the wire sag. Using 100$\mu$m $\phi$ tungsten wire with 600g wire tension introduces a sag of $\sim$ 450 $\mu$m, and this dominates the position resolution of the chamber.

The endcap muon detector has a super-layer configuration similar to the barrel part except that two interleaved super-layers have an xx' configuration while the other two have yy'. The wire lengths differ according to the location and the length of the longest wire is 15m, which needs two mid-supports.

The total number of channels is 7700 for the barrel part and 2400 for each endcap part. These can easily be sent to the electronics hut and read out with conventional TDC's.

### 3.5.3 Expected Performance

The position resolution of each interleaved layer is about $\sim$ 500 $\mu$m, which is dominated by the wire sag. Once the z-coordinate of the hit is determined, the resolution can be improved by making a wire-sag correction. However, 500$\mu$m resolution is good enough to identify muons. The innermost and outermost super-layers can achieve much better position resolution by themselves because they have both z and $\phi$ measurements.

Muons must have a momentum of at least 3.5GeV/c to be identified as a muon by the muon detector. This is due to the large energy loss of $\sim$ 2GeV by the calorimeter.

The polar angle coverage of $\mid cos\theta \mid < 0.99$ is achieved without any insensitive region. A detection efficiency better then 99% can be achieved over this polar angle range.

The effect of the background muons from the beam line has not yet been studied in detail, but we expect that magnets can effectively sweep out these background muons as will be

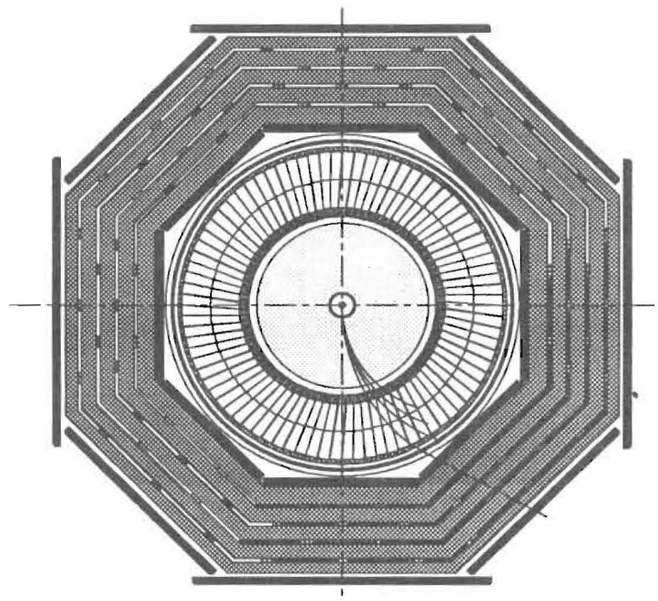

Figure 3.15: Layout of the muon detector.

described in section 4.7.

## 3.6 Superconducting Solenoid Magnet

### 3.6.1 General Characteristics

We require that the superconducting solenoid magnet is placed outside the calorimeter to achieve good hermeticity. The solenoid magnet has a structure shown in Fig. 3.16 and parameters listed in Table 3.3. The bore diameter is 9 m and the overall length is 10 m. To simplify the assembly procedure and also to provide a rigid support for the carolimeter, we divide the magnet into three parts. Each part is 2.6 m in length and is equipped with its own separate cryostat. The central part and both of the end parts consist, respectively, of 257 and 278 turns of double layer coaxial coil windings. This configuration is to compensate the field drop along the beam axis.

The superconducting magnet requires a relatively thick iron yoke to ensure the 2 Tesla uniform field in the central tracking region. In order to keep the maximum field in the iron yoke below 2 Tesla, we need a total amount of 11,500 tons of iron. The flux line distribution is shown in Fig. 3.17, where the magnetic field uniformity in the tracking region is better than $\pm 0.6$ % of the central field.

The overall inductance of the magnet is 5.5 H. Consequently, the total stored energy is 1.1 GJ, when the magnet is operated at 20 kA to produce the 2 tesla central field.

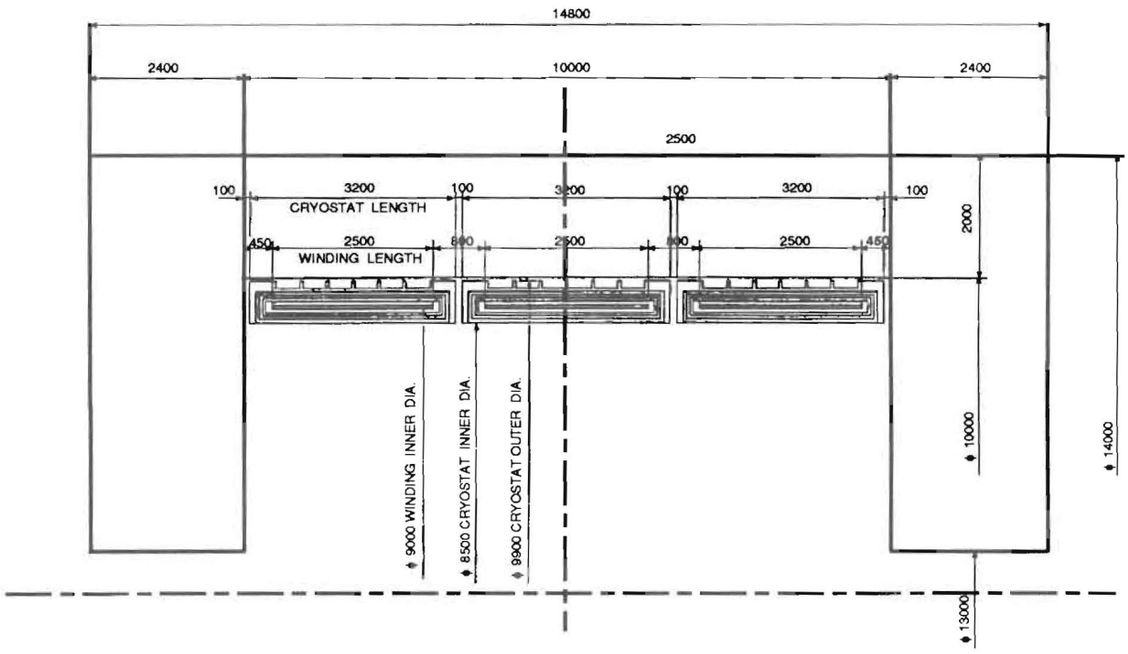


Figure 3.16: Configuration of the solenoid magnet

| | | |
|---|---|---|
| Coil bore diameter | 9 | (m) |
| Total length | 10 | (m) |
| Inner diameter of the cryostat | 8.5 | (m) |
| Outer diameter of the cryostat | 9.9 | (m) |
| Number of modules | 3 | |
| Operation current (2Tesla) | 20,000 | (A) |
| Inductance | 5.5 | (H) |
| Stored energy | 1.1 | (GJ) |
| Refrigeration load at 4.2K | 330 | (W) |
| Weight of the conductor of each module | 52 | (tons) |
| Total weight of the conductor | 151 | (tons) |
| Weight of one piece of the coil | 120 | (tons) |
| Magnet weight without iron | 720 | (tons) |
| Conductor length of each module | 8.0 | (km) |
| Total conductor length | 24 | (km) |
| Total weight of the magnet with iron | 12,000 | (tons) |

Table 3.3: Parameters of the superconducting solenoid

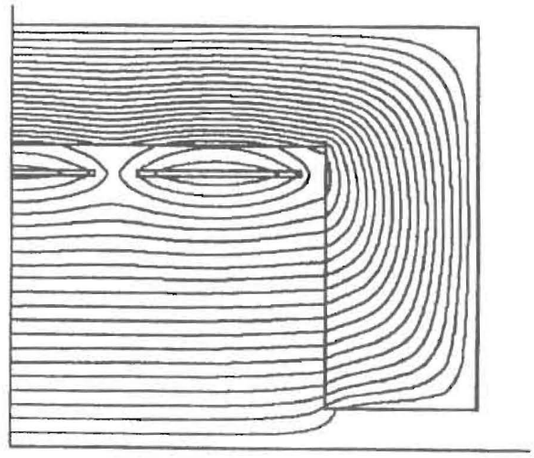

Figure 3.17: Flux line distribution

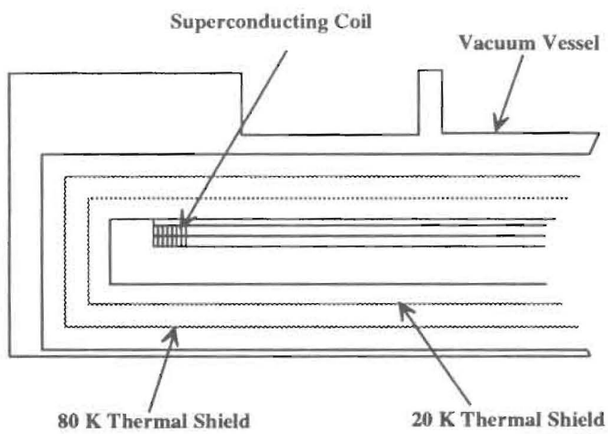


Figure 3.18: Cryostat of the solenoid

### 3.6.2 Cooling System

There are two reliable cooling methods: the conventional pool boiling and the cooling by the flow of two-phase helium that has a large heat capacity owing to the latent heat at the low temperature. The JLC detector magnet needs approximately 15,000 liters of liquid helium, when cooled by a pool boiling system. Such a large volume of liquid helium cannot be brought back to its circulator, when the magnet gets quenched. We are forced to release the resultant helium gas to the atmosphere. The duct system to make it possible is impractical, since the experimental hall is expected to be in deep underground. Therefore, it is absolutely necessary to reduce the amount of the liquid helium in view of safety.

This can be achieved by a direct cooling system employing the flow of two-phase helium through a cooling path in the conductor. The required amount of the liquid helium in this system is about 500 liters, which is 1/30 of that required by a pool boiling system.

The cryostat for this magnet is shown in Fig. 3.18. The cryostat is a vacuum chamber with superinsulation. The two shields covering the coil are kept at 20 K and 80 K, respectively, by the helium gas from the refrigerator. The 20 K shield is essential to help further reduce the

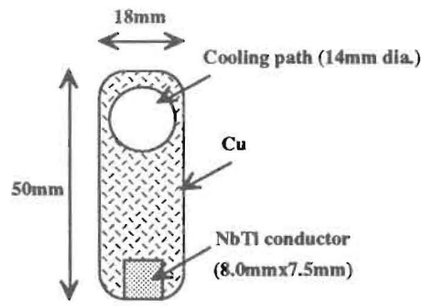


Figure 3.19: Cross section of the superconductor

| | | |
|---|---|---|
| Dimensions | $50 \times 18$ | ($mm^2$) |
| Length of one piece | 800 | (m) |
| Diameter of the cooling path | 14 | (mm) |
| Critical current at 4.2K in 2Tesla | 50,000 | (A) |
| Superconductor | Nb-Ti | |
| Ni-Ti:Cu | 1:2 | |
| Nb-Ti:Cu overall | 1:36 | |
| Number of filaments | 10200 | |
| Diameter of filament | 50 | ($\mu$m) |
| Stabilizer | Cu | |

Table 3.4: Parameters of the superconductor

helium amount by controlling the pressure drop to less than 0.2 kg/cm$^2$.

The total heat load at 4.2 K is estimated to be 330 W. Therefore, a medium class refrigerator with a cooling power of 500 W (corresponding to electric power consumption of 500 kW) is enough to operate the magnet.

### 3.6.3 Superconductor

The coil is made of a Nb-Ti/Cu multifilamentary superconducting composite. The Cu/SC ratio is chosen to be 2.0 for easy mechanical handling. A cross-sectional view of the conductor is given in Fig. 3.19 and the main parameters of the superconductor are listed in Table 3.4. The operation current and the temperature are 20 kA and 5.0 K, assuming that the helium pressure at the inlet is 0.3 $kg/cm^2$ and the local temperature rise is 0.5 K. On the other hand, the critical current of the conductor is 40 kA at 5.0 K in a 3 Tesla field (50 kA at 4.2 K in the same field). The stabilizer of the conductor is made of Cu and the current density of this Cu part is 25 A/mm$^2$ when the magnet gets quenched. This current density is low enough to keep the local maximum temperature rise less than 80K, so that the magnet is safe from local mechanical stress.

### 3.6.4 Energy Extraction

The stored energy has to be safely extracted, on encounter with a quench. In our magnet design, all of the three modules are connected to a single dump resistor of 0.1 $\Omega$, which absorbs all of their stored energy, even when only one of them gets quenched. This ia to avoid unbalanced force between the coils and the iron yoke. The maximum voltage at the energy extraction is 2 kV between the current leads.

## 3.7 Background and Masking System

### 3.7.1 Introduction

Three types of background problems have to be considered for the experiment at JLC-I. They are (a) high energy muons that are produced through electromagnetic interactions between the incoming beam and collimating materials in the upstream collimation section, (b) synchrotron radiations emitted by the beam when it traverses through the beam line magnets, particularly the final focus lens, and (c) $e^+e^-$ pairs created in beam-beam collision at interaction point(IP).

Collision parameters are optimized to minimize these backgrounds while a luminosity is kept to be maximal value. The masking system in the interaction region is carefully designed to minimize such $e^+e^-$ pair background and synchrotron radiation photons. We developed a design where the photons would not enter the active detector volume unless they are emitted by electrons/positrons beyond transverse offsets of $\pm 6\sigma_x$ or $\pm 35\sigma_y$ which are the nominal values of our collimation scheme. Here the $\sigma_x$ and $\sigma_y$ denote the size of the design emittance beam. In this calculation the beam is assumed to have a bi-Gaussian transverse distribution up to $\pm 3\sigma_{x(y)}$, followed by a 1 % flat tail beyond it.

Should synchrotron radiation backgrounds turn out be unacceptably large in the real life, two possibilities have to be examined: (1) the core emittance of the beam is too large, or (2) the lateral tail spread of the beam is too large. In case of (1), if the emittance cannot be rapidly improved, the experiment may be run by increasing $\beta^*$, thus by reducing the lateral spread of synchrotron radiations at IP. In case of (2), if the reduction of beam tails turns out to be difficult, we need to resort to some beam collimation. It should be pointed out that the causes (1) and (2) are likely to occur (if they do) simultaneously. Hence the counter measures will have to be a combination of emittance improvement, optics retuning, beam tail reduction, beam collimation and others.

With beam collimation with metallic slits we create a possibility of high energy muon productions. Such muons can travel along the downstream beam line and penetrate the detector longitudinally, leaving huge energy deposits in the calorimeter and elsewhere. They can cause serious problems in the trigger and data analysis. The flux of muons depends on the tightness of the collimation as well as presence of downstream beam line components. For this reason an excessive beam collimation could turn out to be counter-productive. It should be used with a care, to reduce production of secondary tails off the collimation materials as well as to avoid an emittance growth due to collimator wake fields.

In subsequent sections we describe our strategies on how to handle those backgrounds.

### 3.7.2 Muons

It is difficult to estimate how many muons will be created in the collimation section since we do not know the mechanism to create a beam tail. Of course there is no muon background problem with no tail, *i.e.* gaussian beam. Total number of muons($N_\mu$) per electron are calculated as a function of incident electron energy($E_e$) by MUON89[10] code and it is approximately expressed as,

$$N_\mu = 3.9(2.3) \cdot 10^{-4} \cdot E_e(\mathrm{GeV})/250 \quad \text{for} \quad \mathrm{E}_\mu > 2(5)\mathrm{GeV}. \tag{3.3}$$

The muons may be created as many as $2.8(1.7) \cdot 10^6$ because of $N_\mu \cdot 72$ (bunches/train) $\cdot$ $10^{10}$ (e's/bunch) $\cdot$ $10^{-2}$(1% tail). Typical scattering angle of muon ($\theta_\mu$) is $m_\mu/E_\mu$, *i.e.* $\theta_\mu = 1$ mrad for $E_\mu = 100$ GeV. Since a distance between a collimator and IP is about 1 km, these muons are spread over detector. Low energy muons($E_\mu <$ a few GeV) can be easily absorbed in concrete of 10 m thickness. In order to control them JLC-I has a collimation section in the final focus system. It comprises a collimator(30 radiation length), a muon attenuator[11] and "big bending" magnet( $\sim$ 15 mrad).

The penetrating probability after a collimator is mainly come from an edge scattering and it has been calculated to be $10^{-4}$ by R.Nelson[13]. Our collimation scheme employs "twice" collimation, that is, the beam is collimated twice at least in its phase space($x, x', y, y'$ and energy). Therefore no sizable tail is expected downstream the collimation section. The probability of repopulation in a tail is also estimated to be $10^{-7}/n^2$ per 1km beam line with the vacuum of $10^{-10}$ torr, where $n$ is the position ($n\sigma_{x(y)}$) of the repopulation, provided that the repopulation is due to Coulomb scattering between electron/positron and residual gas ion(CO)[14]. In our case of $\pm 6\sigma_x$ of the collimation and about 1km between the collimation and IP, the probability is less than $3 \cdot 10^{-9}$. The corresponding number of particles in the tails is $3 \cdot 10^3$/train at most , which is acceptable. The detailed description of the collimation section is found in "Final Focus System" of this proposal. It should be stressed that high vacuum ($< 10^{-10}$ torr) is highly desired in final focus system in order to avoid scatterings of tail particles at QC1 pole tips *etc.* as well as synchrotron radiations .

The principle idea of muon attenuation is to confine muons inside iron pipe which has two axial magnetic fields of 1 Tesla in opposite directions corresponding to $\mu^+$'s and $\mu^-$'s, then simultaneously absorb muons[12]. The length of the muon attenuator is mainly determined by muon ranges and it is about 100 m at most, where muon range in iron is 56(98) m for $E_\mu$=100(200) GeV[15]. With this scheme there is expected to be negligibly small number of muons at IP.

### 3.7.3 Synchrotron Radiations

*A. Last Bending Magnet*

Since the last bending magnet is located at 117.4 m from IP and its total bending angle is 0.55 mrad, synchrotron radiations are horizontally spread up to 6.4 cm at IP. The critical energy is about 1 MeV and the intensity is almost same as the beam intensity (O($10^{12}$)/train). As a half aperture of final quadrupole magnet QC1 is 0.67 cm, it is necessary to shield the synchrotron radiations. For this purpose a mask is installed at 61 m from the last bending magnet, near QC3. The mask can be made by 21cm long tungsten which corresponds to $20\lambda$ ( $2 \cdot 10^{-9}$ attenuation ) for a few MeV photons. Since its minimum (half) aperture is 0.3 cm

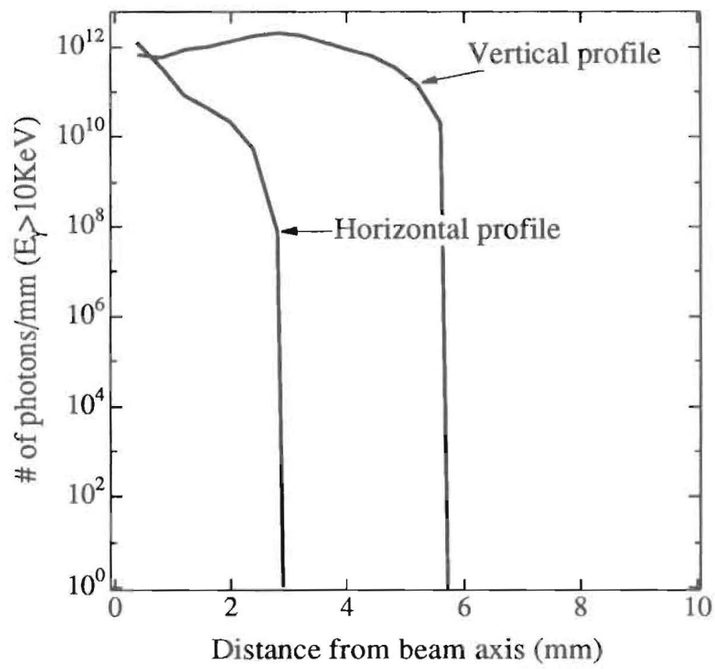


Figure 3.20: Profile of synchrotron radiation per train crossing from QC4-QC1 at the front face of QC1 seen from IP,*i.e.* 2.5m upstream from IP for $E_{beam}$ =250GeV.

in horizontal and vertical directions, which correspond to $22\sigma_x$ and $264\sigma_y$, respectively, there is no emittance growth due to a wake field by the mask. There is no secondary particles ($e^{\pm}$'s and $\mu^{\pm}$'s) created at the mask because no beam tail can hit it. With this mask the synchrotron radiation is well collimated to 1 cm at IP.

*B. Quadrupole Magnets*

There are only 4 quadrupole magnets, QC1 - QC4, in a straight section between the last bending magnet and IP. Among them QC2 is the largest radiation source. Here we do not consider any mask since a doublet of final quadrupole magnets (QC1 and QC2) is so near IP that there is no way to stop back-scattered synchrotron radiations from the mask. The control of synchrotron radiations from the quadrupole magnets is uniquely provided by the optics of the final focus system. The optics is carefully determined in order to have a large bore (1.34 cm $\phi$) of QC1, which is enough for the synchrotron radiations to go through without scattering for the beam collimated at $\pm 6\sigma_x$, $\pm 35\sigma_y$. The tail of the synchrotron radiations is also produced by the tail of beam. Figure 3.20 shows the lateral spread of radiations from QC3,QC4,QC2 and QC1 itself in front face of QC1, *i.e.* 2.5 m upstream of IP. Tolerable number of photons is $O(10^7)$ for x,y > 0.67cm in this figure, which may hit the "iron" pole of QC1 and back-scatter into IP. As discussed in the previous section there must be tails up to $10^4$ photons beyond sharp cuts of the lateral spreads in Fig.3.20. We show Fig.3.21 to see how the radiations go through QC1. In Fig.3.21 cross sectional views of radiations are shown at the entrance and the exit of QC1. The two off-axis profiles are those of the radiations with exit beam (after collision) since a crossing angle is 8 mrad at $E_{beam}$ =250GeV and QC1 is 2.4 m long, whereas the profile at the center is that of focusing beam (before collision). Therefore there is no serious background problem of the synchrotron radiations.

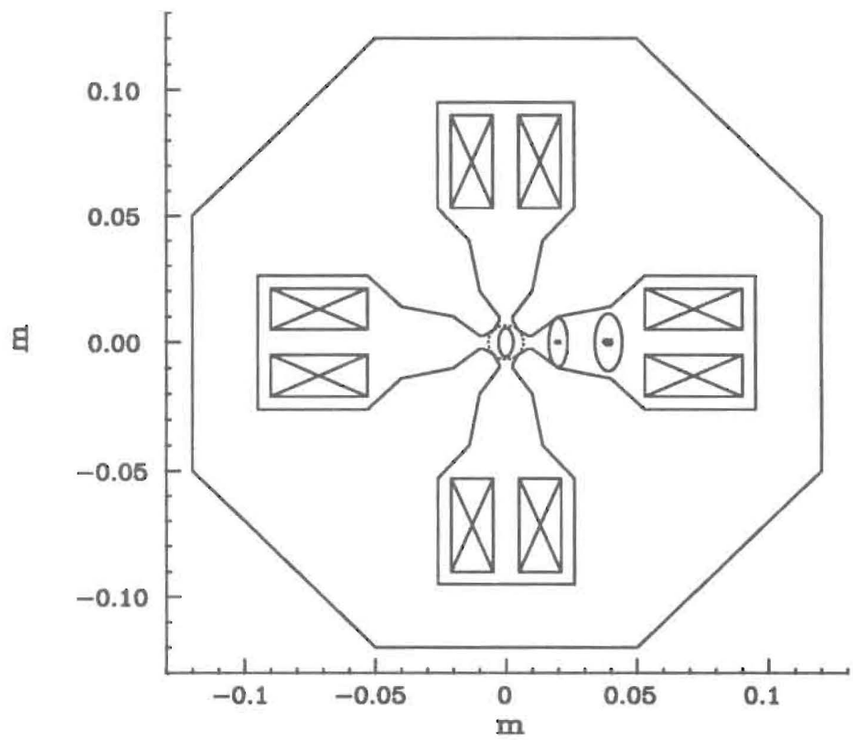


Figure 3.21: Cross sectional views of incoming and outgoing synchrotron radiations, which are shown as ellipses, at the entrance and exit of QC1, for $E_{beam}$=250GeV, where the crossing angle of two beams is 8 mrad. QC1 is located at 2.5m upstream from IP, and its half aperture and length are 6.7mm and 2.4m, respectively. Its coils are indicated by crosses boxes. Disrupted beams after collision are also plotted by dots.

### 3.7.4 $e^+e^-$ pairs

$e^+e^-$ pairs are created in coherent[16] and incoherent processes at linear colliders. The coherent process is the beamstrahlung photon conversion by a strongly collective magnetic field produced by the opposing beam. Its probability depends mainly on a beamstrahlung parameter($\Upsilon$). Since the condition of $\Upsilon \sim 1$ corresponds to a threshold for a photon of beam energy to convert into an $e^+e^-$ pair in the magnetic field and the pair creation with $\Upsilon < 1$ is exponentially suppressed as $\exp(-16/8\Upsilon)$, coherent pairs is only relevant at a linear collider with $\Upsilon \geq 1$. For JLC- I the number of coherent pairs are negligibly small because of $\Upsilon = 0.093(0.19)$ at $E_{beam}$=150(250) GeV. On the contrary, the incoherent process comprising (a) BW (Breit-Wheeler): $\gamma\gamma \rightarrow e^+e^-$, (b)BH (Bethe-Heitler): $\gamma e^\pm \rightarrow e^\pm e^+e^-$, and (c)LL (Landau- Lifshits): $e^+e^- \rightarrow e^+e^-e^+e^-$ has no such energy threshold and it is proportional to luminosity, where $\gamma$ is a beamstrahlung photon, and its number is about one per a beam particle for JLC-I. Their typical cross sections are (a)BW: $1.9 \cdot 10^{-27}\text{cm}^2$, (b)BH: $2.2 \cdot 10^{-25}\text{cm}^2$ and (c)LL: $4.5 \cdot 10^{-26}\text{cm}^2$ at $E_{beam}$=250 GeV. As luminosity per bunch crossing is very high, which is $1.0 \cdot 10^{30}\text{cm}^{-2}\text{bunch}^{-1}$ at $E_{beam}$=250 GeV, enormous number of pairs are created at each collision, then they may kill an experiment.

The backgrounds of the pairs can be classified in two ways, *i.e.* (i) primary and (ii) secondary background. The former comprises pairs which directly enter a detector region, then overlap a physics signal. The most affective region of a detector is for a vertex detector because of the small transverse momenta of the pairs. The latter comprises secondary particles,*i.e.* neutrons and photons, which are created in a collision between the pairs and a pole tip of QC1. The number of neutrons($N_n$) is proportional to the total deposit energy of the pairs ($\Sigma E_e$), *i.e.* $N_n \sim 0.13 \cdot \Sigma E_e$, while the number of photons($N_\gamma$) is proportional to the total number of the pairs ($\Sigma N_e$), *i.e.* $N_\gamma \sim \Sigma N_e$. To quantitatively estimate these backgrounds we simulate the pairs by ABEL. For the generation of the pairs ABEL takes account of inherent scattering angles of the pairs, which can be larger than their characteristic angles of $m_e/E_e$, a geometric reduction due to smaller beam spot size (especially in vertical direction) than the typical impact parameters and an effect of strong external field. In ABEL the pairs are kicked by the strong electromagnetic field produced by the opposing beam, then they can acquire larger transverse momenta than the inherent ones. The final scattering angle ($\theta_e$) is the sum of the inherent angle ($\theta_e^\circ$) and kick angle ($\theta_{kick}$). The detailed description of this simulation is found elsewhere[17].

Figure 3.22 shows a scatter plot of the pairs in a plane of the final scattering angle (horizontal axis) and the transverse momentum (vertical axis). A sharp boundary is clearly seen in this figure, which corresponds to the maximum kick angle of the pairs ($\theta_e^\circ << \theta_{kick}$), and the pairs are seen to be also largely scattered beyond this boundary ($\theta_e^\circ >> \theta_{kick}$). The pairs in very forward angular region ($\theta_e < 0.15$ ) hit QC1 *etc.* , then the secondary photons are back-scattered. For further study of the primary background we plot the pairs of $\theta_e > 0.15$ ( outside of a mask which is described in next section ) as a function of their transverse momenta in Fig.3.23. The results are listed in Tab.3.5 for all cases of JLC-I at $E_{beam}$=150 and 250 GeV together with machine parameters relevant to background study. From $\Sigma E_e$'s in Tab.3.5 the total number of neutrons is $O(10^6)$ per train crossing. Typical energy deposit of a neutron is estimated to be about 0.1 MeV, which is normalized to electron energy, with a detection efficiency of $< 50\%$ in our calorimeters[18]. Assuming the neutrons spread uniformly over 20k channel calorimeter, energy deposit per channel is a few MeV, *i.e.* $10^6 \cdot 0.1(\text{MeV}) \cdot 0.5(\text{eff.})/(2 \cdot 10^4)$ . The other detector is less sensitive to neutrons. Therefore the neutrons cause no serious problem. Possible problems of secondary photons and backgrounds in a vertex detector will be discussed in subsequent sections.

Table 3.5: Characteristics of JLC-I

| $E_{beam}$ (GeV) | 150 | 150 | 150 | 250 | 250 | 250 |
|---|---|---|---|---|---|---|
| Band | S | C | X | S | C | X |
| $L$ (cm$^{-2}$sec$^{-1}$) $\times 10^{33}$ | 3.5 | 6.6 | 3.2 | 4.8 | 11. | 6.3 |
| $L$ (cm$^{-2}$bunch$^{-1}$) $\times 10^{29}$ | 15.3 | 6.1 | 2.4 | 17.5 | 10. | 4.7 |
| rep. rate (Hz) | 50 | 150 | 150 | 50 | 150 | 150 |
| number of bunches | 46 | 72 | 90 | 55 | 72 | 90 |
| bunch separation | 5.6ns | 2.8ns | 1.4ns | 5.6ns | 2.8ns | 1.4ns |
| $N_{e^\pm}$/bunch $\times 10^{10}$ | 1.56 | 1.0 | 0.63 | 1.30 | 1.0 | 0.63 |
| $\sigma_x$ (nm) | 335. | 335. | 335. | 301. | 260. | 260. |
| $\sigma_y$ (nm) | 3.92 | 3.92 | 3.92 | 3.04 | 3.04 | 3.04 |
| $\sigma_z$ ($\mu$m) | 80. | 80. | 85. | 80. | 80. | 67. |
| $\beta_x$ (mm) | 10. | 10. | 10. | 10. | 10. | 10. |
| $\beta_y$ ($\mu$m) | 100. | 100. | 100. | 100. | 100. | 100. |
| $D_x$ | 0.21 | 0.13 | 0.090 | 0.13 | 0.13 | 0.071 |
| $D_y$ | 18.0 | 11.5 | 7.7 | 13.0 | 11.5 | 6.1 |
| disruption angle: $\theta_\circ$ (mrad) | 0.88 | 0.57 | 0.35 | 0.49 | 0.44 | 0.27 |
| crossing angle: $\phi_c$ (mrad) | 11.0 | 10.4 | 9.0 | 7.3 | 8.0 | 7.2 |
| $\langle\Upsilon\rangle$ | 0.14 | 0.093 | 0.059 | 0.23 | 0.19 | 0.15 |
| $\Upsilon_{max}$ | 0.47 | 0.32 | 0.19 | 0.78 | 0.70 | 0.51 |
| energy loss ($\delta$) (%) | 7.0 | 3.5 | 1.7 | 9.0 | 7.0 | 4.0 |
| $n_\gamma$ | 1.7 | 1.1 | 0.74 | 1.6 | 1.4 | 0.91 |
| A | 1.3 | 0.95 | 0.74 | 1.0 | 0.93 | 0.66 |
| $1.65 \times P_t^{max}$ (MeV) | | | | | | |
| at $\theta$ =0.15 | 26.9 | 17.2 | 10.3 | 22.9 | 18.2 | 13.2 |
| $R_{mask}$ (cm) | 9.0 | 5.7 | 3.5 | 7.7 | 6.1 | 4.4 |
| $L_{mask}$ (m) | 0.60 | 0.38 | 0.23 | 0.51 | 0.41 | 0.29 |
| $\eta_{mask}(L_Q = 2.5\text{m}) \times 10^{-4}$ | 6.0 | 1.9 | 0.60 | 3.9 | 2.2 | 1.0 |
| total energy deposits(GeV) | | | | | | |
| and $e$'s/bunch | | | | | | |
| $\Sigma E_e$( no $\theta_e$ cut ) $\times 10^5$ | 1.8 | 0.60 | 0.17 | 5.8 | 3.0 | 0.91 |
| $\Sigma N_e$( 〃 ) $\times 10^4$ | 6.2 | 2.0 | 0.62 | 7.0 | 3.9 | 1.3 |
| $\Sigma E_e(\theta_e > .005) \times 10^4$ | 13. | 4.0 | 0.55 | 11. | 5.8 | 1.3 |
| $\Sigma N_e$( 〃 ) $\times 10^4$ | 5.4 | 1.7 | 0.49 | 5.1 | 2.8 | 0.96 |
| $\Sigma E_e(\theta_e > .050) \times 10^2$ | 5.4 | 4.9 | 0.94 | 21. | 9.2 | 2.2 |
| $\Sigma N_e$( 〃 ) $\times 10^3$ | 8.0 | 5.7 | 1.0 | 11. | 9.4 | 3.2 |
| number of hits($e$'s)/bunch | | | | | | |
| in $\lvert\cos\theta_e\rvert < 0.9$ | | | | | | |
| $r = 2$ cm | 429.4 | 117.8 | 63.1 | 350.2 | 100.4 | 81.6 |
| | (188.5) | (21.1) | (5.8) | (69.8) | (34.4) | (11.1) |
| $r = 5$ cm | 76.8 | 7.3 | 124. | 51.7 | 21.7 | 23.3 |
| | (14.6) | (4.7) | (2.8) | (10.9) | (6.8) | (2.9) |
| $r = 30$ cm | 2.3 | 1.1 | 0. | 1.4 | 0.3 | 0.3 |
| | (1.0) | (0.5) | (0) | (0.75) | (0.2) | (0.2) |

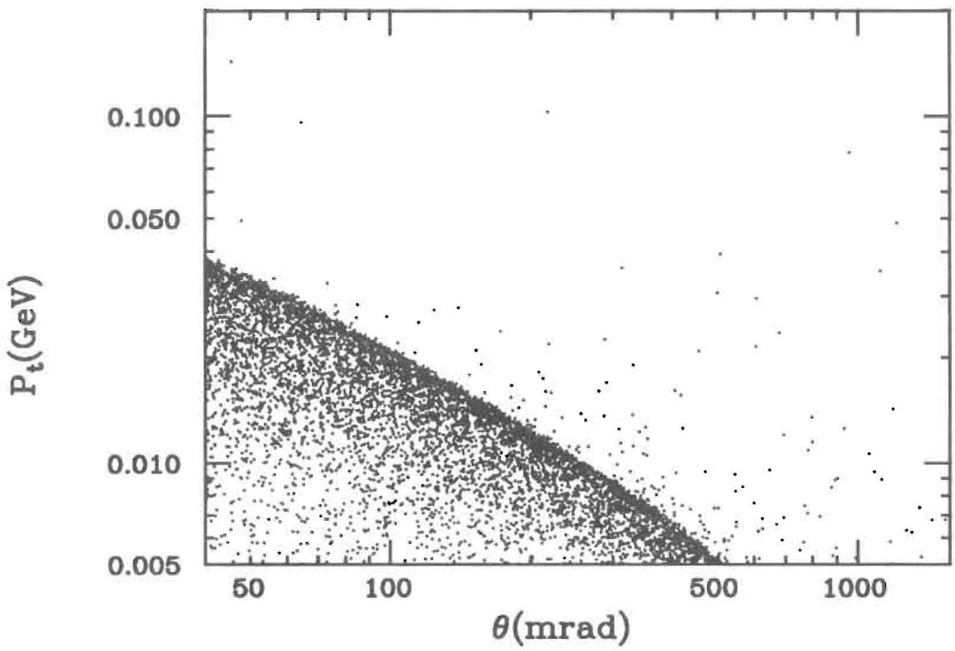


Figure 3.22: Pairs simulated by ABEL on a plane of $p_t$ and $\theta_e$ at $E_{beam}$=250GeV for JLC-I(c-band).

### 3.7.5 Masking System

Our masking system is schematically shown in Fig.3.24. A mask is employed in order to shield against the large amount of the secondary photons. The probability for the O($10^7$) photons/train (see Tab.3.5) to escape from the mask, $\eta_{mask}$, should be less than $10^{-3}$, which is geometrically determined by the front aperture of the mask. Most of the escaped photons hit the mask surface on the opposite side, then they enter the detector region. In addition the mask must have enough thickness to absorb the photons, that is, its attenuation coefficient should be less than $10^{-5}$ for 0.5MeV photons which corresponds to a 5cm thick tungsten. We require that the acceptable number of photons in the detector region is O($10^2$) per train crossing. As we fix the angular region of the mask as $0.15 < \theta_{mask} < 0.2$, it remains to determine only one parameter to fully specify the geometry of the mask. We take the half aperture of the mask, $R_{mask}$ in Fig.3.24, for this parameter. $R_{mask}$ can be linearly related to a diameter of circular trajectory of a charged track in a solenoidal magnetic field(B), *i.e.* $R_{mask} = p_t^{max}/0.15B$ and B=2Tesla. We determine $R_{mask}$ for the pairs, which comprise a shoulder in Fig.3.23, to loop inside the mask. There is another important constraint from the solid angle seen by the photons back-scattered at QC1, *i.e.* $\eta_{mask} = R_{mask}^2/4(L_Q - L_{mask})^2 < 1 \times 10^{-3}$, where $L_{mask}$ and $L_Q$ are the distances of the mask and the final focus quadrupole magnet from the interaction point(IP), respectively(Fig.3.24). The location of the final focus quadrupole magnet has been set to be 2.5 m from IP for the synchrotron radiations to go through QC1 without scattering as mentioned in the previous section. The optimized values of $R_{mask}$, $L_{mask}$ and $\eta_{mask}$ are also listed in Tab.3.5. With this masking system, the total number of charged particles hitting the outer surface of the mask is less than $10^3$/train(72 bunches) as shown in Fig.3.23.

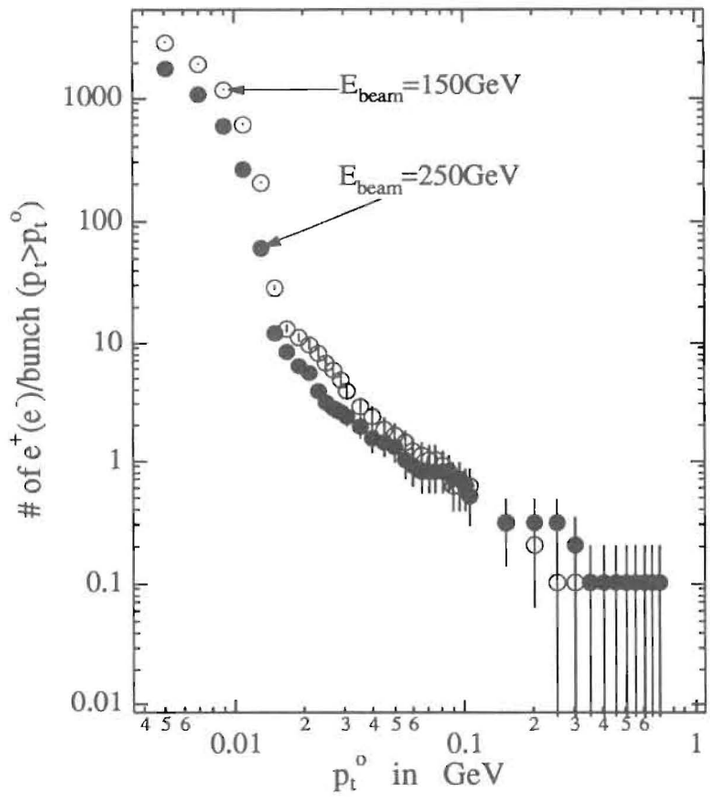


Figure 3.23: Pair yield/bunch crossing as a function of $P_t^o$ for $\theta_e > 0.15$ at JLC-I(c-band).

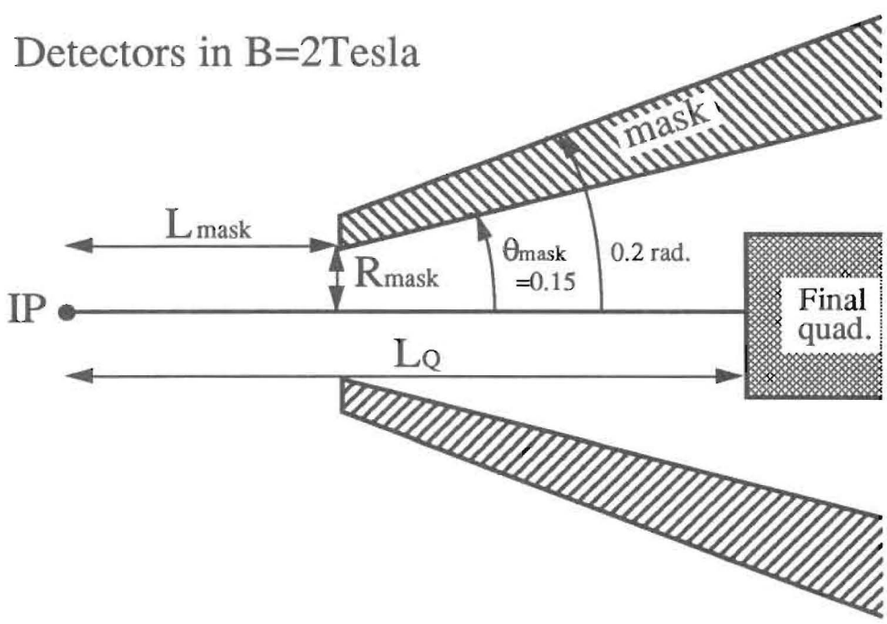


Figure 3.24: A masking system at the interaction region

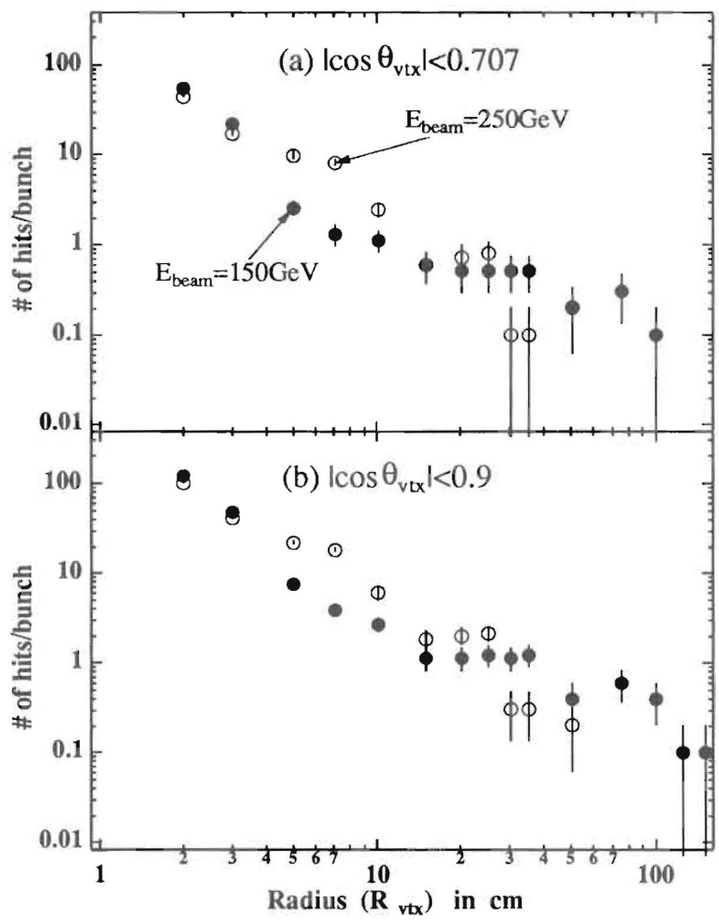


Figure 3.25: background hits by the pairs in B=2Tesla as a function of radius($R_{vtx}$.

### 3.7.6 Background at the Vertex Detector

In general we can use a beampipe of small radius, e.g. $R_{pipe} \sim$ 1cm, at IP because of no fear of synchrotron radiation as discussed in the previous section. Therefore, a vertex detector can be placed very close to the beam line. In order to estimate the background in the vertex detector, the number of hit points , which the pairs make by traversing the surface of the cylinder of radius $R_{vtx}$ and length $Z_{vtx} = R_{vtx}/\tan\theta_{vtx}$ around the collision point, are plotted as a function of $R_{vtx}$ at $|\cos\theta_{vtx}|$=0.707 and 0.9 in Fig.3.25(a),(b). Here we assume the helix trajectories of the pairs in the solenoidal magnetic field of 2 Tesla and we allow for the pairs to register multiple hit points without any interaction. The number of hits decreases rapidly as $R_{vtx}$ increases. The hit numbers per bunch crossing are 117.8(21.1) and 100.4(34.4) at $R_{vtx}$=2cm, $|\cos\theta_{vtx}|$=0.9 for JLC-I(c-band) $E_{beam}$=150 and 250GeV, respectively, where values in parenthesis are the number of particles which make hits. The hit numbers have to be multiplied by 72 for a real background estimation because there are 72 bunches/train. This background apparently prevents us from using a gas chamber as the vertex detector in $R_{vtx}$ <10cm. Our CCD(pixel) device is the best detector. The vertex detector also suffers from the secondary photons. Since the number of these photons is on the order of $10^3$ per train crossing, the corresponding hit number in the vertex detector is always less than those of the pairs with a few % of the conversion probability of the photons.

## 3.8 The Underlying Hadronic Background

The two-photon hadronic background is one of the most important issues in the future $e^+e^-$ linear collider experiments, since which might spoil the clean experimental environment otherwise available. The higher the energy, the severer the problem becomes because of the following reasons.

1. Since the bremsstrahlung photon intensity increases with energy as $\ln(\sqrt{s}/m_e)$, the cross section of a two-photon process increases as, $\sigma \propto (\ln s/m_e)^2$. In addition, according to the DG model[24], the minijet production rate increases as $\sigma \propto (\sqrt{s})^{1.4}$. Therefore, for example, the cross section of the minijet production increases by about a factor of 20, when we go up from the TRISTAN energy region to that of JLC-I.

2. There are, in addition, beamstrahlung photons, whose contribution to the minijet events is comparable to or even larger than that of the bremsstrahlung photons.

3. At linear colliders, the beam size is significantly smaller than that of the present circular colliders and the luminosity per beam crossing is much larger. It is 0.1 $mb^{-1}$ per beam bunch crossing at TRISTAN, while it is 66 $mb^{-1}$ at JLC-I. Since there are about 100 bunches per RF pulse of width 100 to 300 nsec, the effective luminosity for the detector increases further, if it cannot distinguish signals from different bunches.

In the following, we estimate the rate of the hadronic background at JLC-I and show that the rate is low enough to achieve a clean experimental environment, if the detector has a good timing resolution as described in the previous sections.

### 3.8.1 The Model

We calculate the cross section for the two-photon hadron productions, using the DG model[19] and the VDM model. The cross sections are given by

$$\sigma = \int f_{e^-/\gamma} f_{e^+/\gamma} \bar{\sigma} dx_1 dx_2,$$

where the two-photon cross section $\bar{\sigma}$ depends on models:

$$\bar{\sigma} = A + B/W_{\gamma\gamma},$$

with $A = 240$ nb and $B = 270$ nb·GeV for the VDM model, and

$$\bar{\sigma} = \int_{P_{T,min}} D_{\gamma/p}(Q^2, x_3) D_{\gamma/p}(Q^2, x_4) \frac{d\hat{\sigma}}{d\cos\hat{\theta}} dx_3 dx_4 d\cos\hat{\theta},$$

for the DG model. $f_{e^\pm/\gamma}$ is a $\gamma$ density function inside $e^\pm$, $D_{\gamma/p}$ is a parton ( photon, gluon, or quark ) density function inside $\gamma$, and $\frac{d\hat{\sigma}}{d\cos\hat{\theta}}$ represents the differential cross sections of subprocesses. $\hat{\theta}$ is the scattering angle of the subprocess in the CM system. $x_1$ and $x_2$ are photon energies scaled by beam energy, and $x_3$ and $x_4$ are parton energies scaled by the original photon energy. As the energy scale, we took $Q^2 = \hat{s}/4$, where $\hat{s} = x_1 x_2 x_3 x_4 s$ and $s = 4E^2_{beam}$.

As $f_{e^\pm/\gamma}$, we use the Equivalent Photon Approximation function for the bremsstrahlung photons and the analytical formula derived by K. Yokoya and P. Chen[26] for the beamstrahlung photons. The details can be found in [25].

It was reported that, in the TRISTAN energy region, the sum of the DG model and the VDM model well describes the two-photon hadron production data without electron-tag, when $p_{T,min}$ of the DG model is 1.6 GeV[20, 21]. The extrapolation of the models to higher energies, however, suffers from some ambiguities. The parton density functions inside the photon, especially the low x behaviors, still need experimental determinations. J. R. Forshaw and J. K. Storrow pointed out that the eikonalization would reduce the minijet cross section by about a factor of 5 at $\sqrt{s} = 500$ GeV[23], though its proper treatment is not clear. Since our calculation does not include the eikonalization,the background estimate presented below is conservative.

### 3.8.2 The Background Yield

The calculated background rates are summarized in Table 3.6. The total minijet cross sections at $\sqrt{s} = 300$ and 500 GeV obtained from the DG model are shown in Fig. 3.26, as a function of $p_{T,min}$, for the bremsstrahlung photons and the beamstrahlung photons corresponding to the three machine parameters shown in Table 4.1.

As seen in the figure and the table, the main source of the background is the beamstrahlung photons, except for the X-band JLC at $\sqrt{s} = 300$ GeV. The background rate at the lower frequency machine is larger than that of the higher frequency machine because the number of beamstrahlung photons is larger in the lower frequency machine due to larger number of particles/bunch. In the table, the number of minijet events is estimated using $P_{T,min}$ =1.6 GeV. If we use $P_{T,min} = 2$ GeV as suggested by the preliminary TOPAZ results[22], the number of minijet events will be reduced by about a factor of 3. In any case, the rate expected from the VDM model is larger than that of the DG model at JLC-I. The actual rate is the sum of the DG model and the VDM model. The number of background events per RF pulse is greater than one, which is reduced when the detector can separate signals from different bunches as described in the previous sections. In this case, the probability to have a background event in a signal event is about 2% to 25%, depending on the beam energy and the machine parameters.

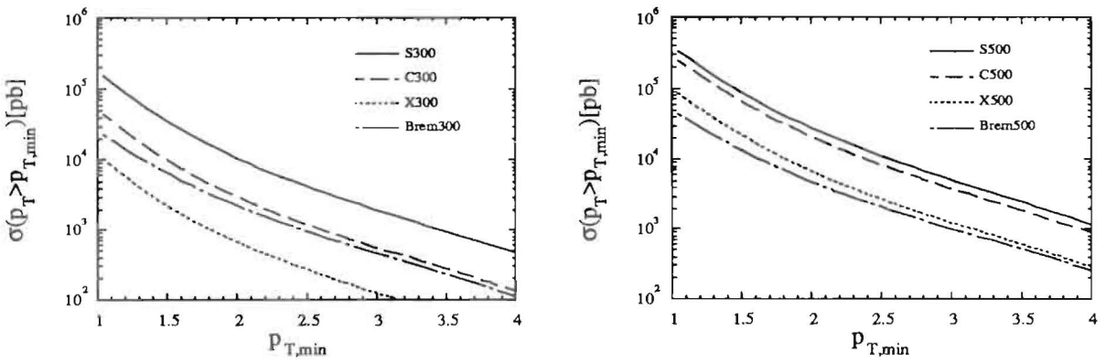


(a) (b)

Figure 3.26: The total minijet cross section integrated from $p_{T,min}$ to the maximum at (a) $\sqrt{s} = 300$ and (b) $\sqrt{s} = 500$ GeV, as a function of $p_{T,min}$, using the DG parameterization. The solid, dashed, and dotted curves show the cross sections due to the beamstrahlung photons of S-, C-, and X-band designs, respectively. The dot-dashed curves show those due to the bremsstrahlung photons.

| $E_{beam}$ (GeV) | $\sqrt{s} = 300$ GeV | | | $\sqrt{s} = 500$ GeV | | |
|---|---|---|---|---|---|---|
| RF frequency | S band | C band | X band | S band | C band | X band |
| # particles/bunch ($\times 10^{10}$) | 1.73 | 1.11 | 0.70 | 1.45 | 1.10 | 0.70 |
| Bunch spacing (nsec) | 5.6 | 2.8 | 1.4 | 5.6 | 2.8 | 1.4 |
| Repetition rate (Hz) | 50 | 150 | 150 | 50 | 150 | 150 |
| # bunches/pulse | 46 | 72 | 90 | 55 | 72 | 90 |
| # of beamstrahlung photons | 1.80 | 1.19 | 0.80 | 1.62 | 1.44 | 0.95 |
| Luminosity/pulse ($\mu$b$^{-1}$/pulse) | 62 | 39 | 23 | 88 | 64 | 42 |
| **by the DG model** | | | | | | |
| $\sigma(p_T > 1.6$ GeV) ($\mu$b) | 0.032 | 0.013 | 0.007 | 0.079 | 0.062 | 0.028 |
| $\sigma_{beam}$ | 0.027 | 0.0076 | 0.0017 | 0.068 | 0.051 | 0.017 |
| # events/pulse | 2.0 | 0.51 | 0.16 | 7.0 | 4.0 | 1.2 |
| # events/bunch | 0.043 | 0.0071 | 0.0018 | 0.13 | 0.056 | 0.013 |
| $P_{clean}$ | 0.958 | 0.993 | 0.998 | 0.88 | 0.946 | 0.987 |
| **by the VDM model** | | | | | | |
| $\sigma(W_{\gamma\gamma} > 2$ GeV) ($\mu$b) | 0.15 | 0.081 | 0.051 | 0.18 | 0.16 | 0.11 |
| $\sigma_{beam}$ | 0.11 | 0.048 | 0.018 | 0.10 | 0.082 | 0.034 |
| # events/pulse | 9.1 | 3.2 | 1.2 | 15 | 10 | 4.6 |
| # events/bunch | 0.20 | 0.022 | 0.013 | 0.28 | 0.14 | 0.05 |
| $P_{clean}$ | 0.819 | 0.978 | 0.987 | 0.756 | 0.869 | 0.951 |

Table 3.6: The summary of the background event rates. $\sigma_{beam}$ is the background cross section due to the collision between beamstrahlung photons. $P_{clean}$ is a probability to have an event without background: $P_{clean} \equiv e^{-<n>}$ where $< n >$ is the average number of background events.

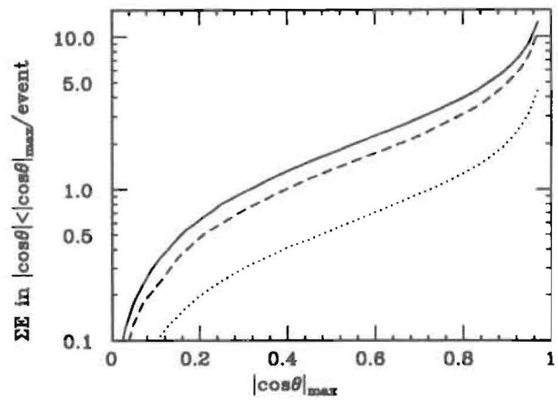


Figure 3.27: The energy deposit of a minijet event in the central region as a function of the maximum $|\cos\theta|$. The solid curve and the dashed curve are the simulation results for the DG model using the independent fragmentation and the string fragmentation, respectively. The dotted curve is for the VDM model. The beam energy is 150 GeV.

### 3.8.3 Effect on Physics Analyses

The energy deposit of a minijet event to the detector is estimated by Monte Calro simulations. In the simulation with the DG model, the spectator partons in the resolved process are produced along the beam axis, and subsequently hadronized together with the hard-scattered partons by the independent fragmentation or the string fragmentation. In the case of the VDM model, two quarks are generated with the angular distribution of $d\sigma/dp_T = e^{-4p_T^2}$ and hadronized by the string fragmentation. According to the simulations, a DG-model event produces about five charged tracks on the avergae in the region $|\cos\theta| < 0.866$. The sum of the energy deposit to the central region of the detector is shown in Fig. 3.27, as a function of the maximum $\cos\theta$. From the figure, we conclude that the energy deposit, for example, in the region of $|\cos\theta| < 0.9$ is 6 , 5, and 2 GeV for the DG with the independent fragmentation, the DG with the string fragmentation, and the VDM model, respectively. If we sum up these numbers weighted by the probability to have background events, the average energy deposit to the detector region of $|\cos\theta| < 0.9$ is less than about 0.6 GeV at $\sqrt{s} = 300$ GeV, which is about 0.2 % of the center of mass energy. Therefore, the effect of the background should be negligible.

As an example of the effect of the minijet background on physics analyses, we show, in Fig. 3.28, the invariant mass distribution of the two jets for the process $e^+e^- \to Z^0H^0$, when one minijet event of the DG-type overlaps every signal event. Although the measured width of the Higgs signal increases from 3.9 GeV to 5.3 GeV, we can still see a clear Higgs signal over the background from the $e^+e^- \to ZZ$ process. Note that the minijet background yield assumed in Fig. 3.28 is at least 20 times larger than our pessimistic estimate.

In conclusion, the hadronic background at JLC-I will not spoil the cleanness of the $e^+e^-$ collisions, if the detector can separate signals from different bunches. Even if the background rate is 20 times larger than that expected from the DG model, we can observe a clear Higgs signal, if the Higgs is in the region accessible by JLC-I.

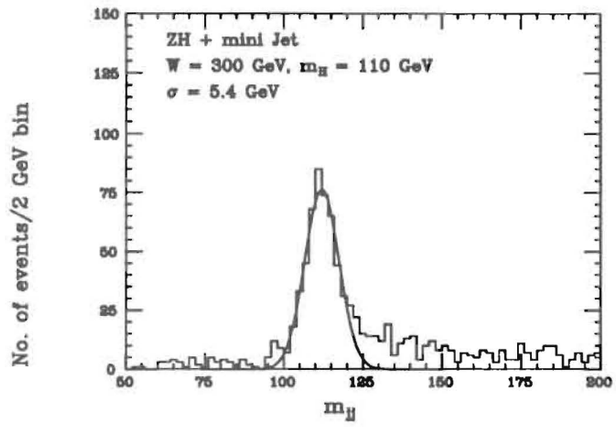


Figure 3.28: The invariant mass of the two-jet system for the process $e^+e^- \rightarrow Z^0H^0$ in a 4-jet mode, when one minijet event overlaps every signal event, at $\sqrt{s} = 300$ GeV and when $M_H = 110$ GeV. The integrated luminosity is 25 pb$^{-1}$ and other conditions are the same as those used in Fig. 3.11.

## 3.9 Data Acquisition and Trigger

### 3.9.1 Channel Count and Read-out Scheme

The total number of channels and a typical data size of each detector part are summarized in this section. A brief summary of the trigger scheme is also given.

#### Vertex Detector

The vertex detector consists of 6k pads of CCD's which have 64k pixel's each. The number of channels is $4 \times 10^8$ channels in total. To separate a minimum-ionizing particle signal from thermal noise, a five $\sigma$ cut from the thermal noize peak is enough. The number of hits caused by thermal noize is estimated to be 12k hits. The number of hits of the background tracks generated by beamstrahlung photons and so on is estimated to be 5 k hits based on the Tauchi's background study. The number of hits of signal tracks is negligible. The typical number of hits per beam crossing is 17k channels which corresponds to 68 kbyte of data size. The induced signals in the pixel's are fed to Flash ADC's serially and stored in the data memories.

#### Central Drift Chamber

The total number of read-out wires of the CDC is $1.7 \times 10^4$ wires (both sides of $8.4 \times 10^3$ sense wires). The signal shape is recorded by 200 MHz flash ADC's in 5 $\mu$sec. The total number of channels is $1.7 \times 10^7$. The number of hits by soft-photons coming from the beam mask in front of the final Q-magnet is estimated to be $8 \times 10^2$ hits per beam crossing. The number of hits from mini-jet background is $2 \times 10^4$ for the worst case. The number of tracks from, for example, W-pair production, which decay hadronically, is about forty. Thus the number of hits per event is $8 \times 10^3$. If we smple the data during 500 $\mu$sec around the signal, one hit has 100 bins each. The typical event size of one hadronic event is 12 Mbyte.

### Calorimeter

The calorimeter consists of $5 \times 10^3$ towers of a electromagnetic ($ECAL$) and hadronic ($HCAL$) calorimeter. Since each tower has one $HCAL$ module, four $ECAL$ modules, and 400 $Si$ pads, the calorimeter has $2 \times 10^6$ channels in total. The parallel data from 400 $Si$ pads are multiplexed and are serially fed to a ADC. The typical channel counts for a hadronic event is $7.5 \times 10^3$, which corresponds to 30 kbyte.

### Muon Detector

The muon detector consists of six super-layers of single-cell drift chambers and one layer of plastic scintillation counters. The total number of channels is 7700 channels for the barrel part and 2400 channels for each endcap part. In total the data size of the muon detector is 40kbyte. The typical data size for one beam-crossing depends on the muon background from the final focus part. Muons will be swept away by toroidal magnets set along a beam line. At any rate, the data size from the muon detector is negligible compared with other detector parts.

## 3.9.2 Trigger Philosophy

We do not have any first-level triggers. In each beam crossing, all data will be stored in memories. A trigger decision will be done based on fast-tracking information and calorimeter information before the next beam crossing which comes 5 msec later. The CDC and CAL are divided into several segments azimuthally including overlap regions. High speed workstations will perform fast-tracking and energy clustering within each segment. A master computer will combine tracking and clustering information from each detector-segment and make a decision to store the data into mass storage or not. The trigger criteria may be easily defined by editing a table. The events which only have the mini-jets are rejected at this stage. The trigger rate is expected to be several Hz, thus, there are no problems with data transfer and mass storage.

| Subsystem | Channel Count | | typical data size |
|---|---|---|---|
| | total | one event | (byte) |
| Vertex detector | | | |
| thermal noise | | 12k | 48k |
| BG track | | 5k | 20k |
| signal track | | - | - |
| Subtotal | 400M | 17k | 68k |
| Central tracker | | | |
| soft photon | | 80k | 0.32M |
| mini jet | | 2M | 8.0M |
| jet track | | 800k | 3.2M |
| Subtotal | 17M | 2.9M | 12M |
| Calorimeter | | | |
| $EM$ | 20k | 1.2k | 4.8k |
| $HD$ | 5k | 0.3k | 1.2k |
| $Si$ | 2M | 6k | 24k |
| Subtotal | 2M | 7.5k | 30k |
| Muon detector | | | |
| barrel | 7.7k | - | - |
| endcap | 2.4k | - | - |
| Subtotal | 10k | - | - |
| Total | 405M | 3M | 12M byte |

Table 3.7: Channel count requirement.

# Bibliography


[1] T. Tauchi, et al., *KEK Preprint* 90-181 (1991).
P. Chen and V. I. Telnov, *SLAC-PUB*-4923 (1989).
T. Tauchi, K. Yokoya, and P. Chen, *SLAC-PUB*-5557 (1991).

[2] M. Drees and R. M. Godbole, *Phys. Rev. Lett.* **67** (1991) 1189.

[3] A. Miyamoto, *Proceedings of the Third Workshop on Japan Linear Collider*, KEK, 1992, ed. by A. Miyamoto, *KEK Proceedings 92-13*, December, 1992.

[4] C. Adolphsen and D. Burke, private communication.

[5] Y.Fujii, *Proceedings of the Third Workshop on Japan Linear Collider*, KEK, 1992, ed. by A. Miyamoto, *KEK Proceedings 92-13*, December, 1992.

[6] E.Bernardi *et.al.*, *Nucl. Instr. Meth.* **A262** (1987) 229.

[7] D.Acosta *et.al.*, *Nucl. Instr. Meth.* **A308** (1991) 481.

[8] C.Zeitnitz *et.al.*, *DESY 92-045*, March, 1992.

[9] H. Fenker, *SSCL-Preprint-120*, May, 1992.

[10] W.R. Nelson and Y. Namito, MUON89 code for calculation of muon shielding.

[11] E.A. Kushnirenko, "MUON ATTENUATION", presented at FFIR workshop at SLAC, March,1992.

[12] Y. Namito, a detailed simulation is under going.

[13] J.Irwin, "Collimating MegaWatt Micron Sized 250-500 GeV Electron Beams", presented at LC92 at Garmisch-Partenkirchen Germany, July,1992.

[14] K.Yokoya, private communication, and also presented at LC91 at Protvino Russia, September,1991.

[15] W. Lohmann, R. Kopp and R. Voss, *CERN 85-03*, March, 1985.

[16] P. Chen and V.I. Telnov, *Phys. Rev. Lett.* **63** (1989) 1796.

[17] T. Tauchi, K. Yokoya and P. Chen, to be published in *Particle Accelerators* .

[18] T.Tauchi *et al.*, "Background Problem at Interaction Point for an $e^+e^-$ TeV Linear Collider" Presented at the DPF Summer Study on High Energy Physics: Research Directions for the Decade, Snowmass, Colorado, June 25-July 13, 1990, SLAC- PUB-5652.

[19] M. Drees and R. M. Godbole, *Nucl. Phys.* **B339** (1990) 355; *Phys. Rev. Lett.* **67** (1991) 1189.

[20] R. Tanaka, *et al.*, *Phys. Lett.* **B277** (1992) 215.

[21] H. Hayashii, NWU-HEP 92-03, June 1992. To appear in the proceeding of the 9th International Workshop on Photon-Photon collisions, San Diego, USA, March, 1992.

[22] M. Iwasaki, talk presented at the JPS meeting, Niigata, September, 1992.

[23] J. R. Forshaw and J. K. Storrow, *Phys. Lett.* **B268** (1991) 116; *Phys. Lett.* **B278** (1992) 193.

[24] M. Drees and R. M. Godbole, *DESY 92-044*, March, 1992.

[25] A. Miyamoto, *Proceedings of the Third Workshop on Japan Linear Collider*, KEK, 1992, ed. by A. Miyamoto, *KEK Proceedings 92-13*, December, 1992.

[26] K. Yokoya, private communication. see also P. Chen, *SLAC-PUB-5615*.

# Schematic Diagram of JLC-1

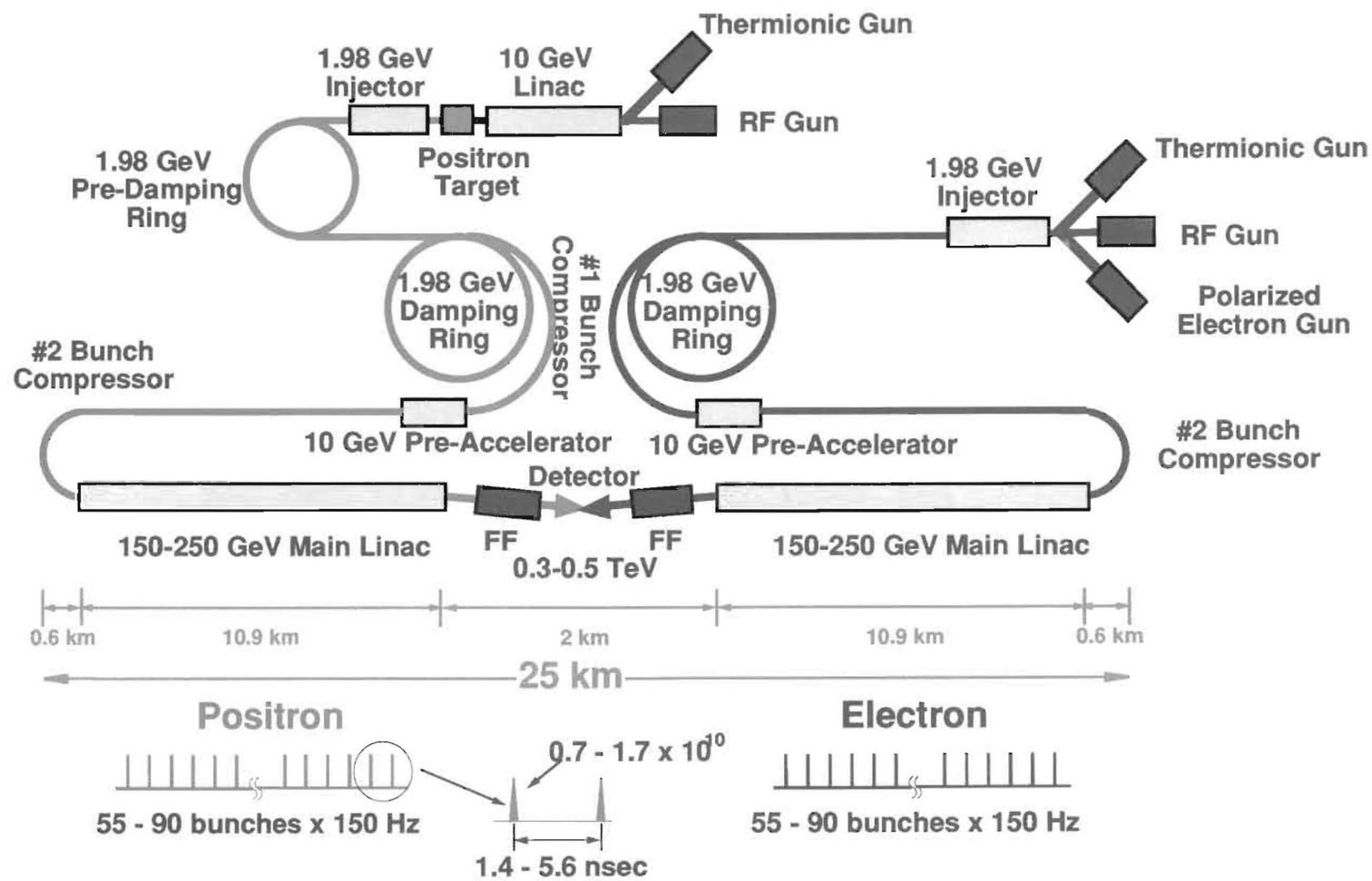

# Chapter 4

# Accelerator

## 4.1 Beam Parameters

The major target of JLC has been the center-of-mass energy range of $\sqrt{s}$= 1 to 1.5 TeV and the luminosity around $1\times10^{34}/\mathrm{cm}^2/\mathrm{sec}$ since 1986 when an intensive R&D started. To achieve this goal with a reasonable total length of 25 to 30 km, we have been thinking of the X-band frequency with multiple bunch operation. In the latest parameter set which was reported in LC91, the number of particles per bunch, $N$, is about $2\times10^{10}$ and the number of bunches per RF pulse, $m_b$ is 20. The recent demand of particle physics, however, puts more emphasis on the relatively low energy range $\sqrt{s}$= 300 to 500 GeV and on earlier start of the experiment around the year 2000.

It is possible that, if we consider these new requirements independently of the previous ones, somewhat different machine might be an optimum. With an observation of the present status of R&D at KEK, in particular if we desire early construction, it seems that the possibility of the frequency range lower than the X-band should also be pursued. Here, we will consider three frequencies, S-band (2856MHz), C-band (5712MHz) and X-band (11424MHz).

The parameter set given in the following is not the one studied fully. It is intended only to serve as the starting point of the design study. It is not intended to decide which frequency is the best. Some parameters are conservative at one frequency but more ambitious at other frequencies. Also, the parameters given here are not necessarily consistent with those referred to in the later chapters. Let us list up the conditions which the parameter set should satisfy.

### Global parameters

We assume the active length (the sum of the lengths of the accelerating structures) should be less than 10 km per beam. This will limit the total collider length to about 25 km, including the linac focusing elements and the final focus system. This requirement comes from the availability of the land. (For the S-band at 500 GeV we relax this condition slightly because otherwise it can only be met by unrealistically reducing the number of cavities to be fed by one klystron, which would be quite costly.)

The wall-plug power has to be less than about 200 MW. The above two requirements set an upper limit on the center-of-mass energy. It will be roughly $\sqrt{s}$= 0.5, 1.0, and 1.5 TeV for the S-, C-, and X-band options, respectively, though the latter two call for considerable innovation in the klystron technologies. Here, however, we shall discuss up to 500 GeV only. We set the upper limit of the repetition rate to be 150 Hz.

We set the upper limit for the number of particles per RF pulse to be $8\times10^{11}$, which is determined by the possible production rate of the positron by an extension of the conventional method. (This limit can be overcome by raising the repetition rate of the positron production linac or by constructing two linacs but these are not practical.)

There is a vast variety of distributing these particles into bunches. Judging from the recent studies of the detuned cavities, we should think of putting more bunches into an RF pulse than the previous value, i.e., 20 bunches. About 100 bunches seem to be possible from the view point of linac beam dynamics and the design of the damping ring. Moreover, Shintake has recently proposed a new-type damped cavity making use of the choke mode. With this cavity many-bunch operations will be quite promising.

We assume that the distance between bunches is 16 buckets for any frequency band. The X-band study has been done with this distance and it turned out that a frequency spread of the $TM_1$ mode as large as 13% is needed to avoid the multi-bunch beam breakup. A distance shorter than 16 buckets is not practical. So long as we adopt detuned structures, 16 buckets seem to be the lower limit. On the other hand, it might be possible to have longer distance. It consumes some more power and calls for a larger damping ring but is better for multi-bunch energy compensation, the background problem, and the multi-bunch crossing instability.

### Main Linac

From the view point of luminosity, a short bunch is preferred because it allows a small beta function at the collision point and because it relaxes the luminosity reduction due to the crossing angle. From the study of the bunch compressor, we set the lower bound of the bunch length to be $80\mu$m. A shorter bunch causes tighter tolerances in the compressor. (Also from the compressor requirement, we set the injection energy to the main linac to be 20GeV.)

The parameters involving the cavity structure, such as the attenuation parameter and the iris aperture, are fixed after some beam dynamics and hard-ware consideration.

The energy spread due to the short range wake is compensated by shifting the bunches off the RF crest. We impose the condition that the resulting peak-to-peak energy spread should be less than 1.5%. Also, we assume that the inter-bunch energy spread due to the transient beam loading can be compensated. When the input pulse shape to the structure is rectangular such as the pulse from SLED II, the energy difference can be compensated almost perfectly by injecting the beam into cavities with various timings of partial fill. If we have, for example, 20 cavities whose timing can be controlled independently, the resulting energy spread can be compensated down to the level of 0.1%. For the S-band, for which SLED II is not practical, the compensation is possible with SLED pulse by using cavities with a small frequency shift. These compensation schemes put a sharp upper bound on $\eta_1 T_f/t_b$ where $\eta_1$ is the single-bunch extraction efficiency, $T_f$ the filling time and $t_b$ the bunch spacing. After these compensation, the net accelerating gradient in the structure becomes considerably smaller than the nominal (unloaded) accelerating gradient. We require the reduction to be smaller than 30%. If this is too large, the tolerance of the charge per pulse would become very tight.

### Final focus and the interaction point

As for the luminosity, smaller beta functions at the collision point are better because the beamstrahlung is not a serious limiting factor in this energy range. ( We define the upper bound of the average energy loss by beamstrahlung $\delta_{BS} \leq 10\%$.) A design study of the final

focus system has concluded that $\beta_x \geq$10mm and $\beta_y \geq$0.1mm are possible within reasonable tolerances.

We assume a horizontal crossing with a crossing angle larger than 5mrad. This is needed in order to let the exhaust beams go outside the field region of the last quadrupole magnet. The bunches coming late are deflected by the exhaust bunches (multi-bunch crossing instability). We require the amplitude blowup factor by this instability to be less than 2. Actually, this requirement calls for a crossing angle larger than 5mrad and, therefore, the luminosity is somewhat reduced by the geometric reduction factor and by the reduction of the pinch enhancement factor. The so-called crab crossing can cure this problem. The luminosity would become larger by a factor of 1.5 to 2 but we do not take this option here.

With the consideration above, we determined the parameters which makes the luminosity as high as possible and listed them in Table 4.1. (We also included possible parameters at the $Z_0$ energy for C-band only.)

The luminosity only is, however, not a good parameter to be optimized. In fact, there are many different solutions which give nearly the same luminosity (e.g., different combinations of $N$ and $m_b$). Also, we prefer a smaller beam energy spread in some experiments, which changes the optimization considerably. The table here gives only one possible set for each frequency. To decide which solution of which frequency is the best, we need many steps of iteration between the global design and those of each part.

## 4.2 Electron and Positron Sources

### 4.2.1 Electron source

#### Introduction

The electron source of JLC-I must be able to produce 55 $\sim$ 90 intense electron bunches separated by a spacing depending on RF band selection( 1.4 ns for X-, 2.8 ns for C-, and 5.6 ns for S-band ) with a repetition rate of 50 or 150 Hz as illustrated schematically in Fig. 4.1. Each bunch consists of 0.7$\sim$ 1.5 $\times$ $10^{10}$ electrons. The resultant total number of electrons is 6 $\sim$ 8 $\times$ $10^{11}$/RF pulse. The number of electrons in each bunch must be controlled to better than $\pm$0.5 % and its emittance must be small enough to be accepted in the pre-damping ring as described in Sec. 4.3.

To meet these requirements, we take the following two approaches: one is to push, to the limit, the conventional technology using a pulsed thermionic gun combined with a grid pulse generator and sub-harmonic bunchers( SHB ), and the other is to develop an RF gun with a laser-triggered photocathode.

Effort is also made to develop a highly polarized electron source which will be discussed in Sec. 4.2.2.

#### Thermionic Gun

**a) Single and double bunch generation** : As the first step of the development program, single- and double-bunch beams were studied to confirm the feasibility of achieving the required number of electrons per bunch. In this study, we used fast pulse generators to produce grid pulses to drive the thermionic cathode. The pulse generators were originally built by Kentech

Table 4.1: Parameters at $E_{CM}$=300 and 500 GeV

| | | | S-band | | C-band | | X-band | | C-band |
|---|---|---|---|---|---|---|---|---|---|
| Frequency | $f_{rf}$ | GHz | 2.856 | | 5.712 | | 11.424 | | 5.712 |
| Beam Energy | $E$ | GeV | 150 | 250 | 150 | 250 | 150 | 250 | 45.6 |
| Number of Particles per bunch | $N$ | $10^{10}$ | 1.73 | 1.45 | 1.11 | 1.10 | 0.70 | 0.70 | 1.11 |
| Number of bunches per pulse | $m_b$ | | 46 | 55 | 72 | 72 | 90 | 90 | 72 |
| Bunch spacing | $t_b$ | nsec | 5.6 | 5.6 | 2.8 | 2.8 | 1.4 | 1.4 | 2.8 |
| Repetition frequency | $f_{rep}$ | Hz | 50 | 50 | 150 | 150 | 150 | 150 | 150 |
| Normalized emittance at damping ring | $\epsilon_x$ | rad.m | $3\times10^{-6}$ | $3\times10^{-6}$ | $3\times10^{-6}$ | $3\times10^{-6}$ | $3\times10^{-6}$ | $3\times10^{-6}$ | $3\times10^{-6}$ |
| | $\epsilon_y$ | rad.m | $3\times10^{-8}$ | $3\times10^{-8}$ | $3\times10^{-8}$ | $3\times10^{-8}$ | $3\times10^{-8}$ | $3\times10^{-8}$ | $3\times10^{-8}$ |
| R.m.s. bunch length | $\sigma_z$ | $\mu$m | 80 | 80 | 80 | 80 | 85 | 67 | 80 |
| Nominal accelerating gradient | $G_0$ | MeV/m | 22.0 | 22.0 | 40.0 | 40.0 | 40.0 | 40.0 | 40.0 |
| Effective gradient in cavities | $G_{eff}$ | MeV/m | 16.3 | 18.4 | 28.2 | 27.8 | 28.0 | 28.0 | 28.5 |
| Active length of main linac per beam | $L_{ac}$ | km | 8.0 | 12.5 | 4.6 | 8.3 | 5.0 | 8.5 | 0.90 |
| Total number of betatron oscillation | | | 200. | 258. | 116. | 171. | 125. | 176. | 33.5 |
| Length of a cavity unit | $l_{cav}$ | m | 3.6 | 3.6 | 1.7 | 1.7 | 1.22 | 1.22 | 1.7 |
| Number of cavity units per beam | | | 2220 | 3470 | 2720 | 4860 | 4100 | 6930 | 530 |
| Iris radius/Wave length | $a/\lambda$ | | 0.12 | 0.12 | 0.13 | 0.13 | 0.18 | 0.18 | 0.13 |
| Cavity filling time | $T_f$ | nsec | 837 | 837 | 297 | 297 | 75 | 75 | 297 |
| Attenuation parameter | $\tau$ | | 0.57 | 0.57 | 0.57 | 0.57 | 0.40 | 0.40 | 0.57 |
| Total average power into cavities for two linacs | | MW | 14 | 20 | 25 | 46 | 11 | 20 | 5.0 |
| Wall-plug power for two linacs | | MW | 70 | 100 | 115 | 210 | 75 | 135 | 23 |
| Assumed efficiency from AC to RF | | % | 20 | 20 | 22 | 22 | 15 | 15 | 22 |
| Peak power per cavity | $P_{peak}$ | MW | 52 | 52 | 60 | 60 | 50 | 50 | 60 |
| Single-bunch extraction efficiency | $\eta_1$ | % | 0.84 | 0.70 | 1.13 | 1.13 | 2.00 | 2.00 | 1.13 |
| Phase shift from the crest | $\phi_{rf}$ | deg | 28.0 | 11.0 | 21.9 | 23.9 | 24.0 | 24.0 | 21.6 |
| Single-bunch energy slope due to wake | $\langle\sigma_z d\epsilon/dz\rangle$ | % | -0.72 | 0.57 | -0.84 | -0.90 | -1.22 | -1.22 | -0.54 |
| Energy slope for BNS damping | | % | -0.008 | -0.007 | -0.06 | -0.06 | -0.16 | -0.16 | -0.06 |
| Number of particles per bunch at IP | $N^*$ | $10^{10}$ | 1.56 | 1.30 | 1.00 | 1.00 | 0.63 | 0.63 | 1.00 |
| Beta function at IP | $\beta_x^*$ | mm | 10. | 10. | 10. | 10. | 10. | 10. | 10. |
| | $\beta_x^*$ | $\mu$m | 100. | 100. | 100. | 100. | 100. | 100. | 150. |
| Rms beam size at IP | $\sigma_x$ | nm | 335 | 301 | 335 | 260 | 335 | 260 | 608 |
| | $\sigma_y$ | nm | 3.92 | 3.04 | 3.92 | 3.04 | 3.92 | 3.04 | 8.70 |
| Crossing angle | $\phi_{cross}$ | mrad | 11.0 | 7.3 | 10.4 | 8.0 | 9.0 | 7.2 | 15.1 |
| Beam diagonal angle | $\sigma_x/\sigma_z$ | mrad | 4.2 | 3.8 | 4.2 | 3.2 | 4.0 | 3.9 | 7.6 |
| Disruption parameter | $D_x$ | | 0.21 | 0.13 | 0.13 | 0.13 | 0.090 | 0.0070 | 0.135 |
| | $D_y$ | | 18.0 | 13.0 | 11.5 | 11.5 | 7.7 | 6.0 | 9.41 |
| Number of beamstrahlung photons | $n_\gamma$ | | 1.80 | 1.62 | 1.19 | 1.44 | 0.80 | 0.95 | 0.71 |
| Maximum Upsilon | $\Upsilon_{max}$ | | 0.37 | 0.58 | 0.24 | 0.51 | 0.15 | 0.39 | 0.041 |
| Energy loss by beamstrahlung | $\delta_{BS}$ | % | 8.2 | 10.0 | 3.9 | 8.1 | 1.8 | 4.5 | 0.46 |
| Geometrical luminosity reduction factor | | | 0.57 | 0.68 | 0.60 | 0.60 | 0.63 | 0.70 | 0.69 |
| Pinch enhancement factor | $H_D$ | | 1.58 | 1.60 | 1.50 | 1.50 | 1.71 | 1.72 | 1.80 |
| Luminosity | $L$ | $10^{33}/\mathrm{cm}^2/\mathrm{s}$ | 3.1 | 4.4 | 5.9 | 9.7 | 3.5 | 6.3 | 2.0 |

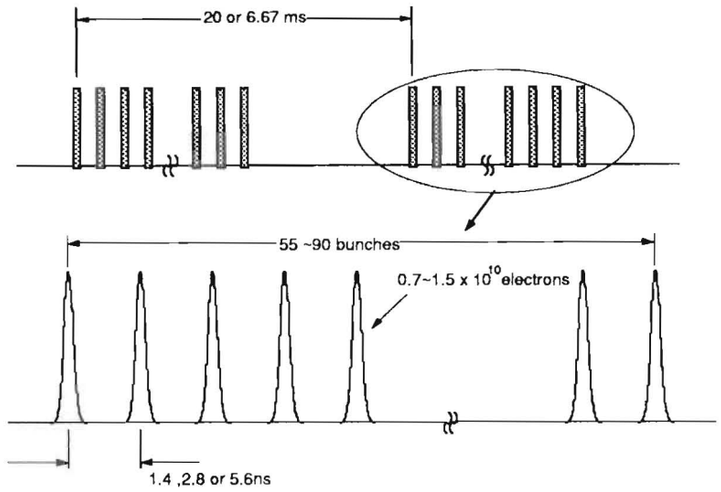


Figure 4.1: Schematic drawing of the electron and positron beam.

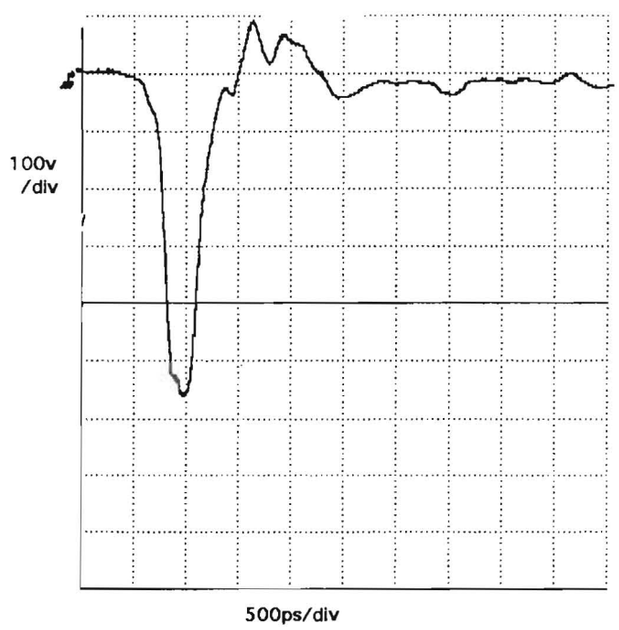


Figure 4.2: Output of the fast avalanche pulse generator (100 V/div, 500 ps/div).

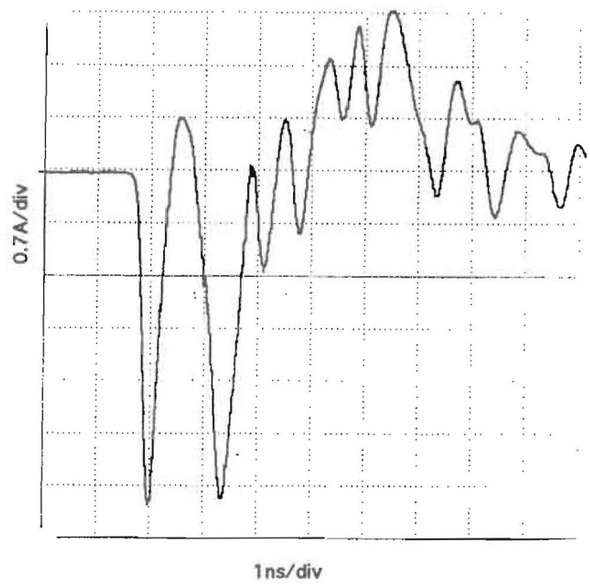


Figure 4.3: Wave shape of double bunch beam, accelerating voltage: 170 kV, heater voltage: 6.0 V, net drive voltage: 260 V

Instruments Ltd, which employ avalanche transistor pulse generator technology. A typical pulse shape is shown in Fig. 4.2. The peak pulse amplitude and the width were $\sim$ 500 V and 500 ps. The double grid pulses required for double-bunch generation were formed by using two avalanche pulse generators, triggered at different timings, and delivering their output pulses to an RF combiner. The peak amplitude and the width of each pulse from the RF combiner were $\sim$ 300 V and 500 ps, respectively. The reduction of the amplitude was due to the power loss in the RF combiner. Fig. 4.3 shows a typical double-bunch beam from the Y-646 cathode driven by the double grid pulses, where the accelerating voltage was 170 kV, the heater voltage 6.0 V, and the net drive voltage 260 V. The peak current of each bunch was 4.3 A which corresponds to $1 \times 10^{10}$ electrons/bunch. Although this value already reached the required single-bunch intensity, generation of more than several bunches is difficult with this pulse generation system because of the power loss in the RF combiner.

**b) Multi-bunch generation** : A new multi-pulse generator under development uses a fast ECL circuit and an RF amplifier to generate more than 20 pulses per train. Fig. 4.4 shows its schematic diagram. The ECL clock is 476 MHz synchronized to the RF of the linac. Required number of pulses are successfully formed by counting and gating the RF signals in the circuit, as shown in Fig. 4.5(a). The RF power amplifier is required to have an output power of $\sim$10 kW and a gain of 60 dB to provide sufficiently large pulses to drive the gun. The band width of such a high gain RF amplifier is not large enough to amplify this pulse train with no distortion, as shown in Fig. 4.5(b) for a 1 W test RF amplifier. The distortion can be cured by a compensation signal from the wave form shaper. Since there is no foreseen technological problem with high power RF amplification, we are confident that this new scheme will meet the JLC requirements.

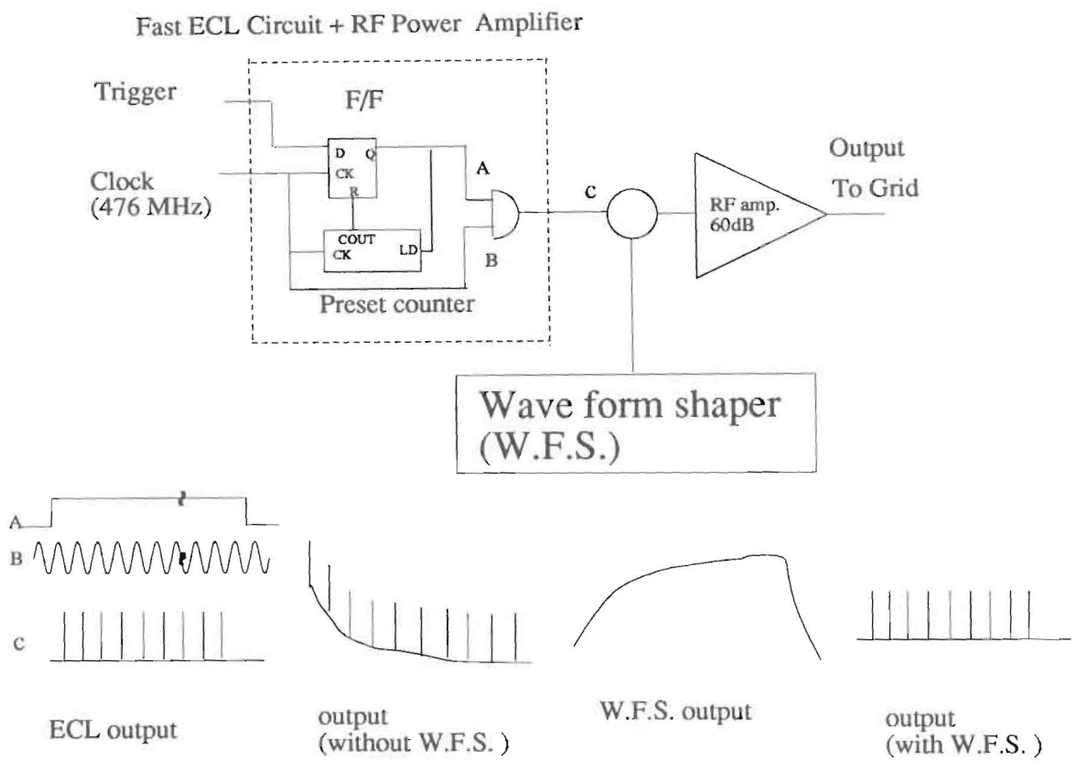


Figure 4.4: Schematic drawing of multi-pulse generator.

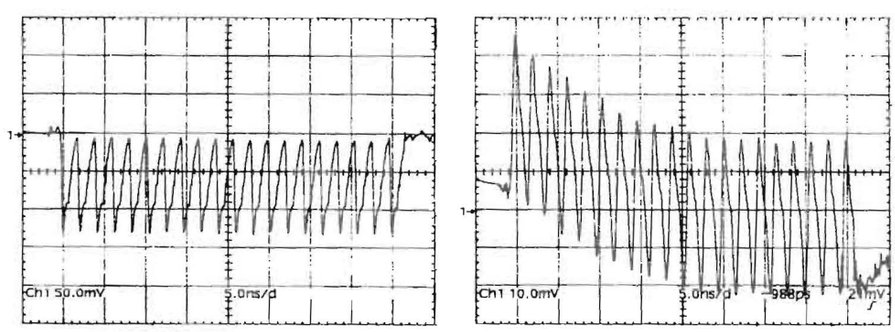


(a) (b)

Figure 4.5: (a) Output of the fast ECL circuit (50 mV/div, 5 ns/div) and (b) Output of the test RF amplifier (1.5 V/div, 5 ns/div)

c) **Test Facility** : The thermionic gun described above has been installed into the first stage accelerator test facility shown in Fig. 4.6, which includes three SHBs( 119/238/476 MHz ), two single-cell pre-bunchers, and a traveling wave S-band buncher followed by a high gradient S-band accelerating structure. The test facility made possible systematic studies of the electron source system and proved its capability of stably delivering at least $1 \times 10^{10}$ electrons/bunch to the injector linac. This source system will be used for single-bunch studies of various components in the full Accelerator Test Facility( ATF ) including a chain of a 1.5 GeV injector linac, a low-emittance damping ring, and a bunch compressor.

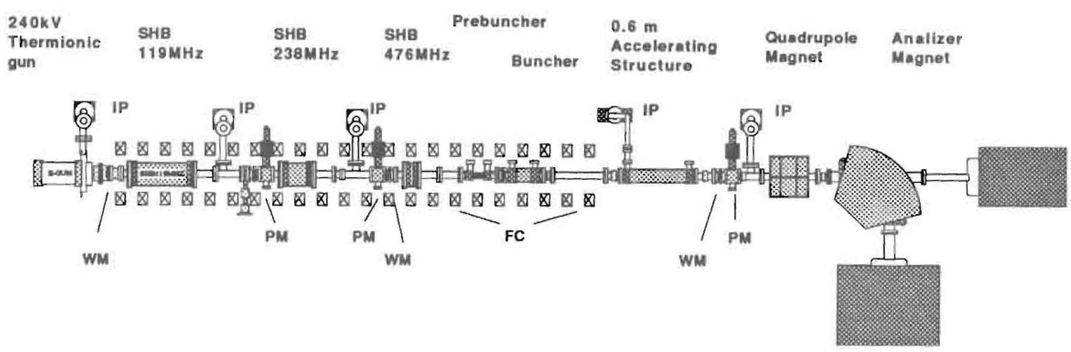


Figure 4.6: Layout of the Accelerator Test Facility.

## RF Gun

An RF gun using a laser-triggered photocathode has many advantages in generating a low emittance and high current pulsed beam. The RF gun directly generates a bunched beam by illuminating, with laser pulses, a photocathode installed in an RF cavity. The RF field accelerates the bunch in synchronization with the laser pulses as illustrated in Fig. 4.7. The

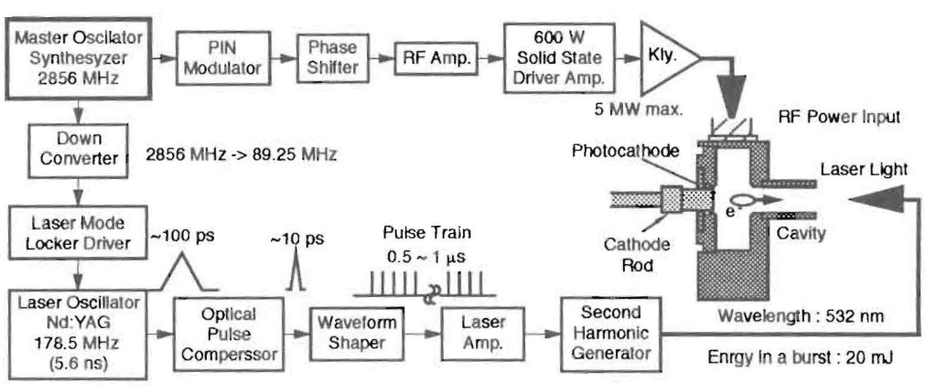


Figure 4.7: A schematic drawing of the RF gun.

accelerating gradient achievable with the RF field is higher than that of a DC or pulsed field of the conventional gun, so that it is possible to generate an extremely low emittance and high current beam. Since the photocathode is triggered with a pulsed laser, the required pulsed beam can be produced only using a mode-locked laser system and an optical system. Furthermore,

compared to the thermionic gun, higher current density is achievable. Motivated by these good characteristics, we are devoting a great deal of effort to the development of a RF gun system which meets the requirements for JLC-I.

**a) Prototype RF Gun** : Fig. 4.8 shows the experimental facility constructed to study the feasibility of the RF gun. The facility consists of a prototype RF gun with a photocathode in a simple half-cell S-band pillbox-type cavity, a beam transport leading to a current monitor, a mode-locked Nd:YAG laser system, and a high power and low level RF systems.

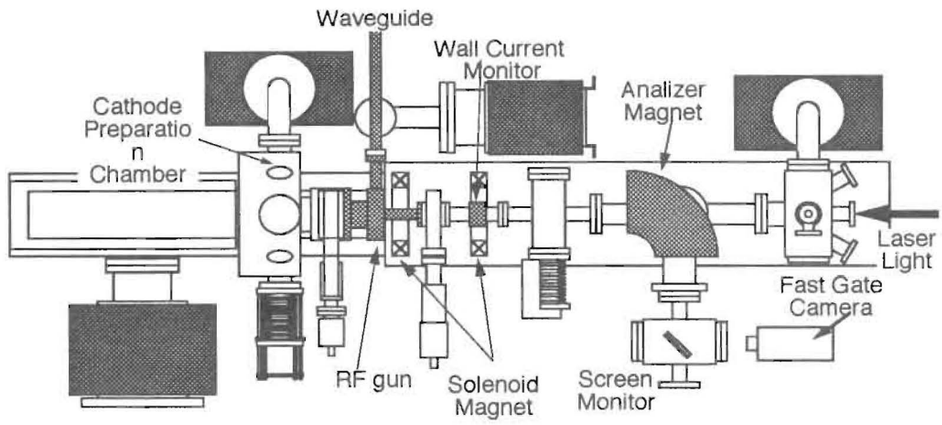


Figure 4.8: An experimental arrangement of the prototype RF gun.

**Photocathode** : We have chosen the Sb-alkali( Cs ) photocathode, whcih is expected to have a high quantum efficiency( Q.E. ) for a laser wavelength around 500 nm and is easy to fabricate.

**Cavity** : In the present experiment, a simple pill-box type cavity is chosen to study the beam dynamics in the RF gun at a high accelerating gradient. The cavity has been processed up to the accelerating gradient of 50 MV/m prior to the experiment. During the experiment at 40 MV/m, no RF breakdown was observed and the vacuum pressure in the cavity was around $1 \times 10^{-9}$ Torr.

**Phase Stability** : In the RF gun, the phase between laser pulses and the RF fields must be synchronized precisely. As shown in Fig. 4.7, the master oscillator is an S-band synthesizer. Its output is simply scaled down to 89.25 MHz to trigger the laser and, in this way, phase jitter can be reduced to less than 10 ps.

**Laser** : A block diagram of the laser system is given in Fig. 4.9. The oscillator is a CW mode-locked Nd:YAG laser with the wavelength of 1064 nm, a power level of 4 W, and the frequency of 178.5 MHz which corresponds to the pulse spacing of 5.6 ns. The width of each pulse is about 100 ps at the output of the oscillator, and is compressed to about 10 ps with an optical pulse compressor composed of an optical fiber and a pair of grating. A pulse train

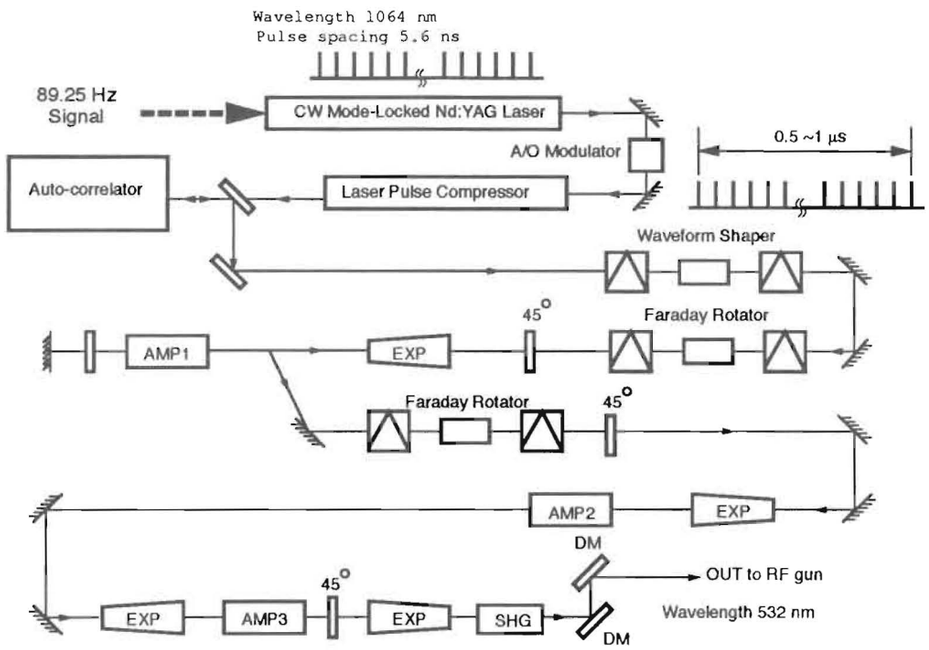


Figure 4.9: A block diagram of the laser system and a picture of a laser pulse.

of 0.5~ 1 $\mu$s in width is obtained from the CW laser pulse with a wave form shaper and then amplified. Finally, the wavelength is converted to 532 nm with a second harmonics generator( KD*P ) and the laser light is guided to the photocathode in the cavity with the mirror system. The energy of the one micro-pulse is 0.1 ~ 0.15 mJ.

**b) Prototype Tests and Perspectives** : Firstly, the photocathode is activated in the preparation chamber and then inserted to the cavity to tune the resonant frequency at 2856 MHz. The laser is fired and the pulse shape of the beam current is observed by the wall current monitor. Fig. 4.10 shows that the beam has the bunch spacing of 5.6 ns, which is precisely the mode locked frequency of the laser system. The number of electrons contained in a pulse was estimated to be $2.3 \times 10^{10}$ and the number of bunches in one RF pulse was 90~180. The maximum beam energy was measured with a magnetic spectrometer to be 900 keV at the gradient of 40 MV/m. These experimental results almost satisfy the required performance for JLC-I. The remaining problems are now confined to the improvements of (1) the quantum efficiency and life time of the $Cs_3Sb$ photocathode and (2) the stability and life time of the laser system. The cathode life is determined by the desorption of Cs and the contamination by bad gases such as $H_2O$ and CO. The improvement of the vacuum system is under way, as well as the development of new methods to supply Cs continuously to the cathode during the operation. The flash lamp of the laser system should be replaced by the laser diode to improve both the stability and life time.

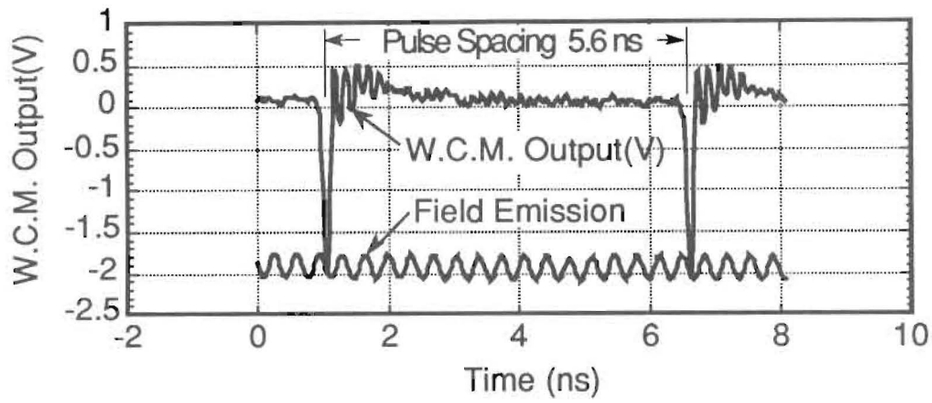


Figure 4.10: Output pulse from the RF gun measured by a wall current monitor.

### 4.2.2 Polarized Electron Source

In circular $e^+e^-$ colliders, the beams spontaneously polarize vertically due to the spin-flip synchrotron radiation. It calls for tremendous efforts, however, to rotate the spin to the longitudinal direction without serious depolarization. One of the advantages of the linear colliders is that it is relatively easy to collide longitudinally polarized beams once polarized particle sources are given. Polarized positron sources are not easy to obtain but a polarization of one of the beams can already bring about rich physics outputs.

We have made an effort to develop a highly polarized electron source using a GaAs photocathode illuminated by circularly polarized laser light. As is well known, the polarization obtainable with conventional bulk GaAs has an intrinsic upper limit of 50 % due to the symmetrical structure of the crystal. To overcome this limit, we have been studying two types of cathodes, an AlGaAs-GaAs superlattice and a strained GaAs.

In order to develop such GaAs sources, we proceeded with the following two R/D works,
a) photocathode development toward the 100 % polarization,
b) construction of an operational gun which meets the requirements from the JLC injection linac.

#### Photocathode Development

We have achieved the polarization of 71% and 86% by developing the newly designed photocathodes, GaAs-AlGaAs superlattice and lattice-mismatched strained GaAs, respectively[1, 2]. SLAC group has also achieved 71% from strained InGaAs[3]. These achievements were the break-through to overcome the 50 % polarization limitation of the traditional GaAs source.

The strained GaAs photocathode was made by growing a GaAs epilayer on a lattice mismatched $GaP_xAs_{1-x}$ buffer substrate with a MOCVD apparatus. The structure of prepared samples is simple as shown in Table 4.2. The polarization( ESP ) and quantum efficiency( QE ) observed for the first successful strained GaAs photocathode are plotted in Fig. 4.11, as a function of laser wavelength. The clear polarization peak at $\lambda \approx 860$ nm is the evidence for the single excitation from the upper heavy-hole band of the strained GaAs. With this sample, the world highest ESP of 86 % was achieved, which was the first proof of the principle to obtain more-than-50 % polarization. However, there still remains another problem, that is

Table 4.2: Parameters of strained GaAs cathode

| |
|---|
| Zn-doped GaAs ($t \approx$Å, $p \approx 5 \times 10^{18}\mathrm{cm}^{-3}$) |
| Zn-doped $GaP_xA_{s_{1-x}}$ ($x \approx 0.17$)<br>($t \approx 2\mu$m, $p \approx 5 \times 10^{18}\mathrm{cm}^{-3}$) |
| Zn-doped GaAs Subtrate<br>($t \approx 350\mu$m, $p \approx 5 \times 10^{18}\mathrm{cm}^{-3}$)<br>Orientation : (1 0 0) |

the relatively poor QE for the new cathodes. For example, the QE was 0.02 % for the above sample at $\lambda \approx 860$ nm, where the maximum ESP of 86 % was observed, while a QE more than 3 % is possible for the bulk GaAs photocathode. We have been trying to improve the quantum efficiency and have achieved so far a more-than-0.1 % QE at 80 % ESP.

The other photocathode of GaAs-AlGaAs superlattice(SL) was fabricated by a MBE apparatus. In Fig. 4.12, the maximum ESPs for 4 samples are plotted as a function of the SL thicknesses, 0.05, 0.1, 0.4 $\mu$m[4]. The clear thickness-dependence of ESP confirmed that the depolarization process inside the SL plays a dominant role to degrade the ESP of conduction electrons before they can escape to the vacuum. We also studied the dopant-concentration dependence of the EPS and the QE. It was found that reduced doping was able to lower the spin relaxation in the interior of the superlattice and improve both the EPS and the QE[5]. The best photocathode so far achived gave the 0.2% QE at the 71.2% ESP.

### Design and Construction of an Operational Gun

The level of required performance for JLC-I is much higher than those of the previously employed, although the GaAs source was already operated at several laboratories for high energy experiments. It is especially true for the performance under high voltage( 100 $\sim$ 200 kV ) and the photocathode performance under high power laser irradiation( 30 $\sim$ 100 kW peak power ).

In order to investigate the above two problems, proto-type guns were constructed both at KEK and Nagoya University. The polarized electron source system build at KEK is shown in Fig. 4.13, where the polarization measuring system, a Wien filter, and a Mott analyzer are also included.

The mechanical construction has been completed and test operation is in progress at moderate high voltage with a moderate power Ti:Sapphire tunable laser system. The vacuum has no problem, already reaching the base pressure of $2 \times 10^{-10}$ Torr( total pressure ), and the initial high voltage up to 100 kV sees no serious dark current. A photocurrent has already been extracted and studies of photocathode performance will start soon. The gun will then be tested with a newly upgraded high-voltage and laser system, which meets the conditions required by the JLC-I injection linac. The first acceleration of polarized electrons at KEK is scheduled in (2 $\sim$ 3) years at the ATF which is under construction.

### Acceleration of the polarized beam

Once a polarized source is given, what is needed next is to maintain the high polarization during the acceleraton and to rotate the spin to the longitudinal direction at the collision point.

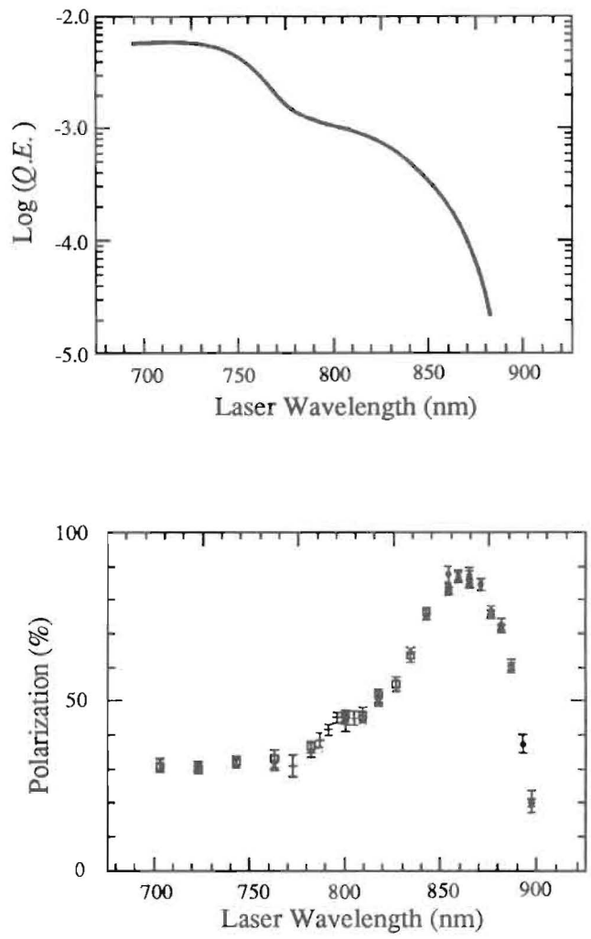


Figure 4.11: Polarization and quantum efficiency for strained GaAs versus laser wave length.

The spin in the damping rings has to be vertical. Otherwise, the beam is immediately depolarized by the precession-frequency spread due to the energy spread. Spin rotators before damping rings for this purpose can easily be designed, since a high beam quality is not required at this stage. The depolarization in the ring is then negligible unless the precession resonates with the revolution frequency or with the betatron frequencies. Since the spin tune (number of precessions during one turn) is simply given by the beam energy divided by $E_\tau \equiv mc^2/a =$ 440 MeV, where $m$ is the rest mass and $a$ the coefficient of the anomalous magnetic moment, the resonances can be avoided by choosing the beam energy to be 440 MeV times a half odd integer. In fact, our design energy 1.98 GeV was selected in this way. This is the safest choice but one need not strictly obey this rule because the resonance widths are expected to be very small.

In the main linac, the spin must be in the horizontal plane and point towards a definite direction which is determined by the bending angle in the final focus system and by the beam energy after the linac. Thus, we need a spin rotator somewhere between the damping ring and the main linac.

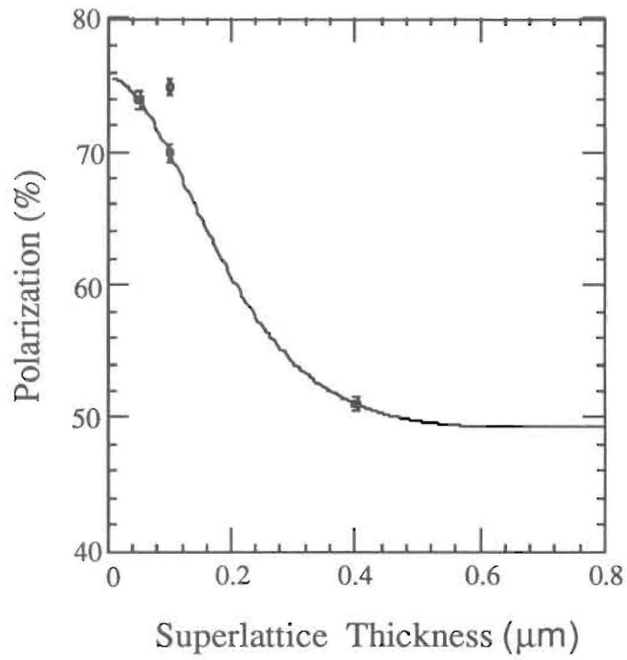


Figure 4.12: Polarization for GaAs-AlGaAs as a function of the superlattice thickness.

If a horizontal polarization can survive in the second bunch compressor, the best location for the spin rotation will be between the first compressor and the pre-linac because the spin manipulation is easier at lower energies. The second compressor consists of a cavity (frequency $f_1$=11.4 GHz, peak voltage $V_1$=534 MV) and an arc with the bending angle 180 degrees (including the sign), followed by another cavity and a chicane scheme (see Sec. 4.4). The depolarization in the chicane is negligible because the net bending angle is zero. The particle energy in the first arc is given by

$$E = E_0 + \Delta E - \alpha z/\sigma_z, \qquad \alpha = 2\pi f_1 V_1 \sigma_z / c = 46\text{MeV}, \tag{4.1}$$

where $E_0$=20 GeV is the average energy, $\Delta E$ and $z$ the energy deviation and the longitudinal position of the relevant particle at the exit of the pre-linac, and $\sigma_z$ the rms bunch length. The precession angle in the first arc is given by $\pi E/E_r$. By assuming a uniform distribution for $\Delta E$ over $\pm\Delta E_{max} = \pm 0.57\% \times E_0$ and a Gaussian distribution for $z$, one finds the reduction factor of the horizontal polarization to be

$$\sin\phi_{max}/\phi_{max} \exp[-(\pi\alpha/E_r)^2/2] = 0.89 \times 0.95 = 0.85, \qquad (\phi_{max} = \pi\Delta E_{max}/E_r). \tag{4.2}$$

Thus, the depolarization in the second compressor is significant if the polarization is in the horizontal plane. Therefore, the spin has to be vertical in the second compressor and must be rotated before injection to the main linac. The rotator to this end has not yet been designed but is believed to be feasible. It inevitably contains either solenoids or vertical bends. Therefore, the increase of the vertical emittance has to be studied carefully.

Since the trajectory in the linac is almost straight, the depolarization there is negligible. The depolarization in the final focus system can come from the horizontal bends but is very small (<0.2%).

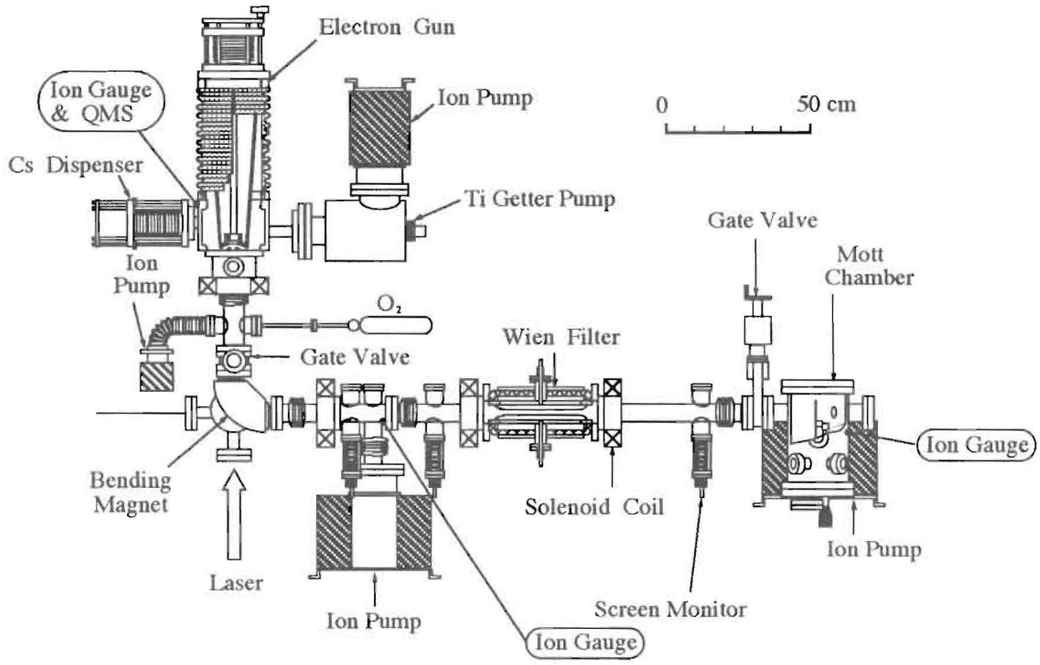


Figure 4.13: An apparatus of polarized electron source.

Finally, the depolarization during the collision has to be examined [6]. In our energy region, where $\Upsilon$, the ratio of the critical energy of the beamstrahlung to the beam energy, is less than unity, the depolarization due to precession in the beam-beam field is estimated to be $0.006n_\gamma^2$, where $n_\gamma$ is the number of photons per electron. Since $n_\gamma$ does not exceed 1.8 (see Sec. 4.1), this depolarization is less than 2%.

At high energies, there is another mechanism of depolarization, namely, the spin-flip synchrotron radiation. The depolarization can be estimated by $2n_\gamma F(\Upsilon)$, where $F(\Upsilon)$ is the ratio of spin-flip to non-flip transition rates. In our region of 300 GeV to 500 GeV, the average of $\Upsilon$ ($\sim \Upsilon_{max}/2.4$) ranges beteeen 0.06 and 0.25, and $F$ between $6\times10^{-4}$ and $4 \times 10^{-3}$. Thus, the depolarization due to the spin-flip is at most 1.5%. When $\Upsilon$ is much smaller than unity, $F$ is approximated by $(7/24)\Upsilon^2$. Therefore, the spin-flip depolarization is totally negligible in the $Z^0$ region.

Note that these values of the beam-beam depolarization are those through the whole process of the collision. The average depolarization during the collision will be about one quarter to one third of them. Also note that the above estimates have some ambiguity due to the disruption and the unknown detail of the bunch shape before collision. If an accurate value of the polarization is needed, one has to measure the polarizations before and after the collision, from which one can evaluate the average polarization during the collision possibly with an accuracy better than ~1%.

### 4.2.3 Positron Source

The JLC-I positron source should be able to produce an intense positron beam of $7 \sim 15 \times 10^9$ particles per bunch and $55 \sim 90$ bunches per RF-pulse, as shown in table 4.3, so that our goal for positron production was set to $8 \times 10^{11}$ positrons per RF-pulse. In this subsection, we will show how to achieve this goal with the conventional positron production method, which exploits electromagnetic cascade showers initiated by high-energy electrons injected on a converter target. Since the thermal stress limits the total acceptable energy by the converter target, we cannot simply increase the number of electrons or the incident energy or both, to meet the JLC-I requirement. We also need to increase the positron capture efficiency as high as possible, by introducing a pre-damping ring which has a large transverse acceptance. The design of such a positron source involves a complicated optimization of various parameters, which necessitates systematic simulation studies. We first define the problem more explicity and then describe the solution obtained from the simulation studies.

Table 4.3: Positron source related parameters of JLC-I (Tentative)

| The center of mass energy[GeV] | 300 | 500 |
|---|---|---|
| Number of particles per bunch | $6.3 \times 10^9$ | $6.7 \times 10^9$ |
| Number of bunches per rf-pulse | 98 | 102 |
| Repetition rate[Hz] | 150 | 150 |
| Bunch spacing [ns] | 2.8 | 2.8 |

#### Statement of the Problem

The positrons emerging from the production target are captured and accelerated to the pre-damping. The number of positrons $N_+$ accepted by the pre-damping ring is roughly proportional to the energy $E_-$ and the number $N_-$ of incident electrons,

$$N_+ = N_- E_- \eta, \tag{4.3}$$

where $\eta$ is the positron production and capture efficiency. The thermal stress limit $\rho$ on the energy density of the incident electrons was obtained at SLC[7, 8] as

$$\rho = \frac{N_- E_-}{\pi \sigma^2} \leq 2.0 \times 10^{12} \mathrm{GeV/mm}^2, \tag{4.4}$$

where $\sigma$ is the rms beam radius. The efficiency $\eta$ is roughly proportional to the accepted normalized emittance $\epsilon$ of the pre-damping ring and the beam transport system, and inversely proportional to the rms beam radius,

$$\eta \propto \frac{\epsilon}{\sigma}. \tag{4.5}$$

Therefore, the number of positrons accepted by the pre-damping ring satisfys

$$N_+ \propto \epsilon \sigma \rho, \tag{4.6}$$

when we operate the target at its thermal stress limit. Since $\rho$ cannot be increased drastically with a conventional metal target, we need to increase $\epsilon$ and $\sigma$. We can increase $\sigma$ as long as the beam power given by Eq. 4.4 is manageable. As for $\epsilon$, we should increase the tranverse acceptance of the transport system including a S-band linac, so as to match that of the pre-damping ring, which has an acceptable normalized emittance of 0.027 rad $\cdot$ m.

### Positron Production System

A schematic diagram of the JLC-I positron-production system is given in Fig. 4.14. The phase-

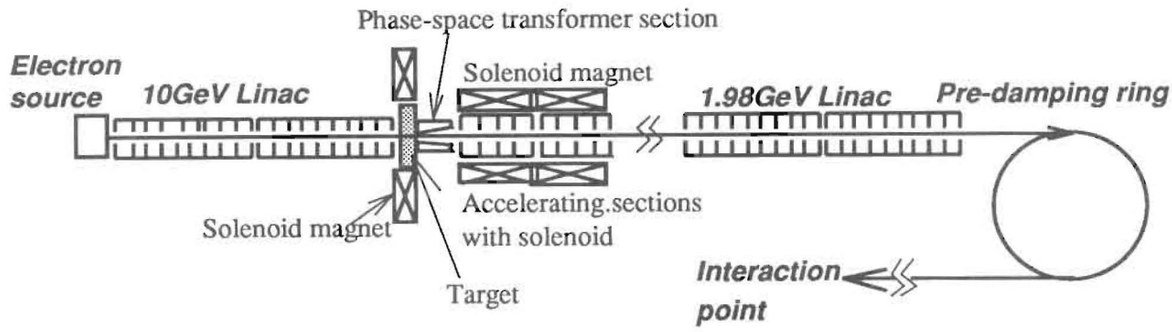


Figure 4.14: A schematic diagram of the positron source for the JLC.

space transformer section, called an adiabatic device[9], just after the target is to accomplish a large radial and energy acceptance. It produces a slowly varying magnetic field along the beam axis, with a flux concentrator[10]. The positrons emerging from the phase-space transformer section are accelerated up to 100 MeV in the accelerating sections surrounded by a long solenoidal magnet. They are then transported to a 1.98 GeV linac leading to the pre-damping ring. In the optimization of various parameters of the positron source system, we have used the EGS4[10] for shower simulations and the Runge-Kutta method for the tracking through the phase-space transformer and the accelerating sections.

**Injected Electron Beam** : Figure 4.15 gives the simulated positron intensity and the required beam power on the target as a function of the incident beam radius. If we set the rms beam radius to 1.2 mm, $9 \times 10^{11}$ electrons per RF-pulse can be injected at an incident energy of 10 GeV, resulting in more than $1 \times 10^{12}$ positrons/RF-pulse. Our goal is to produce $8 \times 10^{11}$ positrons/RF-pulse which requires $5.4 \times 10^{11}$ electrons. This intensity corresponds to a beam power of 130 kW on the target, which is 4.5 times higher than that of SLC.

**Target Section** : W-Re is a suitable material for the converter target because of its high melting point and good fabrication property. Figure 4.16 gives the simulated positron intensity at the interaction point and the rms beam radius at the exit of the target as a function of target thickness for the incident electron energy of 10 GeV. The positron intensity increases linearly with the converter thickness up to 6 radiation lengths($X_0$), so that the 6 $X_0$ appears optimum.

**Phase-space Transformer Section** : Positrons emerging from the target have large transverse momenta of around 3 MeV/c and, therefore, should be transformed in phase-space by an adiabatic device, to be acceptable for downstream accelerating sections. The longitudinal component of the magnetic field in the adiabatic device is given by

$$Bz = \frac{Bi}{1 + \mu z}, \tag{4.7}$$

where $Bi$ is the initial magnetic field at the target exit and $\mu$ is a constant depending on the device. Figure 4.17 shows the simulated positron intensity as a function of $Bi$. It appears

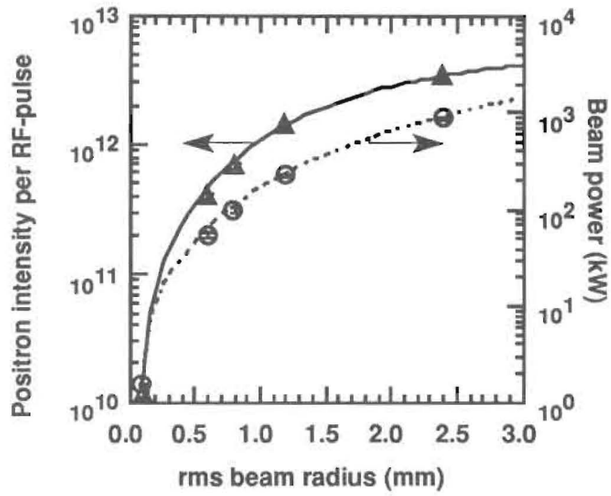


Figure 4.15: The simulated positron intensity and the required beam power on the target as a function of the incident beam radius.

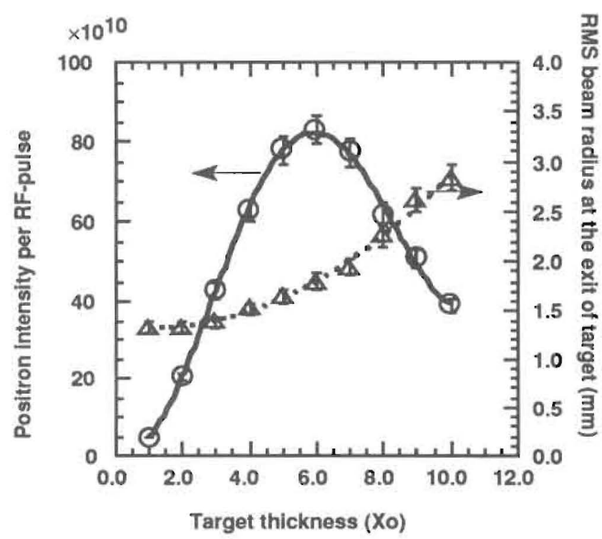


Figure 4.16: The simulated positron intensity at the interaction point and the rms beam radius at the exit of target as a function of target thickness for the incident electron energy of 10 GeV.

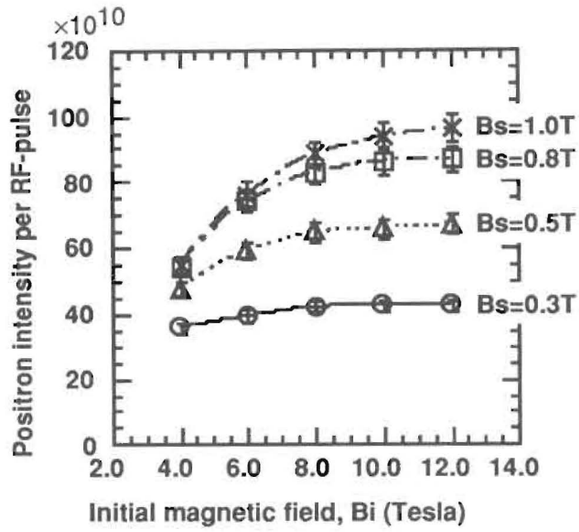


Figure 4.17: The simulated positron intensity as a function of the initial magnetic field $Bi$ and the solenoidal field $Bs$

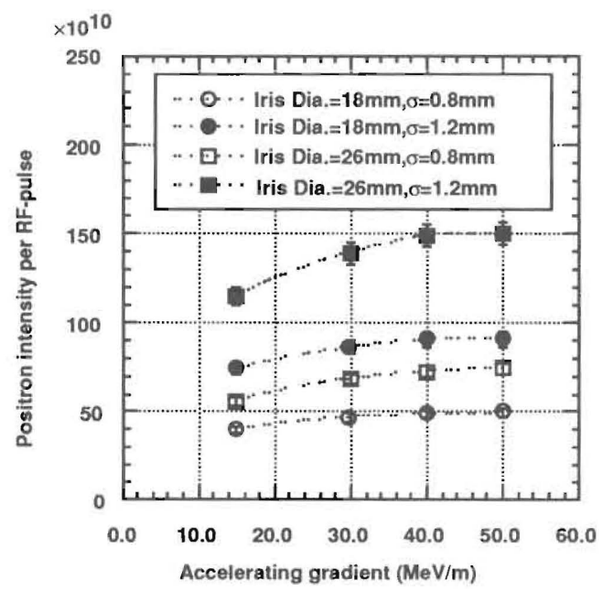


Figure 4.18: Simulated positron intensities as functions of the accelerating gradient, the iris diameter at the exit, and the incident electron beam radius.

that $Bi = 8$ T is a good compromise between the attainable positron intensity and engineering problems to be solved. Given this magnetic field, we get the highest positron intensity when $\mu$ in Eq. ( 4.7) is 50 $m^{-1}$.

**Accelerating Sections with Solenoidal Field** : The energies of the positrons accepted by the phase-space transformer section have a large spread of about 4 MeV, causing a slip in phase during the subsequent acceleration. Furthermore, a finite transverse momentum results in an additional phase slip, since the helical motion has a longer path length than that of straight motion down the axis. Therefore, the accelerating sections should provide a high accelerating gradient, as well as a large aperture desirable in view of the efficiency. Figure 4.18 gives the simulation result, which shows that we can achieve a high positron intensity by enlarging the incident beam radius and the iris diameter. We set the accelerating gradient at 30 MeV/m and the iris diameter at 26 mm. Consequently, the positrons acquire an energy of 90 MeV after the acceleration with two sections of a 1.5 m-long constant gradient accelerating structure in a solenoidal field of 0.8 T,

**1.98 GeV Preinjector Linac** : The 90 MeV positrons are accelerated up to 1.98 GeV by a S-band preinjector linac and are transported to the pre-damping ring. The linac has an accelerating gradient of 30 MeV/m provided by series of 3 m-long constant gradient accelerating structures with an iris aperture of 26 mm. In order to achieve a large transverse acceptance which matches that of the pre-damping ring, the linac should be equipped with 9 FODOs around the first accelerating structure and 3 $\sim$ 6 more around the subsequent structures. Consequently, the system realizes the transverse acceptance of 0.027 rad $\cdot$ m and an energy acceptance of $\pm 1$ %.

### Pre-Damping Ring

Main parameters of the pre-damping ring are given in Table 4.4, where the large transverse

Table 4.4: Main parameters of the JLC pre-damping ring

| | |
|---|---|
| Energy [GeV] | 1.98 |
| Transverse acceptance [rad $\cdot$ m] | 0.027 |
| Extraction normalized emittance [rad $\cdot$ m] | 0.001 |
| Energy acceptance [%] | $\pm$ 1 |
| Damping time [ms] | 3 |
| RF frequency [GHz] | 0.714 |
| Repetition rate [Hz] | 150 |

acceptance of 0.027 radm should be noted. Figure 4.19 gives the simulated positron intensity as a function of the transverse acceptance at the downstream end of the accelerating sections with solenoidal field, for different values of energy acceptance. Clearly, the transverse acceptance is more important than energy acceptance. At the design transverse acceptance of 0.027 radm, $8 \times 10^{11}$ positrons per RF-pulse will be obtained at the interaction point.

It has been shown that the conventional positron-production scheme shown in fig 4.14 can meet the JLC-I requirement of $8 \times 10^{11}$ positrons/RF-pulse. Main parameters of the JLC-I positron source are summarized in Table 4.5. The validity of the conceptual design presented above will be confirmed at the ATF now under construction.

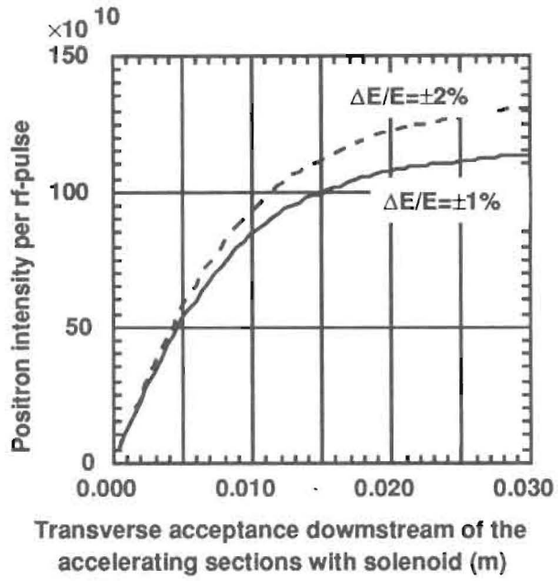


Figure 4.19: The simulated positron intensity as a function of the transverse acceptance at the downstream end of the accelerating sections with solenoidal field, for different values of energy acceptance.

Table 4.5: Main parameters of the JLC positron source Injected Electron Beam

| | |
|---|---|
| Injected Electron Beam | |
| Energy [GeV] | 10 |
| Intensity [ / rf-pulse] | $5.4\times10^{11}$ |
| rms beam radius [mm] | 1.2 |
| Beam power [kW] | 130 |
| Target Section | |
| Material | W–Re |
| Thickness [mm] | 21 (6 Radiation length) |
| Phase-space Transformer Section | |
| Initial magnetic field [T] | 8 |
| Length [mm] | 180 |
| Accelerating Section With Solenoids | |
| Accelerating frequency [MHz] | 2856 |
| Repetition rate [Hz] | 150 |
| Accelerating gradient [MeV/m] | 30 |
| Structure length [m] | 1.5 (×2) |
| Iris diameter at the exit [mm] | 26 |
| Constant solenoidal field [T] | 0.8 |
| Beam Transport To Pre-damping Ring | |
| Transverse acceptance [rad · m] | 0.027 |
| Energy acceptance [%] | ± 1 |

## 4.3 Damping Ring

### 4.3.1 Introduction

The fundamental role of the damping ring is to produce a low emittance beam within the repetition time of the collider system. The key issues are the damping time and the equilibrium emittances. The basic requirements to the damping rings for the three frequency options are summarized in Tab. 4.6. The small ratio of the vertical to horizontal emittances makes it easy to design the final focus system and relaxes the beam-beam effect at the collision point. The value 1% is believed to be achivable in the damping ring with the present technology.

Table 4.6: Requirements to the damping rings for the JLC-I.

| Items | S-band | C-band | X-band |
|---|---|---|---|
| particles per bunch [$\times 10^{10}$] | 1.75 | 1.11 | 0.65 |
| bunches per train | 55 | 72 | 90 |
| bunch spacing [nsec] | 5.6 | 2.8 | 1.4 |
| normalized emittance $\gamma\epsilon_x$[$\times 10^{-6}$radm] | 3.0 | 3.0 | 3.0 |
| normalized emittance $\gamma\epsilon_y$[$\times 10^{-8}$radm] | 3.0 | 3.0 | 3.0 |
| repetition rate [Hz] | 50 | 150 | 150 |

The beam energy of the damping ring is not the primary issue; it is a parameter to be optimized in the damping ring design. Generally speaking, a lower energy is better for the emittance but a higher one is preferred for the damping time. After some optimization processes taking into account the various effects such as the bunch lengthening, particle collision within a bunch (intrabeam scattering), we have decided the energy to be 1.98 GeV. (This fractional value comes from the requirement for the polarized beam. See Sec. 4.2.2.)

The emittance of the extracted beam is given by

$$\epsilon = \epsilon_i e^{-2t/\tau} + (1 - e^{-2t/\tau})\epsilon_{eq}, \tag{4.8}$$

where $\epsilon_i$ is the emittance of the injected beam, $\epsilon_{eq}$ the equilibrium emittance including the effects of intrabeam scattering, $\tau$ the horizontal or vertical damping time, and $t$ the time the bunch stays in the ring. We assume the injected beam emittance of $\gamma\epsilon_i = 5 \times 10^{-5}$radm, which is produced by the RF gun for the electron beam and by the pre-damping ring for the positron beam. The pre-damping ring was designed to accept the positron beam with the normalized emittance $3.0 \times 10^{-3}$radm (rms) and the energy spread 1%. Its circumference is $\sim$ 110m and the damping times $\tau_x = \tau_y \leq\sim$ 4msec [13]. Thus the vertical emittance needs to be decreased by three orders of magnitude. Damping the bunch for five vertical damping times will reduce the first term of above equation by four orders of magnitude. The requirement on the vertical equilibrium emittance is then

$$\gamma\epsilon_{y,eq} \leq 2.7 \times 10^{-8}\text{radm}. \tag{4.9}$$

The required damping times are determined from the desired repetition rate (50Hz or 150Hz), the number of damping times per bunch (5) and the number of trains stored in the ring at once ($N_t$);

$$\tau_x, \tau_y \leq N_t/(f_{rep} \times 5) \tag{4.10}$$

We assume that the rise and fall times of the kickers be less than 60nsec. Such kickers have been already developed. The flat-top length is in the range of $\sim$ 100 to $\sim$ 300 nsec. Thus the trains must be separated by at least 60nsec. Obviously, the circumference of the ring ($L_{ring}$) satisfies the following inequality.

$$L_{ring} \geq c(N_b t_b + 60\text{nsec})N_t, \tag{4.11}$$

where $N_b$ is number of bunches per pulse and $t_b$ the bunch spacing. Since $N_b t_b \geq 60$ nsec, the ring circumference is almost determined by $N_t N_b t_b$.

The damping time is directly proportional to $\varrho_B/\gamma^3$, where $\varrho_B$ is the local bending radius. On the other hand, the normalized emittance is inversely proportional to $\varrho_B/\gamma^3$. In order to reduce both the damping time and the normalized emittance at the same time, we have decided to introduce long wiggler sections in a zero-dispersion region. We also selected a racetrack shape to minimize the space for the dispersion suppression and matching.

Since the equilibrium emittance can be reduced by decreasing the dispersion in the bending magnets or the strength of the bends, we selected a combined function FOBO cell for the arc. The combined function bend has a strong defocussing field and is positioned at the center of a cell in order to minimize the dispersion there.

The ratio of the impedance threshold to the equilibrium normalized emittance, $(Z/n)_t/\gamma\epsilon_{x0}$, is inversely proportional to the cell length[15]. We need a 1.12m drift space in each cell. This length allows a space for sextupole magnets, steering magnets, and position monitors.

Let us consider the scaling formulas including the effects of damping wigglers. After approximations applicable to our case, we find

$$\tau_{eff} \propto \varrho_w^2/L_w, \tag{4.12}$$

where $\tau_{eff} \equiv \tau/N_t$, $\varrho_w$ and $L_w$ are the bending radius and the length of the wiggler. If $\tau_{eff}$ is given(=1.0msec), the impedance threshold goes as

$$(Z/n)_t \propto \theta^2 \varrho_w/L_w \propto \theta^2/\varrho_w, \tag{4.13}$$

where $\theta$ represents the bending angle per cell. Moreover, if $(Z/n)_t$ is given (=0.3$\Omega$), the equilibrium normalized emittance behaves as

$$\gamma\epsilon_{x0} \propto L_{cell}\varrho_w/\varrho_0^2 \propto \varrho_w/\varrho_0, \tag{4.14}$$

where $\varrho_0$ is the bending radius of the main magnet. Conversely, if $\gamma\epsilon_{x0}$ is fixed (=$3.0\times10^{-6}$radm) instead of $(Z/n)_t$,

$$(Z/n)_t \propto \varrho_0/\varrho_w. \tag{4.15}$$

By decreasing the main bending field, one can reduce the emittance without making the impedance requirement tighter, although the cell becomes longer. Therefore, it is desirable to maximize the wiggler fields and minimize the normal bending field. In the next section we present a design which meets all the requirements described above. We can decrease both the damping time and the normalized emittance by increasing the wiggler length. This feature is one of the characteristics of our design.[16]

### 4.3.2 Lattice and Optics

The damping rings are designed for the three frequency options, using the same components as those developed for the Accelerator Test Facility (ATF) at KEK.[17] We describe here the detail only of the C-band option and present a table to compare the three options. The configuration of the ring is illustrated in Fig. 4.20. The ring has a circumference of 320.8m

Table 4.7: Parameters of the damping rings

| Main Linac Frequency | S-band | C-band | X-band |
|---|---|---|---|
| Synchrotron Radiation per turn [MeV] | 0.367 | 0.99 | 0.71 |
| Harmonic Number | 530 | 764 | 660 |
| Total Current [mA] | 410 | 478 | 405 |
| Circumference [m] | 222.5 | 320.8 | 277.1 |
| Number of Trains | 2 | 4 | 4 |
| Number of Bunches per Train | 55 | 72 | 90 |
| Number of Particles per Bunch [$10^{10}$] | 1.73 | 1.11 | 0.65 |
| Longitudinal Impedance Threshold [$\Omega$] | 0.145 | 0.316 | 0.594 |
| Repetition Rate [Hz] | 50 | 150 | 150 |
| Momentum Compaction | 0.00098 | 0.00126 | 0.00140 |
| Natural Emittance [nradm] | 0.512 | 0.569 | 0.618 |
| Horizontal Damping Time [msec] | 6.13 | 3.54 | 4.04 |
| Vertical Damping Time [msec] | 8.01 | 4.30 | 5.20 |
| Bunch Length [mm] | 4.5(4.8) | 4.9(5.0) | 4.9(5.0) |
| RF Voltage (0.714GHz) [MV] | 1.1 | 2.1 | 1.9 |
| Energy Spread [$10^{-4}$] | 8.6(9.09) | 9.1(9.29) | 9.14(9.24) |
| Touschek Lifetime [sec] | 41 | 70 | 130 |
| Emittance with Intra-beam [$10^{-10}$] | 6.73 | 6.41 | 6.18 |
| Horizontal Phase Advance per Cell [degree] | 120 | 90 | 92 |
| K2 values of SF and SD | 33.4,-45.9 | 25.9,-33.4 | 26.3,-33.6 |
| Necessary Total Power [MVA] | 5 | 9 | 7 |

and a superperiodicity of two. The optical functions $\beta_x$ and $\beta_y$ and the dispersion function $\eta_x$ for a half of the ring are plotted in Fig. 4.21. The damping times are $\tau_x = 3.54$msec and $\tau_y = 4.30$msec. This allows each train to stay in the ring for 6.2 vertical damping times when operated at 150Hz. The intrabeam scattering contribution to the emittance is about 13% of the equilibrium emittance.

Each arc consists of 30 combined-function FOBO cells. The bending angle is 6.00°, and the normalized gradient of the quadrupole magnets is 4.17m$^{-2}$. With the magnet aperture r=1.6cm, which is 2mm larger than the beam pipe, the pole tip field of the quadrupoles is 4.4kG. The magnet configulation in a cell is plotted with the lattice functions in Fig. 4.22.

The design of the wiggler is crucial in our design. It has the effective field 1.88T, the period $\lambda_w = 40.0$cm, and the total length 133m with the packing factor 0.36. The configuration of the wiggler section is shown in Fig. 4.23. We use 58 wigglers. A high field quality is required since the non-linear fields can reduce the dynamic aperture and cause a beam loss at the injection.

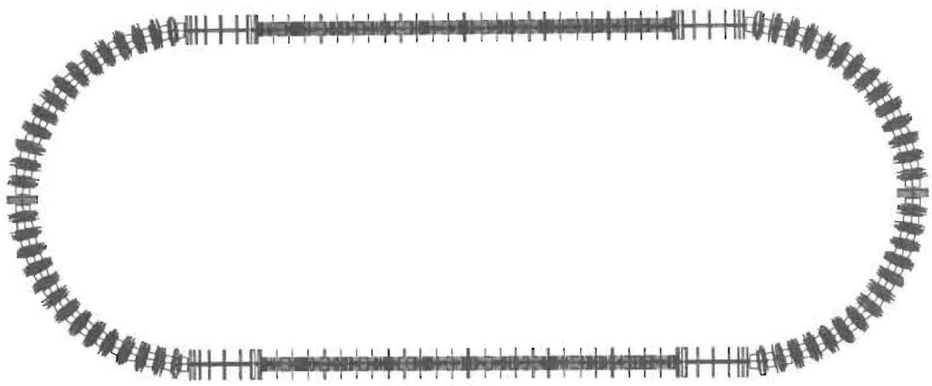

Figure 4.20: Schematic layout of the JLC damping ring.

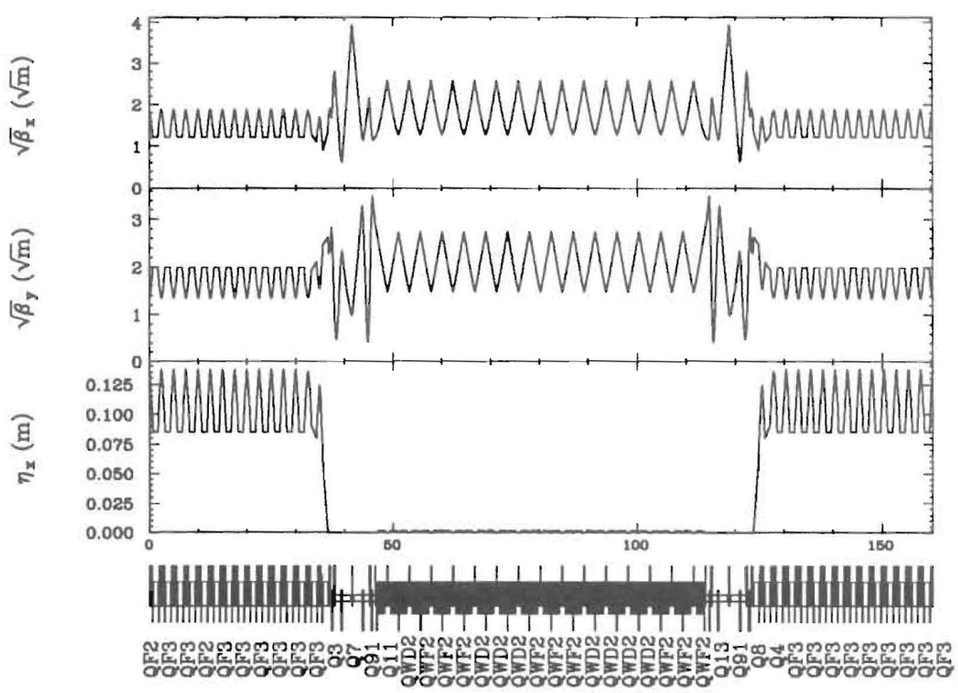


Figure 4.21: Lattice parameters of half of the damping ring.

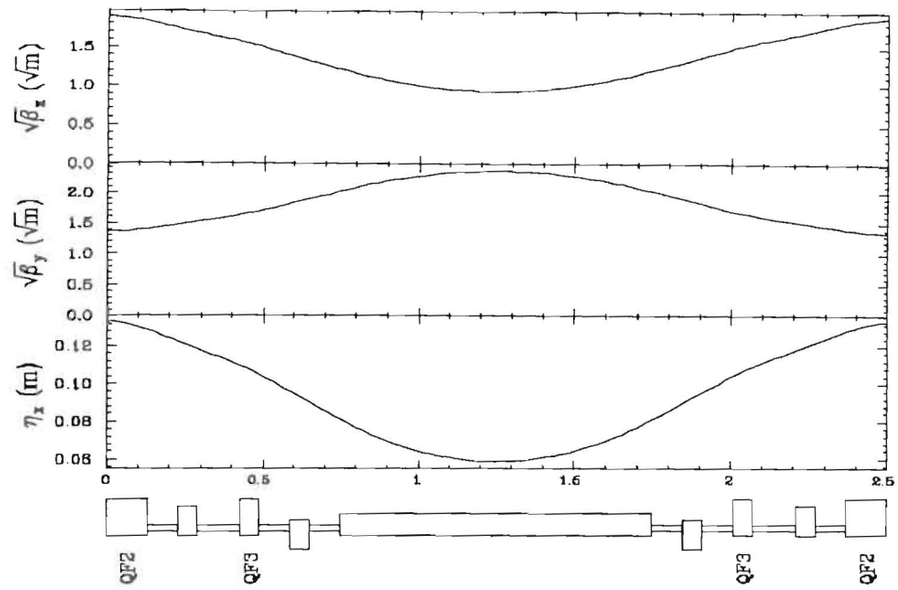


Figure 4.22: Lattice parameters of a single normal cell.

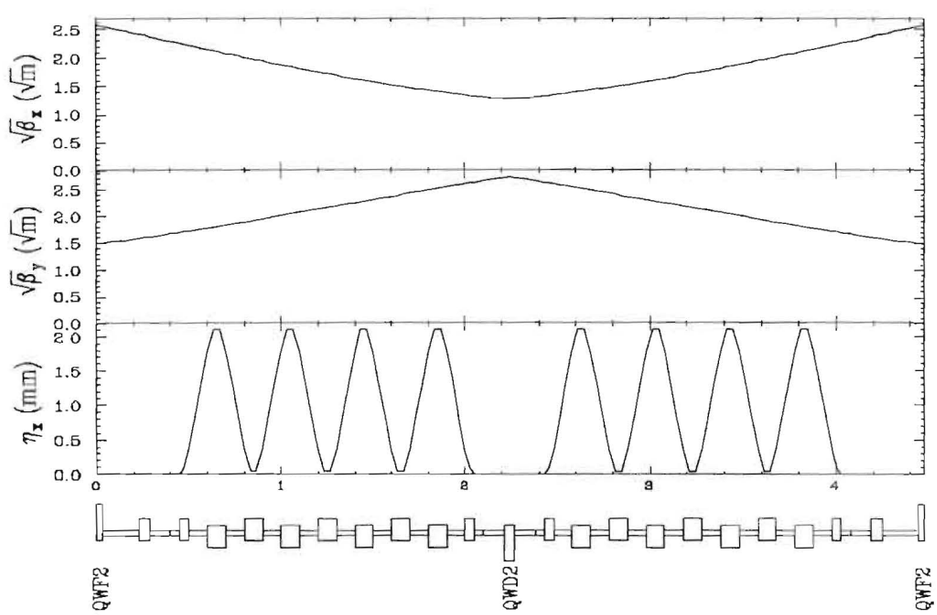


Figure 4.23: Lattice parameters of a wiggler cell.

### 4.3.3 Dynamic Aperture and Alignment Tolerances

Since the damped beam has a much smaller dimension than the injected beam, the requirement of the dynamic aperture comes from the size of the latter. Three times the rms size will be enough in order to avoid a significant beam loss. We will measure the dynamic aperture in terms of the horizontal equilibrium beam size $\sigma_0$. Since the injected emittance is larger than the equilibrium emittance by a factor 50/3, three sigmas of the injected beam size correspond to $13\sigma_0$ ($\sim$1.5mm). The planned beam pipe in the arcs has a 13.5mm inner radius or $\sim 22\sigma_0$.

We correct the chromaticity with only two families of sextupoles in the arcs. The integrated sextupole strengths are: $K_{2SF} = 25.9\text{m}^{-2}$ and $K_{2SD} = -33.4\text{m}^{-2}$. The results from the computer code SAD indicate that the dynamic aperture is more than $80\sigma_0$ without nonlinear fields of wigglers. It will decrease when errors and the wiggler nonlinear field are included. However, the tracking simulations made with a sinusoidal nonlinear field show that the aperture is still more than $40\sigma_0$. A result of tracking over 1000 turns using SAD is plotted in Fig. 4.24. We find that the tolerance of the magnet misalignment and the monitor setting error is 30$\mu$m vertically and 50$\mu$m horizontally and those of rotation and of the field error are 0.5mrad and 0.1%, respectively.

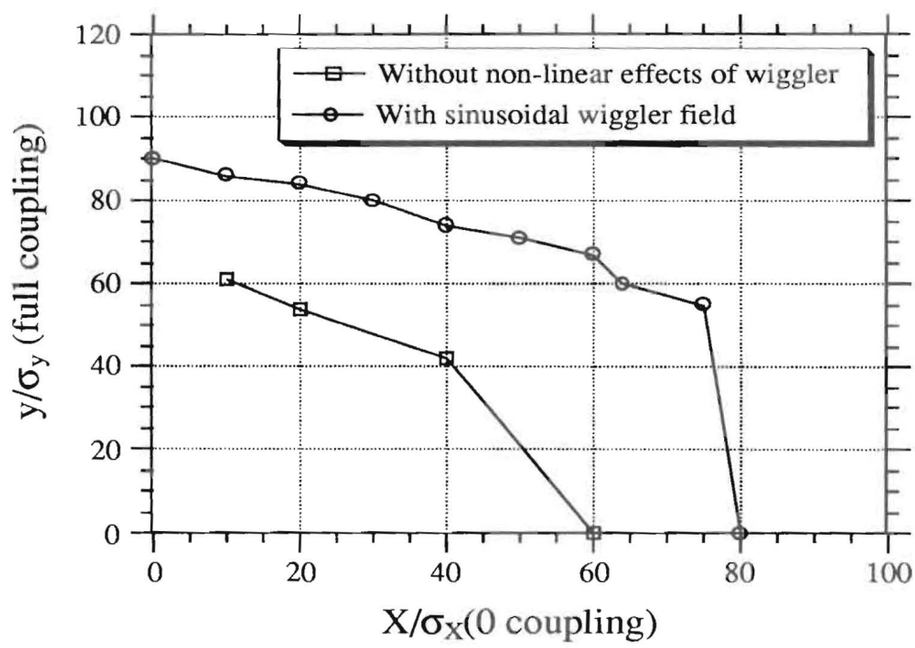


Figure 4.24: Dynamic aperture.

### 4.3.4 Single Bunch Instability

The short-range longitudinal wake causes the bunch lengthening. It was observed in the damping ring of the Stanford Linear Collider(SLC) [18]. This phenomenon restricts the performance of the damping ring operated at a high current. The relevant wake fields are generated at discontinuities of the vacuum chamber. Almost all the vacuum components of the JLC-I damping

The transverse instabilities can be suppressed by the damped cavity and the bunch-to-bunch tune spread within each train. The requirements are estimated by a tracking simulation as

$(R/Q)Q \sim 10^6\ (\Omega/m)$ for each transverse mode,

$\Delta\nu \sim 1 \times 10^{-3}$ ,

where $\Delta\nu$ is peak-to-peak betatron tune difference within a train. These values also agree with analytic results for uniformly distributed bunches with the same total current assuming that bunches in a train are decoupled because of different tunes. These requirements to the RF cavities can be satisfied as will be described later and the tune spread can be obtained by an RF quadrupole.

### 4.3.6 Injection and Extraction

#### Injection

Three septum magnets successively deflect the beam injected from the RF gun or from the pre-damping ring by 110, 132, and 44mrad. The beam is further deflected by about 4.5mrad by a kicker magnet to match the closed orbit of the ring. The injection error will be smaller than $0.1mm$. To keep the beam loading of the cavity in the damping ring almost constant, the RF bucket which has been occupied by the just extracted bunch must be filled immediately by an injected bunch. So, the beam extraction point, the injection point, and the cavity section must be located in the ring in this order.

#### Extraction

The stabilization of the beam extracted from the damping ring is extremely important. The jitter has to be less than one tenth of the beam size.

The beam to be extracted is deflected by about 4.65mrad by a kicker magnet into the first septum magnet. The three septum magnets successively deflect the beam by 44, 132, and 110 mrad. For the septum magnets, DC magnets are chosen, because pulsed ones will introduce larger jitters. The pulse-to-pulse reproducibility in the total deflection angle (286mrad) is better than $\pm 3 \times 10^{-5}$.

Assuming $\beta_x \cong 10$m, the jitter tolerance on the kicker is estimated to be $5 \times 10^{-4}$ [15]. In order to achieve this tolerance, we need to use a double kicker system, separated by a phase advance of $\pi$, to cancel the jitter. The first kicker will be placed in the damping ring and the second kicker in the extraction line, thus reducing the jitter into the range $10^{-4}$ to $5 \times 10^{-4}$. Fig. 4.25 shows a design orbit trajectory for injection and extraction.

### 4.3.7 Magnet System

Conceptual designs have been made for damping wigglers, combined function bends, quadrupole and sextupole magnets. The magnet specifications were determined with consideration for the available space and the cost of the magnets and power supplies. It is necessary to be able to separate upper and lower parts of quadrupoles, sextupoles, and wigglers for the installation of the vacuum chamber. For magnetic field and alignment reproducibility, these magnets should have some precise knock-pins. This reproducibility may affect the alignment accuracy of the damping ring.

The low emittance and fast damping require high-field, short-pitched wigglers. These conditions conflict each other, because a high field needs much space for coils or permanent magnets.

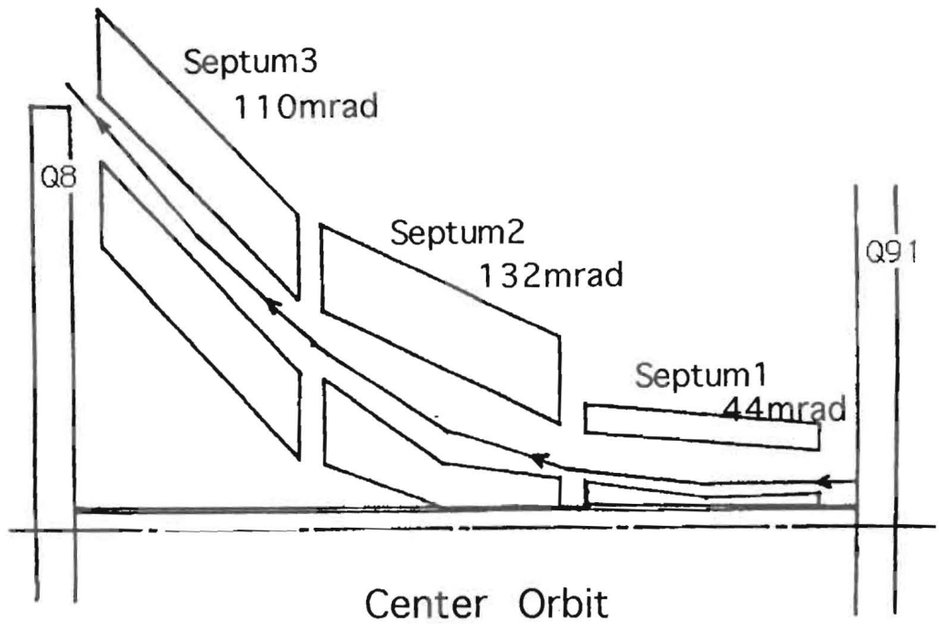


Figure 4.25: Design orbit trajectory for injection and extraction.

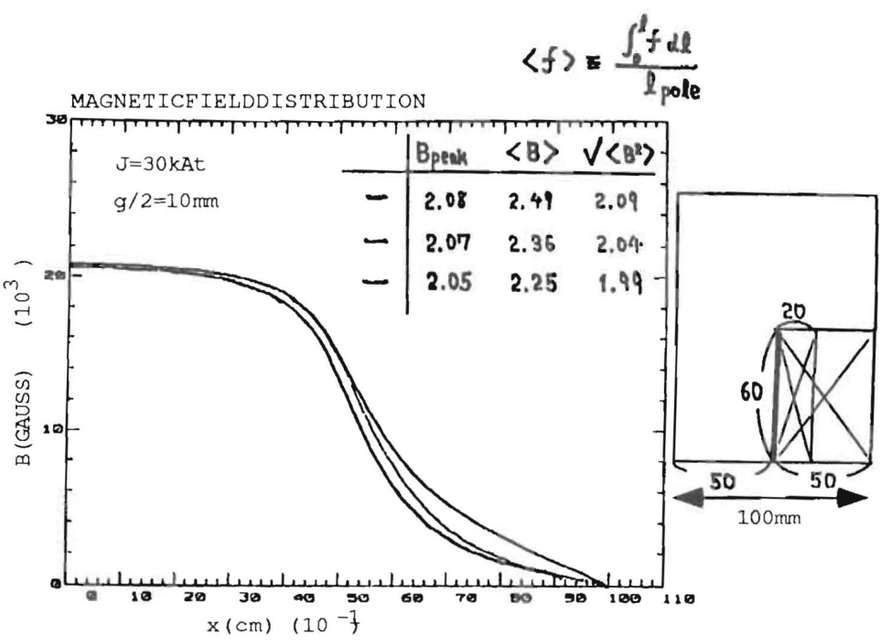


Figure 4.26: Magnetic field distribution of the wiggler.

### 4.3.10 Vacuum system

The main purpose of the damping ring is to get a low emittance beam. The vacuum system must be designed to achieve such pressure that does not disturb the beam emittance through beam-gas scattering. Scattering effect has been evaluated by several persons [25, 26, 27]. Allowing a vertical emittance growth of 10%, we need an average pressure of the ring below $6 \times 10^{-6}$ (Pa). The gas desorption in an electron storage ring is dominantly induced by the irradiation of synchrotron radiation (SR). The density of the SR photons at the chamber wall will reach $2 \times 10^{19}$ and $1 \times 10^{19}$ photons/m/s in the wiggler and arc sections, respectively. We assume that the photo-desorption rate of the chamber is $1 \times 10^{-5}$ molecules per photon. Then we must achieve the pumping speed of 140 and 70 l/s/m for two sections respectively. Basic design concepts of the vacuum system are as follows.

1. Make all vacuum chambers by the extrusion of aluminum alloy. They will be baked to 150 °C for 24 hours before assembly at the beam line, but will not be baked *in situ*.

2. Connect vacuum chambers by clamp-chain flanges and bellows. The chambers will not be weld *in situ* due to the limitation of the connection space.

3. Localize the synchrotron radiation by using photon absorbers, especially in the arc section. It has a merit that we can minimize the area of high gas desorption.

4. The general cross section of the beam duct is a circle of 27 mm in diameter, except for cavities and absorbers. The wiggler chamber has a race-track shape, 15 mm high × 47 mm wide. These chambers must be connected to form a smooth transition keeping the impedance contribution low.

5. Use two types of bellows with race-track and circular apertures that match the chamber's. Insert the RF shield into the bellows and gate valves.

6. Install a cold-cathode gauge to each cell to monitor the pressure of the ring. The additional information will be obtained by monitoring the ion-pump currents.

Most of the above components are similar to those in preparation for the ATF damping ring and, therefore, will be tested soon.

#### Vacuum Chambers

The cross sectional view of the wiggler chamber is shown in Fig. 4.27 (a). The beam duct has cooling channels on both horizontal sides. Along the beam duct, two side channels for non-evaporable getter (NEG) pumps are installed. They are connected with the beam duct through slots that are created in the space between the cooling channel and the outer chamber wall. Three pumping ports are provided on the inner side of the ring to install ion pumps, some vacuum gauges and the roughing pump systems. The cross section of a bending chamber is shown in Fig. 4.27 (b). The bending magnet is a combined type and the gap between the magnet poles is open to the outside of the ring. We will add an antechamber to the beam chamber to localize the area irradiated by SR photons. Ion pumps and NEG pumps will be installed near the photon absorber to evacuate the out-gas effectively. With the beam current of 450 mA (C-band design), the maximum linear power density along the beam duct becomes 1.5 kW/m for both the wiggler and arc sections. These chambers are cooled down by water.

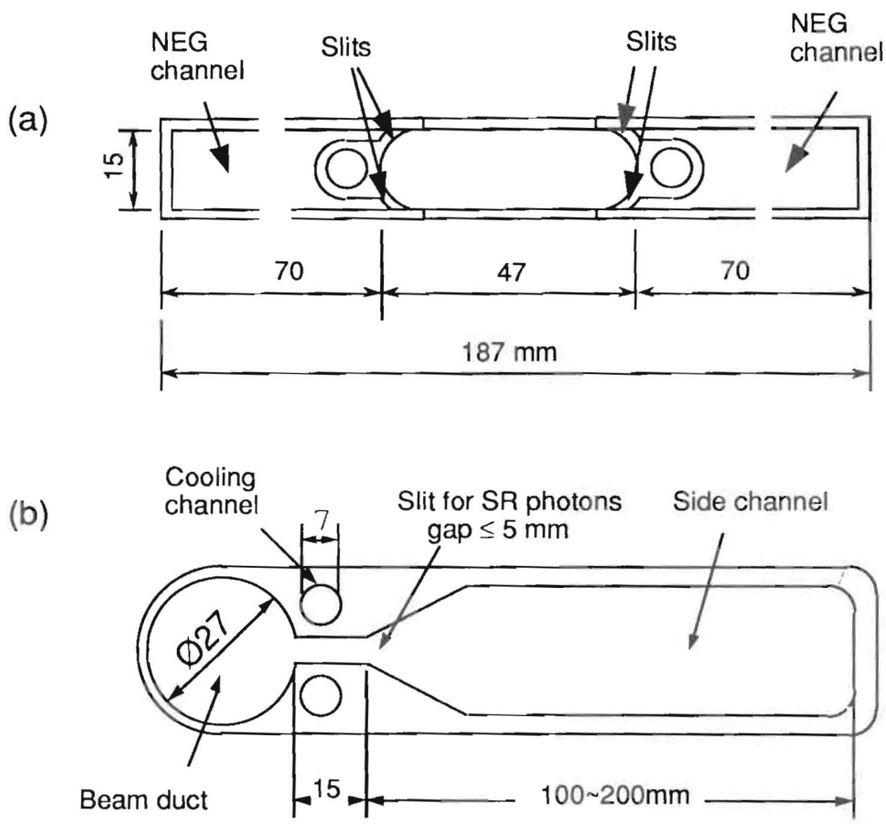


Figure 4.27: Cross sectional views of chambers (a) for the wiggler magnet (b) for the bending magnet.

In the antechamber, the maximum temperature at the surface of the copper photon absorber will reach 100 °C. The first antechamber of the bending section must absorb the power from wigglers, and thus the maximum temperature of the absorber will become several hundred degrees. Therefore, these photons are let out of the ring like SR rings do.

A prototype of 3m vacuum chamber was tested and we obtained much information to improve the production technique of the vacuum chamber. We are planning the design of almost perfect RF contact for bellows and of cooling system for the reduction of the number of absorbers.

### Pumping scheme

The roughing pump system is connected to vacuum chambers by manually operated valves. The system consists of an oil-free turbomolecular pump with magnetic bearings and a rotary pump. The pump will be mounted on a cart and disconnected from the vacuum chamber during operation except for the NEG pump activation. Sputter ion pumps (SIPs) will be mainly used in the ring. They will be placed just before the photon absorber to effectively evacuate desorbed gases. The SIPs will be of 60 l/s nominal pumping speed for straight chambers and 100 l/s for antechambers. Linear NEG ribbons will be installed in two side channels of the wiggler chamber. It effectively evacuates the desorbed gases along the beam duct. Additional lumped NEG modules will be installed in the normal cell to support the SIPs.

## 4.4 Bunch Compressor

### 4.4.1 Introduction

A higher luminosity can be obtained with a given beam emittance by making the beta function at the collision point smaller but, if the beta function becomes about the same as the bunch length, one cannot increase the luminosity any more. Thus, a short bunch is needed for higher luminosity. It also helps to minimize the adverse effect of short-range wake field in the main linac. The proposed beam parameters of JLC-I (Sec. 4.1) require the bunch length ranging from 80 $\mu$m to 150 $\mu$m in the main linacs. The bunch length in the 1.98 GeV damping ring (DR) is about 5 mm and the energy spread is $0.93 \times 10^{-3}$. Thus a compression of bunch length by a factor of 63 is required. Due to the emittance preservation in longitudinal phase space, this process causes an increase of the energy spread by the same factor, which cannot be accepted by the main linac and by the compressor itself. It is therefore necessary to have a system composed of two compressors between which an intermediate linac (pre-linac) accelerates the beam to recover the relative energy spread within bearable values.

In the following sections, the number of particles in a bunch ($N$) and the number of bunches in a train ($m_b$) are assumed to be $(0.7 \sim 2) \times 10^{10}$ and $50 \sim 80$ respectively, while preserving their total charges to be $8 \times 10^{11}$ in a train.

### 4.4.2 Basic parameters

In this section we discuss the choice of the beam energy at the second compressor and the compression factors of the first and the second compressors. Key issue is the energy spread in each stage. We have to consider two points. Firstly, the multi-bunch beam loading in DR, if not compensated within DR, brings about unequal equilibrium distances between the bunches. These deviated positions are mapped to different energies at the exit of the first compressor (referred to as BC1 hereafter) which performs a 90° phase rotation in the longitudinal plane. The position deviation amounts up to 5 mm ($1\sigma_z$(DR)) for the proposed DR cavity. It is converted to an energy shift $1\sigma_\epsilon$ at the cavity of BC1. Secondly the acceleration in the pre-linac yields an energy spread due to the single-bunch beam loading. With S-band structures, the rms energy spread is approximately 0.2% for $N = 2 \times 10^{10}$ and $\sigma_z$=0.5mm [28].

Fig 4.28 shows the energy spread ($2\sigma$) in the BC1 and BC2 as a function of the compression factor of BC1 for various energies of BC2. We have assumed a compensation of multi-bunch energy shifts at the entrance of the pre-linac (S-band). The solid line of BC1 is the energy spread at the entrance of the S-band linac, while the broken line shows that in the second arc of BC1. We have also included weak dependence of single-bunch energy spread in the linac on the bunch length. The multi-bunch energy spread in the S-band linac is assumed to be 0.15% (peak-to-peak). A higher energy of BC2 relaxes the energy spread of BC1 and BC2. There must be a trade-off between the cost of the pre-linac and the difficulties of the transport in BC2 and in the first portion of the linacs. In the following we choose the energy of 20 GeV. The energy spread ($\pm 2\sigma$) at the entrance of pre- and main linac is $\pm 2.58\%$ while at the second arc of BC1 it is $\pm 2.58\% \times 3/2 = \pm 3.87\%$. The compression factors of BC1 and BC2 are 0.072 and 0.222, respectively. Table 4.9 shows the basic parameters of the bunch compressors. Fig 4.29 shows a schematic view of the bunch compressor sysytem.

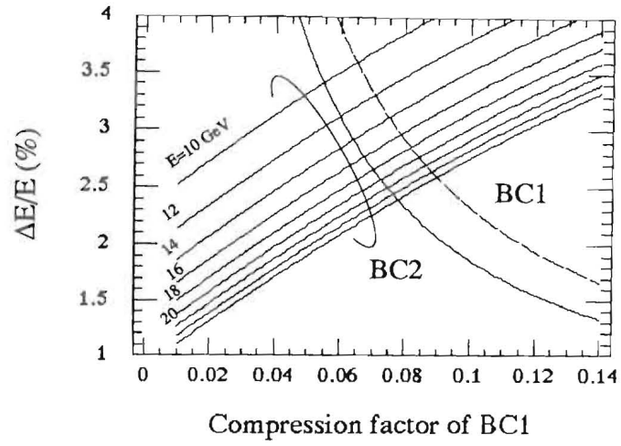


Figure 4.28: Energy spread of bunches (in $2\sigma$) versus compression factor of the first compressor.

Table 4.9: Basic parameters of bunch compressors

| Location | Energy spread($2\sigma$) (%) | Bunch length (mm) |
|---|---|---|
| Damping Ring | 0.186 | 5.0 |
| BC1 (second arc) | 3.23 | $5.0 \rightarrow 0.36$ |
| BC1 (exit) | 2.58 | 0.36 |
| S-band Linac | $2.58 \rightarrow 0.570$ | 0.36 |
| BC2 (exit) | 2.56 | 0.08 |

### 4.4.3 First Compressor

There are two issues which should be taken into consideration in the design of the first bunch compressor (BC1). Both of them are related with the multi-bunch beam-loading effect. Firstly, the beam-loading in the damping ring causes unequal displacements among the bunches in a train, which can result in unequal acceleration in the linac, if the beam is directly injected to the linac. Actually, however, this will make no problem since the longitudinal phase advance 90° of the bunch compressor converts the position shift to an initial energy spread in the linac (Fig. 4.30(a)) which eventually fades out during acceleration. Secondly, the transient beam-loading in the cavity of the bunch compressor itself produces an energy spread among bunches. This brings about an incomplete rotation in the longitudinal phase space, resulting in different longitudinal positions in the linacs which cause an energy spread again (Fig. 4.30(b)).

The parameters of BC1 are summarized in Table 4.10.

#### Longitudinal optics of BC1

These linear or nonlinear position shifts in the DR are converted by BC1 to energy shifts in the following linacs. The condition of 90° phase advance and that of upright ellipses at the both ends give

$$\ell_1 = \ell_2 = -1/k = m_1\beta_1 = m_1\sigma_{z_0}/\sigma_{\epsilon_0} \ , \tag{4.17}$$

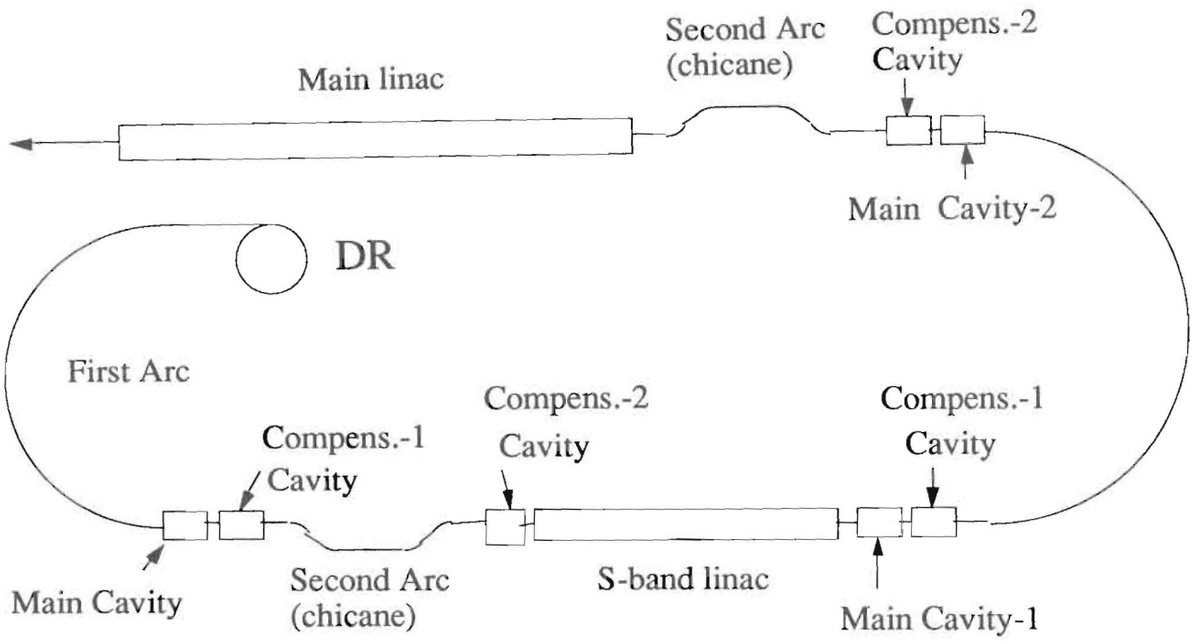


Figure 4.29: Schematic view of bunch compressor system

where $\ell_i (i = 1, 2)$ are the dilation factors of the arcs before and after the cavity, $k$ is the local slope of the RF voltage normalized to the nominal energy, and $m_1$ is the compression factor of BC1. In the present design $\ell_1 = \ell_2 = 0.387$ m and $\hat{V} = 170.9$ MV for the L-band cavity structure. The energy shift after passing the compressor cavity becomes 1.29 %. Adding $2\sigma$ energy spread of single bunch to this, we find the required band width of the second arc to be $\pm 3.24\%$.

### Second arc of BC1

It is essential to transport the beam with such a tremendous energy spread of $\pm 3.5\%$. The usual achromat system seems impossible to apply. We adopt a chicane section instead of arc[30].

Table 4.10: Parameters of the first bunch compressor

| | | | |
|---|---|---|---|
| Momentum compaction of first arc | $\ell_1$ | 0.387 | m |
| Momentum compaction of second arc | $\ell_2$ | 0.387 | m |
| Main cavity voltage | $V_M$ | 171 | MV |
| frequency | $f_0$ | 1.428 | GHz |
| Compensation-1 voltage | $V_{C1}$ | 61.0 | MV |
| frequency | $f_{C1}$ | 1.428 | GHz |
| beat frequency | $\Delta f$ | 0.25 | MHz |
| Compensation-2 voltage | $V_{C2}$ | 62.5 | MV |
| frequency | $f_{C2}$ | 2.856 | GHz |
| beat frequency | $\Delta f$ | 0.25 | MHz |

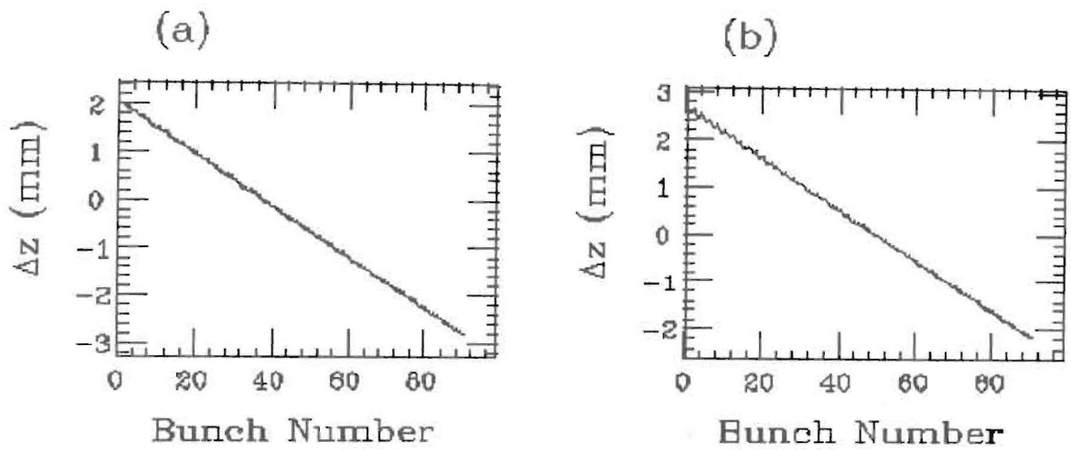


Figure 4.31: The equilibrium position in DR: (a) with the fundamental mode only and (b) including a higher order mode(HOM). The loss parameter of HOM is equal to that of the fundamental mode. $Q$(HOM)=300, $f$(HOM)=4.5$f_0$.

between two successive bunches. In our design, the number of bunches $m_b$ is rather large (50 to 90), meaning that the quadratic term in $n$ in Eq. (4.18) is not negligible.

To compensate for the beam loading, it is desirable to use a steady-state of a structure. A conceivable compensation scheme is to use two structures driven by slightly different frequencies. The principle is shown in Fig. 4.32. Denoting the wave numbers as $k_0 \pm \Delta k$, one can write the

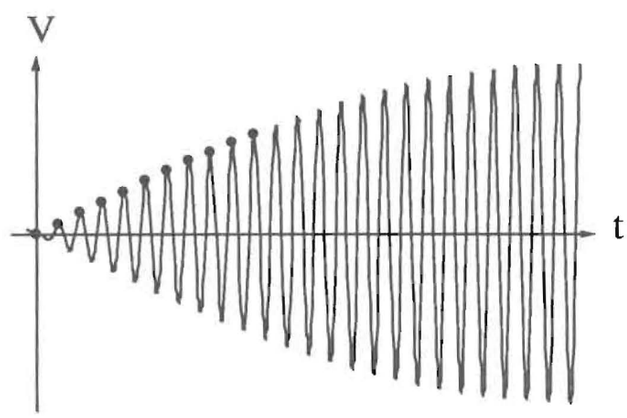


Figure 4.32: Beating method. Each bunch is placed on the crest of modulated rf.

summed voltage as

$$\begin{aligned} \Delta V_n &= V\sin[(k_0+\Delta k)z_n+\phi] - V\sin[(k_0-\Delta k)z_n+\phi] - V_b(n) \\ &= 2V\sin(\Delta k z_n+\phi)\cos k_0 z_n - V_b(n), \end{aligned} \tag{4.19}$$

where $\phi = 2\pi(\Delta k/k_0) \times$ integer is assumed. $V_b(n)$ is the beam loading of the compensation cavity itself. By adjusting the beat phase $\phi$ and the amplitude $V$, the beam-loading voltages of the main and the compensation cavities can be cancelled up to the second order in $n$.

This method can correct the energy deviation of bunches up to the second order without affecting the single bunch energy spread. We attach this compensation system to each main

cavity in the compressors. It is also adopted at the exit of BC1 to compensate for the energy shift which is converted from the position shift in DR.

The heavy beam-loading generates energy and position shifts in the second compressor, too. The beam loading in the first cavity produces an energy shift since the phase advance is 180°, while that in the second cavity yields mainly a position shift since the phase advance between the second cavity and the exit of BC2 is almost 90°. These effects can also be suppressed by the beat method described above.

### Tracking simulation

We made simulation calculations for the first compressor. We have assumed that the loss parameter for the fundamental mode is 4.8 V/pC/m/ scaled from S-band structures. The bunch shape in DR was assumed to be Gaussian. Fig. 4.33(a) shows a phase space plot at the

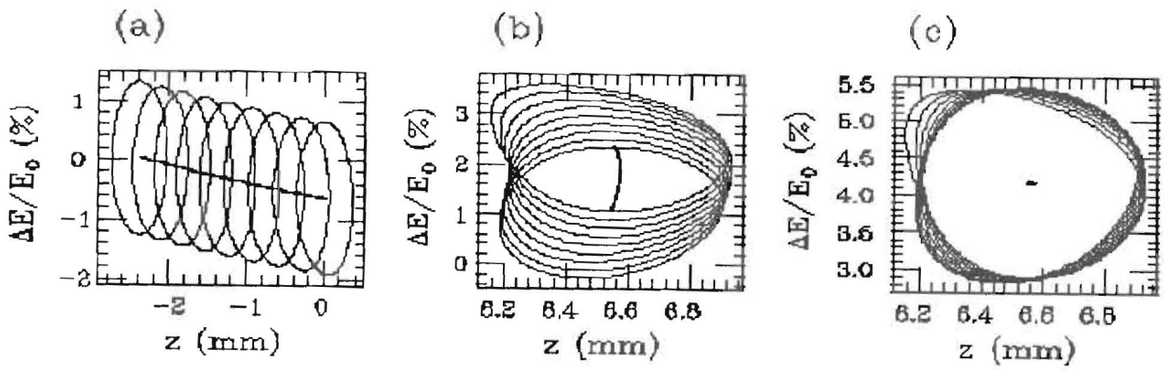


Figure 4.33: Phase space ellipses corresponding to $1\sigma$ beam ellipse. (a) without compensation. (b) with compensation. (c) with full-compensation.

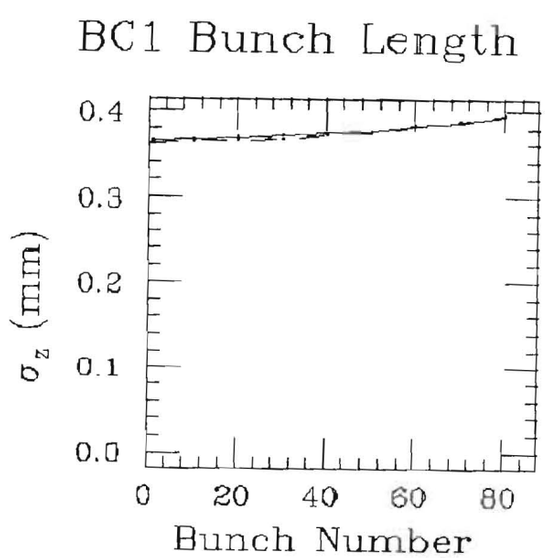


Figure 4.34: Bunch length dependence on bunch number.

end of the arc for the $1\sigma$ ellipse without compensation. It shows that the position shift in DR

is converted to an energy shift and that the energy loss in the compressor cavity results in a position shift. Fig. 4.33(b) is the same plot but with energy compensation. A small position shift ($\sim 0.1\sigma$) is still observed due to a nonlinearity arising from RF sine wave of the main and the compensation cavities. Fig. 4.33(c) shows the results for the full compensation which includes the energy compensation at the end of the arc. The ellipses in the phase space are significantly deformed due to nonlinearities especially for the first and last bunch which are placed far off zero-cross phase of the main RF voltage. In the compensation cavity at the end of the arc we used an S-band structure because the position shifts are already corrected and, therefore, the nonlinear effect is expected to be small.

The bunch length is plotted versus the bunch number in Fig. 4.34. The solid line shows the rms bunch length fitted with Gaussian distribution using all particles and the broken line the rms value of particles within $\pm 3\sigma$ (fitted sigma) only. We find the bunch length varies by about 10 % from the head to the tail of a train.

## 4.5 0.3–0.5 TeV X-band Linac System

The essential advantage of the X-band over lower frequencies is that one can go to higher energies within a given length of the site. Since, however, the main target in this report is a relatively low energy, we will present here an X-band design with an accelerating gradient lower than that we had been planning for the last several years. This low gradient is believed to be feasible in the near future.

A possible RF system is shown in Fig. 4.35 to visualize the X-band system. This system is

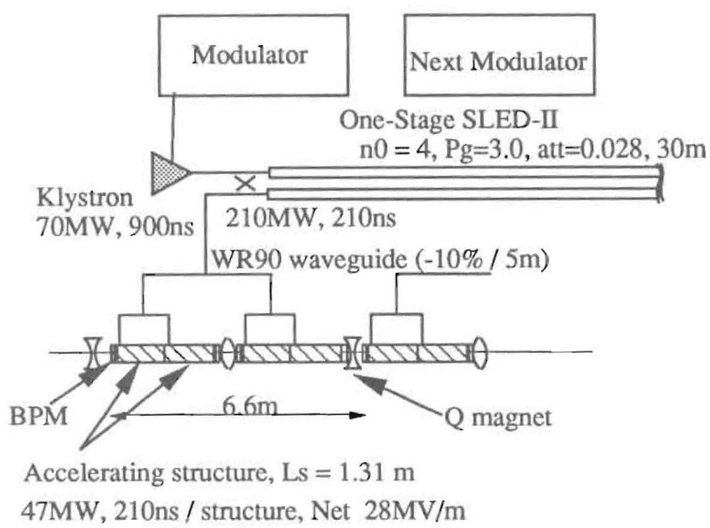


Figure 4.35: A schematic diagram of possible X-band RF acceleration system.

based on the following choice:

1. nominal (unloaded) accelerating field of 40 MV/m,
2. a klystron to power four accelerating structures,
3. one stage SLED-II with the net power gain of three (efficiency 70%),

4. waveguide loss of 5% (assuming 5m long rectangular waveguide).

5. use of 150-cell detuned accelerating structures with $a/\lambda$=0.18.

The accelerating structure and the beam dynamics will be described in the next subsection and the RF source in Sec.4.5.2.

### 4.5.1 Design of X-band linac

#### Design circumferences

The main linac should accelerate number of bunches in a train to the final energy without causing large energy spread nor emittance growth in a single bunch and in a multi-bunch sense. The relevant parameters from Yokoya[34] as of June 1992 are listed in Table.4.12.

Table 4.12: Beam parameters

| | | | | |
|---|---|---|---|---|
| Center of mass energy | $\sqrt{s}$ | 300 | 500 | GeV |
| Final beam energy | $E_f$ | 150 | 250 | GeV |
| Injection energy | $E_{inj}$ | 10 | 10 | GeV |
| Number of particles / bunch | $N$ | 0.70 | 0.69 | $10^{10}$ |
| Bunch length | $\sigma_z$ | 85 | 67 | mm |
| Bunch spacing | $t_b$ | 1.4 | 1.4 | ns |
| Number of bunches / train | $m_b$ | 90 | 90 | |
| Normalized emittance | $\epsilon_y$ | $3 \times 10^{-8}$ | $3 \times 10^{-8}$ | rad m |

In the following discussion, we assume that the betatron amplitude function $\beta$ in the linac varies as

$$\beta = \beta_1 \sqrt{\frac{E}{E_1}} \tag{4.20}$$

where $\beta_1 = 3$ m at $E_1 = E_{inj} = 10$ GeV, giving the total phase advance $\varphi$ through the linac as

$$\varphi = \frac{2\sqrt{E_1}}{\beta_1(dE/ds)}(\sqrt{E} - \sqrt{E_1}). \tag{4.21}$$

In this paper, we assume an optic based on the ordinary FODO structure with the phase advance of 90° per cell. Quadrupole magnets with the field gradient of 100 T/m can be used since the beam hole radius is less than 8mm. Then, they occupy 8.5% of the total length of the linac and the accelerating structures about 90%. This situation is listed in Table.4.13. The net accelerating gradient in the structure with the beam loading is about 28 MV/m. Then the average accelerating gradient $dE/ds$ becomes 25 MV/m.

Table 4.13: Main linac parameters

| | | | | |
|---|---|---|---|---|
| Final beam energy | $E_f$ | 150 | 250 | GeV |
| Total length of a linac | | 5.95 | 9.92 | km |
| Phase advance / linac | $\varphi$ | 760 | 1058 | radian |
| Number of quadrupole magnets | | 968 | 1347 | |

A group of several magnets and accelerating structures are aligned on some kind of a girder and pre-aligned by optical equipment. Then each girder will be aligned by using the beam

and beam monitors. The alignment tolerances depend on the tuning strategy and the feedback method and should be studied in future.

The design of the accelerating structure is closely related to the beam emittance preservation and the needed RF power or wall plug power. Therefore, this design is one of the key issues for the main linac and are discussed in the following.

### Single bunch transverse emittance growth

Single bunch emittance growth due to a random misalignment $X_{rms}$ of cavities with respect to the beam is estimated as[34]

$$\frac{\langle x^2 \rangle}{\sigma_x^2} = \frac{0.218 L_s \beta_f \left\{ e N W_T'(0)\, \sigma_z \right\}^2}{(dE/ds)\epsilon_x (mc^2/e)} X_{rms}^2 \tag{4.22}$$

where $L_s$ is the structure length and $m$ the electron rest mass. It should be noted that the slope of the transverse wake field $W_T'(0)$ scales as $(a/\lambda)^{3.5}$ and the value used here is[34]

$$W_T'(0) = 1.4 \times 10^{20} [V/C/m^3] \quad \text{at} \quad a/\lambda = 0.16. \tag{4.23}$$

(A larger value of $a/\lambda$=0.18 is adopted in the general parameter list in Sec.4.1 to match the requirements at the low gradient in this report. Here, however, we shall use the old value 0.16 since most studies have been done with this aperture.)

The value of $X_{rms}$ is determined by the accuracy of the cavity fabrication and the beam position monitor. It is believed to be better than 10$\mu$m. For $L_s$ = 1.3 m, $E_f$ = 250GeV, $X_{rms}$ = 10 $\mu$m, and $\epsilon_x = 3 \times 10^{-8}$, the above formula gives the emittance growth

$$\frac{\delta \epsilon_x}{\epsilon_x} = \frac{\langle x^2 \rangle}{\sigma_x^2} = 0.14. \tag{4.24}$$

### Multi-bunch emittance growth due to cavity misalignment

The multi-bunch emittance growth $\delta\epsilon$ (normalized emittance) due to the long-range deflecting mode with a low $Q$ value is estimated as[34]

$$\delta\epsilon = \frac{4 A^2 L_s \gamma_1 \sqrt{E_f E_1}}{\beta_1^3 (dE/ds)} X_{rms}^2, \tag{4.25}$$

with

$$A = A_0 \exp(-\frac{\omega_1 t_b}{2Q_1}) \quad \text{and} \quad A_0 = \frac{\beta_1^2 (eN) W_0}{2(E_1/e)}, \tag{4.26}$$

where $\omega_1$, $Q_1$, and $W_0$ are the frequency, the $Q$-value, and the amplitude (per unit structure length) of the deflecting wake field. Let us consider the most severe transverse mode, TM110-like mode, at $\omega_1/2\pi \sim 1.5 \times 11.424$ GHz. Its $W_0$ is estimated to be roughly[35]

$$W_0 = 1.0 \times 10^{17} \left[ V/C/m^2 \right]. \tag{4.27}$$

In this case,

$$A = 0.050 \exp(-75/Q_1). \tag{4.28}$$

If the emittance growth $\delta\epsilon/\epsilon_0$ should be less than 10% when $X_{rms}$ = 10$\mu$m, the $Q$ value for the deflecting mode should be less than 24. The above estimation was performed assuming that the excited wake field can perturb only the next bunch. This assumption will have to be checked by detailed simulations for individual designs.

### Multi-bunch emittance growth due to injection error

The emittance growth due to the long range wake field in the presence of an injection error is examined. When $A\varphi < 1$, the second bunch is most affected, with the oscillation being given by[34]

$$X_2 = X_0\sqrt{1+(A\varphi)^2}\cos(\varphi - \arctan(A\varphi)), \tag{4.29}$$

where $X_0$ is the injection error of the first bunch. In order to suppress the emittance growth below 10%, $A\varphi$ should satisfy

$$\sqrt{1+(A\varphi)^2} < 1.05 \quad \text{or} \quad A\varphi < 0.32. \tag{4.30}$$

The $Q$ value for the dominant TM110-like mode should be below 15 to meet this requirement.

### Structure design

(1) Damped structure

In order to meet this low $Q$ requirement, a damped structure was studied which has four damping waveguides in every cell[36]. Two of the damping ports are aligned in a line. The two lines are perpendicular to each other and one of them is positioned to border a disk in a cell while another to the disk in opposite side of a cell. To realize the $Q$ value of the TM110 mode less than 15, the iris aperture of the damping waveguide should be larger than 9mm as shown in Fig. 4.36(a). Here, the height of the damping port was fixed at 2mm. Though the TE111-like mode seems to have a high $Q$ value, its $r/Q$ is smaller than that of TM110 by a factor of 100[37]. This factor is comparable to the damping of TM110 with $Q_1 = 15$ during the bunch interval. Therefore, a careful study for the actual design is needed. The $Q$ value of this mode, however, must be much smaller than that of the pure TE111-$\pi$ mode, since the mode is a mixture of TE111-like and TM110-like modes, the latter having a very small $Q$ value. Other higher modes are well damped. In this design with 2mm iris width and 2mm damping port height, the $Q$ and the $r/Q$ of the accelerating mode are degraded by 16% and 4%, respectively, compared with the structure without damping port as shown in Fig. 4.36(b). There still remains a possibility to optimize the height of the damping port to obtain a little larger $Q$ value of the accelerating mode.

Since the group velocity changes little by this type of damping waveguide, a structure with $a/\lambda = 0.16$ and $\tau = 0.69$ can be designed as follows. In Table.4.14 compared are the parameters of the structures with damping ports, "Damped", and that without, "Normal", for the unloaded gradient

$$\overline{G} = \sqrt{2\alpha r P_0}\frac{1-e^{-\tau}}{\tau} = 40\text{MV/m}. \tag{4.31}$$

The $Q$ and the $r/Q$ values are estimated using SUPERFISH and the degradation from the normal disk-loaded structure is calculated by the 3-dimensional code MAFIA. Since the degradation of $r/Q$ of the damped structure is only four percent, the required peak power is roughly equal for both the damped and normal structures with the same total attenuation parameter. However, the low $Q$ value of the damped structure makes the structure length 16% shorter than the normal disk-loaded structure. Therefore, the length of a linac should be 16% longer, resulting in the increase of the number of the structures and the power sources by the same amount.

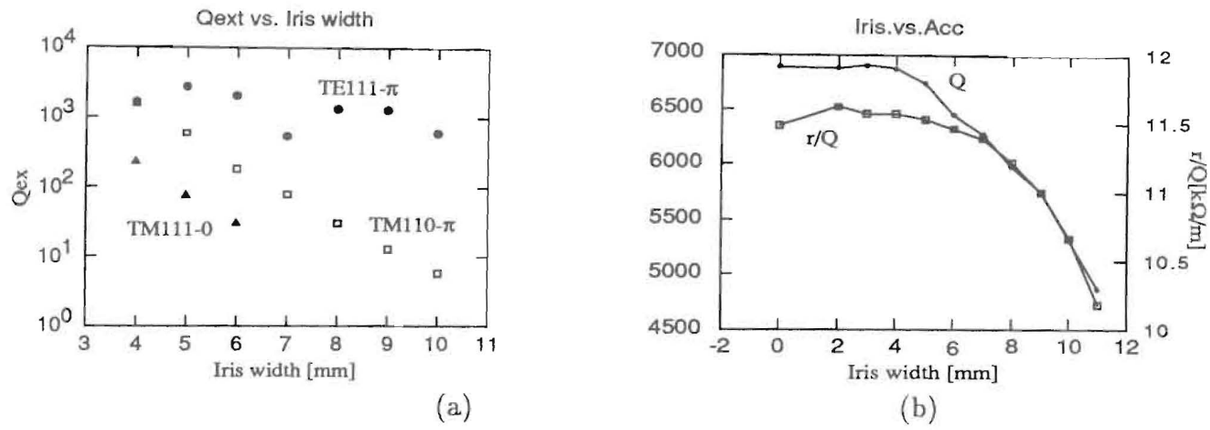


Figure 4.36: (a) External $Q$ values of three important modes to be damped and (b) the $Q$ and $r/Q$ values of the accelerating mode as functions of iris aperture width.

(2) Detuned structure

The $Q$ and $r/Q$ of the accelerating mode in the damped structure decreases due to a large damping hole in the cavity wall. If one can design a structure without holes such that the excited wake fields in all of the cells cancell each other at the arrival time of the following bunches, this degradation will be small while keeping the emittance growth small enough. Following this idea, a detuned structure [38, 39, 40, 41, 42] was examined. Consider a cavity with its transverse mode frequencies of the cells distributed over the range $\Delta f = 1/t_b$ and with the relative frequency difference $(f_i - f_{i+1}) = 1/(N_b t_b)$ between adjacent cells. Then the resultant wake field of the whole structure will be damped at $t_b$ and the cancellation will continue till $N_b t_b$. As shown in the following example, the wake fields of the most severe transverse mode, TM110-like, were shown to be cancelled out below 1% over the period of a bunch train by properly distributing the mode frequency of the cells. In this example, the TM110 mode frequency of each cell in a structure of 150 cells is distributed according to a truncated Gaussian with the standard deviation $\sigma_f/f = 2.4\%$ and the full width $\Delta f/f = 12.5\%$. The wake field of such a structure is shown in Fig. 4.37(a), and the sum of the wake fields of four such kind of structures but with slightly different frequencies is shown in Fig. 4.37(b). The latter scheme is needed for a long bunch train more than 100 ns.

The accelerating field pattern of this structure is shown in Fig. 4.38. The average $a/\lambda$ weighted by the dependence of the slope of transverse short range wake field $(a/\lambda)^{3.5}$ is set to 0.16. The sharp dip and peak near input and output coupler region is due to the Gaussian tail and can be compensated for by changing for example the disk thickness. The field in the figure corresponds to the input power $P_0 = 274$ MW and the average field 114 MV/m. The parameters to realize the unloaded gradient of 40 MV/m are listed in Table.4.14.

The above design is only an example and it still remains to optimize the number of cells in a structure to obtain better characteristics of the accelerating mode. The value $a/\lambda$ may have to be a little larger to relax the alignment tolerance and the single-bunch beam loading. If we adopt 0.18 as in Sec.4.1, the required power will be 47 MW/structure as described in Fig. 4.35.

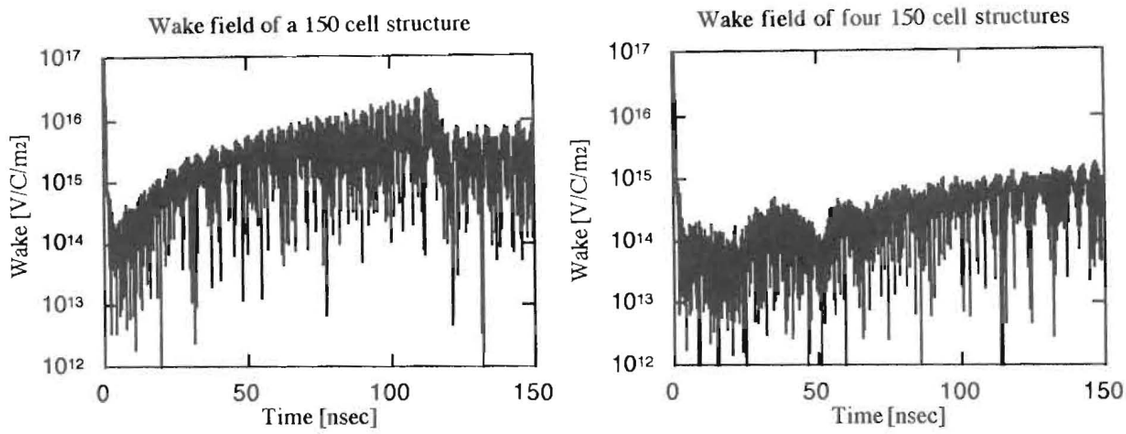


(a) (b)

Figure 4.37: Examples of the wake field of a detuned structure with 150 cells. (a) Wake field of a structure, (b) that of sum of four structures with slightly different frequency distribution.

Table 4.14: Parameters of the accelerating mode of a normal, damped and detuned structures with total attenuation parameter $\tau = 0.69$.

| Parameters | unit | Normal | Damped | Detuned |
|---|---|---|---|---|
| type | | CZ | CZ | |
| $\langle a/\lambda \rangle$ | | 0.16 | 0.16 | 0.16 |
| $a$ | [mm] | 4.20 | 4.20 | 3.14–5.40 |
| $\tau$ | | 0.69 | 0.69 | 0.69 |
| $Q$ | | 6657 | 5592 | 6737–6545 |
| $r/Q$ | [kΩ/m] | 12.23 | 11.74 | 9.44–15.4 |
| $r$ | [MΩ/m] | 81.4 | 65.7 | 63.6–101 |
| $\alpha = \omega/2v_gQ$ | [m$^{-1}$] | 0.471 | 0.561 | 0.204–1.316 |
| $L_s$ | [m] | 1.47 | 1.23 | 1.31 |
| Number of cells | | 167 | 141 | 150 |
| $P_0$ | [MW] | 40.0 | 41.6 | 33.7 |
| $P_0/L_s$ | [MW/m] | 27.3 | 33.8 | 25.8 |
| $T_f$ | [ns] | 128 | 108 | 127 |
| $T_f + N_b t_b$ | [ns] | 257 | 236 | 252 |

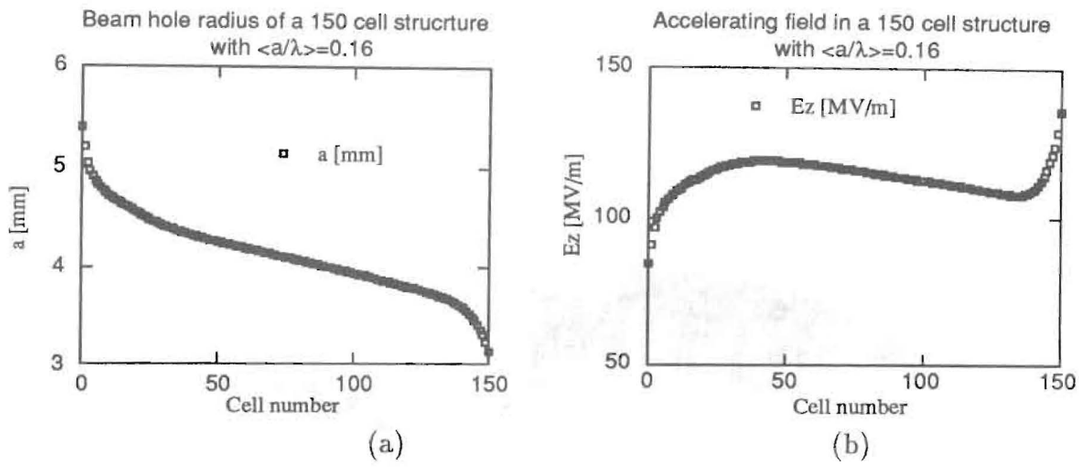


Figure 4.38: Beam hole aperture and accelerating field along a detuned structure with 150 cells.

### Experimental R&D status

Controlling the frequency of transverse mode is very important in suppressing the emittance growth due to the long-range wake field. The precision of the frequency control for the detuned structure, for example, should be of the order of $10^{-4}$. Since the needed accuracy for the accelerating mode is around $3 \times 10^{-5}$ to make the total phase shift along the structure with 100 cells below 2 degrees, the fabrication of the structure without tuning has been studied. If this tuningless structure can be made, the frequency of the dipole mode is automatically well controlled. To this aim, the precise fabrication techniques are studied such as ultra-precision machining, fine brazing, diffusion bonding, and so on. A precise fabrication of a 20-cell brazed structure should be tested in a few months.

A high gradient experiment for a 20 cm long structure which was fabricated in the ordinary manner by a company is underway. After 500 hours' conditioning, a gradient of 70 MV/m level was achieved. A further conditioning seems rather difficult due to frequent RF breakdown. Significant amount of field emission current of the order of mA was observed. However, the operation at the gradient of 40 MV/m level seems easy to realize. At this level, the field emission current is as low as $\mu$A and may not cause severe problem. This low dark current is also explained by a simulation code[43] which shows a critical gradient of 80 MV/m below which any field-emitted electrons cannot be trapped in RF phase to be accelerated to higher energies along the structure.

The requirement on the vacuum in the linac is around $10^{-8}$ Torr to prevent beam halo due to the beam-gas scattering which causes background problem in the final focus region. The vacuum level in the present experiment is estimated to be $10^{-7}$ Torr or worse. The structure was evacuated by four 20 liter/sec ion pumps through two coupler irises with $5 \times 7.5$ mm$^2$ opening and two beam pipes at both ends of the structure with the diameter 6 mm and length 1 cm. In a realistic design, more efficient pumping should be needed.

### Summary and future program

Two kinds of possible X-band accelerating structures were described. A peak power of 35 to 45 MW with pulse length of 240 to 260 nsec is needed for the accelerating field of 40 MV/m

level, which is equivalent to the net accelerating field of 30 MV/m after performing the single- and multi-bunch beam loading compensation.

Engineering R&D for precision fabrication of a detuned structure or a proof of fabrication of a damped structure should be performed soon.

### 4.5.2 X-band RF System

#### Introduction

In the R&D program started in 1988 for X-band klystrons, two types of klystrons have been designed and tested[44]. The first one is a 30 MW class klystron named XB-50K. This rather moderate peak power klystron was designed as the first step to the 100 MW class klystron and produced 18 MW peak power. It supplied the RF power to the first X-band accelerating structure test in 1992.

The second klystron named XB72K was designed as the first 100 MW class klystron which could possibly satisfy the minimum power requirement as the RF power source for an X-band linear collider of several hundred GeV per beam. The first XB-72K was tested in 1992 spring and summer. Its result is also reported here.

#### XB-50 Series

XB-50K's are 30-MW class klystrons developed as the first step toward 100-MW or higher. Design parameters are summarized in Table 4.15. The main purpose of this rather moderate peak power klystron is firstly to produce RF-power useful for high-power tests of X-band RF parts including the accelerating structures.

Table 4.15: Design Specifications (XB-50K)

| | |
|---|---|
| Operating Frequency | 11.424 GHz |
| Peak Output Power | 30 MW |
| RF Pulse Width | $\sim$ 500 nsec |
| Pulse Repetition Rate | 50 $\sim$ 100 pps |
| Beam Voltage | 420 kV |
| Beam Current | 160 A |
| Efficiency | 45% |
| Saturated Gain | 53 dB |
| Focusing Field | 4.6 kG |
| Beam Areal Compression | 80:1 |
| Max. Surface Grad. in Gun | 260 kV/cm |
| Max. Surface Grad. | 1000 kV/cm |
| Average Cathode Current Density | 7.8 A/cm$^2$ |

Prior to the klystron construction, a test diode named XB-50D was fabricated and tested in 1989[45], and reached the cathode voltage of 480 kV. After this diode test, the final design of the XB-50K shown in Table 4.15 was decided, and three XB-50K's have been already completed. The first of them has been tested twice with some modification in the ceramic window[46]. By now XB-50K has been tested up to the RF-power of 18 MW with the pulse duration of 100

ns, and successfully operated for 500 hours up to 18 MW as the power source of the first high gradient test for X-band accelerating structures[47].

Following are the summaries of these tests of XB-50D(test diode) and XB-50K(30 MW class klystron).

### XB-50D

**1) Design and fabrication** XB-50D is a Pierce type electron gun designed for the test of high voltage pulsed electron gun as the beam source of the XB-50K klystrons. The purposes of this tube are 1) to produce the beam power of 80 MW or more, necessary for the RF output power of 30MW, assuming the RF conversion efficiency of 40%, 2) to check the limit of high voltage breakdown in the gun structure, especially in the cathode ceramic part, and 3) to test the new Ir-coated dispencer cathode[49]. As a cathode ceramics, the cylindrical ceramics supplied by WESGO for SLAC #5045 klystrons was selected because of the successful results in the SLC operation.

The design parameters are summarized in Table 4.16. The gun simulation was done using E-GUN code written by W.B.Herrmannsfeldt[48]. To test the high voltage limit in the gun region, the maximum surface field was designed to be high, compared to the present S-band high power klystrons such as #5045 and E-3712. The surface field distribution around the cathode and the anode was calculated by "DENKAI" written by T.Shintake. Over 300 kV/cm surface field strength could be tested at rather low cathode voltages of less than 300 kV. The cathode radius and perveance were determined so as to keep the beam areal compression ratio at 80 to 1 (see Table 4.15), in order to make the focusing relatively easy.

Table 4.16: XB-50D parameters

| | | |
|---|---|---|
| Cathode Voltage | 380 kV | (450 kV) |
| Beam Current | 130 A | (170 A) |
| Beam Power | 50 MW | (80 MW) |
| Maximum Surface Field | 310 kV/cm | (365 kV/cm) |
| Perveance | 0.57 micro-perveance | |
| Cathode Diameter | 50 mm | |
| Cathode Spherical Radius | 60 mm | |
| Cathode Material | Ir-coated dispenser cathode | |

The fabrication of the XB-50K was carried out by TOSHIBA Corporation with the ordinary fabrication method of high power pulsed klystrons. The first XB-50K was delivered to KEK in 1989 spring.

**2) Test results** The high voltage operation test was carried out from 1989 autumn to 1990 spring. To drive XB-50D, a modulator originally designed for #5045 was modified to adjust the pulse length of the PFN by reducing the number of stages down to 3. Also, the impedance of the PFN was adjusted to that of the test diode tube. After a short period of spot-knocking, i.e., the high voltage operation without cathode emission, the high voltage processing started from the cathode voltage of 200 kV. The maximum cathode voltage achieved after 70 hours of conditioning mostly at 2 pps was 480 kV with the pulse half width of about 3 $\mu$sec. No

serious discharge was observed until this voltage was achieved. At 430 kV a reasonably stable operation was sustained at the repetition rate of 100 pps, where the fault rate was once in $10^5$ pulses. A stable operation around 400 kV or slightly higher could be expected for this gun structure with this cathode ceramics.

### XB-50K

**1) Design and fabrication** XB-50K is the first X-band klystron in the R&D program for the future linear collider in Japan. As the first step to the final power source, a rather conservative target of 30MW output power was chosen, since an actual power source was needed for various high-power tests in X-band linac technologies.

The cathode structure of this tube was almost the same as XB-50D with only a slight change applied to the wehnelt and anode geometry for the purpose of relaxing the surface stress without sacrificing the focusing characteristics. At the cathode voltage of 450 kV, the maximum surface stress was reduced to 260 kV/cm from the value of 365 kV/cm in XB-50D. The RF simulations were performed using FCI-code written by T.Shintake[50], and the final design parameters are summarized in Table 4.15.

One of the important parts in a high power pulsed klystron is the ceramic window. The #1 tube had a half-wavelength ceramic-type window. At the first high power test, however, it was broken due to an RF discharge, which will be described later, and was replaced with a new pillbox type window. XB-50K#1a (the repaired one after the failure) and the following XB-50K's have such windows, of which dimensions are shown in Fig. 4.39.

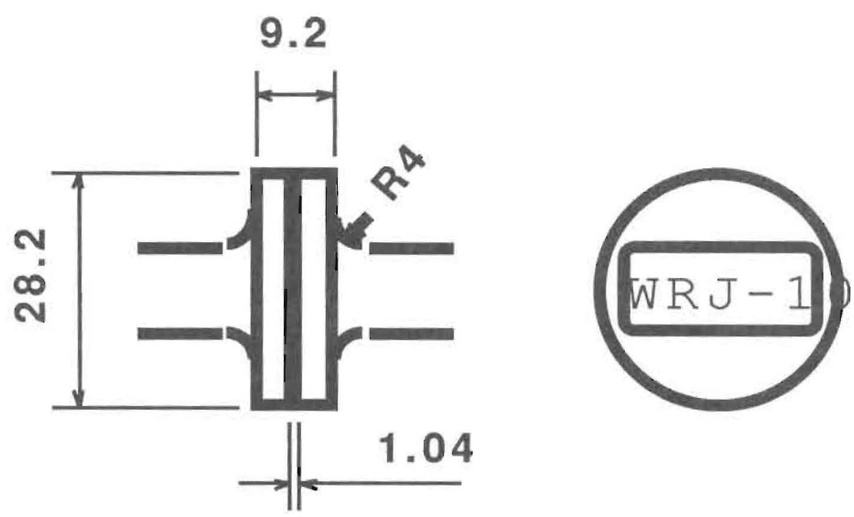


Figure 4.39: Output Window Dimensions of XB72K & XB50K Klystron

By June 1992, #1,#1a,#2, and #3 XB-50K's were delivered to KEK. Among these, #1 and #1a were already tested and #1a has been operated as the RF power source for the X-band accelerating structure test. All of these XB-50K's were fabricated by TOSHIBA Corporation.

**2) Test results** XB-50K#1 was tested up to 11 MW peak power in 1990, and XB-50K#1a up to 18 MW with the pulse duration of 100 ns. Results of these tests are shown in Fig. 4.40 and the experimental set up in Fig.4.41.

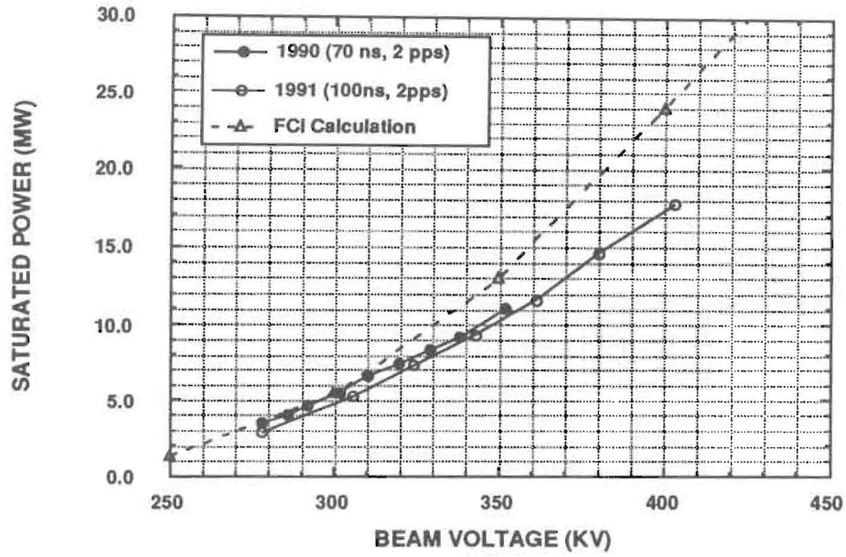


Figure 4.40: XB50K Saturated power.

The half-wavelength type window of XB-50K#1 was broken at the peak power of 11 MW with the pulse duration of 70 ns. This failure was identified as due to a hard RF discharge on the ceramic surface. A serious damage was observed on the atmospheric side of the window. There was an air leak through the ceramics, which is fatal for the vacuum tube. Discharge marks of the sputtered metal film was observed on the ceramic surface and fine powder of chipped ceramics was found inside the wave guide. The damage was harder outside the tube than inside. This was possibly due to the fact that the vacuum pressure in the guide was higher, because no bakeout process was applied to the waveguide vacuum system.

In 1991 summer, XB-50K#1a was tested up to 18 MW with the pulse duration of 100 ns. Up to this power and pulse length, the new pill-box window exhibited only slight discharge and no damage was observed. This same tube was again operated in 1992 spring as the power source for the high gradient test of the 20 cm X-band structure. From April to June, it supplied the RF power up to 16~17 MW with 50nsec at 2~100 pps for 500 hours.

As shown in Fig. 4.40, the measured efficiency at 18MW was still less than the FCI simulation value by 30%. Similar discrepancies have also been seen at SLAC and VLEPP, although the klystrons were designed based on different simulations. The problem might be related to the beam focusing and interception since the drift tube radius is much smaller than in the established S-band klystrons. It is planned as a next step to survey the magnetic field on and near the cathode surface. Also to be analyzed in more detail are the gun design and the beam characteristics around the output cavity, especially at its downstream end.

In Fig. 4.41, the XB-50K#1 and its experimental set-up for high power test are shown.

At the present stage of XB-50K klystrons, the following results have been obtained.

(1) 50-100nsec, 18 MW RF power was obtained and utilized for the X-band acceleration structure test. After 500 hours of operation dedicated to the test at 2 to 100 pps, XB-50K#1a

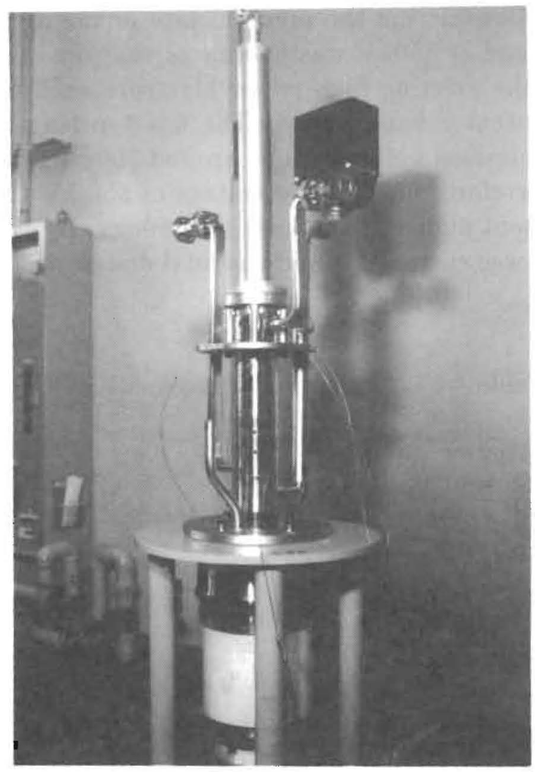

Figure 4.41: Experimental setup for XB50K.

has not shown any degradation in its performance.

(2) RF efficiency was measured as ~30% at the peak power of 18 MW and was lower than the simulation result of 42%.

(3) Diode characteristics, such as cathode voltage, perveance, beam current, and fault rate, are in good agreement with the designed values.

(4) The ceramics window of pill box type had only a slight discharge without damage. For the longer pulse required for the linear collider, further improvements will be needed.

### XB-72K Series

XB-72K is the 100-MW class klystron designed as the prototype which satisfies the minimum peak power requirements for the future X-band linear collider. The main goal of this klystron is to produce the peak RF power of 100 MW or higher. With a help of some RF pulse compression scheme, this klystron can produce the peak RF power of 400 MW. Some problems such as the low modulator efficiency and the power-consuming focusing magnet are left open for future studies.

XB-72K

**1) Design and fabrication** The necessary beam power is more than 250 MW if one assumes the RF efficiency of 40%. Considering the present state of the art in the pulsed high-power klystrons, the cathode voltage of 550kV was chosen as the first step. This voltage is about 30 % higher than that of the existing high-power klystrons such as #5045 or other S-band fleet widely used in the present S-band linacs. The flat top length needed for our klystron with the 4-times pulse compression system will be around 500 nsec which is much shorter than the S-band ones above. Therefore, the cathode voltage of 550 kV to 600 kV is believed to be within the reach of the present high voltage pulse technology. By the use of E-GUN code the diode design of the XB-72k was carried out and the final design parameters are summarized in Table 4.17.

Table 4.17: Design Specifications(XB72K)

| | |
|---|---|
| Operating Frequency | 11.424 GHz |
| Peak Output Power | 120 MW |
| RF Pulse Width | $\sim$ 500 nsec |
| Pulse Repetition Rate | 50 $\sim$ 100 pps |
| Beam Voltage | 550 kV |
| Beam Current | 490 A |
| Efficiency | 45% |
| Saturated Gain | 53 $\sim$ 56 dB |
| Focusing Field | 6.5 kG |
| Beam Areal Compression | 110:1 |
| Max. Cathode Current Density | 17 A/cm$^2$ |
| Max. Surface Grad. in Gun | 273 kV/cm |
| Max. Surface Grad. in Output Gap | 720 kV/cm |

Considering the drift tube radius and the cathode size which is limited by the maximum available current density, the beam areal compression ratio was chosen as 110 and the perveance as 1.2 micro-perveance. This perveance is considered to be the best compromise between the easy beam focusing and the low impedance for the fast rise time of the cathode voltage wave form which is definitely important for the power supply efficiency. Simulations by E-GUN code showed that a good laminar flow can be obtained in the drift tube region with the focusing field of 6.5 kG. The designed gun structure is shown in Fig. 4.42. The beam trajectory obtained by the E-GUN code is shown in Fig. 4.43. Although the cathode voltage is higher by $\sim$30% than that of XB-50K, the surface gradient in the gun structure is kept relatively low, 273 kV/cm at most. The maximum current density on the cathode is 17 A/cm$^2$. This is considered to be feasible from our operating experience of XB-50K which has the same Ir-coated dispencer cathode. Even at this current density, the cathode temperature is estimated to be 1050°C or slightly lower, and the cathode life time longer than $10^5$ hours can be expected at this temperature.

RF simulations were carried out by the use of the FCI code as in the case of XB-50K's. The cavity configuration from the input to the output cavities are shown in Fig. 4.44. The output and penultimate cavities are the so-called "noseless type cavities"[51]. Owing to them the

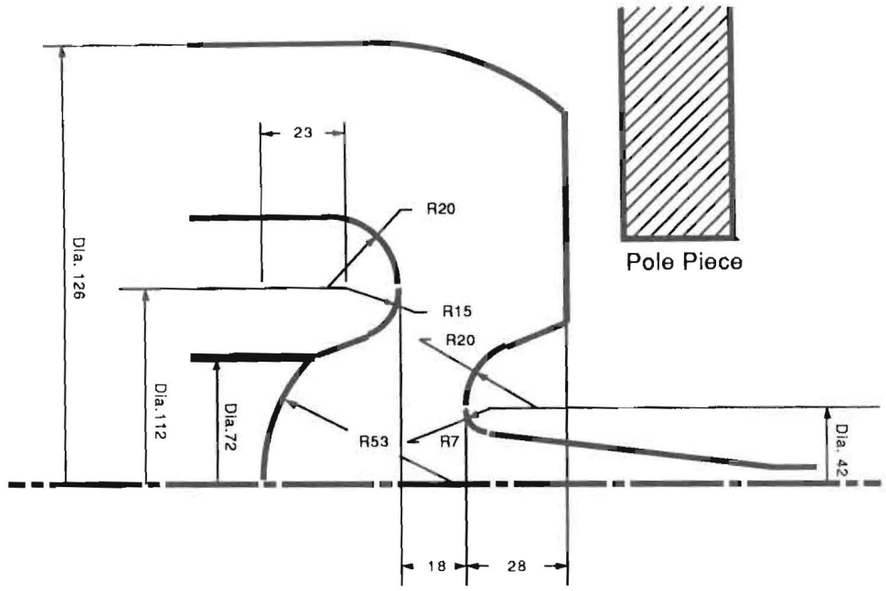


Figure 4.42: Gun dimensions of XB72K Klystron

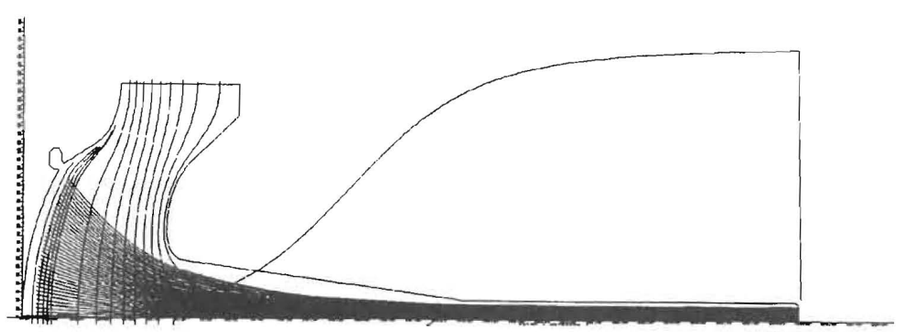

Figure 4.43: The beam trajectory in XB-72K simulated by E-GUN.

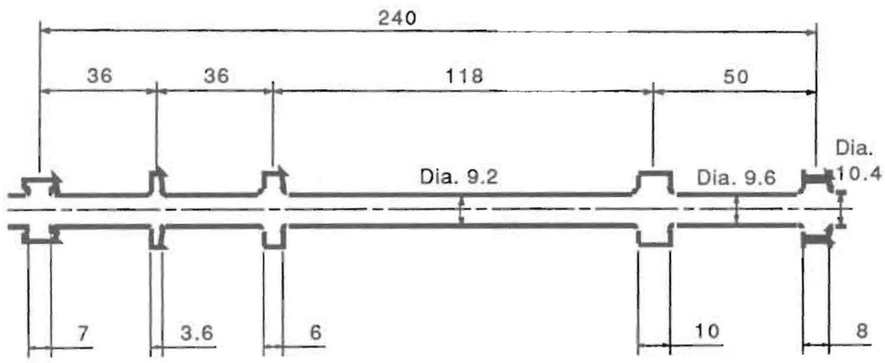


Figure 4.44: Interaction geometry of XB72K Klystron

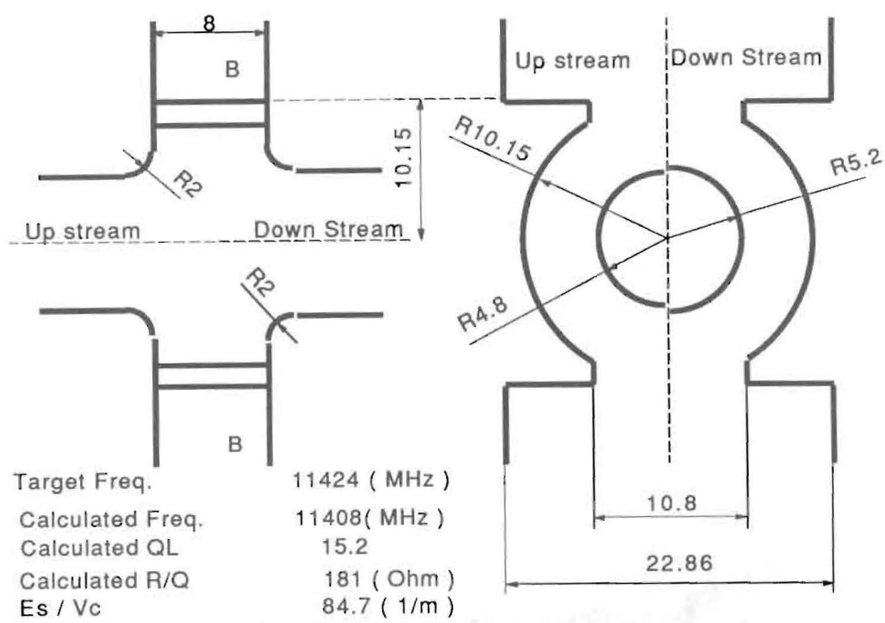


Figure 4.45: Output gap dimensions of XB72K Klystron

maximum surface field in the output gap can be kept as low as 700 kV/cm in spite of the single output gap structure. The output cavity has two output waveguides attached symmetrically, and two pill-box type ceramic windows are set on each waveguide. These windows have the same structure as those in XB-50K's, which have worked up to the RF output of 18 MW with 100 nsec pulse duration.

**2) XB-72K Test results** The first XB-72K fabricated by TOHSHIBA was delivered to KEK in January 1992 and a test system with a new modulator were set up in the assembly hall in KEK site. The setup with the output waveguide system is shown in Fig. 4.46. For

Figure 4.46: The test system for the first XB-72K tube.

the operation of XB-72K to higher cathode voltages than previous tubes, a concrete radiation shield was prepared. The two output windows are connected to individual matched loads and the output RF power was measured separately on each wave guide.

The first high power test of the XB-72K#1 was carried out last April. At the cathode voltage of 430 kV with the RF output power of 22 MW in 100 ns, the gun ceramics had a small but fatal air leak and the test was terminated[52]. After removing this gun ceramics, the inside wall of the drift tube section was examined by a fiber scope for medical use and no visible damage was found from the anode to the downstream end of the output cavity. Apparently, up to this cathode voltage and this RF output power, no serious beam interception did exist in the beam drift section.

XB-72K#1 was rebuilt with a new gun ceramics, cathode, and windows. The high power test was resumed from August 1992[53]. The high power characteristics obtained in these experiments are summarized in Figs. 4.47, 4.48, and 4.49. Fig. 4.47 shows the measured

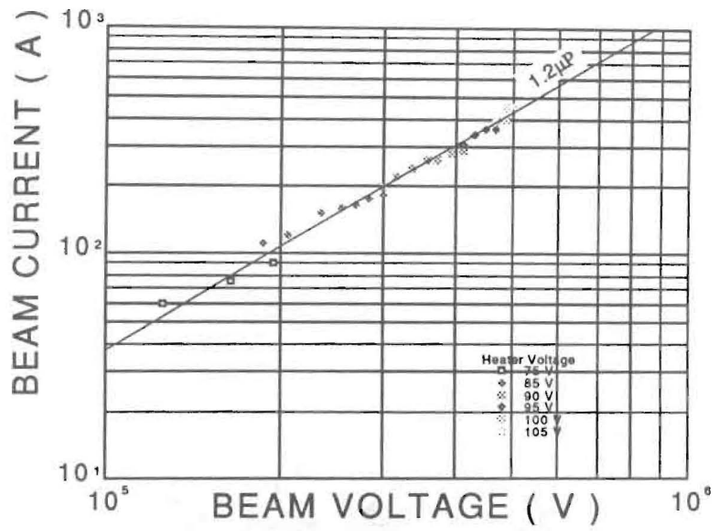


Figure 4.47: XB72K#1A Perveance curve.

perveance of the XB-72K#1a, which is in good agreement with the simulation result shown by the solid line. Fig. 4.48 shows the saturated RF power versus beam voltage. The RF output power reached 41 MW at the cathode voltage of 500 kV. Fig. 4.49 shows the RF conversion efficiency versus beam voltage. The measured efficiency is still lower than the simulation, on which further studies are needed.

The tentative results obtained in these XB-72K high power tests are as follows. This XB-72K#1a is still under conditioning toward higher cathode voltages.

(1) 500 kV beam voltage was achieved.

(2) 230 MW beam power was obtained.

(3) The measured perveance curve is in good agreement with the design value.

(4) RF output power of 41 MW was obtained. The RF efficiency was 18 %.

### Modulator

**1) Modulator for XB-72K** The ordinary modulator which is currently used as the power supply for the XB-72K test cannot have the high power efficiency necessary for the future linear collider due to the rather long rise and fall times of the cathode driving pulse. The switching speed is mainly determined by the stray capacitance and inductance of the pulse transformer in the present modulator system. To shorten the rise and fall times and improve the modulator efficiency, raising the primary voltage thus relaxing the step-up ratio of the pulse transformer will be effective. The Blumlein type configuration of two PFN's can double the output voltage compared to the ordinary single stage PFN. This type of PFN has the advantage of introducing no new components such as a thyratron and a capacitor. A design of

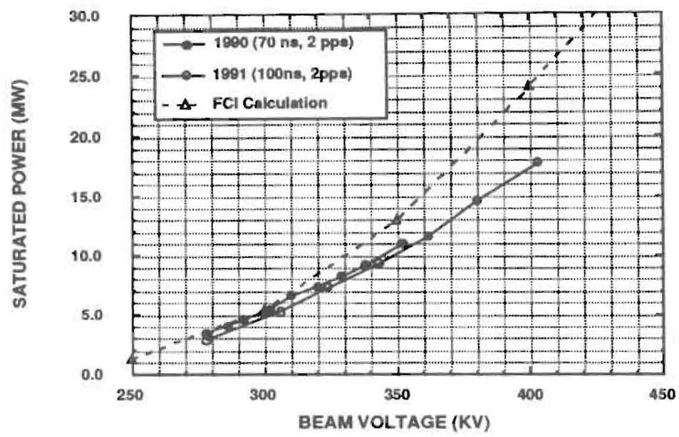


Figure 4.48: Saturated power of XB-72K#1.

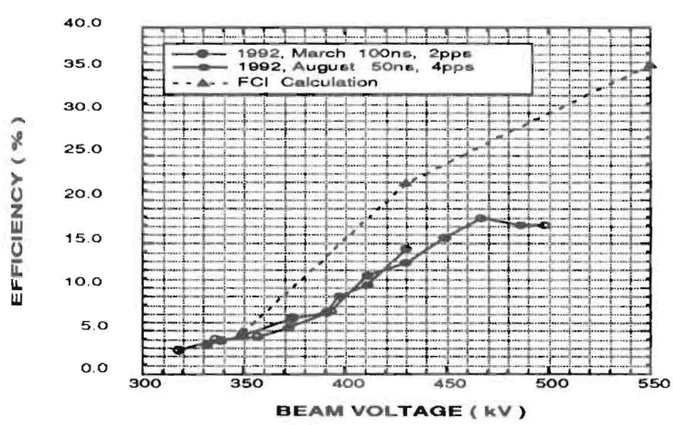


Figure 4.49: Efficiency of XB-72K#1.

this Blumlein type PFN has been completed and an operation test is scheduled in the end of 1992 FY. The design parameters are shown in Table 4.18. This system is expected to reach 80 % modulator efficiency.

Table 4.18: Modulators for X-band Klystron (XB-72K)

Design Parameters

| | |
|---|---|
| (a) PFN (Blumlein Type) | |
| Rise Time (with Trans.) | ~ 150 ns |
| Fall Time (with Trans.) | ~ 230 ns |
| Flat Top | ~ 500 ns |
| Number of PFN | 8-stages + 8-stages |
| Output Voltage(=Charging V) | 80 kV (1:7 Step-up) |
| Impedance | 23 Ohm(XB-72K 550 kV) |
| (b) Pulse Trans. (Primary at 80 kV while charging) | |
| Step-up ratio | 1:7 |
| Leakage L | 830 nH |
| Stray Capacitance | 4 nF (Primary) |
| Loss at 200pps | 100 W (Hysteresis) |
| | 1000 W (Eddy Current) |
| Rise Time (Trans. only) | ~ 100 ns |
| Fall Time (Trans. only) | ~ 200 ns |
| Sag. | 2.8% (after 500 ns) |
| Core Material | Si-Fe (t=25 micron) |

PERSPECTIVES

The recent progress in the X-band RF power sources at KEK described above has shown that the minimum requirement for the linear colliders of the next generation can be satisfied by the X-band klystron system powered by the improved type of modulators. Within a few years, we expect to have a proto-type X-band klystron system with an RF power compression system which satisfy the minimum requirements such as the power efficiency, stability, peak power of 100 MW class and the pulse duration of 500 ns or longer. For this goal, further intensive R&D works including the development of the RF window, the modulator, and the RF power transfer system will be necessary.

## 4.6 0.3–0.5 TeV C-band Linac System

Since several years ago we have been developing an X-band RF system for JLC. Although it can potentially provide a high accelerating gradient, there are still a number of technical problems to be solved. With the S-band, on the other hand, the linac would be very large and long even for 0.5 TeV, albeit less R&D works would be required. In this section we discuss the possibility

of an intermediate frequency range C-band, from which for definiteness we choose 5712 MHz, i.e., twice the SLAC frequency.

Expected advantages of the C-band scheme are as follows.

1. The RF pulse to be generaged by a klystron is a few $\mu$sec in length. Hence, a conventional HV pulse modulator will suffice. Only an engineering study will be required on the modulators to reduce the size and the cost.

2. The peak RF power to be generated by a klystron is less than 50 MW, and the high voltage applied to klystron is only 300 kV. These requirements are moderate and are expected to be met by a straightforward extension of the well-established S-band klystron technologies.

3. The RF pulse compression of the SLED-II type is feasible within a reasonable size by using delay lines of a disk-loaded structure.

For the accelerating structure, we adopt a recently proposed damped cavity which makes use of the radial line damper and the choke structure. With this cavity, multi-bunched beams can be accelerated without serious instabilities. Although this new type of cavity is not instrinsic to the C-band but can be applied to S- and X-band as well, we shall describe it in this section since it was proposed in the course of the design study of the C-band.

### 4.6.1 Outline of C-band Linac

The whole JLC complex should be accomodated in a site at most about 25km in length. If we take into account the length of the final focus system and the space for the linac focusing elements, the active structure length for each linac has to be about 8km. In order to reach 250 GeV within this length, the net accelerating gradient must be at least about 30 MeV/m. If we take into account the beam-loading and the single/multi-bunch energy compensation, a nominal gradient of 40 MeV/m is required. A crude optimization of the collider system is given in Sec.4.1. After some refinement, the basic parameters for the C-band linac are summarized in Table 4.19.

A schematic diagram of the one section of the RF system is shown in Fig.4.50. It consists of a HV pulse power supply (modulator), two klystron amplifiers, two SLED-II type pulse compressors, and four accelerating structures. This section is repeated at every 8.8 meters.

If one simply scales the conventional S-band SLAC structure down to the C-band, the length of a cavity unit becomes about one meter. A longer unit may be more economical because each needs input and output couplers, vacuum jackets, etc. On the other hand, the peak input power increases in proportion to the length, and also the iris radius needs to be larger to make the group velocity fast enough. Consequently, the shunt impedance becomes lower because the electric field concentrates on the disk edge, resulting in a lower ratio of the accelerating gradient to the stored RF power. We therefore choose 2m unit length as a compromise. The filling time is then about 300 nsec as seen in Table 4.19. Since the beam pulse length is 100 bunches $\times$ 2.8nsec = 280 nsec, the RF pulse length into the structure must be about 600 nsec. The required peak power per cavity unit is 85 MW. 3

This RF pulse ( 85MW$\times$0.6$\mu$sec ) or each 2m structure will be provided in the following way. A HV pulse mudulator of conventional type creates an output voltage 302 kV with a flat top length of 3.6$\mu$sec. This power is fed into two klystrons, each of which produces an output RF pulse of 45MW$\times$3.6$\mu$sec. This long pulse is compressed to 0.6$\mu$sec by a SLED-II type

Table 4.19: C-band main linac parameters

| | | | |
|---|---|---|---|
| **Beam Parameter** | | | |
| Frequency | $f_{RF}$ | 5712 | MHz |
| Beam energy | $E$ | 250 | GeV |
| Number of p 71 article per bunch | $N$ | $1 \times 10^{10}$ | |
| Number of bunches per pulse | $N_b$ | $80 \sim 100$ | |
| Bunch spacing | $t_b$ | 2.8 | nsec |
| Repetition frequency | $f_r$ | 150 | Hz |
| **Main Linac** | | | |
| Nominal gradient | $E_{a0}$ | 40 | MV/m |
| Net accelerating grad. | $E_a$ | 28.7 | MV/m |
| Total active length per beam | | 8362 | m |
| **Accelerating Structure** | | | |
| Cavity type | Damped cavity with choke | | |
| Damped Q-value of $TM_{110}$ mode | | $< 5$ | |
| Iris radius/wave length | $a/\lambda$ | $0.16 \sim 0.12$ | |
| Group velocity | $v_g/c$ | $0.042 \sim 0.017$ | |
| Attenuation parameter | $\tau$ | 0.57 | |
| Filling time | $t_F$ | 297 | nsec |
| Q-factor | $Q_0$ | 7932 | |
| Shunt impedance | r | $47 \sim 64$ | MΩ/m |
| average | $\langle r \rangle$ | 55 | MΩ/m |
| Peak RF power per structure | | 85 | MW |
| Loss factor | k | 67.8 | V/pC/m |
| Single bunch loading | kq | 0.11 | MV/m |
| Multi bunch loading | $E_a - E_f$ | 8.0 | MV/m |

compressor. The efficiency is estimated to be 70% so that the peak power becomes 190MW. The output of each klystron drives two accelerating structures. Assuming a loss of 10% in the wave guide, we obtain the required pulse stated above. The pulse structure is depicted in Fig.4.51.

The detail of the klystron and the compressor will be described in the next subsection and the accelerating structure in Sec.4.6.3.

### 4.6.2 C-band RF-Source

The parameters of the C-band RF source are summarized in Table 4.20.

#### The C-band Klystron

**Achievable RF power per klystron** The maximum RF output energy from a klystron generally decreases with frequency. Because the drift tube cross-section in a klystron is inversely proportional to the RF frequency squared, so is the available power. Fig. 4.52 shows the pulse

Table 4.20: C-band RF-system

| | | | |
|---|---|---|---|
| **Klystron** | | | |
| Klystron peak power | $P_0$ | 45 | MW |
| Pulse length | $t_{RF}$ | 3.6 | $\mu$ sec |
| Gun Voltage | $V_0$ | 302 | KV |
| Gun perveance | $K$ | 2.0 | $\mu A/V^{1.5}$ |
| Beam current | $I_0$ | 331 | A |
| Power efficiency | $\eta$ | 45 | % |
| **Pulse Compressor SLED-II** | | | |
| Multiplication index | n | 6 | |
| Loss factor in delay line | $\tau$ | 0.01 | |
| Resistive power loss | | 10 | % |
| Reflection power loss | | 20 | % |
| Energy efficiency | | 70 | % |
| Power gain | $P_0/P_{in}$ | 4.2 | |
| **HV Pulse Modulator** | | | |
| HV Power | | 302kV× 331A | |
| Pulse rise and fall time | | 0.55 and 0.5 | $\mu$sec |
| Pulse efficiency | | 80 | % |
| Pulse energy | 900 | Joul | |
| Repetition frequency | $f_r$ | 150 | Hz |
| Power consumption | $P_{AC}$ | 135 | kVA |
| **System Power Efficiency** | | | |
| Modulator pulse efficiency | | 80 | % |
| Klystron efficiency | | 45 | % |
| Klystron focusing coil power | | 3kW (4.4) | % |
| Pulse compressor efficiency | | 70 | % |
| Waveguide loss | | 10 | % |
| Total power efficiency from AC from to RF input to the structure | | 22 | % |

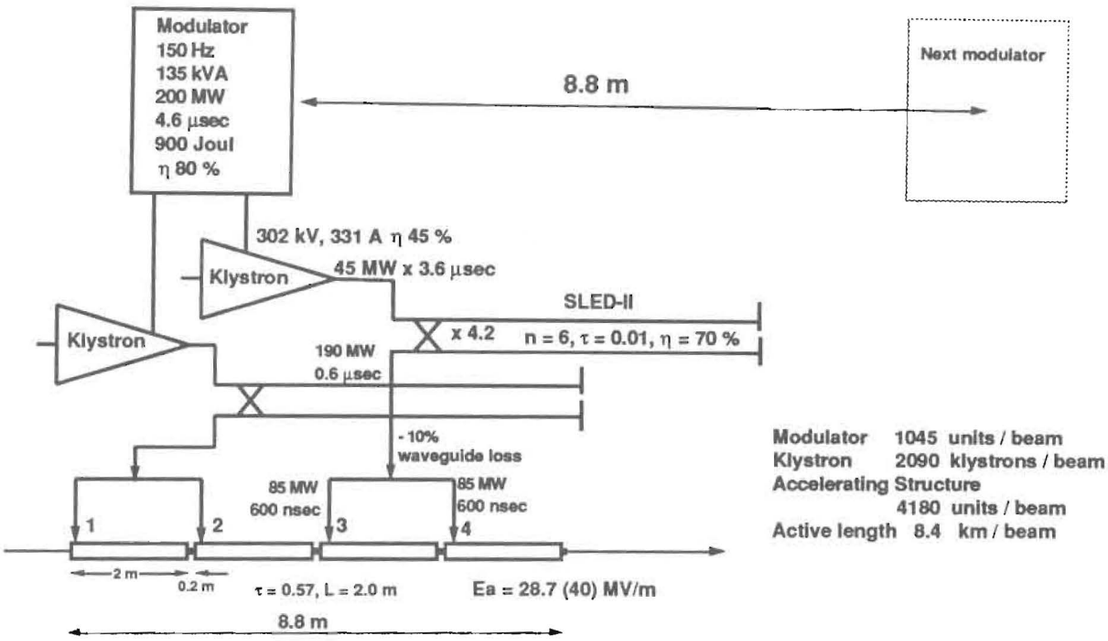


Figure 4.50: The RF system of the C-band main linac.

energy ( peak power multiplied by pulse length ) obtained from existing high power klystrons as a function of the operating frequency. All of them are pulsed klystrons used in linear accelerators. The data near 3 GHz are for the SLAC 5045 klystron developed at SLAC. More than 200 tubes of this type have been successfully operated in the SLC project. The data at 8 and 11 GHz are from R&D tubes developed also at SLAC for the NLC project. The 11 GHz klystron has recently generated 50 MW and 1 $\mu$sec pulse. These data seem to show $1/f^2$ dependence. The lower solid line is a theoretical limit derived under the assumption that the HV break down around the output cavity is initiated by meltdown of the copper drift tube due to collision of infinitely short drive beams. In practice, however, the thermal energy quickly diffuses into the tube body and the surface temperature decays in several tens of nanoseconds. Since the drive beam in klystron is gerenally much longer than this decay time, the surface temperature stays lower than in the impulse case. Therefore, actual tubes work better than the impulse theoretical limit.

The upper solid line shows our guesstimate on the practical limit. This limit for a few $\mu$sec pulse is

$$W_b \sim 1.3 \times 10^4/f^2 \qquad \text{(Joul/pulse)} \qquad (4.32)$$

where $f$ is the RF frequency in GHz, and predicts approximately 400 Joul/pulse at 5.7GHz. Supposing 50% power efficiency from the drive beam power to the RF output, the available maximum RF energy becomes 200 Joul/pulse, corresponding to 56 MW in 3.6$\mu$sec, well above our design value of 45 MW.

**Electron Gun and HV pulse** Suppose the perveance of the electron gun of the C-band klystron to be $2 \times 10^{-6} A/V^{1.5}$, then the HV pulse to drive the klystron becomes 302 kV, and the feeder peak current 331 A. For the reliability of high power klystrons, one of the most important parameters is the gun voltage applied to the electron gun cathode. The 5045 klystron working

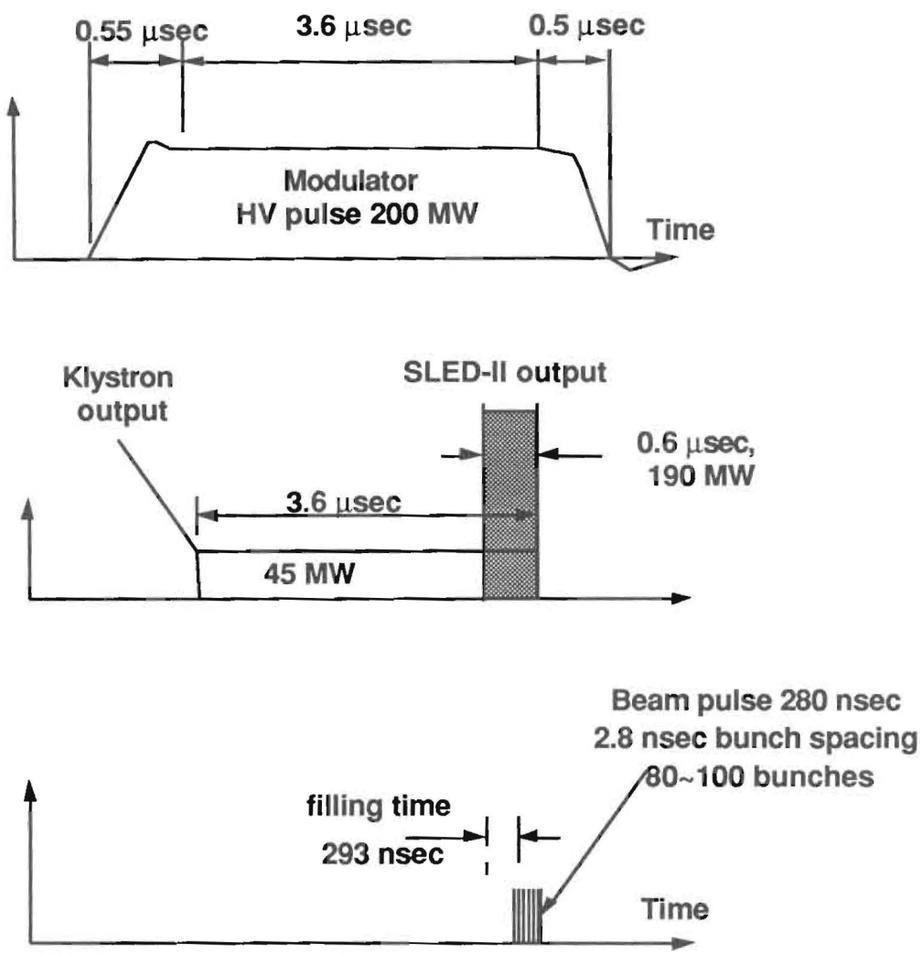


Figure 4.51: The Klystron and beam pulse structure for the JLC C-band linac.

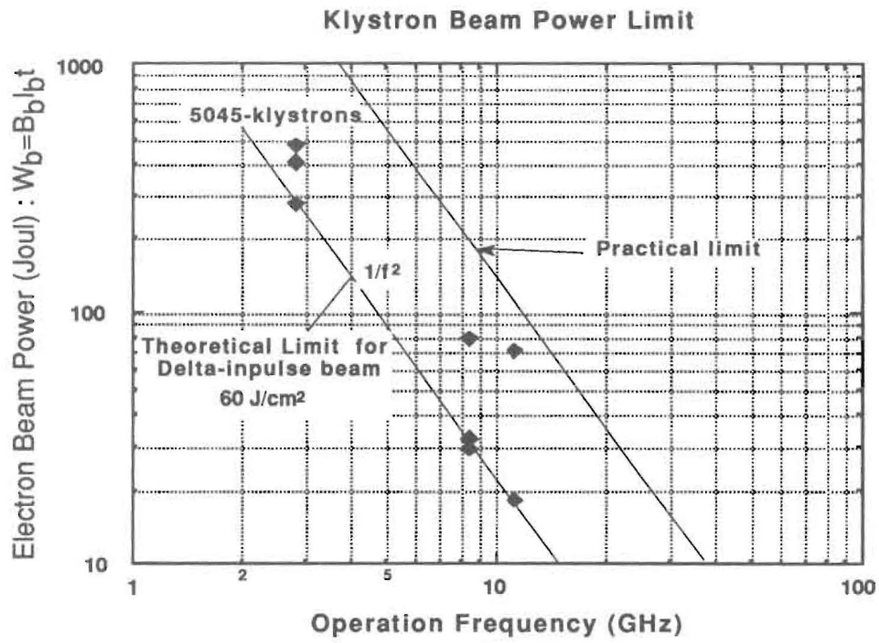


Figure 4.52: Beam power limits of existing klystrons compared with theoretical guesses.

at SLAC uses the gun voltage 320 kV. This voltage is by now standard owing to the R&D works including the new tachnology of the cathode material. Thus, the C-band klystron of the current design seems quite feasible.

**Output Cavity** The output cavity of klystron extracts the RF energy from the high power driving beam by decelerating the beam. A high voltage is excited in the gap to the same order as the gun voltage, or even higher, because the effective deceleration voltage is reduced by the coupling coefficient of 0.6 $\sim$ 0.8. In the case of the 5045 klystron, the output cavity voltage reaches 440 kV at the beam voltage of 320 kV. In order to keep good beam coupling, the gap size must be kept much smaller than the wavelength. Therefore, if the gun voltage is constant, the maximum field gradient on the output gap is lineally proportional to the operating frequency. In the 5045 tube, the maximum field gradient is 440 kV/cm at 100 MW output ( 2 $\mu$sec pulse ), and no break down was observed. In our C-band tube, the maximum field gradient is 590 kV/cm at 45 MW output. This is 30% higher than the maximum field in the 5045 tube at 100 MW full power operation. Therefore, some R&D works must be done on the output cavity structure.

For this purpose, a new type of cavity "Nose-cone removed pill box cavity"[31] has been proposed for the output cavity structure, which does not have the nose-cones at the gap but has a smooth shape just as a simple pill-box cavity. This cavity can considerably reduce the peak field gradient without loosing beam coupling coefficient. The maximum field gradient in a C-band klystron using this cavity, is expected to be 300 kV/cm. This is much lower than that in 5045 klystron, therefore no HV break down is expected.

**Output Ceramic Window** The output window, generally made of high purity alumina ceramics, has to be transparent to RF power, while working as a good vacuum seal. It is susceptible to a HV breakdown problem because the breakdown occurs more often on dielectric surface than in a metal-to-metal vacuum gap.

Because the physical dimension of the window is proportional to the RF wavelength, the RF power density passing through a unit area of the alumna ceramics scales quadratically to the operating frequency, and to the electric field gradient linearly. The 5045 klystron uses two windows in parallel, and there have been no severe problems up to 100 MW. The accepable power per one window is 25 MW at C-band if it scales as the wavelength squared. Therefore, it has to be examined if the conventional ceramic window can stand 50 MW and 3.6 $\mu$sec pulse power at C-band.

### Pulse Compressor

As stated before, the required pulse length into the the accelerating structure is 0.6$\mu$sec, which is relatively short as compared to that for the S-band linac. To efficiently generate this pulse directly from a klystron amplifier, a new HV modulator having shorter rise and fall times has to be developed.

One solution to remove this difficulty is to use an "RF pulse compressor". A compressor temporarily stores a long RF pulse of low peak power and, at the end of the pulse, emits a high-peak compressed power by reversing the input RF phase. The SLED-I has been invented at SLAC and successfully used for doubling the beam energy in the SLC project. However, the output pulse has no flat top and thererfore is not applicable to the JLC in which 100 bunches spaced by 2.8nsec must be equally accelerated.

For this purpose, we adopt the SLED-II type compressor, which utilizes a delay line cavity chain instead of a single storage cavity. It generates a flat RF pulse whose duration is just equal to the electrical length of the delay line. In our case, two RF delay lines of 0.6$\mu$sec delay time are required. If we use a simple wave guide for this purpose, the lines becomes 90m long. In order to reduce the length, we employ a kind of disk-loaded slow-wave structure. The key issue is how to realize a reasonably short delay line with a tolerable power loss on the wall and in the mode conversion. We plan to use a low loss mode $TE_{01n}$ and employ a slot damping structure to minimize the mode conversion loss.

The designed compressor achieves 4.2 times the input RF peak power with 70% power efficiency. The input RF pulse length is 3.6$\mu$sec, which is long enough for a conventional HV pulse generator.

### System Power Efficiency

Expected power efficiencies in the C-band RF system are summarized in Table 4.20. We use the conventional HV modulator, which has 80% pulse efficiency for a few $\mu$sec output pulse. To improve this efficiency, we need R&D works to reduce the rise and fall times.

The klystron efficiency is supposed to be 45%, equal to the S-band 5045 klystron. The power efficiency is a function of the perveance of drive beam and is lower for higher perveance beam. It is also a function of the operating frequency, decreasing with frequency. But this dependence is weak and its mechanism is not clear. Therefore, some work will be necessary to keep 45% efficiency.

The focusing coil of klystron also consumes a noticeable fraction of AC power. In order to reduce the coil power, we directly wind a small coil on the drift tube to create 2 kG peak

field near the output gap. The required average field is 1 kG, which will be generated by a conventional solenoid or permanent magnet. The expected AC power is 3 kW for conventional magnets.

For the waveguide system, we use the standard rectangular waveguide EIA: WR187 ( JIS: WRJ-5 ) of inner cross-section 47.55 × 22.15 mm. The power loss in this waveguide is approximately 0.03 dB/m at 5712 MHz. Suppose the average waveguide length from the pulse compressor to the accelerating structure to be 10 m, the power loss becomes 0.3 dB ( - 7% ). If we can make the waveguide system with reflection loss lower than a few percent at waveguide junction or bends, the total waveguide loss becomes 10%.

Including all the factors, the total power efficiency from AC input to the RF injected into the accelerating structure becomes 22%. This efficiency can be improved up to 30% by future R&D works on the HV modulator, the klystron, and the pulse compressor.

Table 4.21: Number of Linac Units and Power Consumption (two beams)

| | | |
|---|---|---|
| HV pulse modulator | 2090 | |
| Klystron | 4180 | |
| Pulse compressor | 4180 | |
| Accelerating structure | 8360 | |
| Total RF power input to structure | 64 | MW |
| Total power efficiency | 22 | % |
| Total electric power consumption | 291 | MW |

**The Number of Units and Total AC Power Consumption**

As listed in Table 4.21, the total number of linac units is 2090 for two beams. Each unit contains one HV pulse modulator, two klystrons, and pulse compressors and four accelerating structures. Because of such a huge number of parts, we need extensive R&D works for reducing their construction cost.

The total RF power input to the structure is 64 MW, and the system power efficiency is 22%, thus the total AC power consumption in the main linac system for two beams is 291 MW.

### 4.6.3 C-Band Accelerating Structure

In order to get high luminosity under the limited electric power, the multi-bunch acceleration in one RF pulse is essential in the linear collider. However, as described in section 4.5, the multi-bunch instability is expected to be a severe problem, which causes emittance growth and eventually leads to a luminosity loss. A cure of this problem is one of the most important task in our R&D works.

The multi-bunch instability is caused by higher order-mode-resonances in accelerating structures. An electron bunch passing through an accelerating structure generates higher order modes which kick the following bunches and deflect their orbits. If we can extract the electromagnetic power of these modes from the accelerating structure and damp them before the next bunch comes, the multi-bunch instabilities will be suppressed.

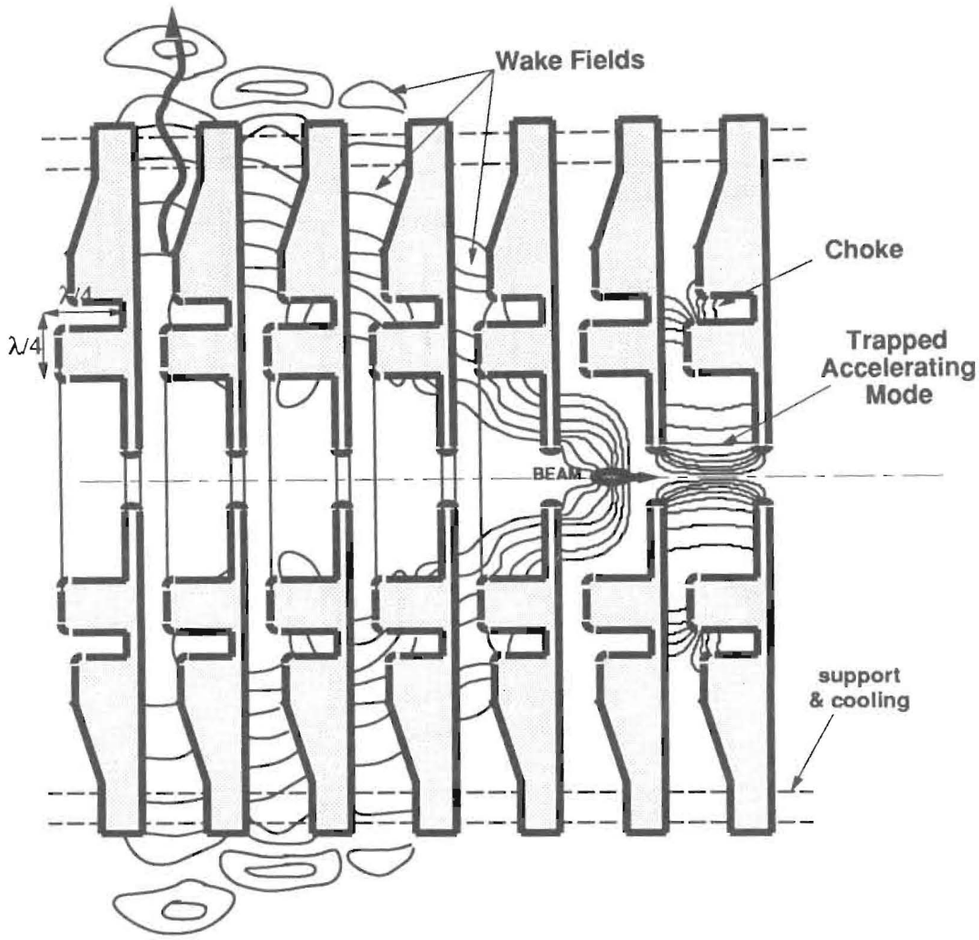


Figure 4.53: Concept of the choke mode cavity with the beam induced field and the accelerating field.

For this purpose, a new type of damped accelerating structure has been proposed[32]. Figure 4.53 illustrates this structure[33]. It consists of a number of disks supported by four rods which are also used as cooling water channels. Because there is no closed metallic boundary around the beam, the wake field immediately propagates outward along the radial line between disks and is eventually absorbed by microwave absorbers mounted on the disks. Therefore, any bunch will not see a wake.

The accelerating mode is trapped inside the structure by means of a choke. The choke length is chosen to be one quarter of the accelerating wavelength to provide an infinitely large impedance, and thus the accelerating RF power is reflected back to the cavity without losing its power by radiation.

A cold model of a single S-band cell has been fabricated and tested[32]. Figure 4.54 shows the measured responce spectrum in comparison with that of a simple pill-box cavity. It can be seen that most of the higher order modes were completely damped. A few modes remain visible, but they are known not to play harmful interaction with the beams. Consequently, this type of cavity will eliminates the multi-bunch problem.

Because this structure has cylindrical symmetry, there is no difficulties in its fabrication. We

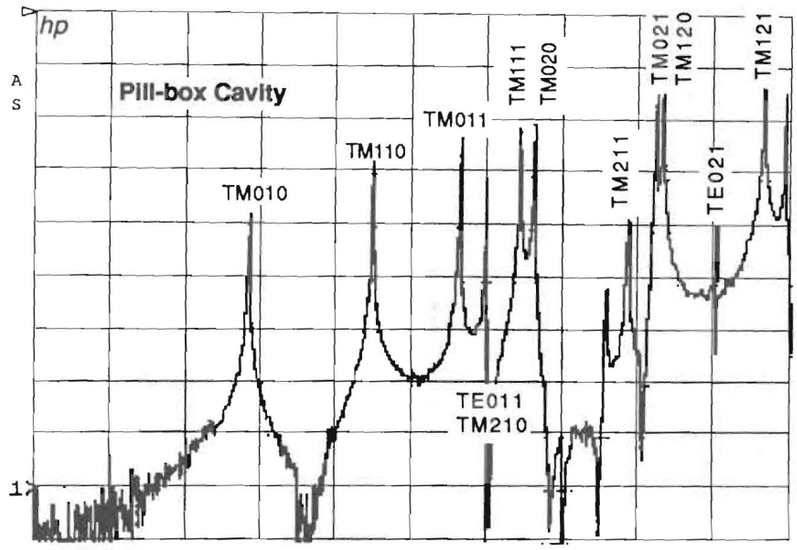


START 0.045000000 GHz
STOP 10.000000000 GHz

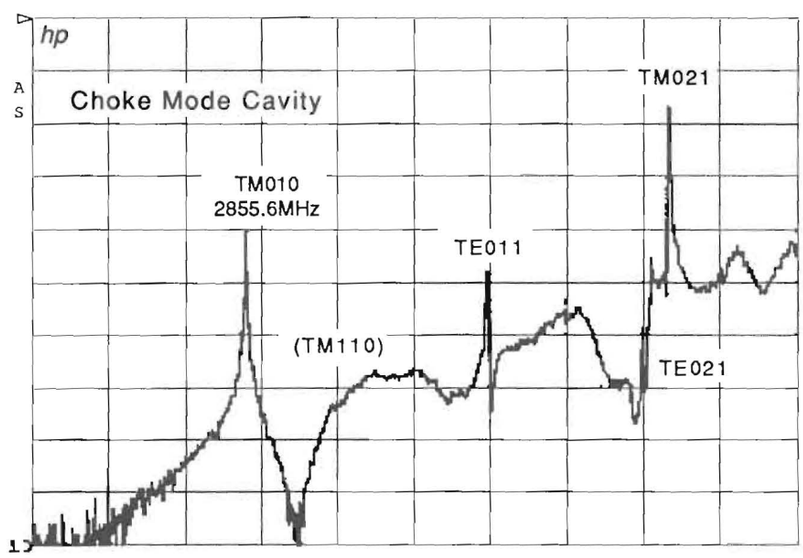


START 0.045000000 GHz
STOP 10.000000000 GHz

Figure 4.54: Measured responces of the pill-box and the choke mode cavity as a function of the frequency (S-band model).

can fabricate cavity disks from a copper rod or plate on a turning lathe, then stack them together inserting spacers and putting a small SiC disk ( microwave absorber ) between each pair of the cavity disks, and braise them together. After mounting the power input and output couplers, the accelerating structure unit will be inserted into a vacuum vessel. We will use ~20mm$\phi$ SiC disks as the microwave absorbers, which are expected to be very cheap for mass production. The overall cost will be comparable to that of the conventional disk-loaded structures.

Not everything is perfect, however. A part of the input RF field leaks into the choke, thus increasing the total wall loss and stored energy. As a result, the $R/Q$ and $Q$ values of the accelerating mode decrease by 10% and 15%, respectively as compared to the conventional disk-loaded structures. Therefore, the shunt impedance becomes 25% lower, and we need to input 25% higher RF power to get the same accelerating gradient.

## 4.7 0.3–0.5 TeV S-band Linac System

### 4.7.1 S-band Linac

#### S-band Linac Design

A design study has been carried out for the 300–500 GeV JLC based mostly on conventional S-band RF technologies. In this energy region, especially at 300 GeV, it is expected that the S-band linear collider would be the most realistic machine which can be realized in several years. The S-band JLC consists of the existing components such as the conventional travelling-wave constant-gradient structures of 3.6 m long, 85 MW klystrons and SLED cavities for RF pulse compression. The optimization of the machine parameters is described in Sec. 4.1. The linacs are operated at 50 pps which is synchronized with commercial electricity. The luminosity of $3\text{–}4\times10^{33}$ is attainable at this repetition rate.

The RF compression system is the key technology to reduce the total number of klystrons and klystron modulators of the main linacs and, therefore, to reduce the total cost. The output pulse from the compression systems like BPC (Binaly Pulse Compression) and SLED-II has a flat top which is desirable in order to equally accelerate many bunches. These systems, however, have relatively long delay lines determined by the sum of the structure filling time and the beam pulse width. Their application to the S-band is unrealistic since the filling time is 500–900 ns and therefore the delay lines would be longer than 150 m.

On the other hand, the conventional SLED cavity used in the SLC, which produces the RF pulse with fast decay, has been thought to be inapplicable to the multi-bunch acceleration. The unequal acceleration due to this decay, however, can be compensated by using cavities driven by slightly different frequencies. It turned out in our study that 70 bunches up to $2.5\times10^{10}$ particles per bunch with the bunch separation of 5.6 ns can be accelerated by this scheme with the resulting bunch-to-bunch energy spread of 0.13–0.14 %.

The unit of the S-band main linac is shown in Fig. 4.55. A klystron feeds the RF power into four 3.6 m long structures via SLED cavity. The peak RF power and the RF pulse width from the klystron are 85 MW and 4.5 $\mu$s. At 3 $\mu$s after the feed into the SLED cavity, the RF phase is made to reverse. As the results, the RF pulse with 1.5 $\mu$s is produced from the SLED cavity. The maximum energy gain produced by the non-square RF pulse is 24.4 MeV/m. However, the net accelerating gain per unit length would be reduced to 20 – 22 MeV/m by heavy beam loading to accelerate intense multi-bunches and by injection timing to obtain the optimum condition of energy compensation.

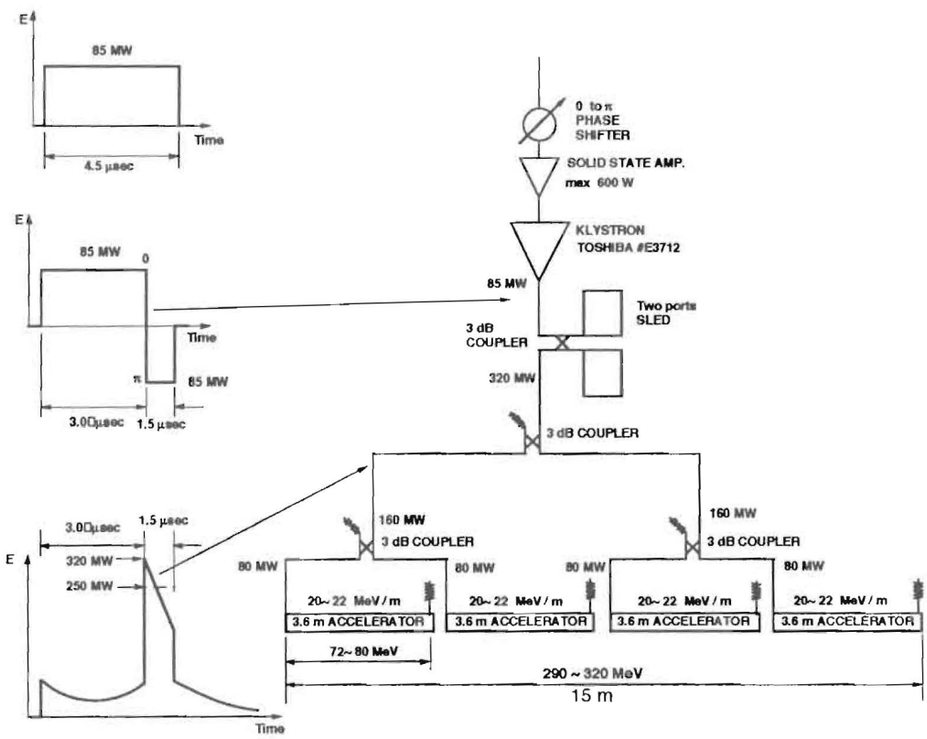


Figure 4.55: Unit of S-band main linac.

### Machine Parameters and Parameter Comparison

The linac unit of SLC consists of four 3 m-long accelerating structures and is 12.5 m in length. The DESY 500 GeV linear collider is composed of 2451 units, each of which is about 12.5 m long and consists of two 6 m-long structures and a 130 MW klystron to attain 500 GeV in center-of-mass.

As shown in Fig. 4.55, the S-band JLC is composed of the existing accelerator components, such as 85 MW klystrons, klystron modulators, SLED cavities, and 3.6 m-long accelerating structures which are being tested or fabricated for the ATF (Accelerator Test Facility). The length of the unit is approximately 15 m. The energy gain of the bunches passing through a unit of the linac is approximately 300 MeV with the beam loading. The number of units are 1000 for 300 GeV and 1670 for 500 GeV in center-of-mass energy as shown in Table 4.22. The higher accelerating gradient and the longer unit resulted in a reduction of the total number of linac units, klystrons, and klystron modulators.

Table 4.22: Machine Parameters and Parameter Comparison

| C.M.E. | JLC 300 GeV | JLC 400 GeV | JLC 500 GeV | DESY 500 GeV |
|---|---|---|---|---|
| Total Length of Structures | 15 km | 20 km | 25 km | 30 km |
| Total Length of linear collider | 18 km | 25 km | 30 km | 30+$\alpha$ km |
| Accelerating gradient | 22-20 MV/m | 22-20 MV/m | 22-20 MV/m | 17 MeV/m |
| Total number | | | | |
| Unit of linac | 1000 | 1350 | 1670 | 2451 |
| Klystron and Modulator | 1000 | 1350 | 1670 | 2451 |
| Accelerating structure | 4000 | 5400 | 7680 | 4902 |
| Structure length | 3.6 m | 3.6 m | 3.6 m | 6 m |
| Peak RF power | 85 MW | 85 MW | 85 MW | 130 MW |
| RF pulse width | 4.5 $\mu$s | 4.5 $\mu$s | 4.5 $\mu$s | 2 $\mu$s |
| RF pulse compression | SLED | SLED | SLED | none |
| Luminosity | $3\times10^{33}$ | $4\times10^{33}$ | $4\times10^{33}$ | $2.4\times10^{33}$ |
| Number of bunch/train | 70 | 70 | 70 | 172 |
| Number of particles in a bunch | $1.1\times10^{10}$ | $1.1\times10^{10}$ | $1.1\times10^{10}$ | $0.7\times10^{10}$ |
| Repetition rate (pps) | 50 | 50 | 50 | 50 |
| Wall plug power | 100 MW | 135 MW | 167 MW | 198 MW |
| Energy Spread of multi-bunch | 0.13 % | 0.13 % | 0.13 % | 0.112 % |

### Energy Compensation System

The SLED cavity is essential to reducing the total number of klystrons and modulators and, therefore, the cost of the RF system which is the major part of the total cost of the collider. Since the output waveform from a SLED cavity is not a square pulse, an energy compensation system is highly required to accelerate many bunches with a small energy spread less than

1 %. We prepare two different RF turn-on timings into the accelerating structures as shown in Fig. 4.56 and Fig. 4.57. In the first group of linac units, the whole bunches are accelerated by the time the RF front reaches the end cell of the accelerating structure. The last bunch then obtains the highest energy gain. With increasing bunch intensity, the RF turn-on time should be delayed further to compensate the steeper beam-loading slope. In the second group of linac units, the first bunch is accelerated at the time the RF front reaches the end cell. The first bunch obtains highest energy gain than the following bunches. The distribution of linac units in two groups depends on the beam-loading. The ratio of the first and second groups is 1000:103 at $2.50\times10^{10}$ particles per bunch, and 157:100 at $1.0\times10^{9}$ particles per bunch. The energy distribution of the bunches is approximately the cosine curve and the energy spread of the bunches is 2–3 % as shown in Fig. 4.56 and Fig. 4.57. The energy spread can be compressed to 0.13 % by using energy compression units which are driven at 2856±1.27 MHz. The total number of the energy compression units is about 20–30 for 300 GeV in center-of-mass.

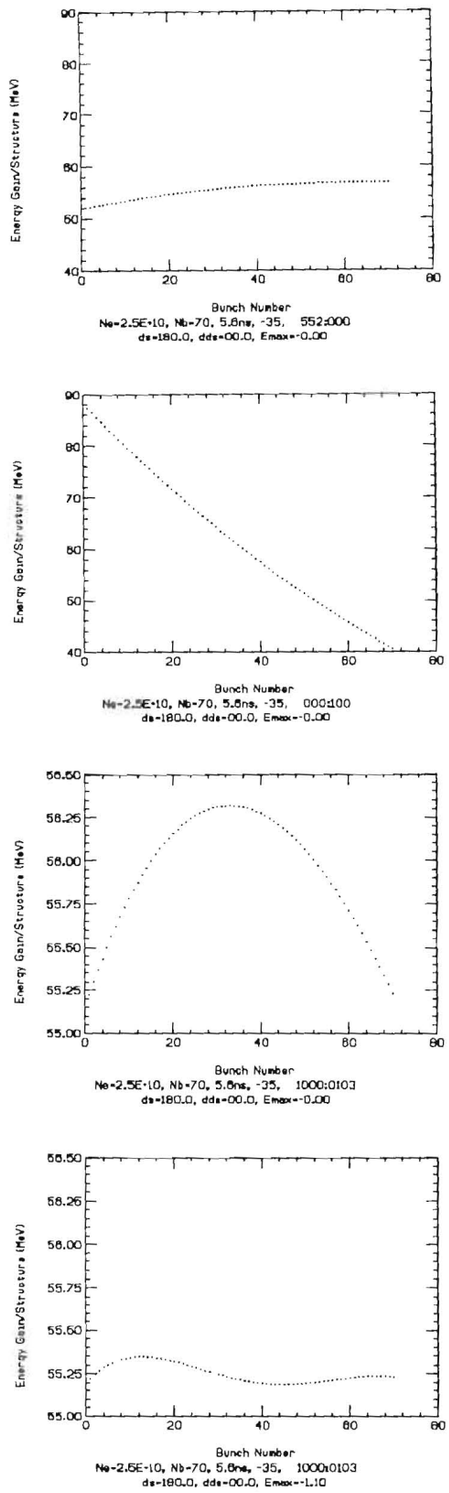


Figure 4.56: Energy spread of multi-bunch. $N_e = 2.5 \times 10^{10}$. Bottom shows the energy distribution after compensation.

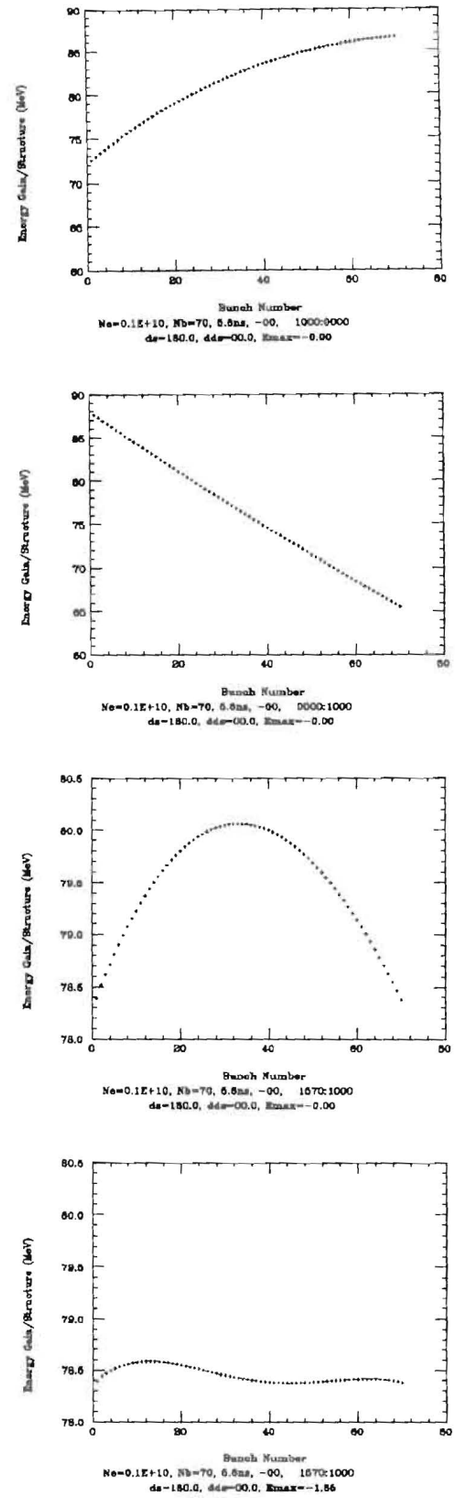


Figure 4.57: Energy spread of multi-bunch. $N_e = 1.0 \times 10^9$. Bottom shows the energy distribution after compensation.

### 4.7.2 S-band RF System

#### Outline of RF System

The RF system for the linac unit consists of an 85 MW klystron, a klystron modulator, SLED cavities, and RF waveguides, as shown schematically in Fig. 4.55. The unloaded accelerating gradient is 20 MV/m. The RF power from the klystron is compressed by the SLED system and is divided into four waveguides to feed four 3.6 m-long accelerating structures.

#### S-band High Power Klystrons

The high power S-band klystrons, Type E3712, have been developed by TOSHIBA Corporation. The tube design has been performed by the computer simulation code FCI. The designed maximum peak power is 100 MW in 1 $\mu$s and 80 MW in 4.5 $\mu$s pulse duration. The diode voltage is 450 kV at 100 MW and 400 kV at 85 MW peak power. Several klystrons have been used for high gradient experiments in the Nikko experimental hall. These klystrons will be used for the injector to the 1.54 GeV damping ring of the Accelerator Test Facility.

The tube stability is one of the important issues in klystron developments. The measured output power was quite stable at various beam voltages up to 450 kV, various beam focusing currents between 12 A and 20 A, and at various drive power levels.

#### RF Pulse Compression System (SLED)

SLED cavities established at SLAC are a standard RF compression system at S-band frequencies and are utilized for SLC at SLAC, the LEP injector at CERN, and LAL at ORSAY. The RF energy from the klystron is stored in two $TE_{015}$ high $Q$ cavities and then emitted through the coupling iris into the waveguide to feed the accelerating structure by changing the phase of the RF input pulse from zero to $\pi$. The RF pulse of 85 MW of peak power and 4.5 $\mu$s in pulse duration builds up the stored RF energy in two high $Q$ (=100,000) cavities, and then the RF power from the klystron triggered at 3.0 $\mu$s by a reversal (0 to $\pi$) in RF phase. The stored energy inside the cavities is released and combined with the direct RF power from the klystron through a 3-$dB$ directional coupler.

The SLED cavities of SLC have been operated with the input RF power level of 60 MW, pulse duration of 2.7 $\mu$s, and repetition rate of 120 pps. At this power level, heavy X-ray is observed from the coupling irises of some cavities due to the RF breakdown occurred occasionally around the irises. In order to reduce the surface field around the coupling iris at 85 MW peak power, a SLED cavity with two sidewall coupling irises has been developed by using the computer simulation cord MAFIA. A simulation showed that the field strength at the irises could be reduced to 34 % by using the two sidewall coupling irises.

#### Klystron Modulators

The klystrons need a 380 kV pulsed voltage with a 4.5 $\mu$s flat top at 85 MW peak power. A line-type modulator has been chosen due to the high efficiency, relatively low cost, and high reliability. A conventional line-type modulator consists of 14 sections of pulse forming network (PFN) and it is resonantly charged and discharged by a single thyratron switch at 50 pps synchronized with the commercial electric line. The regulation of the de-Qing circuit has been chosen to be 5 %. The specifications of the modulators are listed in Table 4.23. Approximately 5 % positive mismatch is used at full voltage for proper operation of the thyratron and the load

impedance is about 5 % higher than the output impedance of the modulator. The charging efficiency of the PFN has been estimated to be 95 %.

Table 4.23: Specification of the modulator

| Klystron Modulator | |
|---|---|
| Peak power output | 198 MW |
| Average power output | 70 kW |
| Transformer ratio | 1:16 |
| Output pulse voltage | 24.8 kV |
| Load impedance | 3.1 Ω |
| PFN impedance | 2.95 Ω |
| Thyratron anode voltage | 51.3 kV |
| Thyratron current | 7984 A |
| Pulse flat top | 4.5 $\mu$s |
| Rise time | 0.8 $\mu$s |
| Pulse height deviation from flatness | 1.0 % (p–p) |
| Pulse amplitude drift in short term | $\ll$ 0.5 % |
| Pulse amplitude drift in long term | $\ll$ 1.0 % |
| PFN total capacitance | 1.19 $\mu$F |
| Repetition rates | 50 pps |
| Efficiency of energy transfer | $\sim$ 85 % |
| Wall plug power of a modulator | 81 MW |
| Wall plug power of peripheral | |
| Low level and control | 4.5 kW |
| Klystron focusing coil | 8 kW |
| Klystron heater power | 0.5 kW |
| Klystron driver | 1 kW |
| The others | 5 kW |
| Total wall plug power/RF system | 100 kW |

## 4.8 Final Focus System

### 4.8.1 Overview

The final focus system for the JLC consists of two parts. The first one is a focusing optical system which provides the required nanometer beam spot at the interaction point(IP). The second is a collimator section located between the linac and the focusing optics. We describe the characteristics of the focusing system first in sections 4.8.2 to 4.8.5, then shortly present the collimators in 4.8.6. Figure 4.58 shows the schematic layout of the entire final focus system.

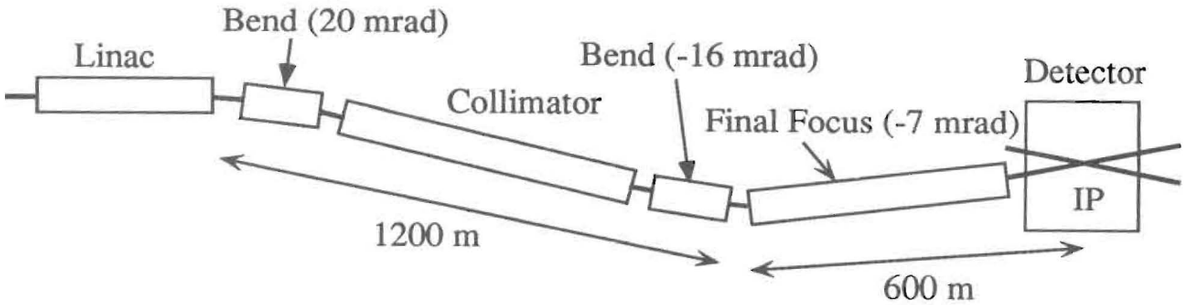


Figure 4.58: A schematic layout of the final focus system.

### 4.8.2 Design of Optics

The JLC final focus system has the design concept based on the chromaticity-correction scheme with non-interleaved two-family sextupoles[54]. Table 4.24 lists the main parameters of the final focus system for the beam energy 250 GeV. We use the same optical parameters in a lower energy case only with the scaled strengths of magnets. In Table 4.24, the incoming emittances are somewhat larger than those at the damping ring. We design the focusing optics to accept a beam with a certain amount of blow-up and an emittance dilution in the linac. The emittances at IP are larger than the incoming, since they suffer from optical aberrations including the synchrotron radiation in the final focus system. The beta functions at IP are chosen considering the chromaticities and the effects of the synchrotron radiation in the final lenses on the focusing. The focusing components including the final lenses are basically conventional ones, and possible to be built under existing technologies.

Table 4.24: Parameters of the JLC final focus system

| | | | |
|---|---|---|---|
| Beam energy | $E_0$ | 250 | GeV |
| Incoming invariant emittances | $\varepsilon_x/\varepsilon_y$ | $3.6 \times 10^{-6}/5.0 \times 10^{-8}$ | m |
| Invariant emittances at IP | $\varepsilon_x/\varepsilon_y$ | $3.8 \times 10^{-6}/6.0 \times 10^{-8}$ | m |
| $\beta$ functions at the IP | $\beta_x^*/\beta_y^*$ | 10/0.1 | mm |
| Spot sizes at the IP | $\sigma_x^*/\sigma_y^*$ | 280/3.5 | nm |
| Free area length | $\ell^*$ | 2.5 | m |
| Half aperture of the final quad | $a$ | 6.8 | mm |
| Pole-tip field | $B_0$ | 1.3 | T |
| Length of the final quad | $L_1$ | 2.2 | m |
| Chromaticities of final lenses | $\xi_x/\xi_y$ | 3200/43000 | |
| Momentum bandwidth | $\chi_m$ | $\pm 0.8$ | % |
| Total bend angle | $\theta$ | 7.1 | mrad |
| Length/beam | $L_0$ | 590 | m |

The optical system is an extension of the FFTB optics[55]. The magnet lattice and the optical functions are shown in Fig. 4.59. We have added several new characteristics on top of the FFTB design. The first one is the long length of the free area for the detector around IP. We set this length $\ell^*$ to 2.5 m, which is sufficient to place the masks for the background, to

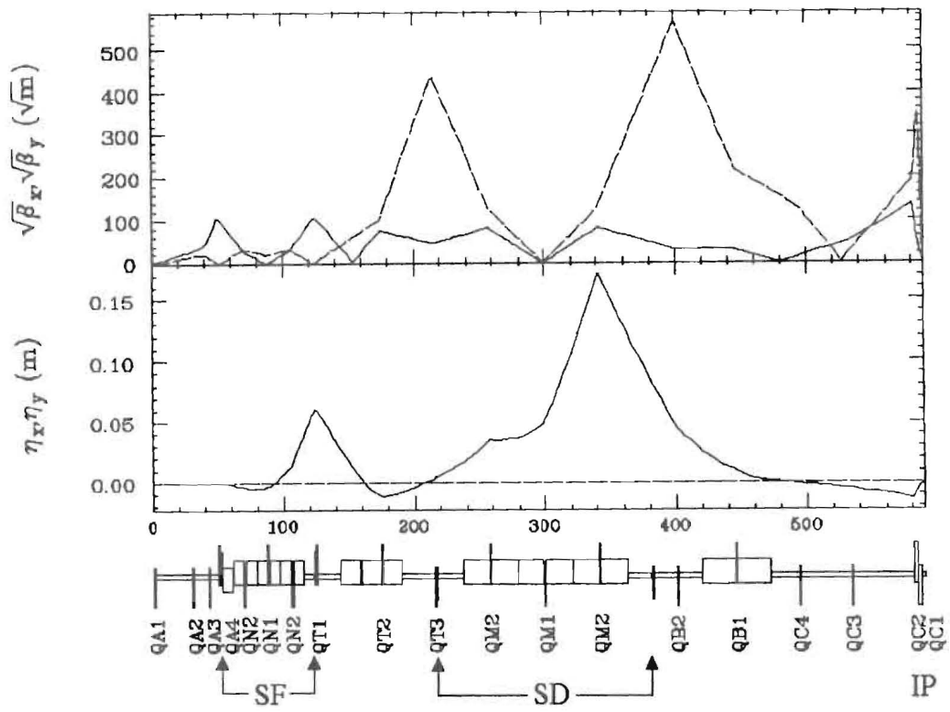


Figure 4.59: Optics of the JLC final focus system.

put BPMs for the beam-beam steering, to make a side-hole at the final quadrupole to let the beam escape after the collision, and to place a super-conducting shield of the quadrupoles for the solenoid field of the detector. Generally a long $\ell^*$ may increase the chromaticity of the final lenses and decrease the tolerance of the system, but our length 2.5 m is still manageable.

The second new point in the design is the choice of the aperture of the final lenses. In the JLC design these lenses have $30\sigma_x$ and $60\sigma_y$ half apertures. This big ratio to the beam size is necessary to avoid a blow up due to the resistive and geometric impedances of the beam chamber and the pole-tips of the quadrupoles. This big aperture ratio is also required to prevent the synchrotron radiation by large amplitude particles from hitting the pole.

The third change in the design is the unequal horizontal dispersions at the sextupole pair to reduce the chromo-geometric aberrations caused by the breakdown of the sign changer between two sextupoles for off-momentum particles[56]. This odd-dispersion scheme is suitable to extend the momentum bandwidth.

The fourth modification is the number of quadrupoles in the system. We have reduced the total number of quadrupoles in the chromaticity-correction system and in the final transformer. Now the transformer between two sextupoles is not a $-I$ but a $\pi$ transformer. The beta exchanger between SF and SD families is no longer a simple magni-demagnifier with $\pi$ phase advances. These changes eliminate unnecessary quadrupoles without any damage on the optical performance. A small number of quadrupoles reduces the tasks for tuning, orbit control, and positioning of the quadrupoles.

### 4.8.3 Optical Characteristics

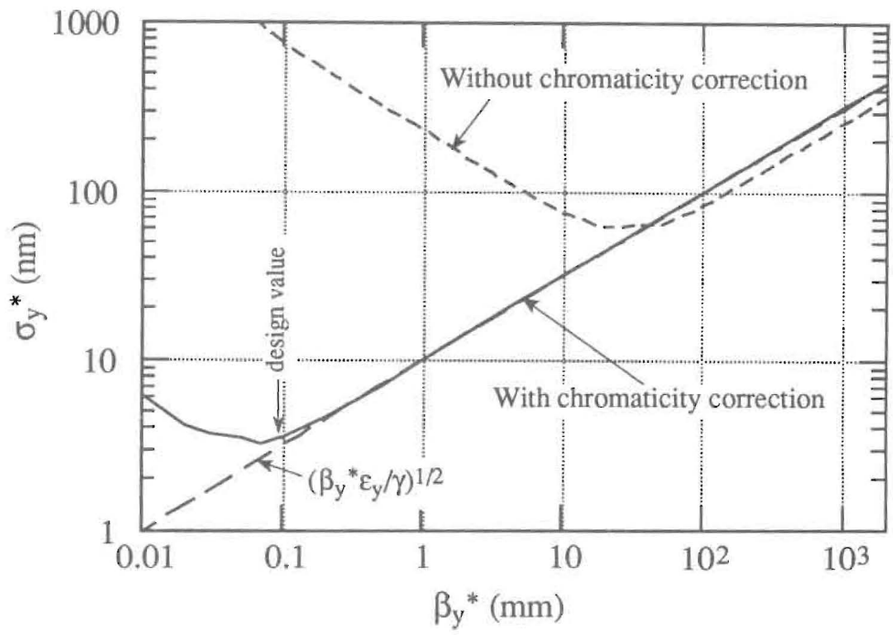


Figure 4.60: The spot size at IP as a function of $\beta_y^*$. The chromaticity correction of the JLC final focus system enables focusing down to $\beta_y^* = 0.1$ mm. The improvement of the vertical spot size by the chromaticity correction is 1/160 at the design $\beta_y^*$.

In this subsection we present several optical characteristics of the JLC final focus system. First we show the performance of the chromaticity correction in Fig. 4.60.

This figure shows the vertical spot size at IP as a function of $\beta_y^*$ which we change by the matching at the entrance of the system. While changing $\beta_y^*$, the rest of the focusing optics is kept unchanged except the sextupole strengths. The dashed curve represents the spot size when the sextupoles are off. This figure shows that the huge chromaticity of the final doublet blows up the vertical spot 160 times bigger than the design value if we do not have the chromaticity correction. The spot size becomes minimum near the design value of $\beta_y^*$ as intended by our optimization. For a smaller $\beta_y^*$, both chromatic and geometric aberrations increase and prevent further focusing.

The momentum bandwidth of the system is determined by the chromaticity correction and also the optical aberrations, which we will mention later. In this design we set the bandwidth to $\pm 0.8\%$ as required by the global optimization of the JLC parameters. Figure 4.61 shows the spot sizes at IP as functions of the momentum spread of the incoming beam. We have assumed a uniform momentum distribution of the incoming beam.

Figure 4.62 displays the spot sizes at IP as functions of the bending angle. The choice of the bending angle is another important issue on the design stage. In drawing this figure, we re-determined the sextupole strengths every time we change the bending angle. Other optical elements are kept unchanged. If the bending angle is small, the aberrations from sextupoles increase. If the bending angle is large, the effects of the synchrotron radiation in the bending

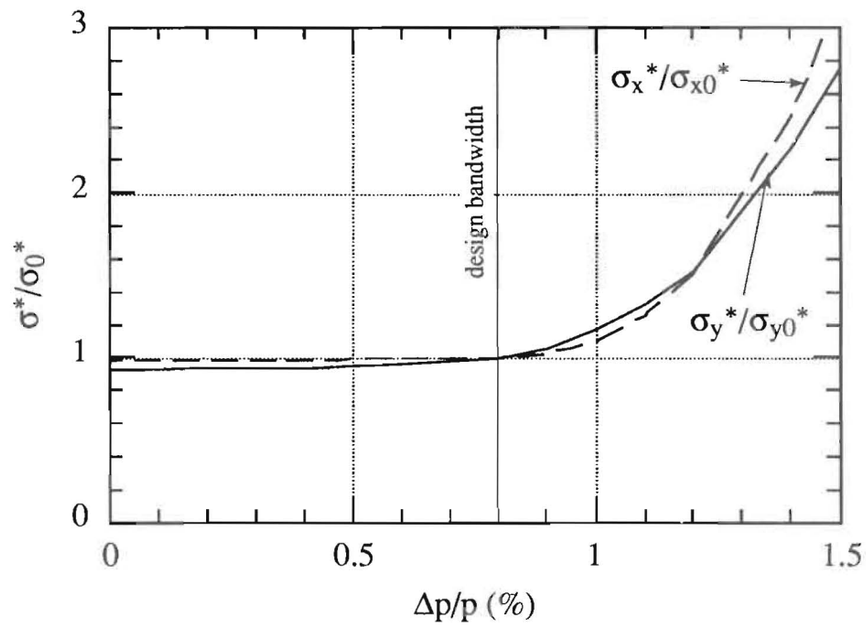


Figure 4.61: The spot sizes at IP as a function of the momentum spread of the incoming beam. The horizontal axis is the half width of the momentum spread with a uniform distribution. The vertical is the ratio of the spot sizes to the design value.

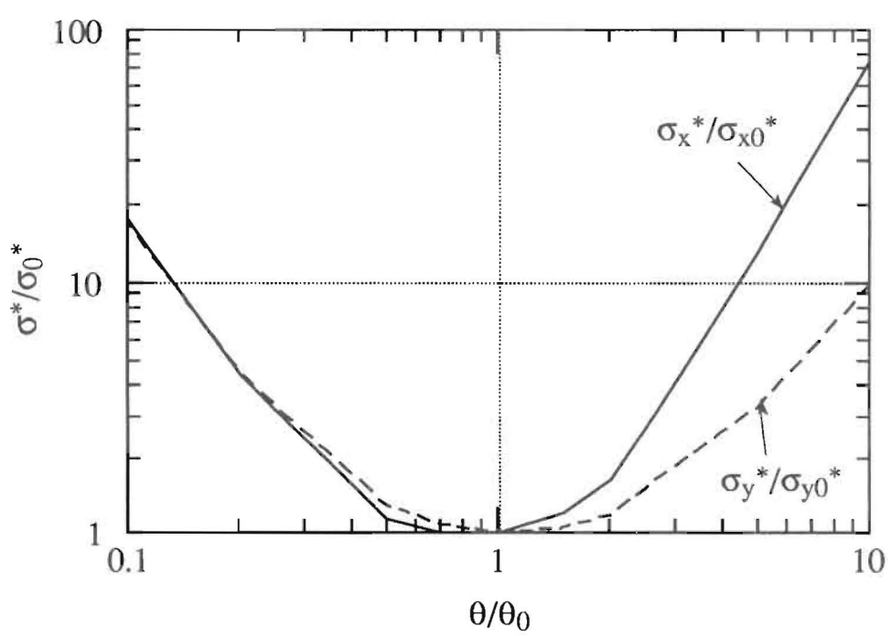


Figure 4.62: The spot sizes at IP as a function of the bending angle. The horizontal axis is the ratio of the bend angle to the design value. The vertical is the ratio of the spot sizes to the design value.

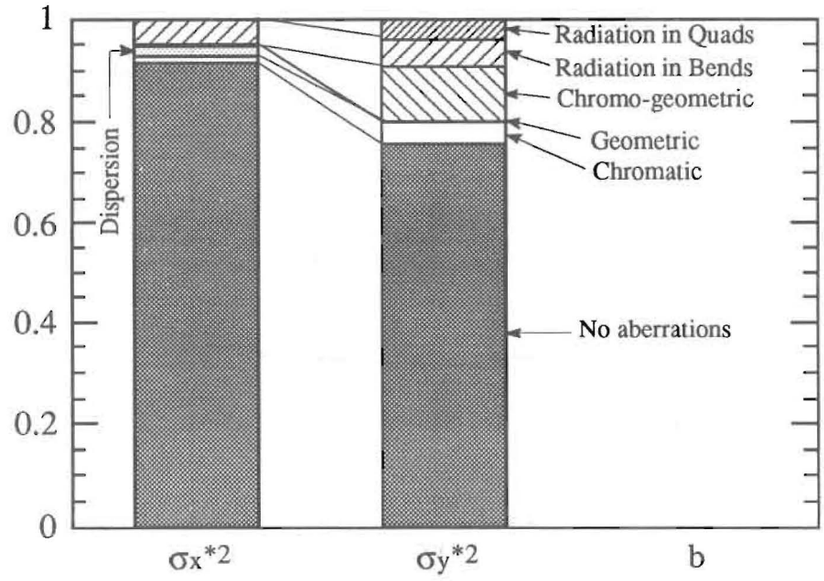


Figure 4.63: The spot sizes at IP have various optical aberrations. Each bar expresses the components of aberrations contained in the design value of the square of the spot size.

magnets blow up the spot sizes. The effect of the radiation is severer in the horizontal in this case. The reason is that the radiation blows up the vertical size through the chromaticity, while producing emittance directly in the horizontal plane. These two effects have different dependences on the bending angle.

Next what we see is the components of the aberrations contained in this design of the optical system, and shown in Fig. 4.63. The part "no aberrations" corresponds to the spot size determined only by the linear optics. Because of the high chromaticity, the vertical spot size has more aberrations compared to the horizontal. One specific aberration in the vertical plane is the chromo-geometric aberration generated by the breakdown of the sign changer of the SD sextupole pairs. The synchrotron radiation in the final doublet also increases the vertical spot. On the other hand, the horizontal higher order dispersion is a special source of the horizontal aberration.

### 4.8.4 Tolerances

In this subsection we examine four kinds of tolerances for machine errors of quadrupoles and sextupoles. The first one is the steering tolerance shown in Fig. 4.64. The most tight tolerance is for the final quadrupole QC1. If QC1 shifts vertically by 0.2 nm, the spot at IP shifts vertically by $\sigma_y^*/10$, which is about 0.4 nm. The steering error is recovered by the beam-beam steering feedback described in the next section for low frequency vibration. Therefore this tolerance can be understood as that for vibration faster than 10 Hz, which is the limit of the feedback with the beam repetition rate of JLC.

The second tolerance is for the displacement of the magnets to keep the spot sizes unchanged. Figure 4.65 displays the amount for each magnet to increase the spot size by 10 %.

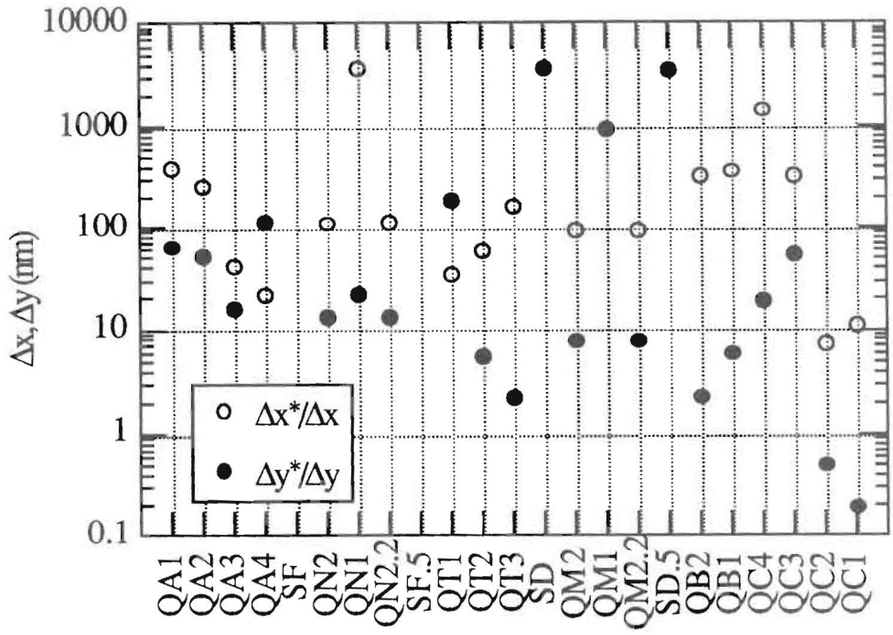


Figure 4.64: The horizontal (blank) and vertical (filled) displacements of the quadrupoles (initial Q) and the sextupoles (initial S) to shift the spot by 1/10 the spot size.

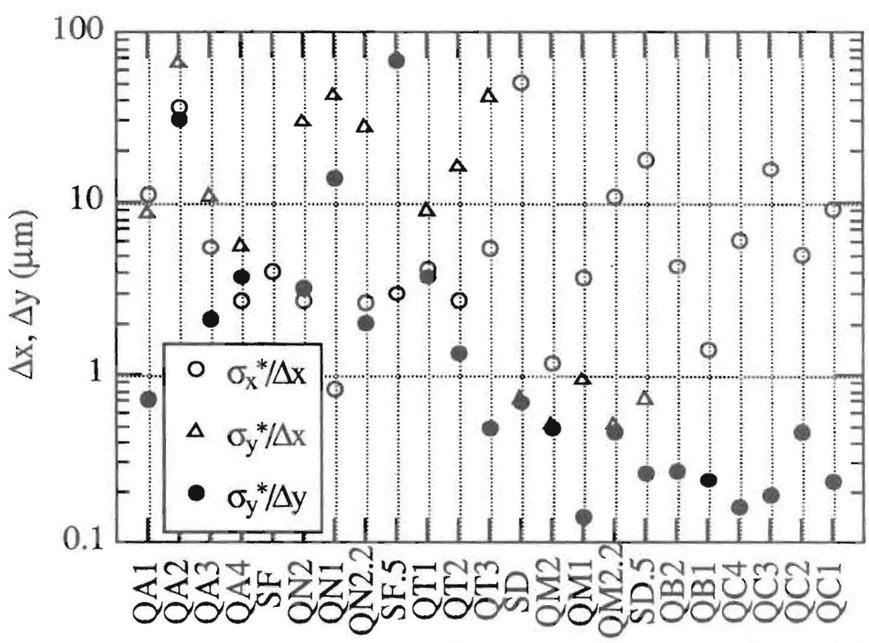


Figure 4.65: The tolerance of the displacements of magnets for the spot sizes at IP. The blank circle is the horizontal displacement which increases the horizontal spot size by 10 %. The triangle is the horizontal displacement to increase the vertical spot by 10 %. The filled circle is the vertical displacement corresponding to 10 % increase of the vertical spot size.

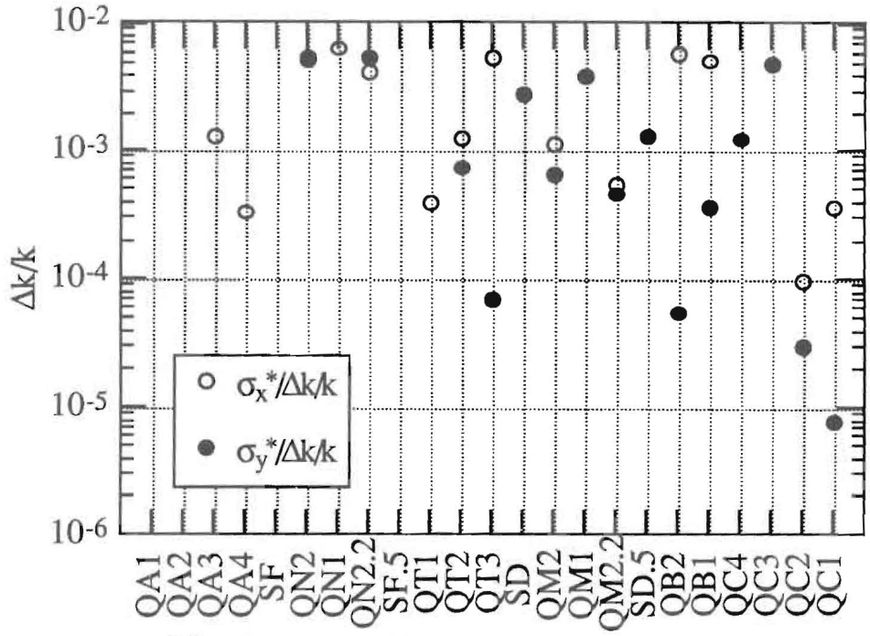


Figure 4.66: The tolerance of the relative strength error of magnets for the spot sizes at IP. The blank and filled correspond to the horizontal and the vertical increases of the spot size by 10 %, respectively.

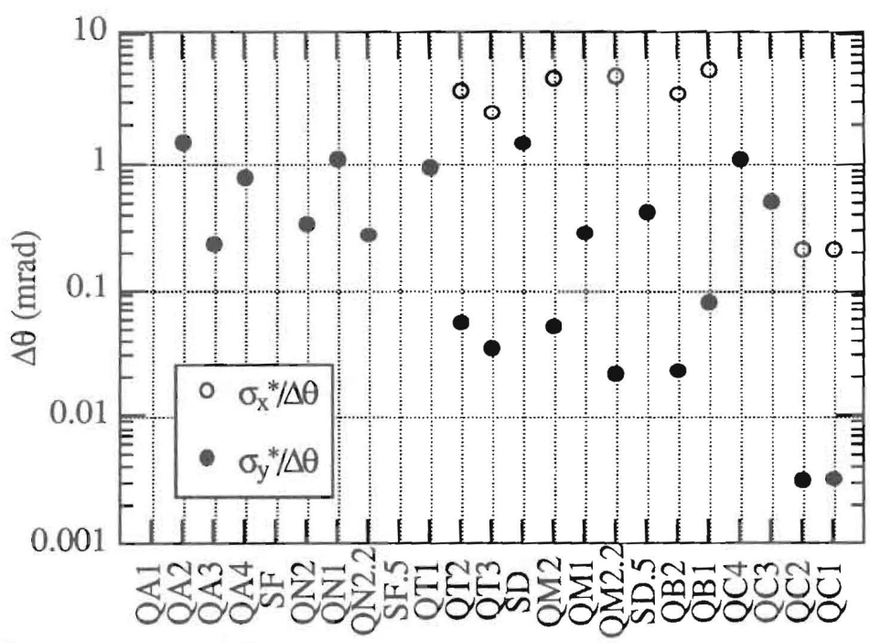


Figure 4.67: The tolerance of the skew rotation error of magnets for the spot sizes at IP. The blank and filled correspond to the horizontal and the vertical increases of the spot size by 10 %, respectively.

This tolerance is tightest in QC4(160 nm) and QM1(140 nm). An orbit feedback using beam position monitors(BPM) at all quadrupoles and sextupoles with an accuracy better than 100 nm maintains the spot as described in the next subsection.

The third kind is the relative strength error shown in Fig. 4.66. Although this tolerance is smallest in QC1, about $1 \times 10^{-5}$, the stability and the ripple of the power supply at this level are not difficult with the present technologies.

The last tolerance is for the skew rotation angle given in Fig. 4.67.

One may worry that in Fig. 4.65 the vertical tolerance for QC4 is 160 nm which is 1/300 of the vertical beam size at QC4. This does not mean that the beam must always pass this magnet within the accuracy of $\sigma_y/300$. If an orbit error is created at upstream of the entire final focus system, the spot size at IP is much more insensitive to those shown in Fig. 4.65. The reason is that this final focus optics is so designed to make a linear map from the entrance to IP for an incoming particle in a certain range of the transverse amplitudes and the momentum bandwidth. Therefore the tolerance in Fig. 4.65 means the displacement of each magnet relative to all other components of the final focus system. If the entire system moves coherently, the tolerance becomes much looser. Figure 4.68 shows that the tolerance for the launch offset of the incoming beam is nearly 1 $\sigma$ in both directions. In other words the entire system can shift 1$\mu$m in the vertical and 10 $\mu$m in the horizontal directions without damaging the spot sizes. The tolerance for the launch angle is similar.

### 4.8.5 The Nanometer Collision

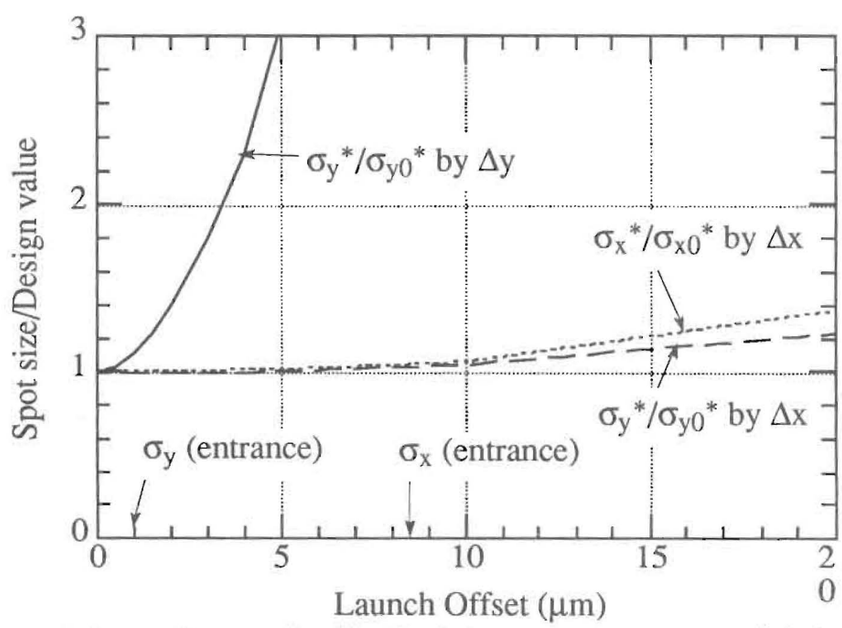


Figure 4.68: The spot sizes at IP normalized by the design values as functions of the launch offset at the entrance of the final focus system.

The key point for a JLC-like future collider is how to maintain the collision of two beams with the nanometer spot size. Basically there are three issues: 1) to keep the head-on collision within

an accuracy of a few nanometer, 2) to hold the spot size against possible perturbations, 3) to boot the system into the nanometer regime under various initial machine errors.

A number of studies have been done at SLC to make a stable head-on collision. The basic idea is to sense the deflection of the beams due to the beam-beam kick using beam position monitors (BPMs) located around the IP and to feedback it to the next collision. The beam-beam deflection angle $\Delta y'$ caused by a vertical offset $\Delta y^*$ at IP is expressed as[57],

$$\Delta y' = \frac{N r_e}{\gamma(\sigma_x^* + \sigma_y^*)} f(D_y) \frac{\Delta y^*}{\sigma_y^*} , \tag{4.33}$$

where $f(D_y)$ is a correction by the disruption of the beam with the disruption parameter $D_y$. This method has been working very well at least for the $1.2\mu\text{m} \times 1.2\mu\text{m}$ SLC spot. In the case of SLC, Eq. 4.33 gives $\Delta y' = 230\ \mu\text{rad} \times (\Delta y^*/\sigma_y^*)$ with $N = 2 \times 10^{10}$ and $f(D_y) \sim 1$. In this case the beam is kicked more than 200 $\mu$rad, which is easily detected by a standard BPM, when their centers are shifted by $1\sigma_y^*$. One may raise an objection for the applicability of this method to the nanometer case, but in the case of JLC, the sensitivity of the deflection angle to the relative offset at IP is $\Delta y' = 56\ \mu\text{rad} \times (\Delta y^*/\sigma_y^*)$, which is 1/4 of the SLC case ($N = 1 \times 10^{10}$, $f(D_y) \sim 0.35$, $D_y = 5$). Therefore it is not much different from the SLC case to detect the offset and to feedback it. The offset of $1\sigma_y^*$ is detectable with a conventional BPM of accuracy 1 $\mu$m. In the JLC case one can use all the information from every collision in a pulse to detect the offset. Thus the accuracy can be even better than SLC. The feedback will be active only below 10 Hz because the repetition is 150 Hz. Thus the perturbation beyond 10 Hz cannot be fed back. Recently the vibrations of tunnels and buildings at KEK site have been measured. It is found that the vibration beyond 10 Hz is only a few nanometer even in the daytime. As the reduction of the loss of the luminosity is suppressed by the disruption[57] even if one build JLC-I at KEK, the loss of the luminosity due to the vibrations higher than 10 Hz is only 5 %. One can imagine that it is not difficult to find out a location which is more quiet than the daytime of KEK. Other measurement at UNK also shows that the vibration over 10 Hz is only 0.2 nm[58] The valid range of Eq. 4.33 is $\Delta y^*/\sigma_y^* \lesssim \pm 5$ in the case of $D_y = 5$, but outside that region the beam-beam is still useful to maintain the head-on collision. For instance one can sweep the vertical offset and draw the deflection pattern which tells the location of the center of the collision.

The second issue is to maintain the nanometer spot size. The tightest tolerance for this point is the vibration of the center quadrupole in the vertical chromaticity correction section. If that quadrupole shifts vertically 140 nm relative to the beam, the final vertical spot size increases about 10 %. Therefore we have to keep the vertical beam position at the quadrupole within an order of 10 nm accuracy. Such a high accuracy requires both the accuracy of BPM attached to the quadrupole and the knowledge of the relative offset of the BPM to the center of the quadrupole. Recently T. Shintake and H. Hayano have proposed a design of a BPM whose sensitivity is better than 10 nm. This device will be tested at the FFTB collaboration. If such a high sensitivity BPM becomes available, the determination of the magnetic field center relative to the BPM is possible by a beam-based alignment[59]. When one change the strength of the quadrupole by 0.02 $\text{m}^{-1}$, which causes 10 nm shift of the beam at 50 m downstream the quadrupole if the beam has an offset of 10 nm at the quadrupole. If one use several shots, the required accuracy becomes less. Once the relative location of the magnet center to the BPM is determined, the orbit feedback maintains the final spot size. The tolerances for the other magnets are looser than the quadrupole. An external position sensor and mover system also help the beam-based method.

Orbit feedback system with precise BPMs plays important role in the game to maintain tiny beam size at IP. Increasing the r.m.s. amplitude of the ground vibration, the beam size at IP without orbit correction grows rapidly as shown in Fig 4.69. This beam size blowup is mainly caused by non-vanishing vertical dispersion function at IP, $\eta_y^*$. Orbit offsets $\delta y(s')$ at quads and sexts in the final focus system create this dispersion.

$$\begin{aligned}\eta_y^* &= \int^{s^*} ds' \sqrt{\beta^* \beta(s')} \sin(\psi^* - \psi(s')) \\ &\quad [-h_y(s') + k_y(s')\delta y(s')] .\end{aligned}$$

When we apply simple orbit correction scheme, in which the strengths of steering correctors are determined so that orbit offsets at quads and sexts vanish, there remains vertical dispersion caused by these steerings. This effect is also seen in Fig. 4.69. This unpleasant effect can be avoided if we apply an additional condition in the determination of strength of steerings[60]. In this scheme, which we call a dispersion-free correction(DFC), the additional condition that the excitation of the steerings does not move the beam position at IP vanishes the dispersion function at IP. In the computer simulation, it is possible to correct this dispersion function completely. Beam sizes after this fictitious correction scheme are also shown in Fig. 4.69. Comparison of these results indicates that our DFC scheme works almost completely for the ground motion less than 3 $\mu$m. In this simulation, we have assumed 100 nm BPM accuracy.

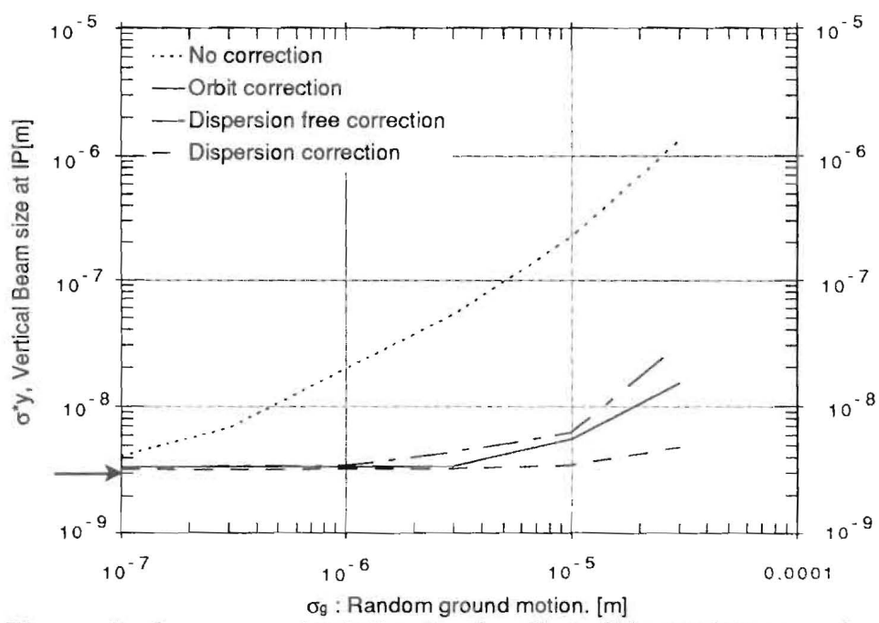


Figure 4.69: The result of computer simulation for the effect of the random ground motion on the beam size at IP. Vertical beam sizes at IP, $\sigma_y*$, before and after orbit correction are shown. Arrow on the left vertical axis denotes the design value.

There are, of course, many other sources of perturbation to the spot size. The stability of the power supply is one of them. Some magnets require a relative stability of order of $10^{-6}$. A stabilization using an NMR detector is expected to be applied for this purpose.

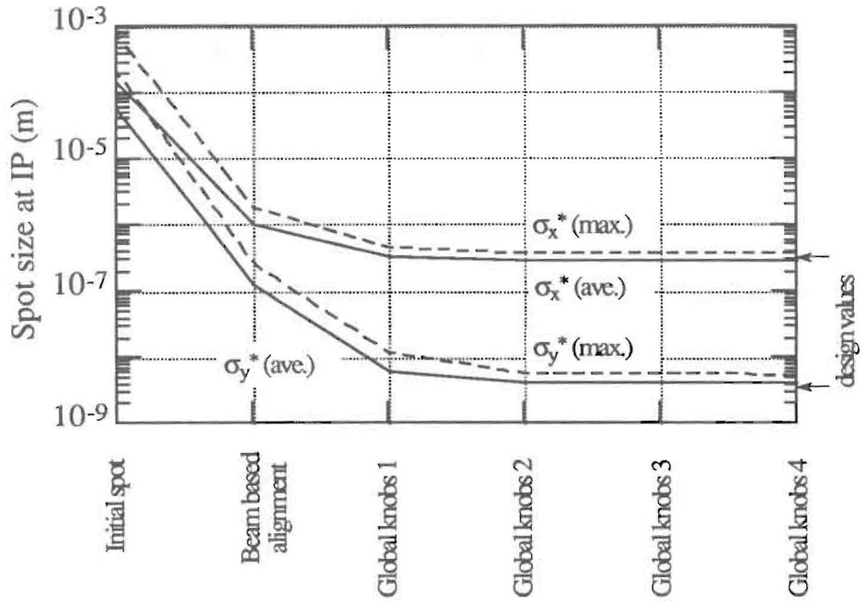


Figure 4.70: Simulation of the tuning of the spot size from initial errors. The beam-based alignment and the global knobs recover the spot sizes. The solid and dashed lines are the average and the maximum of 12 samples, respectively.

The third problem is how to boot the system under several possible initial machine errors. Although there are various ways to do this job as studied at FFTB, we only present here a result with the beam-based alignment method and global knobs. Figure 4.70 shows a result of a simulation. In this simulation we put random Gaussian errors of 100 $\mu$m vertical and horizontal displacements, 0.1 % relative strength errors, and 0.1 mrad skew rotation angles to all quadrupoles and sextupoles. The tail of the distribution is cut at $3\sigma$. We did the simulation for 12 different seeds of the random number. At the beginning the spot sizes are bigger than $100\mu$m with these errors. First we applied a beam-based alignment of quadrupoles and sextupoles with BPMs of $2\mu$m accuracy. The beam-based alignment recovers the spot size about $1\mu\text{m} \times 0.1\mu\text{m}$. After that we searched the minimum of the spot size by changing several global knobs. The knobs are listed in Table 4.25. We have assumed that the spot size is measurable within 5 % accuracy. After applying the global knobs for 3 cycles, the spot size reaches the design value. The worst vertical spot size among 12 samples is 3.9 nm, while the average is 3.5 nm. This simulation tells that the recovery of the spot size from a conventional level of the initial machine errors is possible if we have a good spot size monitor.

### 4.8.6 Collimator Section

The JLC final focus system requires a collimation section to cut possible transverse tails of a bunch to protect the detector from the background noise produced by the tail. We expect two major sources of the noise. One is the synchrotron radiation from the tail in the final quadrupoles and the last bend, and another is the shower caused by a particle hitting the pole of the final quadrupole. To avoid both background noises we need a collimator to cut the tail beyond $6\sigma_x$, $35\sigma_y$, and $\Delta p/p < \pm 1.5\%$. The small vertical emittance of JLC makes it

Table 4.25: Global knobs for the tuning of the spot size. H=Horizontal, V=Vertical.

| Knobs | Functions to be adjusted at IP |
|---|---|
| $\Delta x$ of QB1 | H dispersion |
| $\Delta x$ of SF1 | H focus |
| $\Delta y$, $-\Delta y$, $-0.226\Delta y$ of SF1, SF2, QC4 | V dispersion |
| $\Delta y$, $-\Delta y$ of SF1, SF2 | V 2nd order dispersion |
| $\Delta\theta$ of QC1 | HV coupling |
| $\Delta x$ of SD1, $0.05\Delta x$ of SF1 | V focus |
| $\Delta k$ of SD1 and SD2 | V chromaticity |

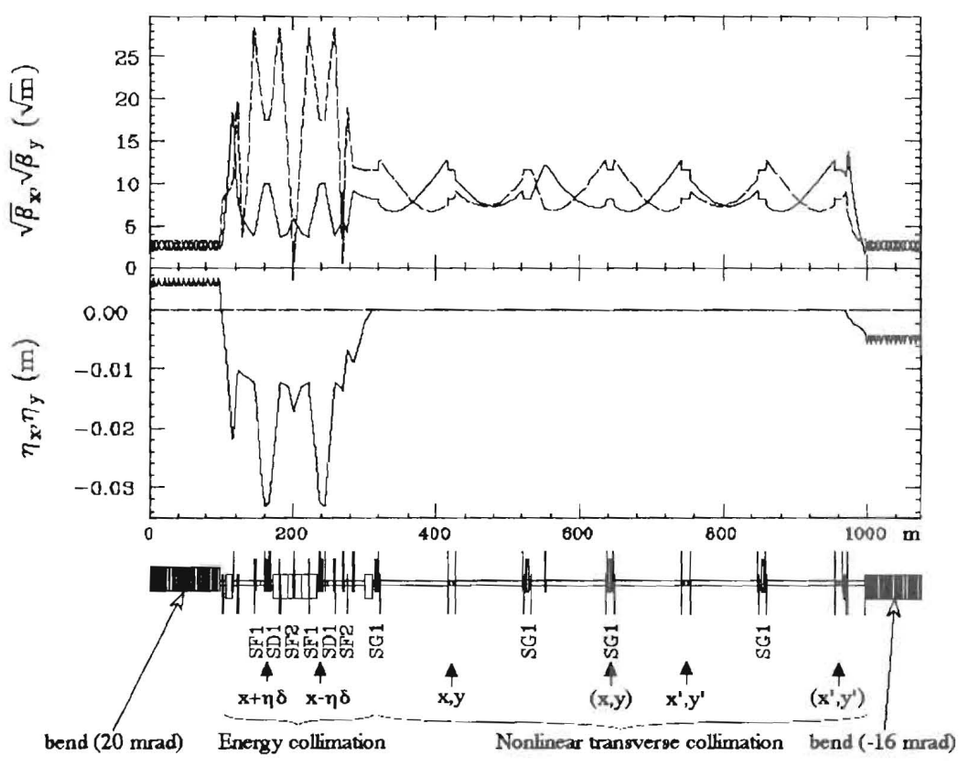


Figure 4.71: Bending and collimation section. The locations of collimators are indicated by filled arrows with their scraping coordinates.

very difficult to place a material very close to the beam because of the resistive and geometric wakefield. Even for a collimator at $35\sigma_y$, we need a special beam optics, so-called a nonlinear collimator[61]. Here we present a design of such a collimator section with parameters listed in Table 4.26. The lattice and the optical functions are shown in Fig. 4.71. This collimation section will be inserted between the linac and the final focus system. This design of the collimation section is also suitable to align two linacs on the same straight line with a finite crossing angle at IP. This design has a capability to install two detectors, because the detector is placed with 15 m horizontal offset to the linacs.

The nonlinear transverse collimation section consists of two identical parts separated by a $\pi/2$ transformer. The first one is the double collimator for $(x, y)$, and the second for $(x', y')$. Each of them has a sextupole pair connected by a $-I$ transformer. Each sextupole accompanies a collimator at $\pi/2$ downstream. Therefore each part works as a double collimator where the secondary collimator sweeps out the particles reflected by the primary collimator. As shown in Fig. 4.71, the nonlinear collimation section also has several long drift spaces which are suitable to accommodate muon traps.

The horizontal emittance is increased by 3 % due to the synchrotron radiation in the bending magnets. The increase of the vertical emittance due to the sextupoles is negligible.

Table 4.26: Parameters of the JLC collimation section

| | | |
|---|---|---|
| Bending section 1 & 2 | | |
| Bending angle | 20 & -16 | mrad |
| Bending radius | 4200 | m |
| Tune $\nu_x = \nu_y$ | 3.5 & 2.75 | |
| Energy collimator | | |
| Acceptance $\Delta p/p$ | $\pm 1.5$ | % |
| Collimator half aperture | 0.5 | mm |
| Beta at col. $\beta_x/\beta_y$ | 100/300 | m |
| Nonlinear transverse collimator | | |
| Acceptance $x/y = x'/y'$ | $\pm 6\sigma_x / \pm 35\sigma_y$ | |
| Collimator half aperture | 0.3 | mm |
| Beta at sextupoles $\beta_x/\beta_y$ | 67/134 | m |
| Sextupole pole tip field | 1 | T |
| Sextupole aperture | 5 | mm |
| Sextupole length | 4 | m |

### 4.8.7 Final Focus Quadrupole Magnet

The requirements for final focus quadrupole magnets are very severe: small aperture, very high pole tip field, long pole and small upper limits of higher multipole components, and in addition, a space for exhaust beams are necessary.

The upper limit of relative ratio of sextupole to quadrupole component is $\sim 1 \times 10^{-4}$ at the $10\sigma$ radius. Consequently, the machining and assembly tolerance relative to the aperture radius is about $(6 \sim 7) \times 10^{-4}$ which is very difficult to achieve by today's technology. However, the octupole limit is about $1 \times 10^{-3}$, which is one order larger than the sextupole limit. Therefore,

our strategy is that we take into account only the octupole tolerance at the fabrication stage and cancel out the sextupole component by independently exciting four trim coils.

The structure of the quadrupole magnet is a simple conventional type with four ferromagnetic poles. The design parameters are listed in Table 4.8.7 and the calculated field line is shown in Fig. 4.72.

Table 4.27: The parameters of a conventional type of a final focus quad.

| | |
|---|---|
| Aperture radius | 6.86mm |
| Pole length | 2.4m |
| Total width | 24cm |
| Pole tip field | 1.3T |
| Current | ~6000AT/pole |
| Total power | 39.6kW |
| Pole and yoke material | FeCo alloy |

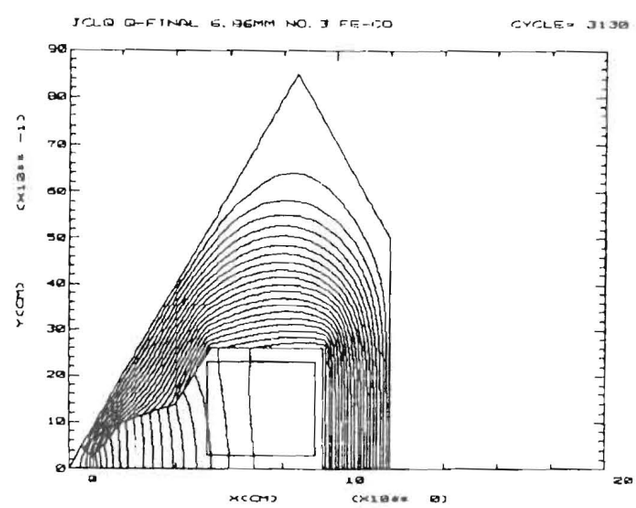


Figure 4.72: Calcurated field line of the octant of the conventional quadrupole magnet.

The calculation shows that the pole tip region is severely saturated so that we need about 1.7 times larger current than the unsaturated case. The current density of the coils is about 14 A/mm$^2$. In order to limit the temperature rise of coils below 40 degrees, we need cooling water with the pressure drop 8kg/cm$^2$.

The final focus quad is placed in the field region of the detector solenoid. We have to enclose the quadrupole magnet with a magnetic shield in order to reduce the solenoid field. If we adopt a superconducting quadrupole magnet, the magnetic shield is not needed, which makes the detector structure simple. Since we need a space for the exhaust beam after collision, however, the aperture radius must be large and, therefore, the field on the superconducting coils will be very strong.

A possible design of a superconducting quadrupole magnet is shown in Fig. 4.73 and the parameters are listed in Table 4.8.7. The maximum field on the superconducting wire is about

10.8T, so we have to cool it with superfluid He. In order to get good field quality, four trim coils are also necessary, which are not shown in the figure.

Table 4.28: The parameters of a superconducting final focus quad.

| | |
|---|---|
| Aperture radius | 6.0cm |
| Coil length | 3.5m |
| Inner radius of coil | 8.0cm |
| Outer radius of cryostat | 30cm |
| Field gradient | 117T/m |
| Current density | $\sim$250A/$mm^2$ |
| Material of SC wire | NbTi |
| Coolant | superfluid He (1.8$K$) |

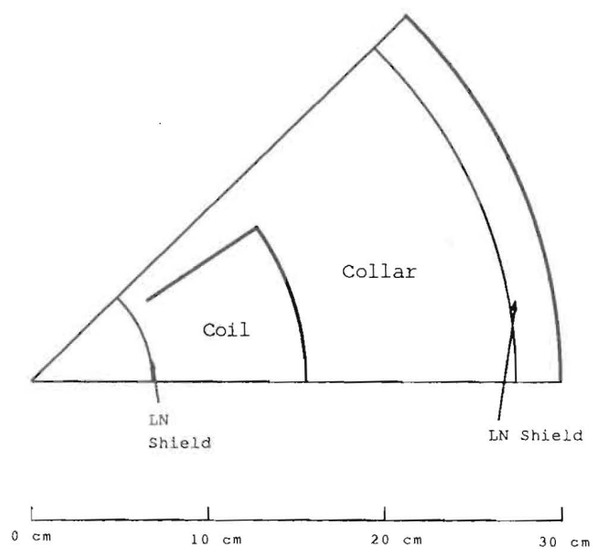


Figure 4.73: The structure of the octant of the superconducting quadrupole magnet.

The requirement for the field stability (current stability) is also severe, about $4 \times 10^{-6}$ during 4 hours between tunings. As for the current ripple, the upper limit is larger by one order of magnitude, if we use block type magnets. One possible way to make such a stable current power supply is to measure the field of a reference dipole magnet connected in series using NMR and to make a feedback loop. This scheme also works to reduce the current ripple. Thus, the current drift will be reduced to the order of $10^{-6}$.

## 4.9 Instrumentation and Control

### 4.9.1 Instrumentation

#### Introduction

Since the beam itself does not have a self-stabilization mechanism, it must be stabilized artificially by a fast feedback system. Thus, the beam measurement and control are essential for the high performance of linear colliders.

What quantities are to be measured are determined from the requirement of operation and beam tuning. The fundamental quantities are the beam position ($X$, $Y$, $Z$), the size ($\sigma_x$, $\sigma_y$, $\sigma_z$), and the intensity ($N_e$). The others are derived from these fundamental quantities by using various methods.

Basically, these measurements have to be done on a pulse-by-pulse basis at the repetition rate, 150 Hz in our case. The control system must also have a fast responce. Collecting and analyzing the data and exciting the correction elements have to be done by the time the next beam pulse comes. In some cases, although rare, the measurement has to be done for each bunch in a train separately, demanding much faster responce down to nanoseconds.

The requirement on the instrumentation for JLC-I is summarized in Tab. 4.29.

Table 4.29: Summary of Instrumentation for Fundamental Quantities.

| Meas. | | accuracy | bunch train | location | number of unit | possible candidates |
|---|---|---|---|---|---|---|
| X,Y | | $\pm 40\mu m$ | average | Injector S-band Linac | 200 | strip line BPM |
| | | $< 1\mu m$ | av. | Damping Ring | 300 | Button BPM(strip line) |
| | Transverse | $< 10\mu m$ | av. | Bunch Compressor | 100 | strip line BPM |
| | Beam | $< 10\mu m$ | av. | Pre Linac | 300 | strip line BPM |
| | Position | $< 10\mu m$ | av. | Beam Transport | 1000 | strip line BPM |
| | | $< 0.1\mu m$ | av. | /each Main Linac | 7000 | strip line/cavity BPM |
| | | $\pm 10nm$ | av. | Final Focus | 200 | cavity BPM |
| Z | Longitudinal | 0.01mm(0.03ps) | each | Bunch Compressor | 8 | streak camera |
| | Beam Position | 0.01mm(0.03ps) | each | Main Linac | 20 | streak camera |
| $\sigma_x, \sigma_y$ | | $10\%(\approx 50\mu m)$ | av. | Injector S-band Linac | 30 | screen monitor/wire |
| | | $10\%(\sigma_y < 5\mu m)$ | av. | Damping Ring | 6 | synchrotron radiation |
| | | $1\%(\approx 1\mu m)$ | av. | Bunch Compressor | 20 | wire scan/synchrotron |
| | | $1\%(\approx 1\mu m)$ | av. | Pre Linac | 20 | wire scanner |
| | Transverse | 10% | av. | Beam Transport | 50 | screen monitor/wire |
| | Spread | $1\%(\approx 1\mu m)$ | av./each | Main Linac | 250 | wire scan/synchrotron |
| | | $\pm 1\mu m$ | av. | Final Focus | 20 | wire scanner |
| | | $\pm 30nm$ | av. | Final Focus | 2 | Compton scattering |
| | | $\pm 3nm$ | av. | Final Focus | 1 | Compton scattering |
| $\sigma_z$ | Longitudinal | 0.5mm(1.7ps) | each | Injector S-band Linac | 4 | streak camera |
| | Spread | 0.5mm(1.7ps) | each | Damping Ring | 3 | streak camera |
| | | 0.01mm(0.03ps) | each | Bunch Compressor | 8 | streak camera |
| | | 0.0mm(0.03ps) | each | Main Lina | 20 | streak camera |
| | | 0.01mm(0.03ps) | each | Final Focus | 2 | streak camera |
| $N_b$ | | 1% | each | Injector S-band Linac | 30 | wall current |
| | | 1% | each | Damping Ring | 12 | wall current |
| | Charge | 1% | each | Bunch Compressor | 16 | wall current |
| | of | 1% | each | Pre Linac | 20 | wall current |
| | each bunch | 1% | each | Beam Transport | 30 | wall current |
| | | 1% | each | Main Linac | 250 | wall current |
| | | 1% | each | Final Focus | 10 | wall current |

These requirements will be attainable by using the following methods and techniques.

### Transverse Position (X, Y)

The transverse position of the beam will be measured by the stripline BPM (Beam Position Monitor ), the button BPM, and the microwave cavity BPM. These monitors can distinguish the position of each bunch in the bunch train using a window gate in front of processing circuits. In most cases, only the average signal is needed for the beam orbit control.

**Strip Line BPM** The strip line beam position monitors will be installed in the injector linac, beam transport, bunch compressor, main linac, and the final focus beam line. The resolution has to be better than about $1\mu$m. To achieve this resolution, the inner diameter of the strip line should be as small as possible and the width as wide as possible. The strip line length should be short enough to avoid the problem of supporting a long strip. The low noise electronics which is an extension of SLC's will be used. A resolution of several tenths of a micron is expected for the average over the bunches in a train.

**Button BPM** The button beam position monitors will be used in the damping rings because of the limited space and the relatively low resistive-wall impedance. It is an extension of TRISTAN BPM which uses pickup multiplexing method for the low cost. A few $\mu$m resolution will be attainable.

**Cavity BPM** In order to condense a position sensitive signal, a microwave cavity is used for high resolution beam position monitor. This cavity monitor uses 12GHz $TM_{110}$ mode which is sensitive to the transverse beam offset. The $Q_L$ should be taken down to about 10 to get several nm resolution for the bunch with $1 \times 10^{10}$ particles. This position monitor will be used at several points in the final focus beam line where an especially high resolution of the relative displacement is needed.

### Longitudinal Position (Z)

The longitudinal position of the beam or the bunch spacing in a train will be measured by the intensity distribution of the Cherenkov radiation or synchrotron radiation. This measurement can be achieved by the autocorrelation method or the streak camera system which is now available with a resolution of 0.6ps. These are within a reasonable extension of the currently available technologies.

### Transverse Size ($\sigma_x$, $\sigma_y$)

The transverse size of the beam which is directly related to the emittance can be measured by phosphor screens, wire scanners, synchrotron radiation monitors, or laser-Compton monitors.

**Screen Profile Monitor** The beam profile measurements around $10\mu$m accuracy will be done by the ordinary phosphor screen method. The screen substrate should be thinner than usual for avoiding multiple scattering of electrons. The optical telescope system which is needed to avoid radiation damages of the screen must have the resolution down to the level of the Rayleigh limit.

**Synchrotron Radiation Profile Monitor** The nondestructive beam profile measurements can be done by using the synchrotron radiation with an accuracy better than $1\mu$m. To avoid the diffraction of the synchrotron light, a short wave length has to be used for imaging. This monitor will be installed mainly in the damping rings to monitor the vertical beam size turn by turn.

**Wire Scanner Profile Monitor** The ordinary beam profile measurements with about $1\mu$m accuracy can be done by the wire scanning method as in the SLC. For a fine resolution, a thin carbon wire of a few $\mu$m in diameter is mounted on a mover driven by a stepping motor with $0.5\mu$m step and the repeatability of $0.1\mu$m. The profile is recontructed by measuring the gamma-ray yield synchronizing with the wire movement at the downstream of the wire scanner.

**Laser Profile Monitor** At the collision point a very precise profile monitor is required for the tuning of the final focus system. The interaction of the beam with laser interference fringe of several nm causes the Compton scattering. The back-scattered gamma-ray is detected at downstream as a function of the steered beam position. The modulation of gamma-ray intensity will bring the information of the beam size. This profile monitor will be installed and tested in FFTB at SLAC.

#### Longitudinal Size ($\sigma_z$)

The longitudinal size of the bunch can be measured by the intensity distribution of the Cherenkov radiation from the beam. This measurement can also be done by the autocorrelation method or by the streak camera system which is the same as the longitudinal position measurement.

#### Charge of each bunch ($N_b$)

The charge of each bunch and total charge of the whole train are measured by the wall current monitor. In order to detect each bunch with 1.4ns spacing separately, the pickup and the digitizer must have a fast responce and the cable must be short. The ordinary wall current monitor with several 100ps response is available by using chip resistors, short high-frequency co-axial cables and the sampling oscilloscope.

#### Other quantities ($\epsilon_x$, $\epsilon_y$, $E$, $\delta E$)

The quantities like transverse emittance $\epsilon_x$, $\epsilon_y$, beam energy $E$, and energy spread $\sigma_E$ can be derived by combinations of the above monitors. For example, the emittances can be estimated from the transverse beam size using optics parameters and the beam energy and the spread from the beam position and profile using a bending field.

The estimated numbers of beam instrumentation units for whole JLC are listed in Table 4.30.

### 4.9.2 Control

The control system for JLC will consist of two levels of computers. The lower level computers interface to the devices directly, take the beam information and device status, and control the devices. The roles of the lower level computers are to be a device driver which can communicate

Table 4.30: Numbers of instrumentation units.

| | (two beams) |
|---|---|
| BPMs | 9100 |
| Profile Monitor | 399 |
| Streak Camera System | 65 |
| Wall Current Monitor | 368 |

with other tasks and the upper level computers, and to be a carrier of the fast feedback for beam stabilization. Each of these computers takes charge of the devices in a small region in the collider complex, such as one for the Injector linac, one for the damping ring, one for 20 klystrons in the main linac, and so on. Each computer has to drive at least 10 crates of CAMAC or VME for the interface boards.

The upper level computers which communicate with operators and the lower level computers, manage the accelerator operations as a whole. For these computers, the collider complex will be divided into five parts, the region from the gun to the entrance of the main linac for electrons, that for positrons, electron main linac, positron main linac, and the final focus region. These five upper level computers should be capable of fast communication with the lower level computers and with the workstations for operator console and should have a capacity for many tasks such as control tasks for many devices and monitoring tasks and so on. The workstation will be used as an operator console instead of console hardware and many TV monitors. The environment of operation will be build easily with flexibility using X-window and TV windows. The idea of workstation console has a great advantage of flexibility.

The modeling of accelerator will be done on an independent calculation server. The program SAD and other tracking and orbit correction programs on the server simulate the beam in the actual accelerator. This server must be capable of very fast calculation. The estimated numbers of various units for this control system are listed in Tab. 4.31

Table 4.31: Numbers of units of the control system.

| | |
|---|---|
| Large Operation Computer | 6 |
| Workstation for console | 50 |
| Medium device driver computer | 210 |
| Interface Crate (assuming CAMAC) | 2100 |

## 4.10 Civil Engineering

### 4.10.1 Technical Site Criteria

An appropriate site for JLC-I should satisfy the following technical criteria.

1) A geologically and geohydrologically stable area for the constructions of a long linac tunnel and a large detector-hall. The low level of seismic and microseismic activity for the alignment of the final focus system, the main linacs, and the damping rings.

2) Availability of large electric power ($\sim$ 300 MW) and enough water cooling capacity for linear collider operation. An area close to the existing AC power line from a power station to industrial cities is favorable in this respect.

3) Easy access to the site from a highway, a Shinkansen, and an airport.

Keeping these criteria in mind, possible main tunnel designs are studied. In this section, we describe the main tunnel design based on the blasting method, after a short histroical review of the design based on the shield method.

### 4.10.2 Construction Methods of Main Tunnel and Detector-Hall

The construction methods for the main tunnel and detector-hall have been investigated for the following two cases, shield method and blasting method. In early stage of the JLC project design, the shield method seemed the most appropriate to reduce the land cost. At that time utilization of deep underground was attracting peopole's attention as a solution to obtain the lands for public use during the inflation period of the land price triggered by the rapid ecnomical growth. The Ministries started the preparation of the draft of a law for the utilization of deep underground in the metropolitan area. The objective of the draft was to allow constructions of public facilities at a depth deeper than 50 m underground without distinction of superficies. Assuming that the law will be concluded in a few years, we have elaborated a plan to construct main tunnels and a detector-hall at a depth of 100 m underground of Tsukuba area, so that the detector-hall could fit in the present KEK site. This could also allow the construction of the injector complex, including damping rings, injector linacs, and a positron production linac, on the ground in the KEK site. Outside the present KEK site, several spot sites were required to construct the pits dug in the ground for the access to the main tunnels as with LEP and HERA. The accelerator and detector components could then be transported through the pits by lifts.

If we use shield machines, the cross section of the main tunnel should be a circle and its diameter should be constant over the full length of the main tunnel. In deep underground, the wall of the tunnel should be strong eneough to sustain high earth pressure and it should also be made water-tight by the chemical processing to put up with high water pressure. The construction cost depends on the depth of the tunnel. The cost has been estimated to be approximately 20–30 MYens/m, referring to the Trans-Tokyo Bay Tunnel to connect Chiba and Kawasaki by a highway under construction. The technical difficulty lies in the construction of the access pits of 100 m in depth. There remains a subtle problem with the interpretation of the word "metropolitan area": whether the law can be applicable to Tsukuba area or not. The sudden collapse of so-called bubble economy in 1990 induced a recession and caused the drop of land price, which diminished the interest in the utilization of deep underground.

The second construction method is the blasting method. The main tunnel can be excavated along a ridge of mountains. Several approach tunnels can then be excavated in horizontal direction from outside the mountains in order to facilitate the transportation of accelerator and detector components by weight cargo carriers. This construction method does not restrict the shape of the tunnels and allows us to excavte them with an optimum cross section along the accelerator: a large diameter for the main linac, a small diameter for the beam transport line and side rooms for storage. The blasting method is the standard technology to construct highway tunnels. The construction cost can therefore be minimized by matching the specification of the main tunnel to that of a standard highway tunnel. The basic design of the tunnels and the detector-hall has been completed.

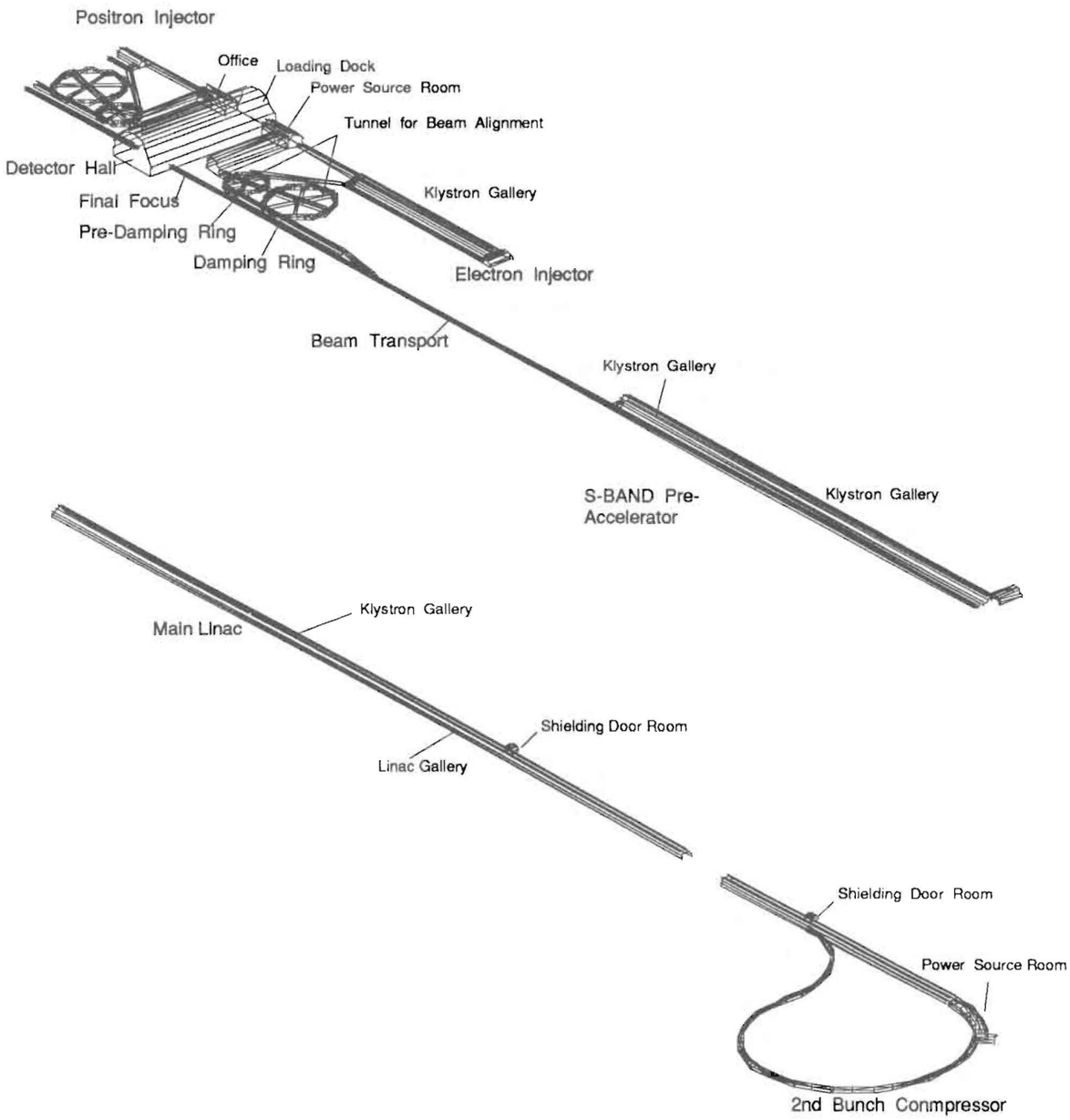


Figure 4.74: Three dimensional schematic drawing of JLC.

Figure 4.74 is a three-dimensional drawing of the JLC-I tunnel. The injector complex including the injector linacs, the positron production linac, the pre-damping and damping rings, and the pre-accelerators will be constructed near the detector-hall. These facilities have a common access tunnel from the outside of the mountain and are connected with short access tunnels to provide an easy mutual access between the facilities. The straight tunnels across the damping ring tunnels ease the alignment of the damping ring components.

Figure 4.75 gives a cross-sectional view of the tunnel for the main linac. The main linac

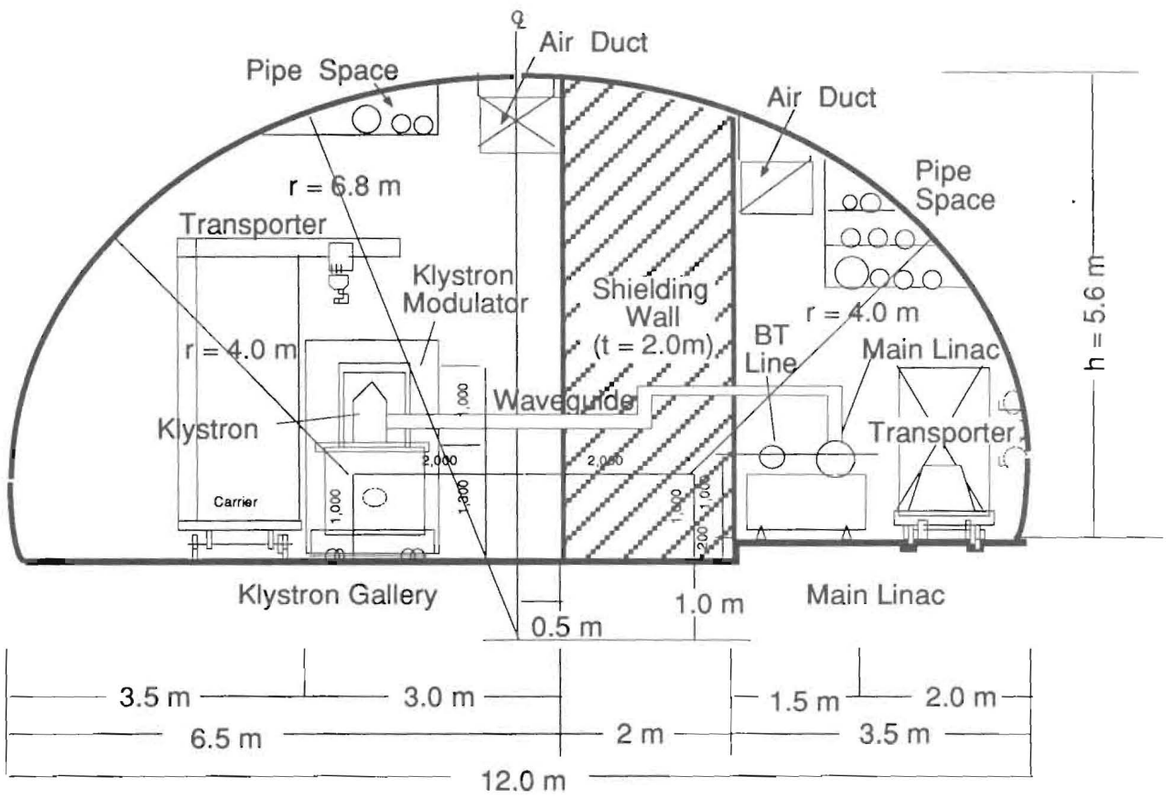


Figure 4.75: Main linac tunnel.

tunnel has a semi-cylindrical shape like a quonset hat, which is 12 m in width and 5.6 m in height. The size of the tunnel is similar to that of a standard highway tunnel for two traffic lanes. A 2 m thick shielding wall divides the tunnel into two galleries. The wider one houses the klystrons and their modulators, while the remaining one is occupied by the accelerating structures and the beam transport line. The klystron tubes and the accelerating structures are connected with RF waveguides through the shielding wall. As shown in Figs. 4.76 and 4.77, the access doors for maintenance are prepared at every 500 m. The cross section of the tunnel for the collimator and the final focus system is shown in Fig. 4.78. The damping ring tunnel is shown in Fig. 4.79 and the detector-hall is shown in Fig. 4.80.

The cost of the tunnels and the detector-hall has been estimated for the following two candidate sites as shown in Table 4.32. Type A mountain consists of a single geological formation with granite of class $B - C_H$, which provides a good geological stability in the tunnels. Type B mountain has a complicated geological formation with peridotite, diabase tuff, and andesite lava of class $C_M - C_L(D)$. The volume to be dug out depends on the thickness of the tunnel

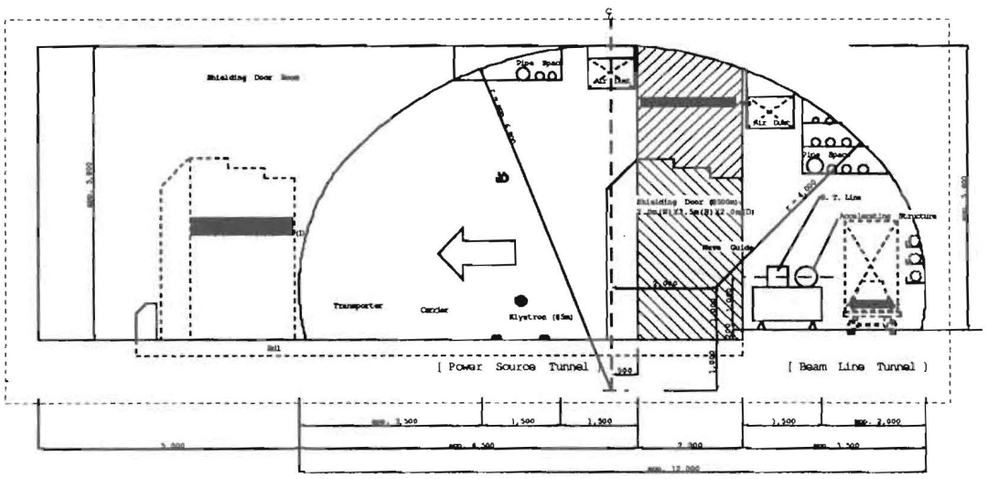


Figure 4.76: Side view of the access door between klystron gallery and accelerator tunnel.

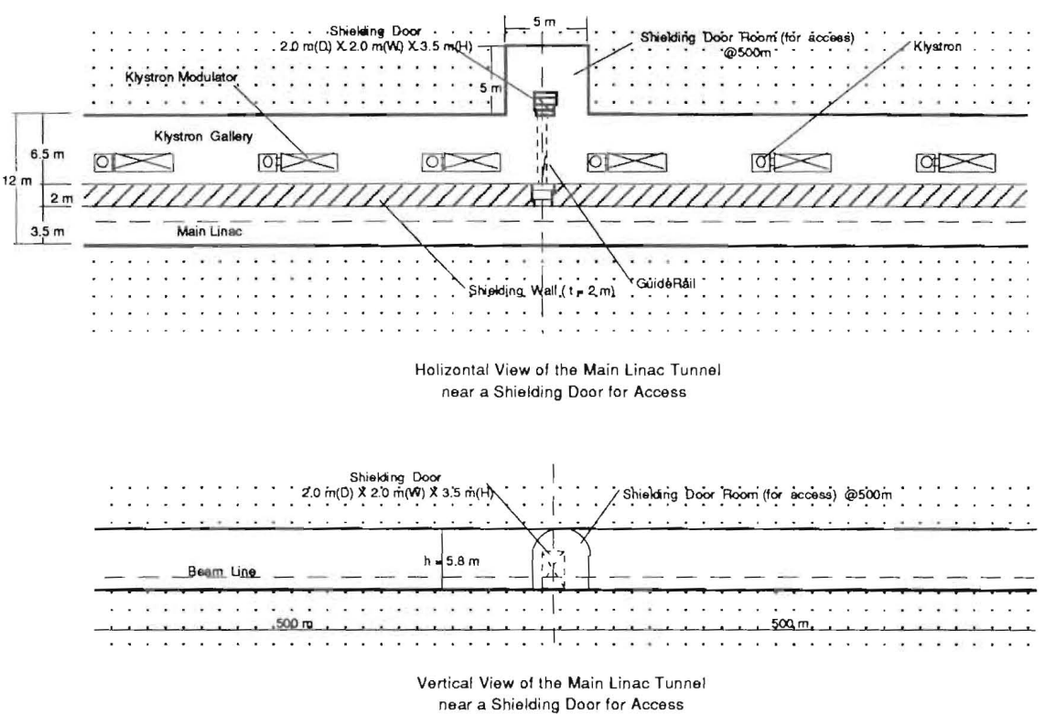


Figure 4.77: Top view of the access door between klystron gallery and accelerator tunnel.

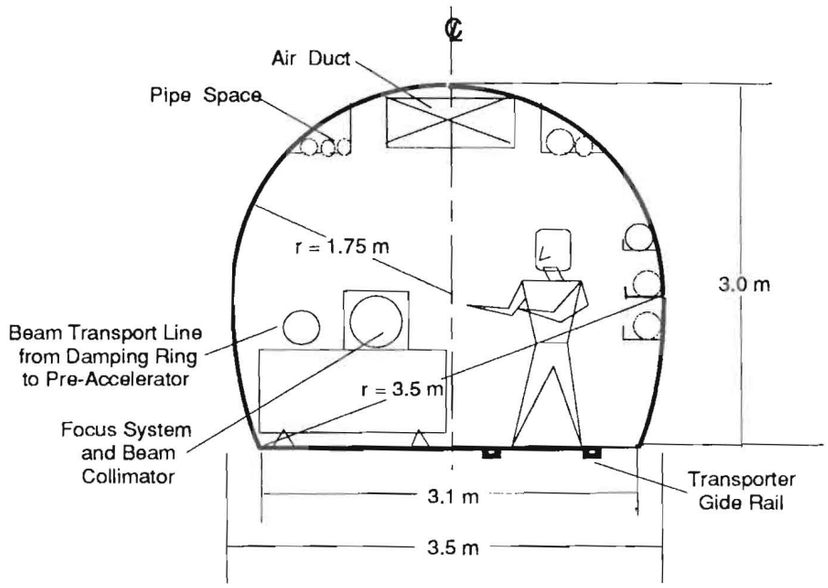


Figure 4.78: Beam line tunnel.

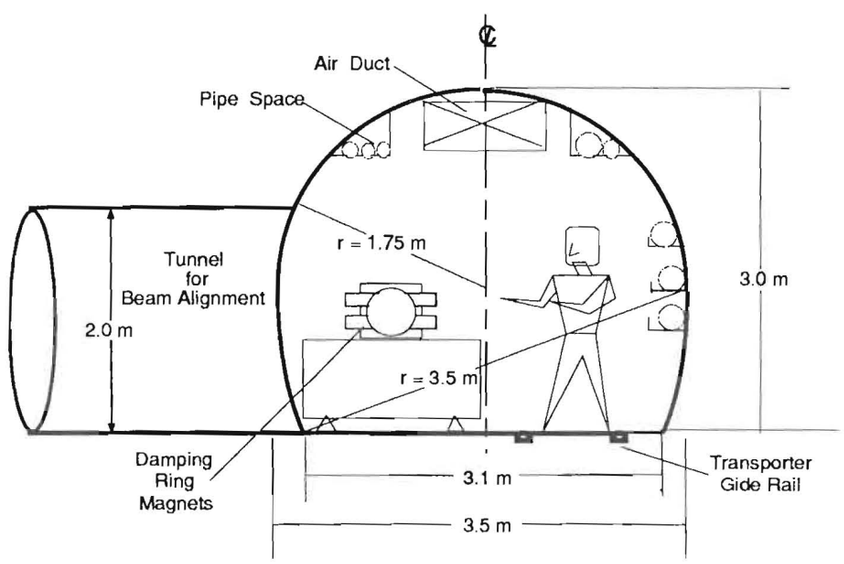


Figure 4.79: Damping Ring Tunnel.

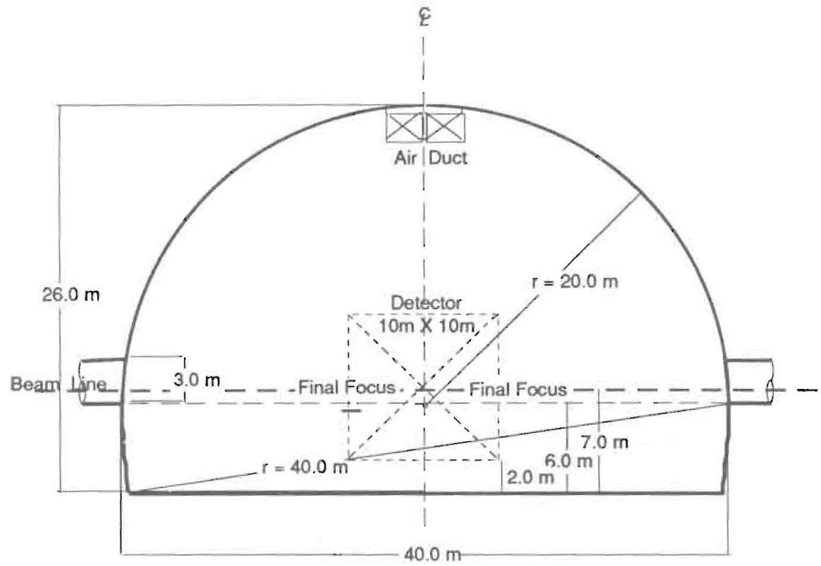


Figure 4.80: Detector-hall.

wall. Type B tunnel requires a thicker primary spray and secondary mask concreate than Type A tunnel. The construction cost of the main tunnel depends on the geological feature but falls in the rage of 2–3 MYens in both cases.

Table 4.32: Cost estimation of the tunnel for main linac

| Mountain | | A | B |
|---|---|---|---|
| Geological formation | | Granite | Periotite, Diabase Tuff, and Andesite Lava |
| Geological class | | $B - C_H$ | $C_M - C_L(D)$ |
| Primary spray concreate $t_s$ | mm | 100 | 150 |
| Secondary mask concreate $t_c$ | mm | 300 | 400 |
| Total Thickness of concreate $t_t$ | mm | 400 | 550 |
| Volume to be dug out | $m^3/m$ | 69.3 | 73.0 |
| Cost | MYen/m | 2.2 | 2.7 |

# Bibliography


[1] T. Nakanishi, H. Aoyagi, H. Horinaka, Y. Kamiya, T. Kato, S. Nakamura, T. Saka, M. Tsubata, Physics Letters **A158** (1991)345,
H. Aoyagi, H. Horinaka, Y. Kamiya, T. Kato, T. Kosugoh, S. Nakamura, T. Nakanishi, S. Okumi, T. Saka, M. Tawada, M.Tsubata, Physics Letters **A167** (1992) 415.

[2] T. Omori, Y. Kurihara, T. Nakanishi, H. Aoyagi, T. Baba, T. Furuya, K. Itoga, M. Mizuta, S. Nakamura, Y. Takeuchi, M. Tsubata, M. Yoshioka, Physical Review Letters Vol.**67** No.23 (1991) 3294

[3] T. Maruyama, E.L. Garwin, R. Prescot, G.H. Zapalac, J.S. Smith, J.D. Walker, Physical Review Letters Vol.**66** (1991) 2351.

[4] Y. Kurihara, T. Omori, T. Nakanishi, H. Aoyagi, T. Baba, K. Itoga, M. Mizuta, S. Nakamura, Y. Takeuchi, M. Tsubata, M. Yoshioka, Nuclear Instruments and Method, Vol.**A313** (1992) 393.

[5] T. Omori,Y. Kurihara, T. Nakanishi, H. Aoyagi, T. Baba, K. Itoga, M. Mizuta, S. Nakamura, Y. Takeuchi, M. Tsubata, M. Yoshioka, KEK Preprint 92-62, DPNU-92-32 (1992)*contribution to $XV^{TH}$ International Conference on High Energy Accelerators, July 20-24, Hamburg, Germany.*

[6] K. Yokoya and P. Chen, *Depolarization due to Beam-Beam Interaction in Electron-Positron Linear Colliders*, Proc. 8th International Symposium on High Energy Spin Physics, Minneapolis, Minnesota, USA, Sep. 12-17, 1988.

[7] S. Ecklund,*Positron Target Material Tests*, SLAC-CN-128, 1981.

[8] H. Braun, et al., *A Possible Design for the NLC e+ Source*, SLAC-PUB-5746, 1992.

[9] R. H. Helm, *Adiabatic Approximation for Dynamics of a Particle in the Field of a Tapered Solenoid*, SLAC-4, 1962.

[10] A. Kulicov, S. Ecklund, and E. Reuter, *SLC Positron Source Pulsed Flux Concentrator*, IEEE Part. Acc. Conf., San Francisco, 1991 .

[11] W. R. Nelson, H. Hirayama, and D. W. O. Rogers, *The EGS4 Code System*, SLAC-265, 1985.

[12] J. Urakawa et. al., *1.54GeV Damping Ring Design for Linear Collider*, KEK Report 90-2 April (1990) pp.33-44.

[13] J. Urakawa, *Preliminary Designs of 1.54GeV Damping Ring and Bunch Compressor for the JLC*, KEK Preprint 90-118 October (1990).

[14] H. Nakayama, *in Proceedings of the SLAC/KEK Linear Collider Workshop on Damping Ring, Ed. by J. Urakawa and M.Yoshioka*, KEK Proceedings 92-6 July(1991).

[15] T.O. Raubenheimer, L.Z.Rivkin, R.D.Ruth, *Damping Ring Designs for a TeV Linear Collider* SLAC-PUB-4808 (1988) and Proceedings of the DPF Summer Study, Snowmass '88.

[16] J. Urakawa et. al., *1.5GeV Damping Ring Design of the Test Accelerator Facility for Linear Collider* Particle Accelerator Vol.30(1990) Part IV, 1135

[17] J. Urakawa, *Accelerator Test Facility*, KEK Proceedings 91-10,1991, pp.18-33.

[18] L. Rivkin and K. Bane, SLAC-PUB-4645 (1988).

[19] M. Takao, T. Higo and K.L.F. Bane, *KEK report* **91-14** (1992).

[20] T. Weiland, Nucl. Instrum. Methods 212, (1983) 13.

[21] R. Klatt and T. Weiland, *Proc. of Linear Accelerator Conference*, SLAC, (1986) 282.

[22] K. Bane and R. Ruth, SLAC-PUB-4905 (1989).

[23] K. Oide and K. Yokoya, *KEK preprint* **90-10** (1990).

[24] K. Oide, *AIP Conf. Proc.* **230** (1990) 266.

[25] K. Kanazawa, *in OHO'91, Seminars on High Energy Accelerators, Ed. by J. Urakawa*, KEK (1991).

[26] K. Hirata and K. Yokoya, *KEK preprint* **91-212** (1992).

[27] T. O. Raubenheimer, *KEK Report* **92-7** (1992).

[28] K. Bane, *Optimizing the Average Longitudinal Phase of the Beam in the SLC Linac*, SLAC-AP-76 (1989)

[29] R. Ruth, *Multi-bunch Energy Compensation*, SLAC-PUB-4541 (1988)

[30] We owe this idea to S. Keifets at SLAC

[31] T. Shintake, *Nose-Cone Removed Pillbox Cavity for High-Power Klystron Amplifiers*, IEEE Trans. ED. vol.38, No.4. April 1991.

[32] T. Shintake, *The Choke Mode Cavity*, KEK preprint 92-51, July 1992, to be published in Jpn. J. Appl. Phys. Part 2, Letters.

[33] T. Shintake, *HOM-free Linear Accelerating Structure Using Choke Mode Cavity*, Proc. 17th Linear Accelerator Meeting in Japan, Sept. 1-3, 1992, Sendai, P.67.

[34] K. Yokoya, private comunication.

[35] M. Takao et al., KEK-Report 91-4, 1991.

[36] T. Taniuchi,KEK-Preprint, 91-152, 1992.

[37] T. Taniuchi, Proc. of the Third Japan Linear Collider Workshop, 1991.

[38] H. Deruyter et al., Proc. 1990 Linear Acc. Conf., Albuquerque, 1990.

[39] M. Yamamoto, Proc. of the Third Japan Linear Collider Workshop, 1991.

[40] R. Miller, Private comunication, LC-91, Protvino, 1991.

[41] K. L. F. Bane and R. Gluckstern, SLAC-PUB-5783,1992.

[42] M. Yamamoto, KEK-Preprint, 91-153, 1992.

[43] S. Yamaguchi, Private communication.

[44] T.Takata; "RECENT PROGRESS IN R&D WORK FOR THE JAPAN LINEAR COLLIDER" Proc. 15-th International Conference on High Energy Accelerators.(1992 July, Hamburg, Germany)

[45] H.Mizuno, J.Odagiri and T.Higo; "X-BAND KLYSTRON DIODE TEST FOR JAPAN LINEAR COLLIDER" Proc. 14th Intenational Conference on High Energy Accelerators Part4.Aug.1989 P-1125.

[46] H.Mizuno, J.Odagiri, T.Higo, M.Akemoto and H.Sakai; "X-BAND KLYSTRON FOR JAPAN LINEAR COLLIDER" Proceedings of the 1990 Linear Accelerator Conference September 10-14, 1990 Albuquerque, New Mexico P-168.

[47] T.Higo et al;"X-band Accelerating Structure for Japan Linear Collider" Proc. 15-th International Conference on High Energy Accelerators.(1992 July. Hamburg, Germany)

[48] W.B.Herrmannsfeldt; "ELECTRON TRAJECTORY PROGRAM" SLAC-226 UC-28(A)

[49] S.Kimura et al. " Long Life High Reliability Ir-coated Dispenser Cathode" Tech. Digest, IEDM. Washington D.C. 689.(1987)

[50] T.Shintake;" High-Power Klystron Simulations Using FCI-Field Charge Interaction Code" KEK report 90-3 MAY 1990 A/D.

[51] T.Shintake; "Nose-Cone Removed Pillbox Cavity for High-Power KLystron Amplifiers" IEEE TRANSACTIONS ON ELECTRON DEVICES. VOL. 38. NO.4 APRIL 1991. P917

[52] H.Mizuno,J,Odagiri,T.Higo and M.Akemoto;"X-band Klystron for Japan Linear Collider" Proc. 15-th International Conference on High Energy Accelerators. (1992 July. Hamburg, Germany)

[53] H.Mizuno,J.OdagiriT.Higo,H.Yonezawa and N.Yamaguchi; "X-Band Klystrons for Japan Linear Collider" Proc. 16-th International Conference (1992 August 23-28 Ottawa Ontario CANADA)

[54] See, e.g., K. Oide, AIP Conf. Proc. **249** (1992), p. 518 and its references.

[55] Final Focus Test Beam Project Design Report, SLAC–Repor–376 (1991)

[56] K. Oide, KEK–Preprint–92–58(1992).

[57] K. Yokoya and P. Chen, in *Frontiers of Particle Beams: Intensity Limitations*, Lecture Notes in Physics 400, Springer Verlag, ed. M. Dienes et. al., 1992, page 415.

[58] B. Baklakov, P. Lebedev, B. Parkomchuk, A. Sery, A. Sleptsov, B. Shiltsev, INP–PREPRINT–91–15(1991).

[59] F. Bulos et al., SLAC–PUB–5488, May 1991. Contributed to IEEE Particle Accelerator Conf., San Francisco, CA, May 1991.

[60] N.Yamamoto and K. Oide, KEK–Preprint 92–60(1992)

[61] L. Merminga, J. Irwin, R. H. Helm, R. D. Ruth, SLAC–PUB–5165(1992).

# Chapter 5

# Time Schedule and Cost Estimation

## 5.1 Time Schedule

The time schedule of the JLC-I project is shown in Fig. 5.1. According to the schedule required by the physics study group, the discovery run should commence around the year 2000. The construction of the straight tunnel for the main linacs is estimated to take three years, which are enough for the parallel construction of the detector-hall and the tunnels for the injector complex. The fabrication of the accelerator components for the startup energy needs four years, excluding the preparatory period for the plant and equipment investment, which match the schedule for the civil engineering. The installation of the machine components will be carried out in parallel with the component fabrication and will be finished no later than two years after the completion of the civil engineering. This schedule assumes that the construction speed is determined not by the funding but solely by technical considerations.

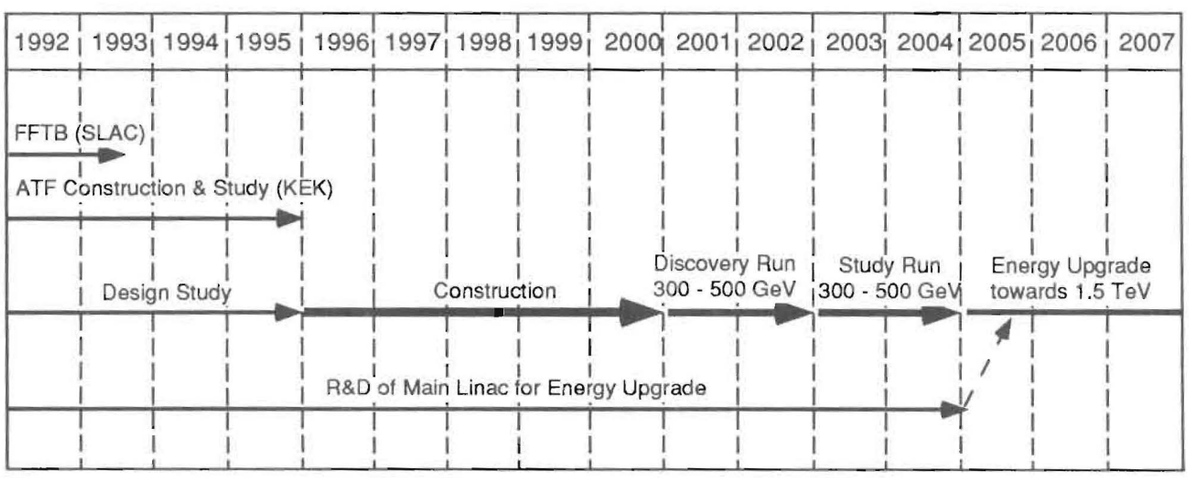


Figure 5.1: The time schedule of the JLC-I project.

## 5.2 Cost Estimations

The manufacturing process and the component massproduction are the two major factors to determine the required budget for machine construction. At present, however, it is not easy to

estimate the cost in the X-band JLC-I case, since the X-band technology is still in a developing stage.

In the case of S-band linacs, however, we know the costs of the 2.5 GeV S-band linac of Photon Factory at KEK and the 1.54 GeV S-band injector linac for the ATF(Accelerator Test Facility) under construction. Taking into account the massproduction effects known by experience, we can thus roughly estimate the total cost of the S-band JLC-I.

As for the C-band JLC-I, we can scale the cost of the S-band linac. The estimated cost turned out to be similar to that of the S-band JLC-I and is listed in Table. 5.1 together with those of the the civil engineering and the detector on the Japanese Yen basis as of 1992.

Table 5.1: Zero-th order cost estimate of JLC-I

| CENTER OF MASS ENERGY | 300 GeV (Billion Yen) | 500 GeV (Billion Yen) |
|---|---|---|
| **ACCELERATOR TOTAL** | **250** | **300** |
| Particle Sources & S-Band Linac (34 GeV total) | 10 | 10 |
| Polarized Electron Source (1 unit) | | |
| Conventional Sources (2 units) | | |
| Damping Ring Injectors (2 GeV ×2) | | |
| Pre-Accelerators (10 GeV ×2) | | |
| Positron Generator (10 GeV) | | |
| Damping Rings | 30 | 30 |
| Pre-Damping Ring (2 units) | | |
| Main Damping Ring (2 units) | | |
| Bunch Compressors (2 units) | | |
| Beam Transport to main Linac (2 units) | | |
| Main Linacs | 150 | 200 |
| Final Focus system | 20 | 20 |
| Instrumentation & Control System | 40 | 40 |
| **DETECTOR TOTAL** | **50** | **50** |
| **CIVIL ENGINEERING TOTAL** | **100** | **100** |
| Main Tunnel for Linac | 60 | 60 |
| Tunnel for Approach | 10 | 10 |
| Tunnel for Injector Complex | 10 | 10 |
| Detector Hall | 10 | 10 |
| Other Facilities | 10 | 10 |
| **ESTIMATED TOTAL COST** | **400** | **450** |

# Chapter 6

# JLC as a spearhead of high technology

## 6.1 Application as a synchrotron light source

### 6.1.1 Introduction

In the wide field of experimental studies using "light beam", it is very important to generate monochromatic and parallel beams with a small spot size, i.e., a high brilliance beam. Needless to say, a laser is the most suitable way to satisfy above requirements. But it is almost impossible to obtain laser beams in the Vacuum Ultra Violet (VUV) and soft and hard X-ray region with the exception of the use of a free electron laser. Another candidate to generate high brilliance beams in this energy region is the synchrotron radiation from high-energy electron and positron accelerators (Fig. 6.1(a)). Recent development of the various types of insertion devices such

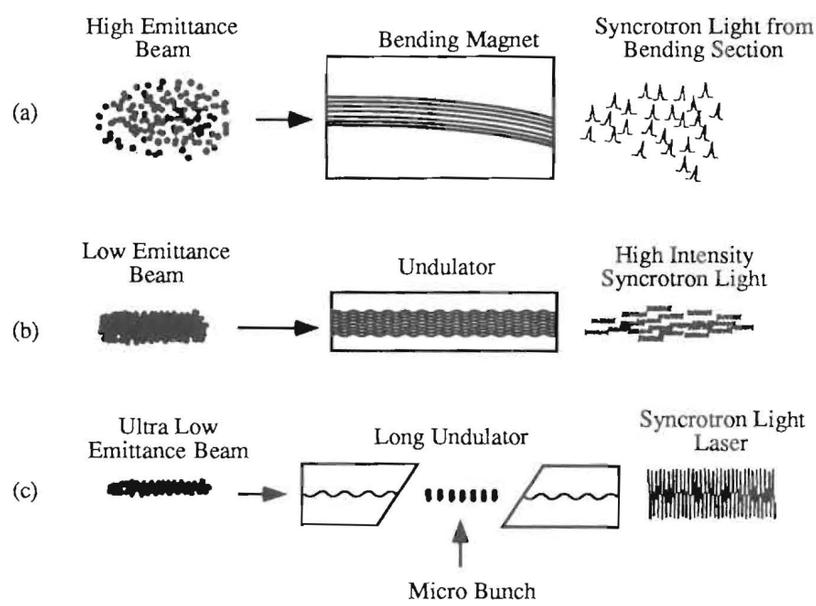


Figure 6.1: A schematic drawing of synchrotron lights (a) from high emittance beam with a bending magnet, (b) from low emittance beam with an undulator and (c) from extremely low emittance beam with a long undulator.

as undulators and wigglers makes it possible to generate a rather monochromatic and intense

synchrotron light in the X-ray region as is shown in Fig. 6.1(b) schematically. The radiation from insertion devices in existing accelerators, however, is still inferior to the laser beams from the view points of monochromaticity and brilliance. The characteristics of the synchrotron lights are influenced very much by the quality of the primary electron beam which passes through the insertion device. As a consequence, we must develop an accelerator which can produce a high brightness beam and a long insertion device to obtain high quality synchrotron lights, as shown in Fig. 6.1(c).

The development of world synchrotron radiation facilities has been closely related with high-energy accelerators to explore the energy frontier physics. A typical example is the utilization of the TRISTAN Accumulation Ring (AR) as a synchrotron light source. A multi-pole wiggler and an in-vacuum undulator are used routinely to generate circularly polarized lights for the magnetic Compton experiments and intense X-rays for the Mossbauer experiments, respectively, as a parasite of injecting the beam to the TRISTAN Main Ring (MR). Also, the application of the MR itself is promising for generating ultra high brilliant beams as is shown in Fig. 6.2. The very low emittance of $4 \times 10^{-10}$ radm is obtained by the MR when it is operated at the

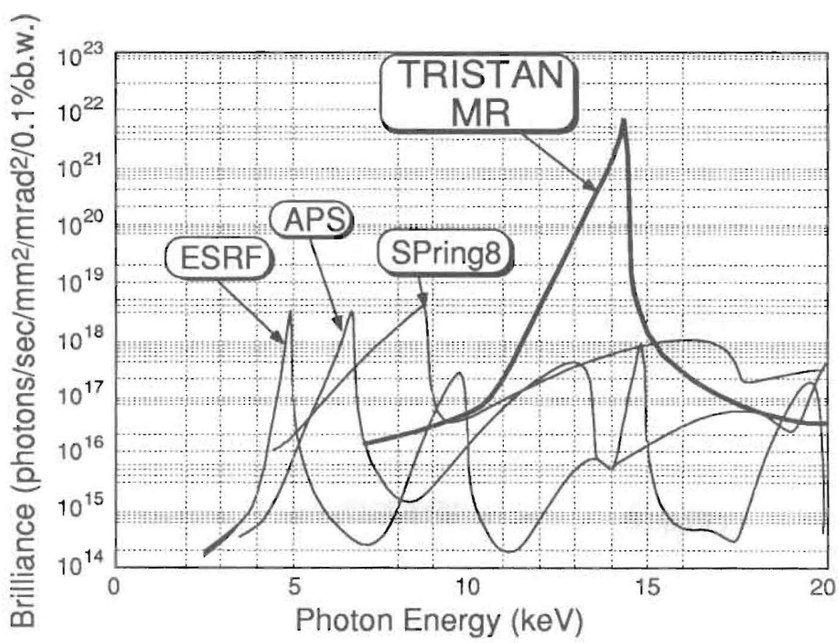


Figure 6.2: Brilliance of synchrotron radiation as a function of photon energy for various facilities.

energy below 5 GeV, with which soft X-ray free electron laser down to $\lambda \sim 1\mathring{A}$ can be realized. However, a hard X-ray below $\sim 1\mathring{A}$ is not obtainable even with TRISTAN. The only possibility to generate a hard X-ray free electron laser is to use the extremely low emittance beam from JLC.

### 6.1.2 Hard X-ray laser with JLC

The condition for the beam emittance ($\epsilon$) to generate a synchrotron radiation laser results from the uncertainty principle and is described as

$$\epsilon \leq \lambda,$$

where $\lambda$ is a wavelength of light. For example, in order to obtain the laser of $\lambda = 500$ Å(VUV region), $\epsilon$ must be smaller than $5 \times 10^{-8}$ radm, which can be realized by operating the Photon Factory Ring (PF) at 0.75 GeV. As is already mentioned above, soft X-ray synchrotron radiation ($\lambda \sim 4\AA$) can be generated by using the MR at 5 GeV, where $\epsilon$ of $4 \times 10^{-10}$ rad m can be achieved.

In order to realize a hard X-ray laser ($\lambda < 1\AA$), the emittance must be smaller than $1 \times 10^{-10}$ radm which can be achieved only by JLC. The extracted beam from the linac of JLC at the various stages between 7.5 and 20 GeV can generate hard X-rays with the use of long wigglers of 85 $\sim$ 330 m if the peak current is as high as 4 kA as is summarized in Table 6.1. The peak power of 8 $\sim$ 18 GW is obtained for the laser wavelength $\lambda$ of 0.2 $\sim$ 2.0 Å. These features are summarized in Fig. 6.3.

Table 6.1: Hard X-rays from JLC with long wigglers $\epsilon_{x,y} = 5 \times 10^{-10}$ at 15 GeV, $I_p$=4kA, $E_{spread} = 3 \times 10^{-4}$

| E | Length of Period | Length of Magnet | Field Strength | $\lambda$ | Peak Power |
|---|---|---|---|---|---|
| GeV | cm | m | gauss | Å | GW |
| 7.5 | 5 | 85 | 2600 | 2.0 | 18 |
| 10.0 | 4 | 100 | 3600 | 1.0 | 18 |
| 15.0 | 4 | 160 | 3750 | 0.46 | 17 |
| 20.0 | 3 | 330 | 5000 | 0.20 | 8 |

### 6.1.3 Application of X-ray laser

The most important application of X-rays is to analyze the structure of materials such as a crystal, amorphous, and liquid, and also to make perspective drawings using the penetrativity. The X-rays from the conventional tube-type sources or from the insertion devices such as those in the PF and AR, however, have no phase correlation between photons: we can make use of the intensity information only. Therefore, for the reconstruction of the three-dimensional structures using the X-ray diffraction, various sophisticated methods are needed such as the heavy atom method.

These complicated problems can be solved easily by using the coherent hard X-rays of $\lambda \sim 1$ Å. The three-dimensional structure of materials can be uniquely obtained by a simple physical method. Thus the impact to the field of solid state physics is drastic.

**Solid state physics**: As is already mentioned above, the array of atoms in a crystal, amorphous, and liquid can be made visible three-dimensionally in the Å accuracy by the information both in intensity and phase. Moreover, the hard X-ray laser enables us to observe, in real time, the transient (dynamic) phenomena such as the atomic motion during the phase transition and martensitic transformation and that in liquid or melted state.

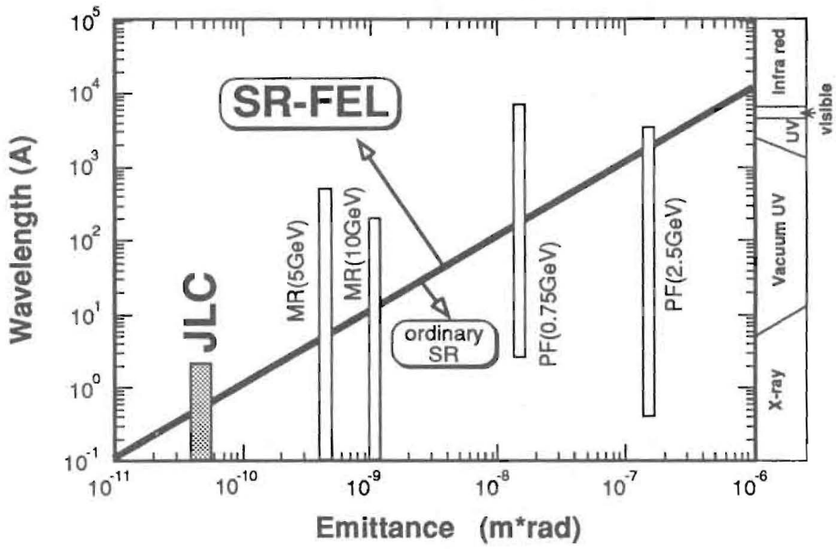


Figure 6.3: Wavelength of synchrotron light as a function of beam emittance

**Life science**: Up to now, the only method to observe the structure of the biopolymer like the double helical DNA which is the source of life is to use an electron microscope. This method is almost analogous to imagining an active fish in the sea by observing a grilled fish. The application of the hard X-ray laser opens the door to observe the activities of "fresh" microscopic living things such as HIV (AIDS Virus) and cancer cells. It will give rise to a quite clear understanding of the mechanism of breedings or proliferations. These studies are essential in finding out the ultimate weapons to attack such diseases.

The hard X-ray laser is not only useful for the above microscopic level but also for the macroscopic applications. Three-dimensional internal examination of a patient's body can be made easily by taking a holographic picture which is useful clinically.

**Manufacturing in nano-meter range**: The limit of the accuracy in manufacturing technologies using visible laser beam is the micro-meter range. The X-ray laser in the Ångrange is a key technology to step into the atomic level. A three dimensional placement and/or removal of individual atoms can be made quite easily. Also, by using the interference phenomena of X-ray lasers, ultra fine manufacturing in the nano-meter range can be realized, which is, for instance, useful to increase the density of computer memories drastically.

## ACKNOWLEDGEMENTS

The authors are indebted to the close collaboration with SLAC, without which they would have been suffered from a serious delay particularly in devoloping high power RF technologies. They should also mention the existence of many people, though not presently in the JLC group, who have encouraged and supported the promotion of the JLC project. This work was supported in part by a Grant-in-Aid for Scientific Research from the Ministry of Education of Japan (No.03302016: Physcs at Linear Colliders).

# JLC Group

The JLC group consists of particle and accelerator physicists who have been involved in the feasibility studies for the realization of the JLC project, and those who intend to join forces to further promote the project. This group always welcoms everybody who shares the same goal. The following are the group members as of December, 1992.


S. Matsumoto
*Department of Physics, Chuo University, Tokyo 112, Japan*

I. Endo, J. Kodaira, I. Watanabe, Y. Yasui
*Department of Physics, Hiroshima University, Hiroshima 730, Japan*

I. Adachi, M. Akemoto, H. Akiyama, M. Ando, S. Araki, Y. Doi, K. Egawa, Y. Fujii, K. Fujii, J. Fujimoto, M. Fukawa, Y. Funahashi, K. Hagiwara, T. Haruyama, H. Hayano, Y. Higashi, T. Higo, H. Hirayama, H. Ida, H. Ikeda, N. Ishihara, R. Itoh, K. Itoga, S. Iwata, S. Kamada, K. Kanazawa, J. Kanzaki, S. Kawabata, T. Kawamoto, M. Kikuchi, Y. Kimura, H. Kitamura, M. Kobayashi, T. Kobayashi, S. Koike, S. Koizumi, K. Kubo, T. Kubo, T. Kubo, Y. Kurihara, S. Kuroda, Y. Makida, K. Manabe, T. Matsui, H. Matsumoto, T. Mimashi, A. Miura, A. Miyamoto, H. Mizuno, T. Naitou, M. Nakai, H. Nakayama, Y. Namito, Y. Nemoto, J. Odagiri, T. Ohama, K. Oide, Y. Okada, T. Omori, Y. Otake, H. Sakai, H. Sakamoto, S. Sakanaka, M. Sakuda, Y. Shimizu, T. Shintake, J. Shirai, H. Sugawara, Y. Sugimoto, T. Sumiyoshi, T. Takashima, K. Takata, S. Takeda, S. Takeda, Y. Takeuchi, M. Tanaka, T. Taniuchi, T. Tauchi, M. Tejima, S. Terada, N. Terunuma, S. Tokumoto, T. Tsuboyama, T. Tsukamoto, S. Uehara, J. Urakawa, Y. Yamada, S. Yamaguchi, M. Yamamoto, N. Yamamoto, A. Yamamoto, M. Yamauchi, K. Yokoya, M. Yoshioka, F. Yuasa
*KEK, National Laboratory for High Energy Physics, Tsukuba, Ibaraki 305, Japan*

H. Fukui, K. Nagai, H. Matsumoto, M. Motoki, M. Nozaki, T. Suda, H. Takeda, S. Tanaka, K. Taruma, C. Yokoyama
*Faculty of Sciences, Kobe University, Kobe 657, Japan*

K. Katoh, N. Nakazawa, K. Tobimatsu
*Kogakuin University, Tokyo 163-91, Japan*

F. Kajino
*Faculty of Science, Konan University, Kobe 658, Japan*

Y. Honma
*School of Applied Medical Science, Kobe University, Kobe 654-01, Japan*

T. Kaneko
*Meiji Gakuin University, Yokohama 244, Japan*

T. Nakamura
*Faculty of Engineering, Miyazaki University, Miyazaki 889-01, Japan*

M. Aoki, H. Aoyagi, R. Kajikawa, T. Kosugou, K. Miyabayashi, K. Nakabayashi,
T. Nakanishi, E. Nakano, Y. Ohnishi, K. Shimozawa, A. Sugiyama, S. Suzuki, M. Tawada,
A. Terayama, T. Toyama, M. Tsubata, T. Yamaki
*Department of Physics, Nagoya University, Nagoya 464, Japan*

K. Miyashita
*Naruto University of Education, Naruto 772, Japan*

N. Tamura
*Faculty of Scienc, Okayama University, Okayama 700, Japan*

J. Haba, Y. Nagashima
*Department of Physics, Osaka University, Toyonaka 560, Japan*

T. Okusawa, T. Takahashi
*Department of Physics, Osaka City University, Osaka 558, Japan*

S. Kobayashi, A. Murakami
*Faculty of Science and Engineering, Saga University, Saga 840, Japan*

T. Kon
*Faculty of Engineering, Seikei University, Tokyo 180, Japan*

T. Takeshita
*Faculty of Liberal Arts, Shinshu University, Matsumoto 390, Japan*

M. Katsuya
*Faculty of Liberal Arts, Shizuoka University, Shizuoka 422, Japan*

R. Tanaka
*SSC Laboratory, 2550 Beckleymeade Ave., Suite 260, Dallas, TX 75237-3946 USA*

M. Igarashi
*Department of Physics, Tokai University, Hiraatsuka 259-12, Japan*

K. Hidaka
*Department of Physics, Tokyo Gakugei University, Tokyo 184, Japan*

M. Jimbo
*Tokyo Management College, Ichikawa 272, Japan*

T. Nakazato, M. Yamaguchi, M. Oyamada, T. Yamakawa, K. Abe, K. Hikasa, H. Murayama
*Faculty of Science, Tohoku University, Sendai 980, Japan*

K. Anraku, S. Asai, K. Kawagoe, T. Kawamoto, T. Kobayashi, S. Komamiya, T. Mashimo,
H. Matsunaga, T. Mitsui, T. Mori, M. Morii, S. Orito, T. Saeki, T. Sanuki, K. Shigekuni,
T. Tsukamoto, I. Ueda, T. Yoshida, K. Yoshimura
*Department of Physics and International Center for Elementary Particle Physics, University of Tokyo, Tokyo 113, Japan*

T. Ishii, H. Okuno
*Institute for Nuclear Study, University of Tokyo, Tokyo 158, Japan*

O. Nitoh, K. Takahashi
*Department of Applied Physics, Tokyo University of Agriculture and Technology, Tokyo 184, Japan*

Z. Hioki
*College of General Education, Tokushima University, Tokushima 770, Japan*

Y. Asano, S. Mori
*Institute of Applied Physics, University of Tsukuba, Tsukuba, Ibaraki 305, Japan*

T. Munehisa
*Faculty of Engineering, Yamanashi University, Kofu 400, Japan*

S. Nakamura, K. Sasaki
*Department of Physics, Faculty of Education, Yokohama National University, Yokohama 240, Japan*

R. Najima
*Yokohama College of Commerce, Yokohama 230, Japan*